Coupling water footprint modelling, satellite earth observation and meteorological data for irrigation volume savings in Mediterranean orchards

Dario De Caro

TUTOR

Prof. Giuseppe Ciraolo

Dipartimento di Ingegneria – Università di Palermo

CO-TUTOR

Ing. Fulvio Capodici

Dipartimento di Ingegneria – Università di Palermo

SUPERVISORS VISITING PERIOD

Prof. Carmelo Cammalleri

Dipartimento di Ingegneria Civile e Ambientale - Politecnico di Milano

Mr. Olivier Merlin

Centre d'Etudes Spatiales de la BIOsphère - Université de Toulouse

EXTERNAL REVIEWERS

Prof. Miguel Angel Jiménez Bello

Research Institute of Water and Environmental Engineering - Universitat Politècnica de València

Prof. Eleni Kokinou

Department of Agriculture – Hellenic Mediterranean University

FINAL EXAMINATION COMMITTEE

Prof. Angela Candela

Prof. Donatella Termini (Alternate Member)

Dipartimento di Ingegneria – Università di Palermo

Prof. Guido D'Urso

Dipartimento di Agraria - Università degli Studi di Napoli Federico II

Prof. Hector Nieto

Institute of Agricultural Sciences – Instituto de Ciencias Agrarias - Consejo Superior de Investigaciones Científic

PR Sicilia FSE+ 2021-2027 - CCI 2021IT05SFPR014
Avviso 01/2022 per il finanziamento di borse regionali di dottorato di ricerca in Sicilia - A.A 2022/2023
CIP BORSE.SICILIA.REG.NAZ/3.10.5/2021.IT.05.SFPR.014/002/04.7/09.02.03/A01_22/0003 CUP G71I22001190006

Dottorato di Ricerca in Chemical, Environmental, Biomedical, Hydraulic and Materials Engineering (D084)
Dipartimento di Ingegneria
Settore Scientifico Disciplinare CEAR-01/B (ex ICAR/02)
COSTRUZIONI IDRAULICHE E MARITTIME E IDROLOGIA

COUPLING WATER FOOTPRINT MODELLING, SATELLITE EARTH OBSERVATION AND METEOROLOGICAL DATA FOR IRRIGATION VOLUME SAVINGS IN MEDITERRANEAN ORCHARDS

Il Dottorando
Ing. Dario De Caro

Il Coordinatore
Prof. Giorgio Domenico Maria Micale

Il Tutor
Prof. Giuseppe Ciraolo

Il Co-Tutor
Ing. Fulvio Capodici

CICLO - **XXXVIII**
ANNO CONSEGUIMENTO TITOLO 2026

De Caro, D.

“Coupling water footprint modelling, satellite earth observation and meteorological data for irrigation volume savings in Mediterranean orchards”
Università degli Studi di Palermo, Dipartimento di Ingegneria
Dottorato di Ricerca in Chemical, Environmental, Biomedical, Hydraulic and Materials Engineering – XXXVIII Ciclo
(2023-2026)

Subject headings: hydrology, micro-meteorology, remote sensing, evapotranspiration

Cover picture: Camille Pissarro - Countryside at Louveciennes I (1870)

***A Cesare**,*

anche se oggi sei ancora piccolo per leggere e capire queste pagine, spero che un giorno tu possa avere la curiosità di sfogliarle. Mi auguro che tu cresca con il desiderio di conoscere, di farti domande e di guardare il mondo con occhi sempre curiosi.

Andrea: “Mi odia Nigel…”
Nigel: “Ed è un mio problema perché..? Ah ah, aspetta, no, non è un mio problema”
Andrea: “Senti, sul serio, io non so più cosa mi devo inventare perché, se faccio una cosa bene non mi viene riconosciuta, lei non dice neanche grazie, ma se sbaglio una cosa, lei… diventa… diabolica”
Nigel: “Allora, vattene”
Andrea: “Come?”
Nigel: “Vattene”
Andrea: “Andarmene?”
Nigel: “Io un’altra che prenda il tuo posto la trovo in cinque minuti, una che lo vuole veramente”
Andrea: “Ma, io non voglio andarmene, non è giusto. Però, io, dico solo che vorrei, insomma, un minimo di riconoscimento. Sto facendo il massimo per lei”
Nigel: “Andy, siamo seri, non stai facendo il massimo. Tu ti stai lamentando. Che cosa vuoi che ti dica, eh? Vuoi che ti dica “Poverina, Miranda ti ha preso di mira. Poverina, povera Andy”? Mmh, sveglia quarantadue! Lei non fa che il suo mestiere. Non lo sai che lavori nel posto che ha pubblicato alcuni tra i più grandi artisti del secolo? Halston, Lagerfeld, De la Renta, e quello che hanno realizzato, quello che hanno creato, è stato più creativo dell’arte stessa. Perché tu ci vivi dentro la tua vita. Beh, tu non, ovviamente, ma alcune persone sì. Tu credi che questa sia semplicemente una rivista. Questa non è semplicemente una rivista, questo è un luminoso faro di speranza per ... non lo so, diciamo un ragazzino che cresce a Rhode Island con sei fratelli che fa finta di andare a giocare a calcio, mentre invece va a scuola di cucito e legge Runway sotto le coperte di notte con una torcia. Tu non sai quanti personaggi leggendari siano passati per questi corridoi e, quel che è peggio, non ti interessa, perché tante persone si ammazzerebbero per lavorare qui, e invece tu ci onori della tua presenza. E ti chiedi anche perché lei non ti dia un bacio sulla fronte e non ti metta la lode quando le consegni i compiti alla fine giornata? Svegliati tesoro”
Andrea: “Ok, perciò sono io che sbaglio”
Nigel: “Uhm Uhm”
Andrea: “Senti, non è mia intenzione, solo che vorrei tanto sapere cosa fare per… Nigel, Nigel, Nigel”
Nigel: “No”

Il Diavolo Veste Prada, 2006

Acknowledgments

Il primo ringraziamento va alla mia regione, la Sicilia, che in un momento difficile è riuscita a offrirmi l'opportunità di sviluppare il mio progetto, finanziando borse di dottorato attraverso l'avviso pubblico "Avviso n. 01/2022 per il finanziamento di borse regionali di dottorato di ricerca in Sicilia A.A. 2022/2023" (*PR Sicilia FSE+ 2021-2027 - CCI2021IT05SFPR014 CIP BORSE.SICILIA.REG.NAZ/3.10.5/2021.IT.05.SFPR.014/002/04.7/09.02.03/A01_22/0003 CUP G71I22001190006*).

C'è una lunga lista di persone che desidero ringraziare; cercherò di citarle tutte, una per una, senza un ordine preciso, ma ciascuna ha contribuito, in modo diverso, alla realizzazione di questa tesi di dottorato.

Mamma e Papà, grazie di cuore per avermi reso la persona che sono oggi. I vostri insegnamenti mi hanno guidato lungo tutta la mia vita, e continuano a farlo, permettendomi anche questa volta di completare un lungo percorso e raggiungere questo importante traguardo. Mi avete sempre fatto vivere con serenità, stando al mio fianco e supportandomi in ogni scelta, senza mai lasciarmi la mano. Sono fiero di essere vostro figlio, ma ancora di più di avere voi come genitori.

Lorenzo merita un ringraziamento speciale per la sua grande pazienza: due anni fa ha deciso di salire su questo treno in corsa guidato da un macchinista un po' matto e, con coraggio, ha scelto di restare al mio fianco. Il "tornado" che sei era quello di cui avevo bisogno nella mia vita. SE LO AVVERTI, INSEGUILO. Grazie per i momenti di leggerezza che mi regali, per la tua premura e per la tua capacità di sostenermi, anche quando serve richiamarmi.

Luigi e **Andrea**, con voi i sorrisi, le risate e la leggerezza non mancano mai. Il vostro DarioDiario vi vuole tanto bene. Grazie per esserci sempre, con affetto sincero, presenza costante e quella capacità unica di farmi sentire a casa, in ogni momento. Siete un punto fermo importante.

Cesare, da quando sei nato hai reso le nostre vite più belle, una boccata d'aria fresca. Vederti crescere in questo anno e mezzo è stata, e continua a essere, una delle esperienze più belle della mia vita.

Questa idea progettuale è nata dalla passione per la ricerca del **Prof. Giuseppe Provenzano**, che purtroppo ci ha lasciati troppo presto. L'esperienza, sia lavorativa che umana, maturata nei due anni trascorsi al suo fianco come collaboratore resterà sempre con me. Aveva un modo di fare ricerca che appartiene a poche persone. Desidero ringraziarlo per gli insegnamenti che mi ha trasmesso e per la curiosità che ha saputo accendere in me, attraverso le tante domande di ricerca che abbiamo condiviso.

Un sentito ringraziamento va al mio tutor, il **Prof. Giuseppe Ciraolo**, che sin dal 2018 mi ha trasmesso la passione per il telerilevamento (*remote sensing*). I suoi insegnamenti mi hanno portato a essere oggi un ricercatore agli inizi del suo percorso, animato da curiosità, spirito di iniziativa e desiderio di approfondire.

Ringrazio il mio co-tutor, l'**Ing. Fulvio Capodici**, per aver sempre chiarito i miei dubbi, fornendomi strumenti e concetti adeguati. La sua disponibilità al confronto ha contribuito a rendere l'ambiente di ricerca stimolante, mantenendo al contempo un clima sereno e piacevole.

Il mio amico, l'**Ing. Matteo Ippolito**, merita un ENORME ringraziamento. Se oggi mi trovo in questo "vortice", in parte è anche colpa/merito suo: pur senza dirglielo mai abbastanza, gli sono profondamente grato. Ha creduto in me, nelle mie capacità e competenze, fin dal nostro incontro nel 2019. Se a volte non ho mollato, è anche grazie a lui. Ha sempre saputo rasserenarmi e trovare le parole giuste al momento giusto. La mia sicurezza è sapere che basta girarmi alla mia sinistra per trovarti sempre lì, pronto ad affrontare con me ogni genere di argomento, sia personale che lavorativo.

Desidero ringraziare anche i miei supervisors durante i periodi lontani dall'Università di Palermo. In particolare, il **Prof. Carmelo Cammalleri**, ricercatore di grande valore scientifico, sempre ricco di idee innovative e capace di offrire spunti di riflessione stimolanti e concreti. Ogni discussione con lui si trasforma in un'occasione di crescita. Inoltre, vorrei ringraziare **Olivier Merlin**, **Vincent Rivalland** e **Vincent Simonneaux** che, durante il periodo trascorso

presso il CESBIO, mi hanno permesso di confrontarmi con una realtà internazionale estremamente stimolante e formativa. Ho avuto l'opportunità di ampliare le mie conoscenze, approfondire nuovi approcci metodologici e acquisire strumenti scientifici e tecnici fondamentali per il mio percorso di ricerca. Il confronto con un ambiente multidisciplinare e internazionale ha rappresentato un'esperienza di grande crescita, sia dal punto di vista accademico che personale, contribuendo in maniera significativa ad arricchire il lavoro svolto e a rendere questa tesi più solida, completa e di alto livello scientifico.

I miei ringraziamenti arrivano anche lontano da Palermo, fino a Novara, dove vive la mia amica **Stella**. Basta sollevare il telefono per trovare conforto, e per esserci l'uno per l'altra: nonostante la distanza, questa si azzera ogni volta che ci sentiamo. Quando ci vediamo è sempre una festa. Riusciamo a sostenerci come solo dei veri migliori amici sanno fare. Per me è una figura fondamentale, un punto di riferimento prezioso.

Un grazie speciale a **Giuliana** e **Viviana**, le mie amiche del cuore, che illuminano il mio tempo libero tra chiacchiere e momenti di spensieratezza. I momenti passati davanti a un cocktail, parlando di tutto e di niente, sono quella leggerezza di cui ho bisogno nei periodi più pesanti.

Grazie a **Federica** e **Matilde**, che a Toulouse sono state la mia casa e il mio luogo sicuro quando mi trovavo lontano dalla mia.

Un grazie di cuore anche a **Simona**, **Peppe**, **Noemi** e **Luca**, per essermi stati accanto in questi tre anni. Ognuno di voi, a modo suo, ha lasciato un segno fatto di presenza, supporto e momenti condivisi che hanno reso questo percorso più leggero.

Ringrazio anche **la mia enorme famiglia** che è riuscita a sostenermi sempre, direttamente o indirettamente, da vicino e da lontano.

Infine, ringrazio tutti i membri del COmitato GEstione SOPpalco (**CO.GE.SOP**) per aver rallegrato le mie giornate tra caffè e pranzi condivisi, rendendo le pause momenti di leggerezza e sorrisi.

Sommario

L'attività di ricerca si concentra sull'analisi, la modellazione e il monitoraggio del *water footprint* (*i.e.*, la valutazione dell'evapotraspirazione effettiva, della traspirazione, dell'evaporazione, del contenuto idrico del suolo e degli apporti irrigui) nei sistemi agricoli irrigui, con particolare attenzione alle colture perenni mediterranee come agrumeti e oliveti. L'attività è inquadrata nel contesto del cambiamento climatico e, in particolare, nella crescente scarsità d'acqua e nella necessità di pratiche agricole sostenibili. Considerando che l'agricoltura rappresenta il principale consumatore di risorse idriche a livello globale (~70% dell'acqua dolce è utilizzata per scopi agricoli), il miglioramento del risparmio dei volumi irrigui e l'ottimizzazione dell'uso dell'acqua sono diventati aspetti fondamentali. In questa prospettiva, la ricerca mira a contribuire allo sviluppo di strumenti avanzati basati sui dati, capaci di supportare i processi decisionali nei sistemi moderni di agricoltura di precisione.

L'obiettivo principale della ricerca si basa sull'integrazione di molteplici fonti di dati e approcci modellistici per comprendere e quantificare meglio i processi che regolano gli scambi idrici nel continuum Suolo–Pianta–Atmosfera (SPA). Il continuum SPA rappresenta un sistema dinamico in cui l'acqua si muove dal suolo, attraverso le radici e le foglie della pianta, fino all'atmosfera tramite l'evapotraspirazione (effetto combinato di traspirazione ed evaporazione). Descrivere accuratamente questi processi è essenziale per stimare il fabbisogno idrico delle colture e migliorare la gestione dell'irrigazione. Per affrontare questa complessità, lo studio combina misure *in situ* con modellistica avanzata e tecniche di *remote sensing* satellitare, consentendo l'impostazione di un approccio analitico completo, multidisciplinare e multiscala.

L'attività sperimentale è stata condotta in due sistemi agricoli rappresentativi situati in Sicilia: un oliveto e un mandarineto. Queste colture sono state selezionate per la loro rilevanza nell'agricoltura regionale e per la loro diversa resilienza alle condizioni di stress

idrico. Entrambi i siti sono dotati di strumenti per la raccolta di variabili chiave del continuum SPA, tra cui sonde per il contenuto idrico del suolo, stazioni meteorologiche standard, sensori di flusso linfatico e torri di *eddy covariance*. Le misure *in situ* hanno svolto un duplice ruolo: fornire dati di input per la calibrazione dei modelli e fungere da riferimento per la validazione dei risultati, garantendo così robustezza e affidabilità.

Parallelamente alle osservazioni *in situ*, la ricerca ha esplorato l'uso di database meteorologici alternativi, in particolare dataset di rianalisi e previsione. Prodotti come ERA5-Land sono stati analizzati per valutarne l'affidabilità come sostituti delle misure *in situ*, soprattutto nelle aree dove i dati di campo sono scarsi o assenti.

Un elemento chiave della ricerca è l'integrazione, nei modelli di *water footprint*, dei dati di *remote sensing* satellitare, che consentono il monitoraggio dello stato delle colture e delle condizioni del suolo su ampie superfici in modo non invasivo e distribuito spazialmente. Piattaforme satellitari come MODIS, Sentinel-2, Landsat-8 e -9 e PlanetScope sono state utilizzate per ricavare indici di vegetazione e variabili biofisiche, tra cui *Normalized Difference Vegetation Index* (NDVI), *Normalized Difference Water Index* (NDWI) e *Fractional Vegetation Cover* (FVC). Inoltre, l'uso dei dati satellitari ha migliorato significativamente l'accuratezza delle stime, permettendo il passaggio da analisi puntuali a valutazioni distribuite a scala di campo e di distretto irriguo.

Esclusivamente per il mandarineto sono stati valutati diversi approcci, tra cui: un modello di bilancio idrico del suolo denominato *SAtellite Monitoring of Irrigation* (SAMIR); un modello di bilancio energetico superficiale denominato *Soil Plant Atmosphere and Remote Sensing Evapotranspiration* (SPARSE); e un metodo di partizionamento basato sulla misura della concentrazione di CO_2.

SAMIR è stato utilizzato per simulare l'evoluzione giornaliera del contenuto idrico del suolo e per stimare la traspirazione e l'evaporazione. I modelli di bilancio idrico del suolo sono relativamente semplici e hanno un impatto diretto sulla gestione irrigua (applicazioni operative). SPARSE è stato impiegato per

stimare l'evapotraspirazione effettiva come termine residuo del bilancio energetico superficiale. I modelli di bilancio energetico superficiale beneficiano dell'integrazione dei dati di *remote sensing* e della temperatura della superficie, ma soffrono di incertezze legate alle variabili atmosferiche. Il modello basato sulla concentrazione di CO_2 ha permesso di suddividere l'evapotraspirazione effettiva misurata dalla torre di *eddy covariance* in traspirazione ed evaporazione per confronti successivi. I risultati di SAMIR, SPARSE e del metodo di partizionamento sono stati confrontati tra loro.

Sia per il mandarineto che per l'oliveto, una tecnica di *Machine Learning* (ML) è stata utilizzata per determinare l'evapotraspirazione effettiva. Lo sviluppo di questo modello ML rappresenta una delle principali innovazioni della ricerca, in quanto consente di catturare relazioni complesse e non lineari tra variabili meteorologiche, contenuto idrico del suolo e indici di vegetazione. Il modello è stato addestrato utilizzando dati *in situ* (o di rianalisi) e dati satellitari, sfruttando i punti di forza di diverse fonti di dati.

Sulla base di questi risultati, è stato sviluppato un modello innovativo per la gestione irrigua, denominato IRRILEARNING. Inizialmente sviluppato e calibrato nell'oliveto sperimentale, è stato successivamente applicato ad altri oliveti dello stesso distretto irriguo. Il modello è progettato per supportare le decisioni irrigue in funzione di diversi obiettivi produttivi, sia per la produzione di olio che di olive da tavola. IRRILEARNING integra il modello ML con un modello bilancio idrico del suolo per la stima dei fabbisogni idrici. È stato configurato per tre finalità: i) supporto e verifica; ii) previsione; iii) gestione di scenari.

I principali risultati possono essere così riassunti:

• I dati di rianalisi rappresentano una valida alternativa alle variabili meteorologiche, soprattutto per applicazioni su larga scala e analisi di lungo periodo, sebbene presentino alcune discrepanze a scala locale;

• SAMIR è efficace per la gestione irrigua grazie alla sua semplicità e alla connessione diretta con la dinamica dell'acqua nel suolo, pur richiedendo una corretta parametrizzazione;

• SPARSE offre una migliore rappresentazione spaziale ma è più sensibile agli errori di misura;

• Il modello basato sulla concentrazione di CO_2 fornisce risultati soddisfacenti, ma richiede serie temporali complete e senza interruzioni;

• Il modello ML rappresenta un potente approccio *data-driven*, la cui efficacia dipende dalla qualità e quantità dei dati;

• IRRILEARNING è in grado di simulare la gestione irrigua in diversi scenari, migliorando significativamente l'efficienza d'uso dell'acqua.

In conclusione, la ricerca dimostra che l'integrazione di tecnologie avanzate, come il *remote sensing*, ML e assimilazione di dati multi-sorgente, rappresenta una strategia efficace e innovativa per migliorare il risparmio idrico in agricoltura. Questi approcci contribuiscono a ridurre i consumi idrici, aumentare l'efficienza e rafforzare la resilienza dei sistemi agricoli ai cambiamenti climatici, in linea con i principi dell'Agricoltura 4.0, le priorità di Horizon Europe e gli Obiettivi di Sviluppo Sostenibile (SDGs).

Abstract

The research activity focuses on the analysis, modelling, and monitoring of water footprint (i.e., the assessment of actual evapotranspiration, transpiration, evaporation, soil water content and, irrigation supplies) in irrigated agricultural systems, with particular emphasis on Mediterranean perennial crops such as citrus and olive orchards. The activity is contextualized within the climate change topic and, particularly, on the increasing water scarcity and sustainable agricultural practices. Given that, agriculture represents the largest consumer of freshwater resources worldwide (~70% of freshwater is used for agriculture purposes), improving irrigation volume savings and optimizing water use have become pivotal. In this perspective, the research aims to contribute to the development of advanced data-driven tools capable of supporting decision-making processes in modern precision agriculture systems.

The main goal of the research is based on the integration of multiple data sources and modelling approaches to better understand and quantify the processes ruling water exchanges within the Soil–Plant–Atmosphere (SPA) continuum. SPA continuum represents a dynamic system in which water moves from the soil, through plant roots and leaves, and finally to the atmosphere via evapotranspiration (joint effect of transpiration and evaporation). Accurately describing these processes is essential for estimating crop water requirements and improving irrigation scheduling. To address this complexity, the study combines in situ measurements with advanced modelling and satellite remote sensing techniques, allowing the setup of a comprehensive, multi-disciplinary and multi-scale analytical approach.

The experimental activity was conducted in two representative agricultural systems located in Sicily: an olive and a citrus orchard. These cultivars were selected due to their relevance in regional agriculture and their different resilience to water stress conditions. Both sites are equipped with instruments collecting key variables data of the SPA continuum, including soil water content probes, standard meteorological stations, sap flow probes and, eddy covariance flux

towers. In situ measurements served a dual role: as input data for model calibration and, as a reference for validating model outputs; thus, ensuring robust and reliable results.

In parallel with in situ observations, the research explored the use of alternative meteorological databases, particularly, reanalysis and forecasting datasets. Products such as ERA5-Land (reanalysis database) were analyzed to assess their reliability as surrogate of in situ measurements, especially in areas where in field data are scarce or unavailable.

A key component of the research is the integration within water footprint models of satellite remote sensing data, which enables the monitoring of crop health and soil conditions over large areas in a non-invasive and spatially distributed way. Satellite platforms such as MODIS, Sentinel-2, Landsat-8 and -9 and PlanetScope were used to retrieve vegetation indices and biophysical variables, including the Normalized Difference Vegetation Index (NDVI), the Normalized Difference Water Index (NDWI) and the Fractional Vegetation Cover (FVC). Furthermore, the use of satellite data significantly improved the estimation accuracies, allowing the transition from point-scale analyses to spatially distributed assessments at field and irrigation district scales.

Exclusively for the citrus orchard several approaches were assessed including: a Soil Water Balance (SWB) model, named SAtellite Monitoring of Irrigation (SAMIR); a Surface Energy Balance (SEB) model named Soil Plant Atmosphere and Remote Sensing Evapotranspiration (SPARSE); a carbon-based partitioning method.

SAMIR was used to simulate the daily evolution of soil water content and to estimate actual transpiration and evaporation. SWB models are relatively simple with a direct impact on irrigation management (operational applications). SPARSE was also set up to estimate actual evapotranspiration as a residual term of the energy balance at surface. SEB models benefit from the integration of remote sensing data and land surface temperature particularly, even if they suffer uncertainties of atmospheric input variables. A partitioning

model based on the relationship between carbon assimilation and water vapor exchange allowed to split *in situ* actual evapotranspiration, monitored by the flux tower, into transpiration and evaporation for further comparisons. Outcomes from SAMIR, SPARSE and partitioning method were also cross compared.

On both citrus and olive orchards, a Machine Learning (ML) technique allowed determining actual evapotranspiration. The setup of this ML model is one of the major innovations of this research. The ML model allows capturing complex, nonlinear relationships among meteorological variables, soil water content, and vegetation indices. This model was trained using both *in situ* (or reanalysis) and remotely sensed data, allowing to leverage the strengths of multiple data sources.

Building on these findings, the step forward was the development of an innovative model for irrigation management, named IRRILEARNING. It was initially developed and calibrated within the olive orchard experimental site and, subsequently applied to other olive orchard fields located within the same irrigation district. The model was specifically designed to support irrigation decision-making under different production objectives, allowing analyses for both oil production and table olive production. This model integrates the ML model with a SWB model providing crop water need assessments. IRRILEARNING was set up to operate for three different aims: i) support and check; ii) forecasting; iii) scenario management.

Main general results are here following summarized:

• Reanalysis data represents reliable alternatives to meteorological variables, making them particularly suitable for large-scale applications and long-term analyses. Nevertheless, some discrepancies were observed at the local scale, mainly due to differences in spatial resolution limiting their ability to capture site-specific conditions. Despite these limitations, reanalysis data represents a valuable resource for supporting both water footprint modelling and irrigation management, especially in data-scarce environments;

- SAMIR was found to be effective for irrigation management due to its simplicity and direct connection to soil water content dynamics, even if it requires accurate parameterization. It is simple to be applied, and it provides continuous daily outcome time-series; however, by solving the daily soil water balance, it relies on vegetation stress needing irrigation data or the setup of rules on irrigation strategy;
- SPARSE offers better spatial representation but is more sensitive to measurement errors. Although model applications are limited to cloud-free satellite acquisitions, it provides high accuracy estimation of all the instantaneous components of the surface energy balance;
- Carbon-driven model results are quietly good; it requires no-gap and long input data timeseries to be implemented; thus, it is limited by sensors operativeness;
- ML model provides a powerful data-driven alternative, although its performance heavily depends on the quality and quantity of input data;
- IRRILEARNING is capable to simulate irrigation scheduling under different management strategies and climatic conditions. At the field scale, IRRILEARNING can reproduce the temporal evolution of key variables such as actual evapotranspiration, soil water content and, water stress coefficient. Overall, results demonstrate that IRRILEARNING is a flexible and robust tool for irrigation management, capable of adapting to different production objectives and climatic scenarios while promoting significant water savings allowing improvements in water resource use efficiency.

In conclusion, this research demonstrates that the integration of advanced technologies, such as remote sensing, ML, and multi-source data assimilation, represents an effective and innovative strategy for improving irrigation volumes savings in agriculture. These approaches contribute to reducing water consumption, increasing water use efficiency, and strengthening the resilience of agricultural systems to climate variability and change, in line with the principles of Agriculture 4.0. Furthermore, they are consistent with the strategic

priorities of Horizon Europe, particularly the missions on Climate Change Adaptation and Soil Health and Food, as well as with the Sustainable Development Goals (SDGs), including Goal 2 (Zero Hunger), Goal 13 (Climate Action), and Goal 15 (Life on Land), thereby supporting the transition towards more sustainable and climate-resilient farming systems.

Contents

List of Figures

List of Tables

List of Symbols

Symbol	Unit	Description
A	km	Swath width
(e_s-e_a)	kPa	Actual vapor pressure deficit
$(x-x')^T(x-x')$	-	Squared Euclidean distance between two eigenvectors
α	-	Albedo
$\alpha\beta$	-	Absorbance
AW	-	Available water
cp	J g^{-1} K^{-1}	Air-specific heat capacity at constant pressure
Cws	-	Short-term water stress factor
Δ	kPa $°C^{-1}$	Slope of saturation vapor pressure curve
D_r	mm	Depletion
E_a	W m^{-2}	Absorbed energy
$ea(T_{dew})$	kPa	Actual vapour pressure
ε_b	-	Dielectric constant
E_i	W m^{-2}	Incident energy
E_r	W m^{-2}	Reflected energy
$es(T_a)$	kPa	Saturated vapour pressure
E_t	W m^{-2}	Transmitted energy
ET_a	mm d^{-1}	Actual Evapotranspiration
ETo	mm d^{-1}	Crop Reference Evapotranspiration
ET_p	mm d^{-1}	Potential Evapotranspiration
f(x)	-	Latent variable in the GPR model
F_a	Hz	frequency measured by the sensor in air
F_s	Hz	frequency measured by the sensor in soil
fs	-	Shape coefficient
FVC	-	Fraction Vegetation Cover
F_w	Hz	frequency measured by the sensor in water
γ	kPa $°C^{-1}$	Psychrometric constant

Symbol	Unit	Description
g_f	-	Constant that depends on the geometric configuration of the electrode
G_0	W m^{-2}	Soil Heat Flux
GPP	mmol m^{-2} s^{-1}	Gross Primary Production
GWC	g g^{-1}	Gravimetric Water Content
H	W m^{-2}	Sensible Heat Flux
I	mm or m^3	Irrigation
K_c	-	Crop Coefficient
K_{cb}	-	Basal Crop Coefficient
K_e	-	Soil Evaporation Coefficient
K_s	-	Water Stress Coefficient
LAI	m^2 m^{-2}	Leaf Area Index
LE	W m^{-2}	Latent Heat Flux
LST	°K	Land Surface Temperature
M_d	g	Mass of the dry sample
MSWP	MPa	Midday Stem Water Potential
M_w	g	Mass of the wet sample
n	-	Number of the data
NDVI	-	Normalized Difference Vegetation Index
NDWI	-	Normalized Difference Water Index
NEE	mmol m^{-2} s^{-1}	Net Ecosystem Exchange
P	mm	Precipitation
p_{FAO}	-	FAO depletion factor
P_r	W	Received power
P_s	W	Emitted power
$P_{VAR\%}$	%	Precipitaion percentage variation
Re	mmol m^{-2} s^{-1}	Ecosystem Respiration
Re_{day}	mmol m^{-2} s^{-1}	Diurnal respiration
Re_{night}	mmol m^{-2} s^{-1}	Nocturnal respiration
RH	%	Relative Humidity
RH_{Max}	%	Maximum relative humidity
RH_{Mean}	%	Average relative humidity
RH_{Min}	%	Minimum relative humidity
R_n	W m^{-2}	Net Radiation
R_s	W m^{-2}	Global solar radiation

Symbol	Unit	Description
σ_n^2	-	Variance
SWC	$cm^3\ cm^{-3}$	Soil Water Content
SWC_{fc}	$cm^3\ cm^{-3}$	Soil Water Content at Field Capacity
SWC_r	$cm^3\ cm^{-3}$	Residual Soil Water Content
SWC_s	$cm^3\ cm^{-3}$	Saturated Soil Water Content
SWC_{wp}	$cm^3\ cm^{-3}$	Soil Water Content at Wilting Point
$T_{a\text{-}Max}$	°C	Maximum air temperature
$T_{a\text{-}Mean}$	°C	Mean air temperature
$T_{a\text{-}Min}$	°C	Minimum air temperature
T_c	°K	Canopy temperature
T_{day}	°C	Mean diurnal air temperature
T_{dew}	°C	Dew point temperature
T_{night}	°C	Mean nocturnal air temperature
$\tau\pi$	-	Transmittance
T_s	°K	Soil surface temperature
U_{10}	$m\ s^{-1}$	Wind speed measured at 10 m above ground
U_2	$m\ s^{-1}$	Wind speed measured at 2 m above ground
x	-	Input training dataset
X		Indicator function
$\bar{x}$	-	Mean of the reference data
x_i	-	Reference data
Y	MPa	Water potential
y	-	Output training dataset
y_i	-	Estimated/modelled data
z_r	cm	Root zone depth
Γ	-	Gamma function
ε	-	Noisy observations of the true function
λ	$J\ kg^{-1}$	Latent heat of vaporization
λ	nm	Wavelenght
λ_S	-	Relative characteristic length scale
ρ	-	Reflectance
ρ	$g\ m^{-3}$	Air density
ρ_a	$g\ cm^{-3}$	Soil bulk density
ρ_{NIR}	-	Near Infrared reflectance

Symbol	Unit	Description
ρ_{RED}	-	Red reflectance
ρ_{SWIR}	-	Short-Wave Infrared reflectance
ρ_w	g cm^{-3}	Density of water
σ_0	dB	Backscattering coefficient
σ_S, λ_S, σ_ε, σ_M, λ_M, λ_f	-	Hyperparameters
σ_{wC}	mmol m^{-2}	Covariance between vertical wind and CO2 concentration
σ_{WQ}	g m^{-2} s^{-1}	Covariance between vertical wind speed and water vapor density
σ_{WT}	m K s^{-1}	Covariance between vertical wind speed and air temperature
σ_ε^2	-	Measurement error
υ	-	Matern kernel parameter

List of Acronyms

Acronyms	Description
3DVAR	Three-Dimensional Variational Data Assimilation
4DVAR	Four-Dimensional Variational Data Assimilation
a.g.l.	above ground level
a.s.l.	above sea level
ANBI	Associazione Nazionale Bonifiche Irrigazioni e Miglioramenti Fondiari
b.g.l.	below ground level
BOA	Bottom Of Atmosphere
BOLAM	BOlogna Limited Area Model
BS	Bare Soil
CO_2	Carbon Dioxide
CPR	Capillary Rise
CR	Closure Ratio
CSI	Critical Success Index
CWR	Crop Water Requirement
D.P.R.	Decreto del Presidente della Repubblica
DESA/POP	Department of Economic and Social Affairs / Population Division
DisTrad	Disaggregation procedure for thermal sharpening
DN	Digital Number
DOY	Day Of Year
DP	Deep Percolation
E	Evaporation
e.g.	exempli gratia
EC	Eddy Covariance
ECMRWF	European Centre for Medium Range Weather Forecasts
EF	Electric Field
EM	ElectroMagnetic
EnKF	Ensemble Kalman Filter
EOS	Earth Observing System
EPS	Ensemble Prediction System
ESA	European Space Agency
ET	Evapotranspiration

Acronyms	Description
EVI	Enhanced Vegetation Index
Exp	Exponential
F	Subsurface and deep flow
FA	Flight Altitude
FAO	Food and Agriculture Organization
FAR	False Alarm Ratio
FDR	Frequency Domain Reflectometry
FIS	Feature Importance Score
FOV	Field Of View
GCM	General Circulation Model
GFS	Global Forecast System
GIS	Geographic Information System
GPR	Gaussian Process Regression
GSD	Ground Sample Distance
H_2O	Water
HV	Highly Vegetated
i.e.	id est
IFOV	Instantaneous Field Of View
IoT	Internet of Things
IPCC	Intergovernmental Panel On Climate Change
k(x,x')	Kernel Covariance function
L	Fixed value of inductance
LAM	Limited Area Model
LDAR	Light Detection And Ranging
LRWC	Leaf Relative Water Content
m(x)	Mean function
MAE	Mean Absolute Error
MBE	Mean Bias Error
MIS	MultiSpectral Instrument
ML	Machine Learning
MODIS	Moderate Resolution Imaging Spectroradiomete
MOLOCH	(non-hydrostatic limited-area meteorological model)
MV	Moderately Vegetated
NASA	National Aeronautics and Space Administration
NCEP	National Centers for Environmental Prediction
NIR	Near Infrared
NOAA	National Oceanic and Atmospheric Administration

Acronyms	Description
NSE	Nash–Sutcliffe Efficiency
NWP	Numerical Weather Prediction
OLI	Operational Land Imager
PBL	Planetary Boundary Layer
PDEs	Partial Differential Equations
PoD	Probability of Detection
R^2	Coefficient of Determination
R^2 [b]	Determination coefficient (forced-origin regression)
RAW	Readily Available Water
RCP	Representative Concentration Pathways
RDI	Regulated Deficit Irrigation
RGB	Red Green Blue
RMSE	Root Mean Square Error
RQ	Rational Quadratic
RQs	Research Questions
RS	Remote Sensing
RWC	Relative Water Content
SaC	Support and Check
SAMIR	SAtellite Monitoring for Irrigation
SAR	Synthetic Aperture Radar
SAVI	Soil Adjusted Vegetation Index
SDGs	Sustainable Development Goals
SE	Squared Exponential
SEB	Surface Energy Balance
SEBAL	Surface Energy Balance Algorithm for Land
SF	Scaled Frequency
SIAS	Servizio Informativo Agrometeorologico Siciliano
SILAM	SIcilia Limited Area Model
SPA	Soil–Plant–Atmosphere
SPARSE	Soil Plant Atmosphere and Remote Sensing Evapotranspiration
SR	Surface Runoff
SV	Sparsely Vegetated
SWB	Soil Water Balance
SWIR	ShortWave Infrared
T	Transpiration
τ	Momentum flux

Acronyms	Description
TAW	Total Available Water
TC	Total Capacity
TDR	Time Domain Reflectometry
TIR	Thermal Infrared
TIRS	Thermal Infrared Sensor
TSEB	Two Source Energy Balance
UASs	Unmanned Aerial Systems
UNESCO	United Nations Educational, Scientific and Cultural Organization
USDA	United States Department of Agriculture
UTC	Universal Transverse Mercator
UV	UltraViolet
VIS	Visible
VIs	Vegetation Indices
VPD	Vapor Pressure Deficit
vs	versus
WGS	World Geodetic System
WRF	Weather Research and Forecasting model
WUE	Water Use Efficiency

Introduction

Water footprint analysis in agriculture: an overview

Monitoring the water footprint in agriculture is pivotal for evaluating actual crop water requirements and for identifying strategies aimed at water saving. Agriculture accounts for 70% of total global freshwater withdrawals and represents the largest user of fresh water. In recent decades, the growing pressure on natural resources has made water management a central issue for agricultural sustainability. According to the Intergovernmental Panel On Climate Change (IPCC) (2023) report, the world will face serious water, energy, and food challenges in both the near and long term due to increasing food demand and progressive resource degradation. At the same time, global population growth is expected to further exacerbate these pressures. The World Population Prospects 2022, recently released by the United Nations Educational, Scientific and Cultural Organization (UNESCO), indicate that the population will reach ~8.5 billion by 2030 and is projected to peak at ~10.5 billion by 2080, leading to a substantial increase in the demand for food and freshwater resources (DESA/POP, 2022).

In this context, the adoption of sustainable agriculture practices is of paramount importance to minimize water consumption while ensuring food security. Climate change has significantly altered precipitation patterns at both regional and global scales, affecting the natural availability and distribution of freshwater resources. These changes are manifested through more frequent and intense drought events, unpredictable rainfall regimes, and a general decrease in surface and groundwater availability. In Mediterranean ecosystems, characterized by hot and dry summers and precipitation mainly occurring in autumn and winter, the increase in atmospheric evaporative demand and the reduction in water availability have further aggravated drought-related problems. Recent studies highlight

the need to encourage farmers, especially in drought-prone regions, to adopt innovative solutions that optimize water quantity and quality, ensuring a more environmentally friendly agricultural future for coming generations (Lap et al., 2023).

Italy represents a critical case within the European context, being among the countries with the highest irrigation water demand. For example, during the 2009–2010 irrigation seasons, ~12 Mm^3 of water were used to irrigate about ~2.5 million hectares (ISTAT, 2014). However, irrigation efficiency remains low, with an estimated 50% of water losses during distribution and application. Water management for irrigation in Italia involves multiple professional figures operating across different administrative levels and coordinated through a complex network of institutions. Irrigation distribution is managed by the *Associazione Nazionale Bonifiche Irrigazioni e Miglioramenti Fondiari* (ANBI) through 141 territorial reclamation consortiums, covering ~60% of the national territory and supporting diverse agricultural systems adapted to local climatic conditions. In Sicily, irrigation management is entrusted to two main reclamation consortiums, instituted with the *Decreto del Presidente della Repubblica* (D.P.R) n. 467 of 12/09/2017: the *Consorzio di Bonifica della Sicilia Occidentale* and the *Consorzio di Bonifica della Sicilia Orientale* which oversee areas dominated by typical Mediterranean crops such as olives, citrus, vineyards, open-field vegetables, and arable crops.

To address water scarcity and improve water use efficiency, the adoption of sustainable and dynamic irrigation strategies is essential. The optimization of irrigation water use can be achieved by accurately estimating crop water requirements and by implementing advanced irrigation management approaches, such as Regulated Deficit Irrigation (RDI) (GonzÁlez-Altozano and Castel, 2000; Consoli et al., 2014; Stagno et al., 2015; Rallo et al., 2017; Puig-Sirera et al., 2021). These strategies aim to reduce water consumption by controlling irrigation in real time as a function of soil and plant water status, without negatively affecting crop growth and productivity. This requires the integration of sensors, data aggregation techniques, and

models to develop Decision Support System tools capable of supporting farmers and water managers. Such approaches are fully aligned with the 2030 United Nations Agenda for Sustainable Development and with several Sustainable Development Goals (SDGs). They directly contribute to: SDG 2 (Zero Hunger) by supporting sustainable agricultural practices capable of increasing productivity while reducing pressure on water resources; SDG 13 (Climate Action) by enhancing the adaptive capacity of agricultural systems to climate variability and increasing resilience to drought conditions; SDG 15 (Life on Land) by promoting the sustainable management of soil and water resources and limiting land degradation. Moreover, the proposed approaches are consistent with the strategic priorities of Horizon Europe, especially within the missions and clusters addressing Adaptation to Climate Change and Soil Health and Food. In this context, improving irrigation efficiency, monitoring the Soil Plant Atmosphere (SPA) continuum, and optimizing water use through data driven and precision agriculture tools represent key actions to support climate resilient farming systems, preserve soil functionality, and ensure long-term food security.

In this framework, Agriculture 4.0 represents the most recent evolution of precision farming technologies, focusing on increasing crop productivity, improving the sustainable use of natural resources, enhancing resilience to climate change, and reducing food waste. To achieve these objectives, it is necessary to monitor the SPA continuum by measuring the parameters governing the hydrological, hydraulic, and physical functioning of the system. Monitoring activities can be carried out through *in situ* sensors, such as soil water content probes, standard weather stations, and micrometeorological eddy covariance towers, or indirectly through modelling approaches.

Evapotranspiration represents the key variable in linking SPA continuum, agricultural management, and water resources (Fisher et al., 2017). Modeling evapotranspiration has many applications in agricultural water management. Evapotranspiration represents one of

the primary components of the hydrologic cycle; its accurate estimation is mandatory to optimize agricultural water management.

Among these, Soil Water Balance (SWB) models estimate evapotranspiration by accounting for the temporal evolution of water stored in the root zone as a function of precipitation, irrigation, runoff, drainage, and atmospheric demand. These models describe the partitioning of available water between soil storage and evapotranspiration, linking crop water use to soil hydraulic properties, root depth, and crop specific parameters. Their strength lies in their conceptual simplicity and their direct connection with irrigation management, making them particularly suitable for operational applications and scenario analyses, although their accuracy depends on the correct representation of soil–plant parameters and initial conditions (Allen et al., 1998; Marletto et al., 2007; Pereira et al., 2020).

Surface Energy Balance (SEB) models estimate evapotranspiration as a residual term of the surface energy balance, partitioning net radiation into latent and sensible heat fluxes. By combining radiometric surface temperature and vegetation information with meteorological inputs. Their main advantage is the capability to provide assessments without requiring detailed soil information, although they are sensitive to uncertainties in radiation, surface temperature, and atmospheric forcing (Norman et al., 1995; Bastiaanssen et al., 1998; Cammalleri et al., 2012b; Awada et al., 2019).

Evapotranspiration can also be inferred from carbon flux measurements by exploiting the physiological coupling between carbon assimilation and water vapor exchange. Measurements of CO_2 fluxes allow the partitioning of ecosystem-scale exchanges into transpiration and evaporation components through water carbon coupling frameworks. These approaches provide physically based estimates of evapotranspiration and its components, serving as valuable references for model calibration and validation (Li et al., 2019).

Finally, Machine Learning (ML) models offer a data-driven alternative for estimating evapotranspiration by learning nonlinear relationships between meteorological variables, vegetation characteristics and, soil conditions. By integrating multi-source data, these models can capture complex interactions within the SPA continuum. While their performance strongly depends on data quality, ML approaches provide flexible and scalable tools that complement physically based models (Kim et al., 2020; Bellido-Jiménez et al., 2021; Chen et al., 2022).

These models can benefit from remote sensing techniques as input data for evapotranspiration estimation, through the retrieval of vegetation biophysical properties from observations acquired in the VISible (VIS), Near InfraRed (NIR), ShortWave InfraRed (SWIR) and, Thermal InfraRed (TIR) regions of the electromagnetic spectrum. The increasing availability of satellite remote sensing observations further enhances these approaches, offering new opportunities for large-scale, continuous, and non-invasive monitoring of crop water status and irrigation practices. Two main remote sensing-based approaches have been proposed. The first is an analytical approach in which crop related input parameters (*e.g.*, Leaf Area Index, crop height, and albedo) are derived from multispectral VIS–NIR images. This approach explicitly links surface biophysical properties to evapotranspiration through physically based formulations (Papadavid, 2011; Jégo et al., 2012). The second approach relies on Vegetation Indices (VIs) (*e.g.*, NDVI, SAVI, or EVI), computed from VIS–NIR reflectances. In this case, evapotranspiration is indirectly estimated by parameterizing crop development and water use as a function of vegetation spectral response (Pôças et al., 2020). In addition, the use of remote sensing enables the transition from point-scale estimates to spatially distributed assessments at field (*i.e.*, satellite and/or Unmanned Aerial Vehicle) or irrigation district scales (*i.e.*, satellite).

Several gridded weather and climate datasets are currently available at the global scale and can be freely accessed, providing quasi-continuous meteorological information with adequate temporal

coverage and moderately high spatial resolution. These products are generated through the combination of numerical weather prediction models and data assimilation techniques, which integrate heterogeneous observations to produce spatially and temporally consistent fields of atmospheric and land-surface variables. Owing to their gap-free structure and long-term continuity, reanalysis datasets are widely used in hydrological and agro-meteorological applications, particularly in areas where *in situ* measurements are sparse or unavailable, and represent a reliable alternative source of meteorological forcing for evapotranspiration and crop water requirement assessments (Parker, 2016).

Finally, the use of short-term meteorological forecasting data represents a key asset for irrigation management, as it allows anticipating boundary conditions of models, supporting timely irrigation scheduling, while remaining consistent with the temporal scale of decision-making processes in agricultural systems (Jones et al., 2003).

Thesis objectives

The planning of irrigation water uses through strategies that meet environmentally sustainable policies is one of the main challenges of the 21st century.

The overall objective of this thesis is to investigate the potential of integrating satellite Earth observation and meteorological data, derived from *in situ* measurements, reanalysis products, and short-term forecasts, for the modelling and monitoring of the water footprint in irrigated orchards, with particular emphasis on Mediterranean perennial cropping systems (*i.e.*, citrus and olive orchards).

Overall, the work is willing to answer the following Research Questions (RQs):

- *RQ1.* Can reanalysis data be considered reliable surrogates of *in situ* measurements, and what is the impact of their use as model inputs on the estimation of crop water requirements in terms of latent heat flux, actual evapotranspiration, and soil water content?

- *RQ2.* What are the performances of modern Machine Learning models in estimating actual evapotranspiration when trained using key variables of the soil–plant–atmosphere continuum (from *in situ* measurements or reanalysis products) and satellite images, with the aim of developing spatially distributed models?
- *RQ3.* How can actual evapotranspiration estimates derived from Machine Learning models be integrated with soil water balance models to improve irrigation management and irrigation forecasting, also in the context of climate change scenarios?
- *RQ4.* What are the strengths, limitations, and potential synergies among soil water balance models, surface energy balance models based on remote sensing data, and Eddy Covarince-based partitioning method for estimating transpiration and evaporation?

Through these RQs, the thesis seeks to highlight the complementarities and synergies between models, data-driven approaches, and remote sensing techniques, contributing to the development of scalable, data-efficient, and operational tools for sustainable irrigation management in the context of Agriculture 4.0.

Thesis structure

The thesis is organized into introduction, 6 chapters and, conclusions and reccomendations. Chapters are divided into three parts: PART I – Theoretical background (Chapter 1: Hydrological cycle, Chapter 2: Input data for actual evapotranspiration modelling, Chapter 3: Actual evapotranspiration modelling); PART II – Materials and methods (Chapter 4: Materials, Chapter 5: Methods); PART III – Applications, results and discussions (Chapter 6: Results and discussions). In the following a brief description of the contents are given.

- Introduction

In introduction the key points of the water footprint monitoring and the and the enhancements in spatially distributed evapotranspiration modelling, related to increasing data availability are briefly introduced. The main objectives of the research are introduced through the RQs, with the addition of this outline of the thesis structure.

PART I – Theoretical background

- Chapter 1. Hydrological Cycle

This chapter introduces the hydrological cycle, describing the continuous circulation of water between the atmosphere, land, and oceans. The chapter focuses on evapotranspiration, the combined process of soil evaporation and plant transpiration, highlighting its dependence on meteorological conditions and plant characteristics. Understanding ET is crucial for studies related to water footprint and for an efficient and sustainable irrigation water management, linking atmospheric processes with crop water requirements.

- Chapter 2. Input data for actual evapotranspiration modelling

This chapter presents the input data required for modelling actual evapotranspiration. It covers variables within the Soil-Plant-Atmosphere (SPA) continuum, including *in situ* measurements of soil and plant-atmosphere layers, as well as data derived from reanalysis and forecasting products. The chapter also discusses the use of remote sensing data as an additional source of information for accurate actual evapotranspiration estimation.

- Chapter 3. Actual evapotranspiration modelling

This chapter focuses on modelling actual evapotranspiration using different approaches. It covers surface energy balance models, soil water balance models, carbon cycle models, and explores the use of machine learning as a smart solution to support precision irrigation.

PART II – Materials and methods

- Chapter 4. Materials

This chapter describes the materials used for the study, including the experimental fields. It also presents the data sources employed for actual evapotranspiration modelling, including in situ, reanalysis and forecasting meteorological variables and remote sensing data from satellite platforms.

- Chapter 5. Methods

This chapter describes the models used for actual evapotranspiration estimation and analysis. It covers data processing of in situ, reanalysis, forecasting, and remote sensing data, and describes different modelling approaches as well as the statistical indices adopted for model evaluation.

- Chapter 6. Results and discussion

The application and results are the main components of the thesis, where all the results obtained from the application of the previously introduced methodologies were assessed and critically analysed, also by means of objective criteria based on the computation of statistical indices.

- Conclusions and recommendations

Finally, in this chapter the main results and findings of the research are summarized, including also recommendations for further work and possible future advances.

PART I

Theoretical Background

Chapter 1. Hydrological Cycle

The present water on Earth, in the subsurface and on the surface, constitutes the hydrosphere; within it, circulation takes place through the hydrological cycle (Shiklamanov, 2009).

Like all cycles, the hydrological cycle of water has neither a beginning nor an end. The mechanisms that make up the hydrological cycle connect atmosphere, lands, and oceans. In each cycle, water undergoes changes in its physical state: from vapor to liquid or solid, and then back to vapor again (Narasimhan, 2009; Inglezakis et al., 2016) (**Figure 1.1**).

The hydrological cycle expresses the principle of mass conservation and establishes a relationship between the hydrological fluxes associated with a fixed control volume and the variation in the amount of water contained within that volume. The nature of the balance strongly depends on the scale chosen for the control volume, which also determines the characteristic times involved. A system the size of the entire globe has characteristic times of a seasonal or annual scale, while for smaller systems (*i.e.*, river basins) the relevant times are those of precipitation events (*i.e.*, hours).

One of the surfaces that delimit the control volume usually coincides with the ground surface, so that the flux terms are:

- the flow of water from the atmosphere to the surface (precipitation and snow);
- the flow of water over the land surface (surface runoff);
- the flow of water from the atmosphere into the soil (infiltration);
- the flow of water within the soil (subsurface flow and deep percolation);
- the flow of water from the soil to the atmosphere through vegetation (transpiration);
- the flow of water from the soil surface to the atmosphere (evaporation).

The storage terms, on the other hand, are:

- soil water content (*SWC*);

- groundwater;
- ocean water;
- surface water (*e.g.*, streams, lakes).

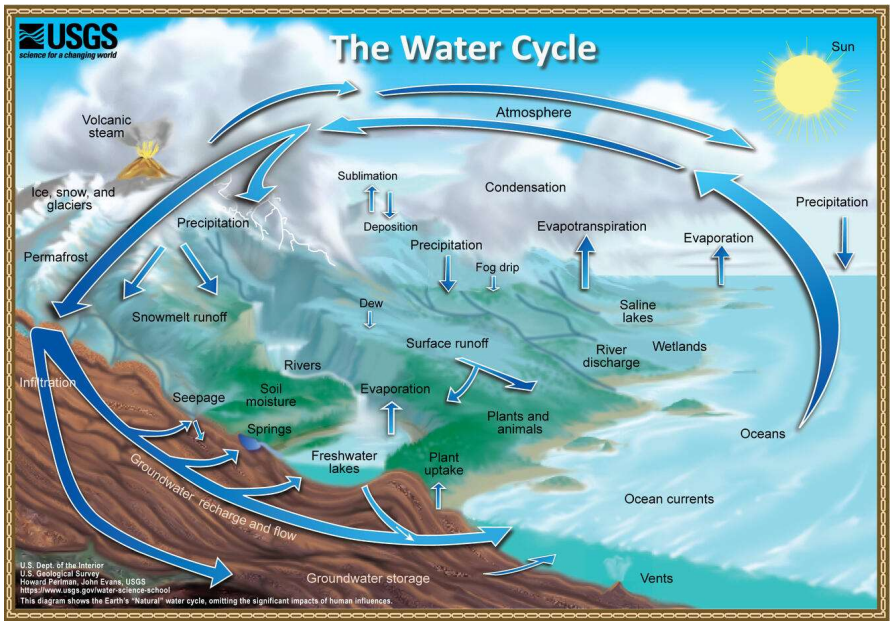

Figure 1.1 Hydrological cycle (from: *https://www.usgs.gov/media/images/natural-water-cycle-jpg*)

All the processes involved in the formation and transport of water vapor are driven by solar energy, while the formation of runoff from precipitation is essentially governed by gravity (Bales, 2003).

Water contained in vegetation and in bodies of water evaporates under the action of solar radiation and, in the form of clouds, is transported by atmospheric movements. About 90% of atmospheric water comes from Evaporation (E), while the remaining 10% originates from Transpiration (T).

Under peculiar temperature and pressure conditions, clouds condense again, and water returns to the ground as Precipitation (P), snow, or hail. Solid precipitation tends to accumulate on the surface until it melts due to solar radiation and rising temperatures. In the case of liquid precipitation, the soil can retain all or part of it, depending

mainly on the type of soil, vegetation cover, and initial soil water content conditions.

Once infiltrated into the soil, part of the water is absorbed by plant roots and released into the atmosphere through transpiration, part drains downslope through the soil, and part recharges the underlying aquifers. The portion of precipitation that does not infiltrate tends to flow over the land surface, collecting into the hydrographic network, composed of streams and channels that gather surface runoff and convey it to the outlet section of the drainage basin.

To the water flowing through the drainage network are added, over time and depending on the permeability of the soils it crosses, volumes of water coming from the unsaturated zones (as subsurface or interflow runoff) and from the saturated zones (as groundwater flow) (Waring and Running, 2007; Rai et al., 2017).

1.1 Hydrological balance

Hydrological phenomena involve a large number of variables, and for this reason they can only be represented in a simplified manner, using schematizations (Pokorný and Rejšková, 2008).

The global hydrological cycle can be represented as a system divided into three subsystems:

- the first subsystem, represented by water in the atmosphere, involves the processes of P, E, interception, and T;
- the second subsystem concerns surface waters, which are subject to surface flow processes;
- the third subsystem is represented by waters undergoing subsurface flow, groundwater flow, and infiltration.

A quantitative analysis of the global hydrological cycle requires, for practical reasons, the use of a limited portion of the surface (*i.e.,* control volume). For this reason, it is necessary to refer to a simplified model, or hydrological system.

For a volume bounded at the top by the ground surface and at the bottom by a zero-flow surface (which can be imagined as arbitrarily deep), the hydrological balance (Hartmann, 2016) can be written as:

$$\frac{dV}{dt} = P - SR \pm F - ET \quad \textbf{(1.1)}$$

where $\frac{dV}{dt}$ encompasses all the storage terms contained within the control volume in a certain time window, P is precipitation, SR is the surface runoff leaving the control volume, F is the subsurface and deep flow leaving the control volume (*e.g.*, capillary rise, deep percolation), and ET is evapotranspiration. The infiltration flux does not appear explicitly due to the choice of the control volume, but it is implicitly included because it determines the partitioning of the meteoric input into surface runoff and deep flows.

Thus, in hydrological studies, it is important to understand the processes through which water is returned to the atmosphere, either by evaporation from the soil or by traspiration from vegetation. This knowledge is also of primary importance in the agricultural field, where the efficient management of irrigation practices, closely linked to Crop Water Requirement (CWR), requires a thorough understanding of these processes. For this reason, particular attention must be devoted to the study of the first subsystem, represented by the water present in the atmosphere, which encompasses the processes of evaporation and transpiration (Burt et al., 1997; Clemmens and Burt, 1997).

1.2 Evaporation

Evaporation is the process through which surface liquid water is vaporized and transferred to the atmosphere via turbulent motions of the air near the surface. Water can evaporate either from a water surface or directly from the soil.

E over a given time interval is defined as the ratio between the volume of water evaporated during that interval and the area of the evaporating surface. The average evaporation rate is the ratio between the evaporation depth and the time interval over which it occurred. The evaporation depth is influenced by several factors: *i*. atmospheric conditions such as radiation, air temperature, pressure and relative air humidity, and wind speed, which determine the evaporative potential of the atmosphere; *ii*. nature of the evaporating surface such as open

water, snow, ice, bare soil, or vegetated soil, which affects its capacity to supply water for *E*. The capacity is unlimited for a large water surface until the water is exhausted, whereas for soil it is limited by the capillary rise of water from deeper layers to the surface.

Soil evaporation refers to the transfer of water from the soil into the atmosphere without passing through the plant system (Penman, 1948; Monteith, 1986; Dolman et al., 2014), and is generally considered a non-productive water loss, even though it contributes to microclimate cooling. Soil texture influences *E* since macroporosity enhances evaporation in the surface layers, while microporosity generally acts as a hindrance. Therefore, under the same environmental conditions, *E* is more intense in coarse-textured soils and more limited in fine-textured to medium-textured soils (Eames et al., 1997).

1.3 Transpiration

Plant transpiration is the process through which water is absorbed by plant roots and released into the atmosphere as vapor *via* leaf transpiration. This process not only impacts the CWR but also plays a crucial role in cooling plants and maintaining their thermal balance (Penman, 1948).

This process is regulated both by atmospheric conditions and by a series of mechanisms related to plant biology and morphology: *i*. the root system greatly influences the ability of the plants to absorb water; generally, *T* is more intense in plants with shallow roots when soils are wet, and in plants with deep roots when soils are dry; *ii*. the larger the leaf surface, the higher the *T*; *iii*. stomatal openings are the main pathway through which the plant releases water into the atmosphere. Transpiration is more intense in plants with many stomata, but it is important to consider their ability to close, since the guard cells of stomata respond to unfavorable humidity conditions, plants capable of closing their stomata exhibit lower *T*; *iv*. The phenology affects *T* by altering plant behaviour, morphology, and physiology according to the season. Transpiration decreases when the plant enters dormancy, with or without leaf loss, and is higher during periods of active growth, such as vegetative growth, flowering, and fruit development.

1.4 Evapotranspiration

Given the simultaneous nature of evaporation and transpiration, it is very difficult to study them separately. Therefore, they are generally referred to together as evapotranspiration, considered as a single process equal to the sum of the two (Irmak, 2008; Katul and Novick, 2009; Miralles et al., 2020) (**Figure 1.2**).

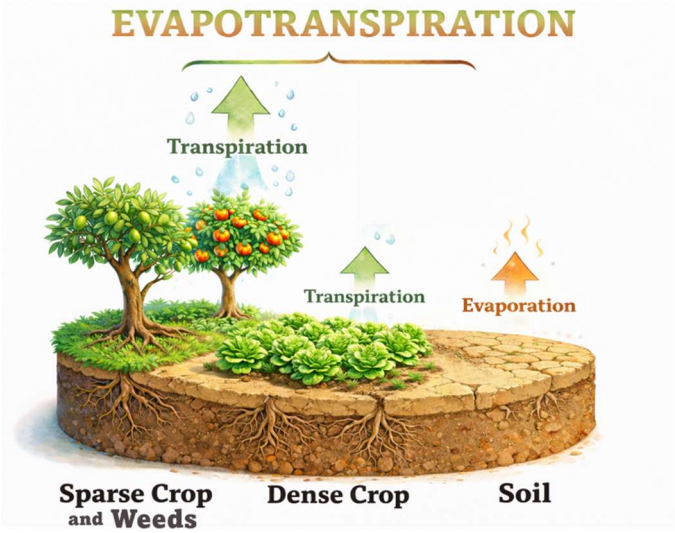

Figure 1.2 Evapotranspiration scheme

Meteorological variables, like solar radiation, air temperature, relative air humidity, wind speed, play a particularly important role in the *ET* study (Thornthwaite, 1948; Priestley and Taylor, 1972; Shuttleworth and Wallace, 1985; Allen et al., 1998).

Solar radiation is the primary energy source driving evapotranspiration. It provides the latent heat necessary to transform liquid water into vapor, thus controlling the rate at which water is transferred from the land surface to the atmosphere. Moreover, solar radiation influences plant physiological processes, such as stomatal opening and photosynthesis, which regulate T rates. High radiation levels promote greater vapor pressure deficits and, consequently, higher transpiration, if *SWC* is not a limiting factor.

Since both *T* and *E* are processes that absorb heat from the environment, *ET* is more intense at higher temperatures. It is also

greater when the air is dry, because the evaporative demand of the atmosphere increases as air humidity decreases.

Wind speed plays a crucial role as well: in stagnant air, a gradient of decreasing relative air humidity forms from the layers near the soil and vegetation to higher layers. Wind generally creates turbulence that mixes these layers, thereby enhancing *ET*, with intensity increasing alongside wind speed. However, the nature of the wind must also be considered: warm and/or dry winds intensify *ET*, while cold and/or humid winds reduce it.

In summary, evapotranspiration is most intense during the day, in the warmer months, and on dry, windy days, while it decreases at night, in cooler months, on humid or overcast days, and in the absence of wind.

Three important conditions are necessary for *ET* (the combined process of *E* and *T*) to occur: *i*. availability of water at the surface; *ii*. sufficient energy to allow the phase change from liquid to vapor; *iii*. a transport mechanism to remove the vapor from the area. Without this transport, the atmosphere above the surface gradually reaches saturation, which prevents further evaporation (Stanhill, 2019).

In estimating *ET*, it is common to refer to three different definitions (Yang, 2023):

- crop reference evapotranspiration or Atmospheric water demand (*ETo*): represents the atmospheric evaporative demand, calculated using mathematical models or measured over a hypothetical, extensive grass-covered surface under optimal water and nutrient conditions (Allen et al., 1998; Sabzevari and Eslamian, 2023);
- potential evapotranspiration under standard conditions (ET_p): refers to evapotranspiration from a well-watered and optimally managed crop surface of sufficient extent (Thornthwaite, 1948; Monteith, 1986; Allen et al., 1998)
- actual evapotranspiration (ET_a), under non-standard conditions: this is the definition that most closely represents real conditions, when the crop is subject to water stress or suboptimal growth conditions (Allen et al., 1998).

Thus, the understanding and quantification of ET_a are pivotal for the sustainable management of water resources in agriculture. *ET* is therefore directly linked to CWR. Accurate estimation of ET_a allows the determination of the irrigation volumes needed to maintain plant health and productivity while minimizing water waste.

Irrigation management and hydrological studies often focus on *ET* as a whole (Gong et al., 2024). However, since only *T* corresponds to the actual physiological water use by plants, greater emphasis should be placed on this component. A precise assessment of *T* enables a more precise understanding of CWR and contributes to the development of irrigation strategies that are both efficient and sustainable, aligning water supply more closely with plant needs and environmental conditions.

Chapter 2. Input data for actual evapotranspiration modelling

As discussed in *Chapter 1*, Evapotranspiration (*ET*) plays a fundamental role in the hydrological cycle and balance. It was also emphasized that monitoring this process is pivotal for irrigation management and for the preservation of water resources in agriculture. *ET* is governed by a complex interaction between meteorological variables and the specific characteristics of soil and vegetation. For this reason, understanding and studying the Soil Plant Atmosphere (SPA) continuum is essential. Equally important is the identification of the key variables that describe and control this continuum. Some of these variables are easier to measure than others. In most practical applications, the more easily measurable variables are used as inputs to models, whose outputs correspond to the ET_a.

2.1 Soil-Plant-Atmosphere (SPA) continuum variables

The SPA continuum is an ecohydrological concept that describes the continuous pathway through which water moves from the soil, passes through plants, and ultimately enters the atmosphere. This movement follows a pressure (or water potential) gradient, linking together soil, plant, and atmosphere in a single and dynamic system. The term SPA was introduced by Philip (1957), emphasizing the continuity of the water connection along this pathway.

Water transport in the SPA continuum is driven by differences in water potential (Ψ), a measure of the free energy of water. The atmosphere has extremely low (highly negative) water potential compared to that inside the leaves, where the potential is less negative. This gradient drives transpiration (*T*), as water vapor diffuses out through the stomata. The resulting loss of water from leaf cells is replenished by water drawn upward through the xylem, pulled by the cohesion-tension mechanism, which transmits the tension created by evaporation down to the roots.

When *SWC* is sufficient and atmospheric demand is moderate, the movement of water through the SPA continuum occurs with relatively

low resistance. However, under drought conditions, Ψ gradients become steeper, and the xylem experiences increasingly negative pressures. Excessively low Ψ can lead to cavitation, where air bubbles form in the xylem, interrupting the continuity of water flow and reducing hydraulic conductivity. This disruption can cause tissue damage and, if prolonged, plant mortality.

To cope with declining Ψ, plants employ osmotic regulation, increasing solute concentration within cells to lower their osmotic potential and maintain positive turgor pressure. This mechanism allows cells to retain water and continue basic physiological functions even as external Ψ drop. The overall water status of the plants can be assessed through its Relative Water Content (RWC), which reflects the balance between water availability, xylem tension, and osmotic adjustment. High RWC indicates healthy turgid cells, while low RWC signals water stress and potential desiccation.

In summary, the SPA continuum represents an integrated hydrological and physiological system through which water moves continuously from the soil to the atmosphere. It illustrates how plants act as biological conduits within the water cycle, dynamically responding to environmental changes to regulate water transport, maintain cell function, and survive under varying conditions of water availability.

Monitoring the three main components of the SPA continuum is essential for effective irrigation management. Understanding the dynamics of water flow within each component allows for precise assessment of plant water status and the timely application of irrigation volumes to prevent stress and optimize Water Use Efficiency (WUE).

This monitoring can be carried out through *in situ* instruments deployment. Alternatively, modern modelling approaches integrate meteorological, soil, and plant data to estimate key hydrological and physiological variables across the SPA continuum. These models, often supported by Remote Sensing (RS) and data assimilation techniques, provide continuous and spatially distributed information,

enabling the optimization of irrigation scheduling and promoting sustainable water resource management in agricultural systems.

2.2 *In situ* measurement

2.2.1 Soil layer

To monitor the soil water status, several methods are available, but none of them can yet be considered ideal; each of them, despite the progress made in recent years, may lead to evaluation errors resulting either from the method of use or from the spatial variability of the hydrological characteristics of the soil and its water content. The determination of the SWC can be carried out by measuring quantities that are directly or indirectly correlated with the water content.

Direct methods involve extracting the water from the soil and determining the amount extracted.

Indirect methods, on the other hand, are based on measuring the physical or chemical properties of the porous medium (*e.g.*, dielectric constant, electrical conductivity, thermal capacity, hydrogen atom content), which are strongly influenced by the amount of water molecules present.

Gravimetric method. For the direct measurement of *SWC*, the gravimetric method is the most used. A known mass of wet soil is collected and weighed to obtain wet weight. The sample is then dried in an oven at a temperature of approximately 105 °C for 24 hours, or until it reaches a constant weight (Giardini, 2004). The dry weight is subsequently measured, and the Gravimetric Water Content (*GWC* [g g^{-1}]), is calculated as:

$$GWC = \frac{M_W - M_d}{M_d} \quad \textbf{(2.1)}$$

where M_w [g] is the mass of the wet sample and M_d [g] is the mass of the dry sample. Finally, to determine the soil water content, it is necessary to apply the following formula:

$$SWC = GWC \cdot \frac{\rho_a}{\rho_w} \quad \textbf{(2.2)}$$

where ρ_a [g cm^{-3}] and ρ_w [g cm^{-3}] represent the soil bulk density and the density of water, respectively.

The gravimetric method is considered the reference standard for *SWC* determination due to its accuracy and simplicity. However, it is destructive, time-consuming, and not suitable for continuous monitoring.

Among the indirect methods to continuously measure *SWC*, the most recognized are those based on the Time Domain Reflectometry (TDR) and Frequency Domain Reflectometry (FDR) (Robinson et al., 2008).

Time Domain Reflectometry. The first method is based on the measurement of the dielectric constant of the soil (ε_b). ε_b is a physical property that reflects how much a material can store electrical energy when exposed to an electric field. In the context of a three-phase system, composed of solid particles, air, and water, the overall ε_b is strongly influenced by the proportion of water, since water has a much higher dielectric constant than either air or solids. Once this value is measured it is possible to obtain the *SWC* value (Roth et al., 1990) through empirical methods or conceptual models, referring to the sensor installation point. Such as an example, (Topp and Reynolds, 1998) based on the value of ε_b suggested an empirical expression to derive the *SWC* values in soil with different textures:

$$SWC = -5.3 \cdot 10^{-2} + 2.92 \cdot 10^{-2} \cdot \varepsilon_b - 5.5 \cdot 10^{-4} \cdot \varepsilon_b^2 + 4.3 \cdot 10^{-6} \cdot \varepsilon_b^3 \quad \textbf{(2.3)}$$

The good performance of universal equation of Topp has been widely confirmed by studies conducted on soils of different textures (Nadler et al., 1991; Dasberg and Hopmans, 1992). However, other research has shown that this relationship overestimates the water content in organic soils (Herkelrath et al., 1991) and underestimates it in soils with a high clay content (Dirksen and Dasberg, 1993).

A TDR probe consists of two or three parallel metallic rods (waveguides) connected to a coaxial cable and supported by an insulating body (*i.e.*, PVC). A fast electromagnetic pulse is sent

through the rods, and the travel time of the reflected signal is measured (**Figure 2.1**).

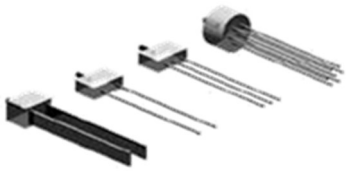

Figure 2.1 Geometric configuration of TDR probes (from: *Zegelin et al., 1989*)

This travel time depends on the apparent dielectric constant (ε_b) of the surrounding soil.

Frequency Domain Reflectometry. In the FDR method, the soil is considered as a portion of a capacitor, in which the dipoles in the dielectric medium are polarized under the action of an Electric Field (*EF*). The capacitive probes allow to measure of ε_b that depends on the amount of water in the soil. In particular, an high value of water content in the soil corresponds to an high value of dielectric constant and consequently a low frequency of oscillation of the EF, measured by the sensor (Williams et al., 2003). Therefore, given the frequency and the electrode configuration, the relation between ε_b and Total Capacity (*TC*) can be expressed as follow:

$$TC = g_f \cdot \varepsilon_b \quad \textbf{(2.4)}$$

where g_f is a constant that depends on the geometric configuration of the electrode (*i.e.,* size, shapes, and distance between the electrode).

The frequency of oscillation of the *EF*, for a fixed value of inductance (*L*) depends only on the *TC*, of the capacitor identified by the electrode-field system:

$$EF = \left(2\pi \cdot \sqrt{L \cdot \mathrm{TC}}\right)^{-1} \quad \textbf{(2.5)}$$

specifically, *EF* is proportional only to the ratio of air and water present in the soil. The values of *EF* are stored in a datalogger, and

processed using a normalized equation to obtain a Scaled Frequency (*SF*):

$$\mathrm{SF} = \frac{F_a - F_s}{F_a - F_w} \quad \textbf{(2.6)}$$

where F_a, F_s and F_w are the frequency measured by the sensor in air, soil and water, respectively. Finally, the values of *SF* are converted in *SWC* through a calibration equation, specific to each type of soil.

An FDR probe typically consists of metallic electrodes (often arranged as concentric rings or parallel rods) inserted into the soil and connected to an oscillator circuit. The circuit generates a sinusoidal electromagnetic signal, and the shift in frequency or phase of the returning signal is proportional to the soil's volumetric water content (**Figure 2.2**).

Figure 2.2 SentekTM "Drill & Drop" FDR probe
(from: *https://www.fondriest.com/sentek-drill-drop-soil-moisture-probe.htm*)

Although TDR and FDR techniques are generally less accurate than the gravimetric method, they offer significant practical advantages, as they are non-destructive, allow rapid and continuous measurements, and can be deployed at multiple locations in the field, providing a more comprehensive spatial and temporal characterization of *SWC* dynamics (Zotarelli et al., 2011).

Lysimeter. The lysimeter is a fundamental instrument for studying the water balance in soils, as it allows for the direct measurement of evapotranspiration. Unlike indirect methods based on models or estimates, lysimeters provide empirical, high-precision data at the local scale (Schrader et al., 2013).

A lysimeter is a container (typically metal or plastic) holding a representative soil sample with vegetation on its surface (**Figure 2.3**).

Figure 2.3 Mini lysimeter
(from: *https://www.riclic.unimib.it/PDF_convegno/Riclic_Parisi_21_11_07.pdf*)

The container is installed flush with the surrounding ground, with a drainage system at the bottom to collect percolated water and a system for runoff collection. Mounted on a weighing platform or scale, the lysimeter continuously monitors weight changes caused by water loss through evapotranspiration (**Figure 2.4**).

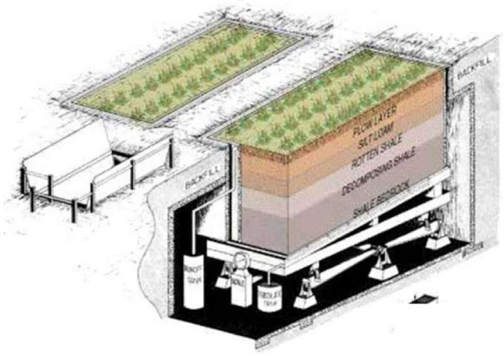

Figure 2.4 Weighing lysimeter
(from:*https://www.riclic.unimib.it/Cola%20SEMINARIO%20RICLIC%20WP5_6%2010aprile06%20Approfondimento%20metodologie%20del%20WP5_6.pdf*)

These measurements allow precise calculation of water losses over time, providing essential data for the soil water balance (Benli et al., 2006; Evett et al., 2025).

The lysimeter is described in this section because its primary function is to monitor *SWC* dynamics directly. It captures the variations in *SWC* and percolation, providing a foundation for

understanding how water is retained, transmitted, or lost in the soil profile. By focusing mainly on soil behaviour, the lysimeter data establish a baseline for quantifying the interactions between SWC and atmospheric processes.

Although it resides in the *2.2.1 Soil Layer* discussion, the lysimeter naturally serves as a bridge to the *2.2.2 Plant-Atmosphere Layer*, as it also measures the water lost through T. Data collected from the lysimeter can thus inform studies on SPA continuum interactions, linking *SWC* dynamics with atmospheric demand and CWR. In this way, the lysimeter provides a continuous connection between soil hydrology and plant-atmosphere processes.

Lysimeters are particularly useful for validating water balance models, calibrating indirect *SWC* sensors (*e.g.,* TDR or FDR), evaluating irrigation efficiency, and monitoring the hydrological behavior of different crops (Soldevilla-Martinez et al., 2014). Their high precision and ability to provide direct measurements make them an invaluable tool in research and water management.

Despite their advantages, lysimeters have some limitations, including high cost, technical complexity, potential invasiveness affecting the surrounding soil and vegetation, and sensitivity to environmental factors such as air temperature and humidity, and salinity, which require careful calibration (Gao et al., 2025).

2.2.2 Plant-Atmosphere layer

Evaporimeter. The evaporimeter (also known as evaporation pan) is an instrument used in meteorology and hydrology to measure the rate of water E from an open water surface exposed to the atmosphere (Feldhake and Boyer, 1988; Awe et al., 2020). It is widely employed to estimate *ET*, providing valuable information for understanding the water demand of crops and for irrigation management.

The evaporimeter measures the decrease in water level within a standardized container over a known period, typically expressed as millimeters of water lost per day. The measured water loss represents the evaporation occurring under given meteorological conditions, integrating the effects of air temperature and humidity, wind speed, and solar radiation.

The most common standard instrument is the Class A evaporation pan, consisting of a circular metal tank (1.22 m in diameter and 0.25 m deep) placed slightly above the ground on a wooden or metal platform (**Figure 2.5**).

Figure 2.5 Class A evaporation pan
(from: *https://www.awmeasurements.com/weather-sensors-systems/p/class-a-evaporation-pan*)

The pan is filled with water, and the daily drop in water level is measured manually or automatically using a micrometric screw or an electronic sensor.

Another type is the Colorado pan, a square tank (92 × 92 cm, 46 cm deep) usually buried at ground level to reduce temperature fluctuations and more closely simulate natural soil–atmosphere interactions (**Figure 2.6**).

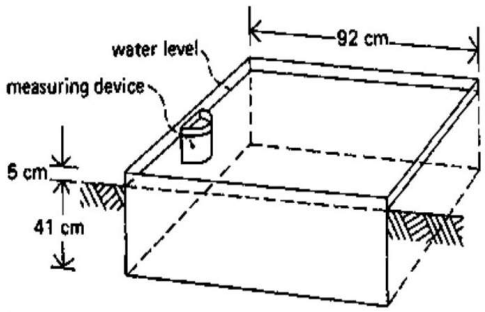

Figure 2.6 Sunken Colorado pan
(from: https://www.slideserve.com/ciara/estimation-of-evapotranspiration-of-kumulur-by-pan-evaporation-method)

The evaporimeter is an essential tool for quantifying the atmospheric component of the water balance. It complements

measurements obtained from soil-based instruments such as lysimeters, allowing for the evaluation of surface E and ET_p under varying climatic conditions.

By integrating evaporimeter data with *SWC* observations, it is possible to establish a comprehensive view of SPA continuum interactions, particularly the processes governing water loss and energy exchange between the land surface and the atmosphere.

Although conceptually simple and widely used, the evaporimeter has several limitations. The measured evaporation does not perfectly represent *ET* from vegetated surfaces, as the thermal and aerodynamic characteristics of a free water surface differ from those of soil and canopy surfaces. Therefore, the use of appropriate correction factors and calibration against lysimetric or micrometeorological data is necessary to obtain accurate *ET* estimates.

The evaporimeter provides a direct link between meteorological variables and water loss to the atmosphere. Together with soil-based measurements such as those obtained from lysimeters, it enables a complete assessment of the hydrological exchange within the SPA continuum, forming the basis for water balance modeling and sustainable irrigation management.

Sap Flow Technique. One technique commonly used to estimate transpiration fluxes is the sap flow method developed by (Granier, 1987). The sensors consist of an electric resistance embedded in a cork support (acting as a resistive heater) wrapped around the tree trunk, together with thermocouples inserted into the sapwood by means of thin needles (**Figure 2.7**).

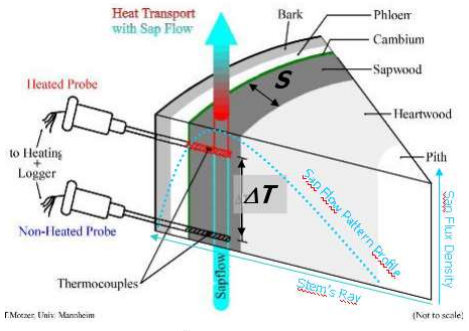

Figure 2.7 Schematic representation of the Granier system for measuring sap flow

The method is based on the principle of thermal dissipation: the temperature difference between the upper heated probe (continuously supplied with energy) and the lower reference probe (recording the natural wood temperature) is proportional to the sap flow density, which reflects the *T* activity of plant.

This approach accounts for the natural thermal gradients within the trunk, continuously monitored by the paired thermocouples. By observing changes in the temperature differential, it is possible to infer variations in sap velocity and thus in the *T* rate of the plant.

However, the method has some limitations. It assumes that sap flow is zero at night, implying the absence of nocturnal transpiration (Granier, 1987) and considering the nighttime stem refilling process as negligible. Moreover, the technique does not fully account for natural temperature gradients in the wood, which can vary by ±1.5 °C and may cause significant measurement errors (Do and Rocheteau, 2002).

Despite these limitations, the Granier method remains one of the most widely used and robust techniques for estimating *in situ* plant transpiration, offering valuable insights into plant–atmosphere water exchange within the SPA continuum (Cammalleri et al., 2013; Hölttä et al., 2015).

Standard Weather Station. A standard weather station is an essential component of any experimental setup aimed at analyzing the SPA continuum, as it provides continuous monitoring of the meteorological variables that control energy and mass exchanges at the surface. These variables are fundamental for estimating *ETo*, evaluating microclimatic conditions, and validating hydrological and crop growth models (Thornthwaite, 1948; Priestley and Taylor, 1972; Shuttleworth and Wallace, 1985; Allen et al., 1998).

A standard weather station typically consists of a suite of sensors mounted at standardized heights (*i.e.*, 2m), often on a mast placed in an open, unobstructed area to ensure representative measurements of ambient conditions (Mokhtarzadeh et al., 2025) (**Figure 2.8**).

Figure 2.8 Standard Weather Station

The main parameters measured include air temperature, relative air humidity, wind speed and direction, global solar radiation, and precipitation depth.

All sensors are connected to a data logger, which continuously records data at fixed intervals, typically every 10–30 minutes. These data are often transmitted remotely for real-time monitoring and analysis.

The standard weather station plays a pivotal role in hydrological and meteorological studies, providing the boundary conditions necessary to describe the exchanges of energy, water vapor, and momentum between the surface and the atmosphere. When used in combination with instruments such as lysimeters, evaporimeters, and sap flow sensors, it enables a comprehensive assessment of the water balance and plant WUE under different climatic and management conditions.

Within the *2.2.2 Plant–Atmosphere Layer*, the standard weather station serves as the reference point for all atmospheric measurements. It provides the meteorological context required to interpret data from other sensors and to quantify the driving forces of *E* and *T*. By integrating weather data with soil and plant measurements, the station supports a holistic understanding of the interactions governing the SPA continuum.

Pyrgeometer. The shortwave radiometer, also known as a pyranometer, is an instrument used to measure the global solar

radiation incident on a horizontal surface. This measurement represents the incoming shortwave radiation, which is the primary source of energy driving the surface energy balance and the *ET* process within the SPA continuum.

The shortwave radiometer measures the total hemispherical irradiance received from the sun and the sky within the spectral range of approximately 0.3 to 3 μm. The instrument operates based on the thermopile principle: solar radiation is absorbed by a blackened surface, generating a temperature difference between the absorbing surface and a reference body. This temperature difference produces a voltage signal proportional to the radiant flux density, typically expressed in W m^{-2} (Reda et al., 2002).

To ensure accuracy, the sensor is installed horizontally and kept level. It is equipped with a transparent dome that protects the sensing element while allowing solar radiation to pass through. Regular cleaning and calibration are essential to maintain measurement reliability (**Figure 2.9**).

Figure 2.9 Pyrgeometer
(from: *https://www.directindustry.it/prod/meteo-omnium/product-72296-2256312.html*)

The shortwave radiometer provides the key radiative input required to compute the energy available for *ET* and photosynthesis. By quantifying the amount of solar energy reaching the surface, it allows to evaluate the diurnal and seasonal variability of incoming radiation and its effects on CRW, canopy temperature, and microclimate.

When integrated with data from lysimeter, and sap flow sensors, shortwave radiation measurements help quantify the energy

component of the SPA continuum, linking atmospheric forcing with surface and biological responses.

The shortwave radiometer represents a fundamental tool within the *2.2.2 Plant–Atmosphere Layer*, as it quantifies the incoming solar energy that drives surface processes such as evaporation (*E*), transpiration (*T*), and photosynthesis. Its integration with meteorological and hydrological sensors provides a comprehensive understanding of the energy–water interactions controlling ecosystem functioning.

Anemometer. The cup and vane anemometer is a classical and widely used instrument for measuring wind speed and direction in meteorological applications. Within the *2.2.2 Plant–Atmosphere Layer*, wind is a key variable influencing turbulent exchanges of energy, water vapor, and carbon dioxide between the surface and the atmosphere. Consequently, accurate wind measurements are essential for quantifying *ET* and aerodynamic resistance. The cup anemometer consists of three or four hemispherical cups mounted symmetrically on horizontal arms attached to a vertical shaft (**Figure 2.10**).

Figure 2.10 Cup and vane anemometer (from: *https://shop.meteoproject.it/prodotto/anemometro-completo/*)

When exposed to wind, the difference in drag between the concave and convex sides of the cups causes the system to rotate. The rotational speed is directly proportional to the wind velocity, which is recorded as an electrical signal or pulse frequency by a magnetic or optical sensor.

Attached to the same assembly, the wind vane (or tail) aligns itself with the wind direction. The angular position of the vane relative to a fixed reference, usually North, is detected by a potentiometer or magnetic encoder, providing continuous information on wind direction.

Cup and vane anemometers are typically installed at a standard height of 2 m or 10 m above the ground, depending on the scope of the measurement.

In meteorological studies, wind data are also used to assess canopy ventilation, aerodynamic conductance, and the transport of heat within and above plant canopies. When combined with radiometric and air humidity measurements, they help to characterize the energy and mass transfer processes within the SPA continuum system.

The cup and vane anemometer remains one of the most reliable and robust instruments for surface wind measurement. Its simplicity, mechanical stability, and long-term reliability make it particularly suited for field installations. Within the *2.2.2 lant–Atmosphere Layer*, wind data collected by this instrument provide essential inputs for understanding atmospheric turbulence, evapotranspiration (*ET*) dynamics, and surface–atmosphere coupling in agricultural and environmental monitoring.

Rain gauge. The rain gauge, also known as pluviometer, is an instrument designed to measure precipitation, both its amount and intensity, over a given period. Within the *2.2.2 Plant–Atmosphere Layer*, precipitation represents the primary input of water to the SPA system, directly influencing *SWC*, runoff, and *ET* dynamics.

A standard rain gauge consists of a collector funnel that directs rainfall into a measuring device (Lanza et al., 2022). The two most common types are:

- Tipping-bucket rain gauge: rainwater is funneled into a small, double-bucket mechanism balanced on a pivot. When one bucket fills to a calibrated volume (*e.g.*, 0.25 mm of rain), it tips, emptying the water and automatically triggering an electronic pulse. The number of tips recorded over time corresponds to the total precipitation (**Figure 2.11**).

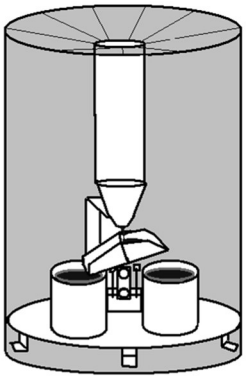

Figure 2.11 Tipping-bucket rain gauge
(from: *https://vortex.plymouth.edu/dept/tutorials/precip/precip3a.html*)

- Weighing rain gauge: collects precipitation in a container mounted on a load cell, continuously recording the weight change to measure both amount and rate of rainfall, including snow or mixed precipitation (**Figure 2.12**).

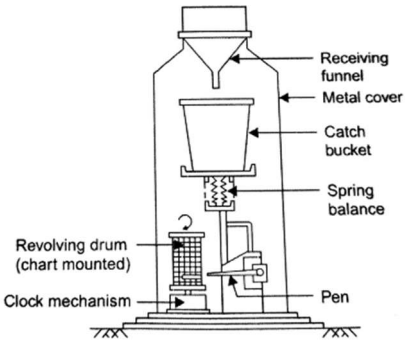

Figure 2.12 Weighing rain gauge
(from: *https://cementconcrete.org/water-resources/hydrology/rain-gauge/2637/*)

All measurements are typically expressed in millimeters of water depth, representing the equivalent water layer uniformly distributed over a unit area.

Rain gauges are fundamental for hydrological and meteorological monitoring, as they provide the input term for the soil water balance. In agricultural systems, precipitation data are used to evaluate irrigation requirements, and to validate water balance models.

In combination with lysimeters and *SWC* sensors, rain gauge data allow to quantify infiltration, percolation, and surface runoff.

For accurate measurements, rain gauges are typically installed on a level surface, at a standard height of 1.0 m above ground, and away from obstacles that could cause wind turbulence or rain shadowing. Regular maintenance, such as cleaning the funnel and verifying calibration, is essential to ensure long-term data reliability, especially in remote or automated monitoring systems.

The rain gauge provides direct and indispensable information on atmospheric water inputs within the *2.2.2 Plant–Atmosphere Layer*. When used together with radiometric, wind, and humidity sensors, it completes the set of meteorological variables required to quantify the driving forces of the hydrological cycle and to interpret the temporal variability of the SPA continuum water exchange.

Scintillometer. The scintillometer is an optical or microwave instrument that measures turbulent fluctuations in the refractive index of air caused by temperature and humidity variations.

The instrument emits a continuous electromagnetic beam (in the optical or microwave spectrum) from the transmitter to the receiver. As the beam travels through the atmosphere, small-scale variations in air temperature and humidity create turbulent eddies, which induce random fluctuations in signal intensity, a phenomenon known as scintillation (**Figure 2.13**).

Figure 2.13 Scintillometer (from: *https://nn.wikipedia.org/wiki/Scintillometer*)

By analyzing these fluctuations along the path between a transmitter and a receiver, the instrument provides estimates of the

sensible heat flux, which can be combined with the surface energy balance to infer latent heat flux (Chehbouni, 2000; Hemakumara et al., 2003). Scintillometers are non-intrusive, cover a large spatial footprint, and are particularly useful over heterogeneous surfaces (De Bruin et al., 2002; Hartogensis et al., 2002).

Eddy covariance flux tower. The eddy covariance method is based on high-frequency measurements (*e.g.*, 10–20 Hz) of the three-dimensional wind components and the scalar quantities (such as water vapor, CO_2 concentration, and air temperature) that are transported by turbulent eddies (**Figure 2.14**).

Figure 2.14 Eddy covariance flux tower

The Eddy Covariance (EC) tower provides direct measurements of key ecosystem fluxes, including latent heat flux (*LE*), sensible heat flux (*H*), CO_2 exchange, also called Net Ecosystem Exchange (*NEE*), and momentum flux (τ). These data allow the quantification of ET_a, photosynthetic uptake, and respiration, offering insights into the coupling between biophysical processes and atmospheric dynamics (Cammalleri et al., 2013; Rozenstein et al., 2019; Saitta et al., 2020; Corbari et al., 2020; French et al., 2020; Yang, 2023; Liu et al., 2025).

EC flux towers are generally installed above the canopy layer, ensuring that the measurement footprint is representative of a homogeneous upwind surface. The system requires high-frequency data acquisition, strict calibration, and rigorous post-processing, including coordinate rotation, frequency response corrections, and

flux partitioning (Rosenberg et al., 1983; Stull, 1988; Kaimal and Finnigan, 1994).

Despite its complexity, the EC method is one of the few approaches capable of directly measuring ET and carbon exchange without relying on empirical parameters, making it invaluable for ecosystem and agriculture studies.

The Eddy Covariance Tower represents the most comprehensive tool for quantifying the turbulent exchange of mass and energy in the 2.2.2 *Plant–Atmosphere Layer*. Its integration with *in situ* meteorological and physiological measurements enables a full understanding of the energy–water–carbon interactions that control ecosystem functioning and response to environmental variability. A standard EC tower is composed by a net radiometer, a gas analyzer, a soil heat flux plate, and a sonic anemometer.

Net radiometer and four-component net radiometer. Net Radiometer and four-component are instruments designed to measure the net radiation (R_n) at the surface, which is the balance between incoming and outgoing shortwave and longwave radiation. The net radiative flux can be measured directly using a net radiometer, or indirectly by separately measuring shortwave radiation with a pyranometer and longwave radiation with a pyrgeometer (**Figure 2.15**).

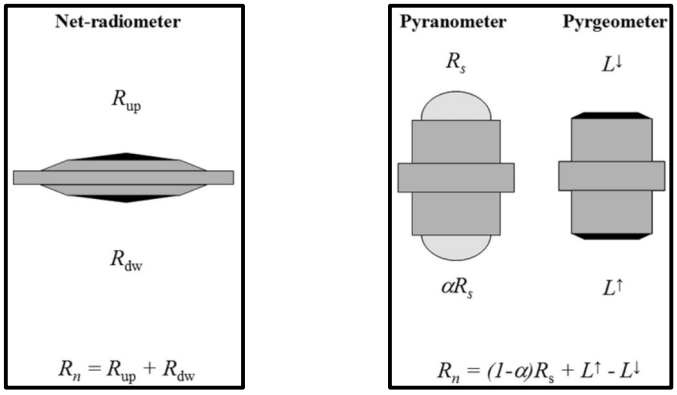

Figure 2.15 Net-radiometer and four-component net radiometer (pyranometer + Pyrgeometer)

The net radiometer operates over a spectral range from approximately 0.3 to 40 μm and determines the net flux as the

difference between the radiative power received from (or emitted to) the upper hemisphere and that received from (or emitted to) the lower hemisphere on the same horizontal plane. Its operation is based on measuring the difference between the case temperature of the instrument and the temperatures of two horizontal sensor planes, one facing upward and one downward. While this method provides a simple measurement of net radiation, it does not separate the shortwave and longwave components.

For more detailed analysis, the combined use of a pyranometer and a pyrgeometer, known as a four-component net radiometer, is employed. The pyranometer measures shortwave radiation (0.3–2.5 μm) using a blackened thermopile, ideally with a cosine response to account for the solar angle of incidence. Incoming and reflected radiation can be measured by orienting the sensor upward or downward; simultaneous upward and downward measurements allow the estimation of surface albedo. The pyrgeometer measures longwave radiation (4–40 μm) using a thermistor and a case temperature sensor for compensation. When two pyrgeometers are used in upward and downward orientations, net longwave radiation can be computed directly. Coupling pyrgeometer data with surface temperature measurements also allows the estimation of surface emissivity using the Stefan-Boltzmann law and the analysis of the relationship between lower-atmosphere variables and apparent atmospheric emissivity.

Thus, these instruments provide essential measurements of the surface radiative energy balance, which is fundamental for assessing ET, energy partitioning, and surface-atmosphere interactions.

Gas Analyzer. A gas analyzer is an instrument used to measure the concentration of gases in the atmosphere, such as carbon dioxide (CO_2), water vapor (H_2O). Within the *2.2.2 Plant–Atmosphere Layer*, gas analyzers play a fundamental role in quantifying photosynthesis, respiration, and *ET*, as they allow the measurement of gas fluxes exchanged between vegetation and the atmosphere.

Gas analyzers commonly employ infrared absorption spectroscopy to detect gas concentrations. Open-path analyzers

measure the gas content along a path in the air directly, providing high-frequency data suitable for EC flux measurements (**Figure 2.16**).

Figure 2.16 Gas analyzer
(from: https://labinstruments.ru/equipment-gazoanalizatory-otkrytogo-i-zakrytogo-tipa/li-7500rs)

The instrument provides high temporal resolution, often in the order of 10–20 Hz, which is essential for capturing turbulent fluctuations in CO_2 and H_2O required for EC flux computations. The measured gas concentrations can be combined with high-frequency wind measurements from a sonic anemometer to compute turbulent fluxes of water vapor and carbon dioxide, providing direct estimates of *LE*, *H* and *NEE*.

Gas analyzers are central to ecosystem monitoring, carbon budget studies, and hydrological research. Gas analyzers provide a direct, high-resolution measurement of atmospheric gas concentrations and fluxes, enabling the quantification of plant-atmosphere interactions. When integrated with meteorological and physiological data, they allow a comprehensive assessment of *ET*, carbon exchange, and ecosystem functioning, making them indispensable tools in modern agriculture research.

Soil heat flux plate. The soil heat flux plate is an instrument used to measure the soil heat flux (G_o), which represents the rate of heat transfer into or out of the soil. This measurement is a critical component of the surface energy balance, as it quantifies the portion

of R_n that is conducted into the soil rather than used for latent or sensible heat flux.

The soil heat flux plate is a thin, flat sensor installed horizontally at a fixed depth, typically 5–10 cm below the soil surface (**Figure 2.17**).

Figure 2.17 Soil heat flux plate (from: https://www.hukseflux.com/products/heat-flux-sensors/heat-flux-sensors/hfp01-heat-flux-sensor)

It measures the heat flux passing through the sensor using thermopiles or heat flux transducers, generating a voltage proportional to the temperature gradient across the plate. The measured signal is often corrected for soil thermal conductivity and the temperature gradient above the plate to obtain an accurate estimate of the soil heat flux at the surface.

Soil heat flux plates are widely used in energy balance studies. They provide essential data for calculating surface energy partitioning when combined with measurements of R_n, H, and LE. Proper installation requires good thermal contact with the surrounding soil and minimal disturbance to the soil structure. Plates should be horizontally leveled and carefully backfilled to avoid air gaps, which can lead to measurement errors. Multiple plates at different depths may be installed to better characterize the vertical distribution of heat flux. The soil heat flux plate provides direct, continuous measurements of energy conduction into the soil. Its integration with other meteorological and hydrological instruments enables a detailed understanding of energy balance dynamics, which is essential for accurate estimation of ET, soil temperature regimes, and microclimatic interactions within the SPA system.

Sonic anemometer. The sonic anemometer is an advanced instrument used to measure three-dimensional wind velocity with high temporal resolution, typically in the order of 10–20 Hz. Unlike conventional mechanical anemometers, the sonic anemometer operates without moving parts, using ultrasonic sound pulses to determine the wind speed and direction by measuring the time of flight of acoustic signals between pairs of transducers (**Figure 2.18**).

Figure 2.18 Sonic anemometer (from: *https://www.campbellsci.com/csat3*)

The instrument emits ultrasonic pulses along three non-coplanar paths between transducers. The time delay of each pulse is affected by the wind velocity along the path. By continuously measuring these time delays, the sonic anemometer calculates the instantaneous wind components in three orthogonal directions. In addition, it can provide virtual temperature measurements by detecting the speed of sound in the air.

Sonic anemometers are widely used in micrometeorology, EC systems, and boundary layer studies. Their high-frequency measurements are essential for computing turbulent fluxes of momentum, heat, and water vapor, allowing the direct estimation of H and LE when combined with gas analyzers. In ecosystem research, sonic anemometers form a critical component of EC towers, enabling continuous monitoring of turbulent exchanges between vegetation and the atmosphere.

Compared to traditional cup or vane anemometers, sonic anemometers offer higher temporal resolution, no mechanical inertia,

and the ability to capture rapid fluctuations in wind velocity that are essential for turbulent flux computations. They are also less affected by icing or mechanical wear, making them suitable for long-term field installations.

The sonic anemometer is a key instrument for characterizing turbulent wind fields and for calculating surface-atmosphere fluxes. When integrated with gas analyzers, radiometers, and soil-based instruments, it provides a complete picture of the energy, water, and gas exchanges within the SPA continuum.

Plant optical properties. The interaction between solar radiation and vegetation is fundamentally governed by the optical properties of plants, which determine how ElectroMagnetic (EM) energy is absorbed, transmitted, and reflected by leaves and canopies. To fully understand these processes, it is essential to consider the electromagnetic spectrum, which encompasses the complete range of radiation frequencies emitted by the Sun. Solar energy reaching the surface of the Earth spans wavelengths approximately between 300 nm and 2500 nm, covering the UltraViolet (UV), VISible (VIS), Near-InfraRed (NIR), and ShortWave InfraRed (SWIR) regions (**Figure 2.19**).

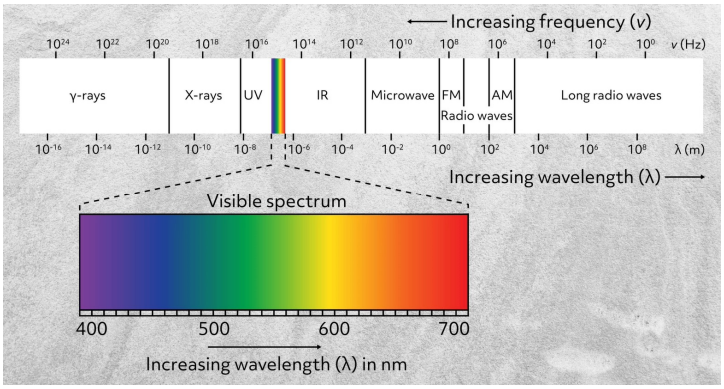

Figure 2.19 Electromagnetic spectrum (from: *https://www.xrite.com/it-it/blog/uv-spectrophotometer*)

Each of these spectral domains interacts differently with plant tissues according to their biochemical composition and structural characteristics.

It is possible to conceptualize in three components the energetic interactions between a generic surface (S) to the incident EM energy (E_i): reflected energy (E_r), absorbed energy (E_a), and transmitted energy (E_t) (**Figure 2.20**).

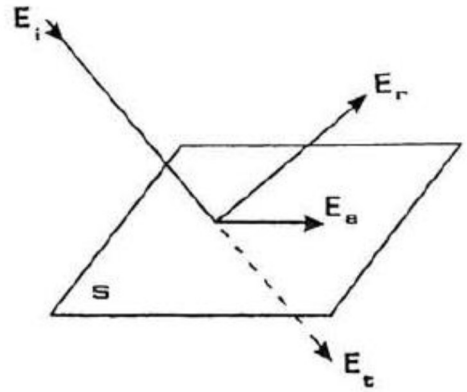

Figure 2.20 Conceptual schematization of the interaction between incident energy Ei and a generic surface S (from: *Lechi (2001)*)

The ratio between each component and E_i, defines three different optical properties: reflectance (ρ), absorbance ($\alpha\beta$) and transmittance ($\tau\pi$), specific for every material and dependent only on the chemical-fiscal proprieties of the surface of the material. The sum of these components expresses the principle of energy conservation.

$$\boldsymbol{\rho + \tau\pi + \alpha\beta = 1} \qquad \textbf{(2.7)}$$

The values of the three coefficients, for the same surface change in function of the wavelength (λ), of the *Ei*.

The distribution of absorbed, transmitted, and reflected radiation across these spectral regions provides critical information on the physiological status and biophysical parameters of vegetation, including chlorophyll concentration, Leaf Area index (*LAI*), and water content. *LAI* represents the total one-sided leaf surface area per unit ground area and is typically measured using direct destructive sampling. It is a key biophysical parameter for assessing vegetation structure, productivity, and canopy–atmosphere interactions.

Thus, ρ variation in function of the different λ is represented in a graph called spectral signature. Based on the analysis of the spectral signature acquired from a vegetated surface (**Figure 2.21**) (Moroni et al., 2019), it is possible to observe different regions of the EM spectrum representative of the plant water status.

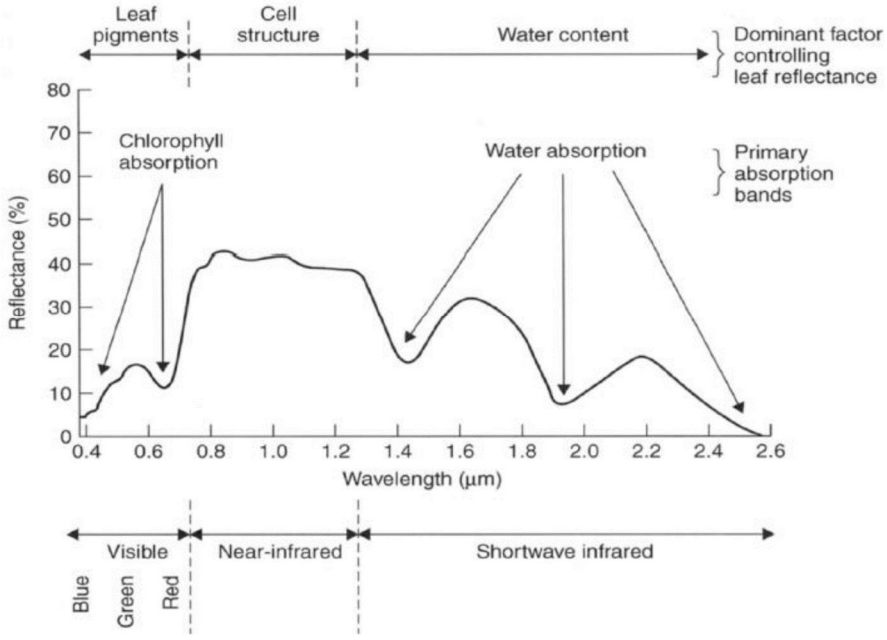

Figure 2.21 Generic vegetation spectral signature (from: *Moroni et al., 2019*)

In the region of the VIS spectrum (400-750 nm) almost the energy is absorbed because the main interactions are controlled by pigments such as chlorophylls, carotenoids, and anthocyanins, in fact, there are two evident minimums values of ρ in correspondence the pigment absorption peaks (420-490 nm) and in the red region (660 nm). While in correspondence of the 540 nm and 690-720 nm wavelengths, there are two peaks named green peak, hence the characteristic color of vegetation, and red edge, respectively. The region of the NIR (750-1350 nm) is characterized by high values of ρ representative of the morph-anatomical characteristics of the leaf (Boyer et al., 1988). The absorption by pigments decreases sharply, and leaf reflectance becomes dominated by internal structure, namely, the arrangement of mesophyll cells and intercellular air spaces, which causes multiple scattering and high reflectance.

The reflectance in the VIS bands is therefore responsible for the color exhibited by crop leaves (**Figure 2.22**).

Figure 2.22 Plant color and health status (from: *https://www.agricolus.com/indici-vegetazione-ndvi-ndmi-istruzioni-luso/*)

When a plant is healthy, the leaves appear bright green because the reflectance in the blue and red regions is largely absorbed by the crop for photosynthetic processes, while the reflectance in the green region remains predominant (Healthy Leaf). In this condition, the NIR band shows a strong reflectance value. As the crop enters stress conditions, the leaves tend to yellow, and the reflectance values in the red, green, and NIR bands become similar in magnitude (Stressed Leaf). When the crop reaches a state of death, all reflectance values become comparable, and the leaf color turns brownish (Dead Leaf).

Moreover, considering again the spectral signature, in the 970 nm and 1200 nm wavelengths, there are two minimums due to the absorption of water (Jacquemoud et al., 2003). Other characteristic peaks of absorption of water can be seen in the Short-Wave-Infrared (SWIR) region (1400-2500 nm) centered around 1450 nm, 1940 nm and 2200 nm. Thus, water molecules within leaf tissues play the primary role, absorbing radiation at specific bands corresponding to vibrational modes of water.

The spectral signature analysis can be supported introducing Vegetation Indices (VIs) (Moroni et al., 2019). Regarding the plant water status detection, the stressing agents affect reflectances in certain wavelengths representative to the physiological characteristics of plants, the appropriate combination of these bands allows to monitor health state of plant (Moroni et al., 2019). The VIs tries to assess the possible changes in reflectances values in specific bands of the EM spectrum, as these can be a symptom of biological alteration.

Many VIs has been empirically obtained combining bands associated to specific wavelengths of the vegetation spectral signature. Xue and Su (2017) published an interesting review of VIs available in the literature, showing their specific application field according to the vegetation of interest and environmental condition. Among the VIs based on the variation of the biochemical and morpho-anatomical characteristics the Normalized Difference Vegetation Index (*NDVI*) (Rouse et al., 1974) is commonly used to monitor plant vigour, amount of green biomass, plant stress, photosynthetic and agricultural crop yield (Asrar et al., 1984; Sellers, 1987; Moriondo et al., 2007).

$$NDVI = \frac{\rho_{NIR} - \rho_{RED}}{\rho_{NIR} + \rho_{RED}} \quad \textbf{(2.8)}$$

where ρ_{NIR} and ρ_{RED} are the reflectance of the NIR and red, respectively. The ρ_{RED} is representative of the absorption of light by chlorophyll, while the ρ_{NIR} is sensitive to changes in the internal structure of the leaves (Zhang, 2012). Usually, *NDVI* assume values ranging between -1 and +1. In general, water surface has typical values less than 0, bare soils between 0 to 0.30 and vegetation over 0.35 until 0.75-0.80 (Kriegler et al., 1969).

The *NDVI* value is also widely used for crop stress detection: high values close to one indicate healthy vegetation, where NIR reflectance is much greater than red reflectance; conversely, values approaching zero correspond to stressed vegetation, in which the two reflectances have similar magnitudes (**Figure 2.23**).

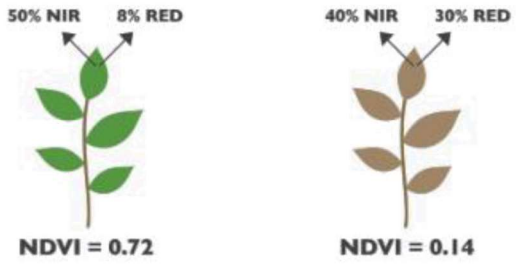

Figure 2.23 Characteristic values of the NDVI for plants in good health or water stress conditions
(from: *https://blogs.upm.es/tfb/wp-content/uploads/sites/813/2021/06/Presentacio%CC%81n-Planthy.pdf*)

However, when a specific vegetated surface is fully covered and chlorophyll content is saturated, *NDVI* is not able to describe the real amount of chlorophyll and increase of this variable does not result in proportional increase of the *NDVI* (Huete et al., 1997).

The VIs can be useful also to monitor the surface humidity; in this way, the Normalized Difference Water Index (*NDWI*) is sensitive to monitor the surface humidity (Gao, 1996).

$$NDWI = \frac{\rho_{NIR} - \rho_{SWIR}}{\rho_{NIR} + \rho_{SWIR}} \quad \textbf{(2.9)}$$

where ρ_{NIR} and ρ_{SWIR} are the wavelengths of NIR and SWIR respectively. Ceccato et al. (2001) demonstrated that *NDWI* is able to remove the variation caused by leaf internal structure and leaf dry matter content, improving the reliability in assessing the vegetation water content.

The study of the plant's optical properties can be considered a useful solution for indirect evaluations of water status of plant (Pugnaire and Valladares, 1999).

Moreover, authors demonstrated that the the Fraction Vegetation Cover (*FVC*) is correlated to vegetation indices with different functions (Jiang et al., 2006).

FVC is an important variable for describing the quality and changes of vegetation in terrestrial ecosystems. *FVC* refers to the proportion of a land surface covered by green vegetation, capturing the fraction of the ground area concealed by leaves, stems, and other plant components. This parameter serves as a critical metric in ecological studies, agricultural monitoring, and climate change research, providing scientists, policymakers, and land managers with essential information to make informed decisions. *FVC* defined as the percentage of the vertically projected area of vegetation (including leaves, stems, and branches) within the totally statistical area, is an important quantitative parameter that plays a crucial role in indicating biophysical processes such as evaporation, transpiration, and photosynthesis (Barlage and Zeng, 2004; Jiapaer et al., 2011; Arneth,

2015). Thus, The *FVC* is obtained as the ratio between the total area occupied by the plants and the area of the portion examined.

As shown by Baret et al. (1995), confirmed by Carlson and Ripley (1997) and Gutman and Ignatov (1998), there is a good relationship between the *FVC* and the *NDVI*. Buyantuyev et al. (2007) estimated *FVC* from Landsat data by computing several vegetation indices. Among all the estimation methods, the linear mixture model has been widely applied (Zeng et al., 2000; Scanlon et al., 2002; Montandon and Small, 2008; Delamater et al., 2012; Yang et al., 2013; Zhang et al., 2013; Iordache et al., 2014; Guo et al., 2015; Waldner et al., 2015).

2.3 Data from Reanalysis and Forecast Models

In situ data from field instruments provide essential insights into the SPA continuum, yet they are often limited in spatial coverage and temporal continuity. To complement these measurements, reanalysis datasets and numerical weather forecast models offer a consistent, spatially extensive, and temporally continuous representation of atmospheric and land-surface variables (Mendelsohn et al., 2007).

Reanalysis products combine historical observations with modern Numerical Weather Prediction (NWP) models through data assimilation, producing gridded datasets of variables such as air temperature, relative air humidity, wind speed, precipitation and, solar radiation (Parker, 2016). These datasets are particularly valuable for climate studies, long-term trend analysis, and model validation.

Similarly, forecast models provide short- to medium- range predictions of atmospheric and surface conditions, allowing the assessment of future scenarios (Wu and Xue, 2024) and supporting operational decision-making in agriculture, hydrology, and water resources management. The integration of *in situ* data with reanalysis and forecast products enables a comprehensive characterization of the environmental drivers affecting energy and water exchanges in the SPA continuum.

2.3.1 Reanalysis data

Reanalysis data represents the most significant advancements in atmospheric and climate sciences, providing a comprehensive,

temporally consistent reconstruction of the atmospheric state of the Earth over extended periods. Unlike standard forecasting outputs, which are designed to predict future conditions, reanalysis products are produced retrospectively by assimilating a wide range of historical observations into a fixed, state-of-the-art NWP model. This approach combines the dynamical consistency of physical models with the empirical richness of *in situ* data, resulting in a globally complete and homogeneous dataset that extends back several decades.

The process of reanalysis relies on advanced data assimilation techniques, such as Three-Dimensional (3DVAR) or Four-Dimensional VARiational analysis (4DVAR), and, more recently, Ensemble Kalman Filtering (EnKF) (Zhang et al., 2011). These methods optimally merge observations from multiple sources, *in situ* stations, radiosondes, aircraft, satellites, and buoys, with short-term model forecasts to produce an estimate of the most probable atmospheric state at each time step. By keeping the underlying model and assimilation system constant throughout the entire reanalysis period, systematic biases and discontinuities are minimized, ensuring temporal consistency and allowing for robust trend analysis.

Several gridded of climate data, with different spatial and temporal resolutions, have been developed and are freely available by research agencies (*e.g.*,, National Aeronautics and Space Administration (NASA) and European Centre for Medium-Range Weather Forecasts (ECMWF)).

Global datasets of meteorological, Soil Water Content (*SWC*), surface fluxes, radiation balance, and atmospheric circulation fields, are provided in 'maps without gaps' typically at temporal resolutions ranging from hourly to monthly and spatial resolutions down to 30 km in the latest releases.

Reanalysis data have become indispensable not only for climate monitoring and research but also for a wide range of applied environmental and engineering studies. In the field of hydrology (Anderton et al., 2002; Newham et al., 2003) and water resource management (Gong et al., 2006; Liang et al., 2008; Koudahe et al., 2018), they serve as key inputs for hydrological modelling, drought

assessment, and irrigation planning. For regions with sparse observational networks, reanalysis products offer reliable and spatially continuous estimates of meteorological variables (Sheffield et al., 2004; Negm et al., 2017; Pelosi, 2023; De Caro et al., 2023; Ippolito et al., 2024; Ghazouani et al., 2025; Amato et al., 2026), enabling improved water balance computations and long-term evaluations of irrigation requirements. Furthermore, reanalysis datasets provide the baseline for model validation and calibration, ensuring that forecasting systems are accurately tuned to historical climatic variability.

Reanalysis data bridge the gap between observational limitations and modelling needs, offering a coherent, physically consistent view of the past and present climate of the Earth. Their persistent development represents a cornerstone for advancing predictive modelling, supporting climate adaptation strategies, and fostering sustainable management of environmental and water resources.

2.3.2 Forecasting data

Forecasting models, particularly those developed within the framework of NWP, represent one of the most advanced and complex achievement in environmental modelling. These models are designed to predict the temporal evolution of the atmosphere by solving the fundamental equations governing fluid dynamics and thermodynamics. The underlying principle is deterministic: given a sufficiently accurate description of the initial state of the atmosphere, it is theoretically possible to predict its future state through the numerical integration of the governing equations.

The conceptual foundation of numerical forecasting dates back to the early twentieth century. Bjerknes (1904) proposed that atmospheric motion could be described deterministically through a set of differential equations derived from physical laws, provided that the initial conditions were known. A practical attempt to apply this approach was made by Richardson and Lynch (2007), who manually computed a forecast for a case study over Europe. However, his results were inaccurate due to insufficient observational data and numerical instability in the finite-difference approximations. It was

only with the advent of electronic computing, that the first operational numerical forecasts were successfully produced. Charney et al. (1950) developed a barotropic model at one vertical level (500 mb), integrated using the ENIAC computer, marking the beginning of modern numerical weather prediction.

At the core of forecasting models lies a set of primitive equations, a system of Partial Differential Equations (PDEs) that describe the evolution of momentum, mass, energy, and water vapor in the atmosphere. These include the Navier–Stokes equations for momentum conservation, the thermodynamic equation for energy conservation, the continuity equation for mass conservation, and the equation of state for air, which links pressure, temperature, and density. Additionally, the hydrostatic equation approximates the vertical pressure gradient balance against gravity, an assumption valid for large-scale motions. Together, these equations form a highly nonlinear system that cannot be solved analytically; instead, numerical methods are required to obtain approximate solutions.

The process of numerical discretization transforms the continuous PDEs into algebraic equations that can be handled computationally. Discretization is performed in space and time, converting the atmosphere into a finite grid. In the horizontal dimension, two primary schemes are used: grid-point (Haltiner and Williams, 1980) and spectral methods (Charney and Phillips, 1953). Grid-point approaches employ finite-difference approximations on regular or variable meshes, which are intuitive but can face issues near the poles. Spectral models, by contrast, expand the variables into spherical harmonics, providing smoother global representations and avoiding polar singularities, though at the cost of higher computational effort due to frequent transformations between physical and spectral space.

Depending on the spatial resolution and scale, forecasting models are classified into General Circulation Models (GCMs) (Mechoso and Arakawa, 2015) and Limited-Area Models (LAMs) (Bates et al., 1998). GCMs integrate primitive equations over the entire globe, with typical horizontal resolutions ranging from 25 to 100 km. These models capture large-scale atmospheric dynamics, such as planetary

waves and synoptic-scale systems, and provide boundary conditions for higher-resolution regional models. LAMs, on the other hand, focus on smaller domains (5–20 km or even finer resolutions below 2 km) and include more detailed representations of mesoscale and local processes. Examples include the Weather Research and Forecasting (WRF) model (Skamarock et al., 2008), the BOlogna Limited Area Model (BOLAM) model developed by the Italian National Research Council (CNR), and its non-hydrostatic counterpart MOLOCH, which explicitly resolves convective phenomena (Mariani et al., 2005).

As model resolution increases, sub-grid processes, those occurring at scales smaller than the grid spacing, cannot be directly resolved and must be represented through parameterizations. These include radiative fluxes, surface exchanges of heat and moisture, cloud microphysics, convection, and the turbulent processes of the Planetary Boundary Layer (PBL). Each parameterization introduces empirical relationships or simplified formulations based on theoretical and observational knowledge, yet they remain a primary source of uncertainty in numerical forecasts. Non-hydrostatic modeling becomes essential when vertical accelerations are comparable to horizontal ones, as in deep convection or mountain-induced flows. In these cases, the full three-dimensional equations are solved without hydrostatic approximation, requiring shorter time steps and more intensive computation (Warner, 2010).

Another critical aspect of forecasting systems is data assimilation, which aims to construct the best possible estimate of the atmospheric initial state by optimally combining observations and short-term model forecasts. Observations are gathered from multiple sources: surface stations, radiosondes, aircraft, ships, and satellites. Data assimilation systems apply statistical and dynamic techniques, such as 3DVAR, 4DVAR, and EnKF to minimize the differences between observed and modeled variables (Bouttier and Courtier, 2002). The process is sequential: each new forecast cycle begins with a model background (the short-range forecast), which is corrected using available observations to generate a new analysis field. This iterative

procedure ensures that model trajectories remain close to the observed atmosphere and mitigates the so-called "spin-up" problem, where the model initially deviates from reality before stabilizing (Kalnay, 2002).

Given the intrinsic nonlinearity and chaotic nature of the atmospheric system, small perturbations in initial conditions can lead to large divergences in model outcomes, a concept famously illustrated by Lorenz (1963) with the "butterfly effect." To account for this inherent uncertainty, modern forecasting centers employ Ensemble Prediction Systems (EPS) (Toth and Kalnay, 1993; Palmer, 2018). Instead of producing a single deterministic forecast, an ensemble consists of multiple simulations initialized with slightly perturbed initial conditions or different model configurations (**Figure 2.24**).

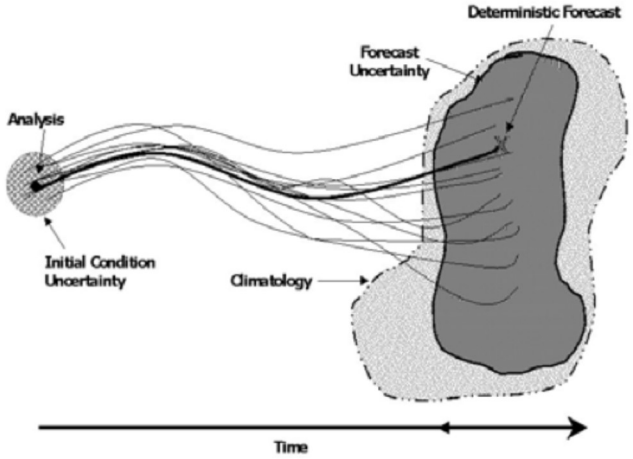

Figure 2.24 The analysis represents the starting point of numerical forecasting, while the deterministic forecast represents the end point (for each forecast valid hour), which lies within the forecast uncertainty—a range that progressively widens as one moves further from the initial forecast time, eventually blending into the realm of climatology (from: *https://content.meteoblue.com/it/ricerca-istruzione/risorse-formative/modelli-nmm/ensembles*)

The resulting ensemble spread quantifies the degree of forecast uncertainty and provides probabilistic guidance for decision-making.

Multiple simulations (**Figure 2.25**) are performed to account for the three sources of uncertainty in weather prediction models:

- errors introduced by incomplete initial conditions (which vary across different simulations);

- errors caused by chaos or sensitivity to different initial conditions;
- errors introduced by imperfections in the models, such as discontinuities at the grid boundaries of a model.

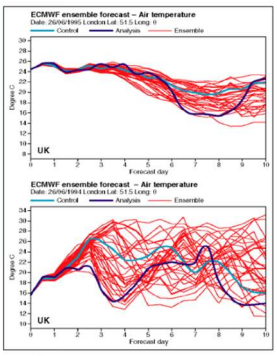

Figure 2.25 Example of a time series of numerical integrations corresponding to ensemble forecasts from the ECMWF IFS model for surface temperature over London. The two maps correspond to exactly one year apart. In each map, the thick solid light blue line represents the deterministic model forecast, while the thick violet solid line shows the observations. The forecasts from the various runs obtained by perturbing the initial conditions (ensemble forecasts) are shown in red (from: *https://content.meteoblue.com/it/ricerca-istruzione/risorse-formative/modelli-nmm/ensembles*)

Visualization tools such as "spaghetti plots" (**Figure 2.26**) illustrate the dispersion of ensemble members, indicating forecast reliability: tightly clustered members suggest a high-confidence prediction, while wide dispersion reflects a low-confidence scenario.

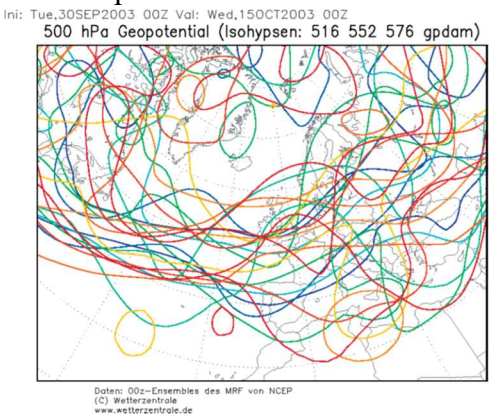

Figure 2.26 Example of spaghetti plots for 500 hPa geopotential heights from GFS ensemble forecasts (from: *wetterzentrale.de*)

In **Figure 2.26**, the 500 hPa contour lines appear highly dispersed, indicating that the 15-day forecast is unreliable.

The evaluation and validation of forecasting models rely on statistical indices derived from contingency tables comparing predicted and observed events. Metrics such as the bias, Hit Rate Ratio (HRR), and Equitable Threat Score (ETS) quantify model performance in terms of accuracy, reliability, and discrimination capability (Wilks, 2011). In precipitation forecasts, for instance, the model output is typically compared to observed rainfall exceeding specific thresholds. Common tendencies include overestimation on windward slopes and underestimation on leeward sides in complex terrain, reflecting both model and observational limitations (Baldauf et al., 2011).

Forecasting accuracy is influenced by three primary sources of error (Kalnay, 2002): *i*. intrinsic predictability limits, due to the chaotic dynamics of the atmosphere; *ii*. model errors, associated with incomplete or approximate representations of physical processes and finite resolution; *iii*. initial condition errors, arising from observation gaps, measurement uncertainties, or imperfect data assimilation. Among these, the latter is often the dominant contributor to forecast degradation.

In conclusion, modern forecasting models are the result of over a century of interdisciplinary development integrating physics, mathematics, and computational science. NWP models have evolved into powerful tools for understanding and predicting atmospheric behavior. Despite remarkable progress, the forecasting challenge remains constrained by the chaotic nature of the system and the finite accuracy of available data. Nevertheless, continuous advances in high-performance computing, observation networks, and algorithmic techniques promise further improvements in both resolution and reliability, driving the field toward increasingly precise and adaptive predictive frameworks (Bauer et al., 2015).

Forecasting models play a crucial role in sustainable water resource management. The outputs they generate, such as precipitation forecasts, soil water content estimations,

evapotranspiration rates, and temperature projections, represent essential inputs for irrigation scheduling and optimization (Jones et al., 2003). Accurate and timely weather predictions allow decision-makers and farmers to anticipate periods of water scarcity or excess, adapt irrigation strategies, and minimize waste. In regions facing increasing hydrological variability due to climate change, these models provide the foundation for data-driven irrigation planning, helping to balance agricultural productivity with environmental conservation.

In this context, the coupling of meteorological forecasting with models enables a more integrated management of water cycles across scales, from local irrigation districts to entire watersheds. By transforming complex atmospheric dynamics into actionable information, forecasting models serve not only as predictive instruments but also as strategic tools for water sustainability. Their continuous refinement, through enhanced resolution, improved parameterizations, and advanced data assimilation, represents a key pathway toward more resilient agricultural systems and a more responsible use of water resources in a changing climate.

2.4 Remote Sensing data

Remote Sensing (RS) is the technical–scientific discipline that enables the acquisition of environmental information and the characterization of objects or surfaces from a distance through measurements of EM radiation that is emitted, reflected, or transmitted by the target. This approach allows the retrieval of the physical and morphological properties of an object or a system of objects without direct contact.

Depending on the distance between the sensor and the target (such as land surface or plant canopy), it is possible to distinguish between proximal sensing systems, where the sensor is located close to the target, and RS systems, where measurements are collected from airborne or satellite platforms (**Figure 2.27**).

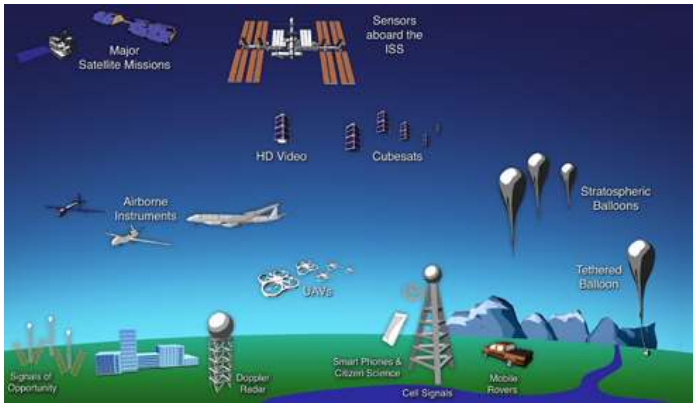

Figure 2.27 Proxymal and remote sensing common sensors (from: *https://www.asi.it/wp-content/uploads/2024/04/Aliano_Oddone.pdf*)

This discipline is closely related to the study of *plant optical properties* (see *2.2.2 Plant-Atmosphere layer*), as the interaction between electromagnetic radiation and vegetation provides essential information on biophysical parameters such as leaf water content, chlorophyll concentration, canopy structure, photosynthetic activity, and crop health. Therefore, RS represents a fundamental tool for monitoring vegetation dynamics and for scaling up observations from the leaf level to ecosystem and regional scales.

RS offers several significant advantages for environmental monitoring and analysis. It provides information over large spatial extents, enabling the assessment of vast and inaccessible areas that would be difficult or impossible to cover with *in situ* measurements alone. Moreover, it allows for multitemporal observations of the same area, thus supporting the analysis of temporal dynamics such as vegetation growth, land use changes, and hydrological variations.

Another important advantage lies in the spectral capabilities of remote sensors. Unlike the human eye, which perceives only the visible portion of the electromagnetic spectrum, remote sensors can detect a much wider range of wavelengths, including the infrared and microwave regions. This feature allows the use of specific spectral bands, or combinations of multiple bands, tailored to the analysis of biophysical or biochemical properties of the observed targets.

Additionally, remote sensing provides georeferenced and digital data, which can be easily integrated with other spatial datasets in

Geographic Information Systems (GIS) for advanced spatial analysis and modeling. Finally, some remote sensors can operate in all seasons, during night-time, and under cloudy or adverse weather conditions, ensuring continuous and reliable data acquisition regardless of environmental constraints.

Moreover, the manner of acquiring EM signals can distinguish active and passive sensors, since the former emit their own radiation to illuminate the target and measure the returned signal, while the latter simply record the natural energy, typically solar radiation or thermal emission, reflected or emitted by the surface of Earth. Focusing on satellite, **Figure 2.28** shows the main differences between the two sensors.

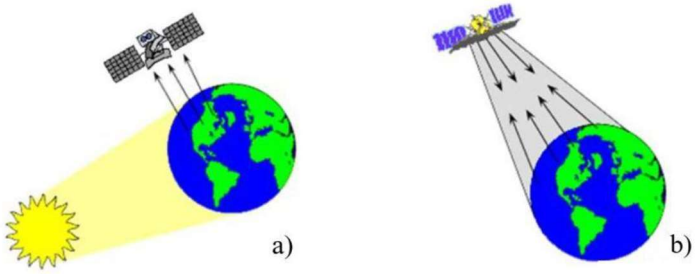

Figure 2.28 Schematization of functioning of passive a) and active b) remote sensors (from: *Boyer et al., 1988*)

Passive remote sensors use solar radiation and measure the amount of energy reflected from the earth surface. These sensors, usually acquire the EM energy in the range of VIS, NIR, SWIR and TIR regions of the EM spectrum. The passive remote sensors are installed on the specific satellites named “payloads”; which play a significant role in the sense of the number of information that a single satellite can provide. The first RS systems were based on a single sensor, but with new technology and computers advancement processes, the multisensory platform has become more affordable and economically advantageous (Nagai et al., 2009; Paparoditis et al., 2014).

The characteristics and the quality of the RS data depend on the spectral resolution, radiometric resolution, spatial resolution, and temporal resolution.

Spectral resolution. The spectral resolution indicates, for fixed wavelength range, the number of spectral bands available from a given sensor. The spectral band is an area of the EM spectrum centred in a specific wavelength.

Radiometric resolution. The memory space storage expresses in terms of BInary digiT (bit) depends also on the radiometric resolution. Remotely sensed data are represented by positive Digital Numbers (DN) which vary from 0 to a fixed power of 2. This range corresponds to the number of bit used for coding numbers in binary format. Each bit records an exponent of power 2. The maximum number of radiance levels detectable depends on the number of bits used in representing the energy recorded. If a sensor uses an 8 bits coding to record the data, this means that there are 256 DN values, ranging from 0 to 256 to represent the different energy levels.

Spatial resolution. The spatial resolution represents the portion of geographical area covered by the survey, also known as pixel.

Low-altitude systems, such as ground-based sensors and small unmanned aerial systems (UASs), operate at a few meters to hundreds of meters above the ground, capturing high-resolution data over limited areas. Airborne platforms, including fixed-wing and rotary-wing aircraft or airships, cover larger regions at intermediate altitudes, offering a balance between spatial detail and coverage. Stratospheric platforms and unmanned airships operate at higher altitudes, extending their observation range while reducing spatial resolution. Finally, satellite systems, such as remote sensing and geostationary satellites, function at altitudes of hundreds to tens of thousands of kilometers, providing broad global coverage but coarser spatial resolution (**Figure 2.29**).

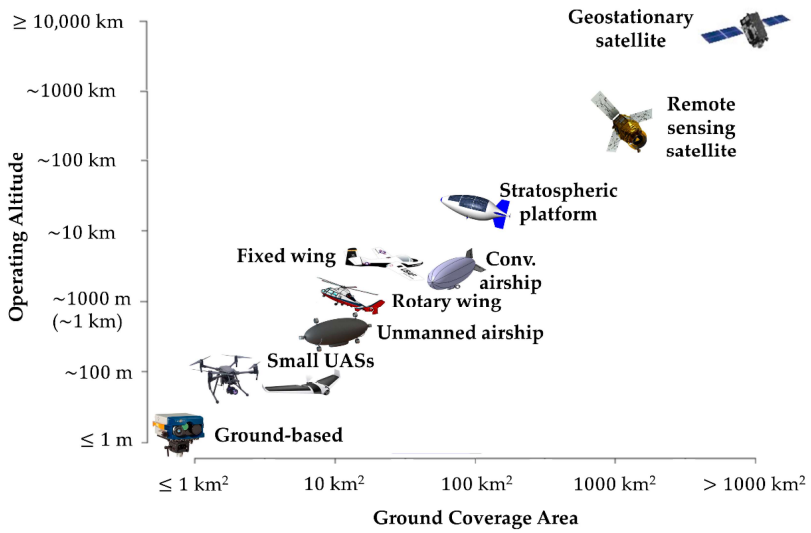

Figure 2.29 Ground coverage area *vs* operating altitude (from: *Gili et al., 2021*)

Temporal resolution. Temporal resolution represents the frequency with which a sensor revisits the same part of the surface of earth. This value depends on the design of the satellite sensor and its orbit pattern.

It is important to note that spatial, spectral, and temporal resolutions are not independent parameters; rather, they are interrelated aspects of sensor design and data acquisition. An increase in spectral resolution, that is, the ability to distinguish narrower wavelength bands, typically results in a reduction of spatial resolution (**Figure 2.30-left**), as the sensor must divide the incoming energy among more spectral channels. Similarly, an increase in temporal resolution, meaning more frequent revisit times, often implies a narrower swath width (**Figure 2.30-centre**), since the satellite must scan a smaller area to achieve higher revisit frequency. Conversely, as the swath width increases to cover larger portions of the surface of the earth, the pixel size generally becomes coarser (**Figure 2.30-right**).

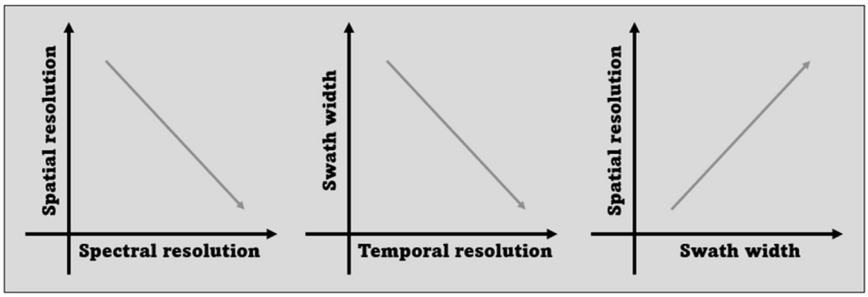

Figure 2.30 Correlation between remote sensing parameters

These trade-offs reflect the physical and technical limitations of remote sensing systems and highlight the need to balance spatial detail, spectral information, and temporal frequency according to the objectives of the observation.

Chapter 3. Actual evapotranspiration modelling

As discussed in *Chapter 2*, there are several approaches available to monitor the variables of the SPA continuum. Some techniques are capable of directly measuring actual evapotranspiration (ET_a); however, these methods are often highly complex, time-consuming, and require the processing of large volumes of data. Moreover, the necessary instruments are expensive, making these techniques impractical for routine use by farmers in irrigation management.

For these reasons, a more feasible and efficient alternative is to rely on modelling approaches. Models use as inputs those SPA variables that are relatively easy to measure, such as meteorological variables and basic soil or vegetation properties, to estimate as output quantities that are more difficult to measure directly, such as ET_a Through this approach, modelling provides a practical tool to simulate and understand the water exchange processes within the SPA continuum, supporting informed decision-making in irrigation planning and sustainable water resource management.

A model, in this context, can be defined as a simplified mathematical or computational representation of a system or a process, designed to simulate its behavior under specific conditions. Models are built based on known physical principles, empirical relationships, or a combination of both, and they use input variables to estimate quantities that are otherwise difficult or impossible to measure directly.

When developing or selecting a model, it is essential to consider the trade-off between its complexity and the accuracy of its results, as increasing model sophistication does not necessarily lead to better performance. This relationship is illustrated in **Figure 3.1**, which shows the balance between model complexity and overall model error.

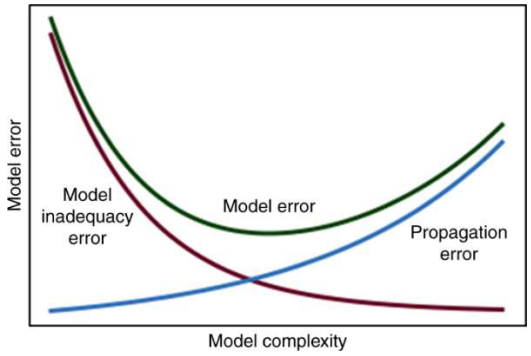

Figure 3.1 Model complexity vs model error
(from: *https://www.nature.com/articles/s41467-019-11865-8*)

The red curve represents the model inadequacy error; this refers to the error arising from an overly simplified model structure, which fails to accurately represent the real physical processes. Such error is high in very simple models and decreases as model complexity increases, since more complex models can capture a greater portion of the variability and dynamics of the system.

The blue curve represents the propagation error; this error originates from the sensitivity of the model to uncertainties in input data, initial conditions, and parameters. It tends to increase with model complexity, as more complex models require a larger number of variables and parameters, thus offering more opportunities for small uncertainties to propagate and amplify in the output.

Finally, the green curve represents the total model error, which is the combined effect of the two components. Its U-shaped trend indicates that there is an optimal level of model complexity at which the total error is minimized.

Figure 3.1 highlights that models which are too simple suffer from high inadequacy error, whereas overly complex models are prone to higher propagation error. The goal in model development and application is therefore to find an optimal balance between simplicity and complexity, ensuring that the model is both accurate and robust.

In the case of ET_a, models integrate information from meteorological data and soil/crop characteristics to estimate the amount of water transferred from the soil as evaporation (E) and plant surfaces as transpiration (T) to the atmosphere.

Depending on their complexity, ET_a models can range from empirical formulations, based on statistical relationships between variables, to physically based models that solve the equations governing mass and energy transfer within the SPA continuum. In both cases, the goal is to represent the underlying physical processes as accurately as possible, while ensuring that the model remains practical and applicable for irrigation planning and water resource management.

Among the different modelling approaches, the most widely used frameworks for estimating ET_a are those based on the analysis of carbon fluxes, surface energy balance, and soil water balance. These three components represent complementary perspectives for describing the exchanges of matter and energy that occur within the SPA continuum.

The carbon flux approach relies on the relationship between photosynthesis and *T*, where both processes are regulated by stomatal conductance and atmospheric conditions. Measurements or simulations of Gross Primary Production (*GPP* [μmol m^{-2} d^{-1}]), and Net Ecosystem Exchange (*NEE* [μmol m^{-2} d^{-1}]), often derived from EC towers, can be partitioned to estimate the *T* and *E* components of *ET* (Li et al., 2019). This approach directly links water and carbon cycles and provides valuable insight into ecosystem productivity and WUE.

The Surface Energy Balance (SEB) approach is grounded in the conservation of energy at the land surface, where the available net radiation (R_n [W m^{-2}]), is partitioned among sensible heat flux (*H* [W m^{-2}]), soil heat flux (G_0 [W m^{-2}]), and latent heat flux (*LE* or λET_a [W m^{-2}]). By solving this balance, the *LE* can be derived, allowing ET_a estimation (Norman et al., 1995; Bastiaanssen et al., 1998).

The Soil Water Balance (SWB) approach, on the other hand, represents ET_a as one of the main terms in the hydrological balance of the root zone, together with precipitation (*P* [mm d^{-1}]), Irrigation (*I* [mm d^{-1}]), CaPillary Rise (*CPR* [mm d^{-1}]), and Deep percolation (*DP* [mm d^{-1}]). This method is often applied in agricultural and

hydrological studies due to its direct link to SWC dynamics and irrigation management.

As illustrated in **Figure 3.2**, these three approaches, carbon, energy, and water, are interconnected within the SPA continuum, forming the physical basis for most modern ET_a models. Each approach emphasizes different aspects of the system, but all share the common goal of describing the exchange of energy, water, and carbon between the soil, vegetation, and atmosphere. Their integration within a unified modeling framework enables a comprehensive understanding of ecosystem working and supports the development of sustainable water resource management strategies.

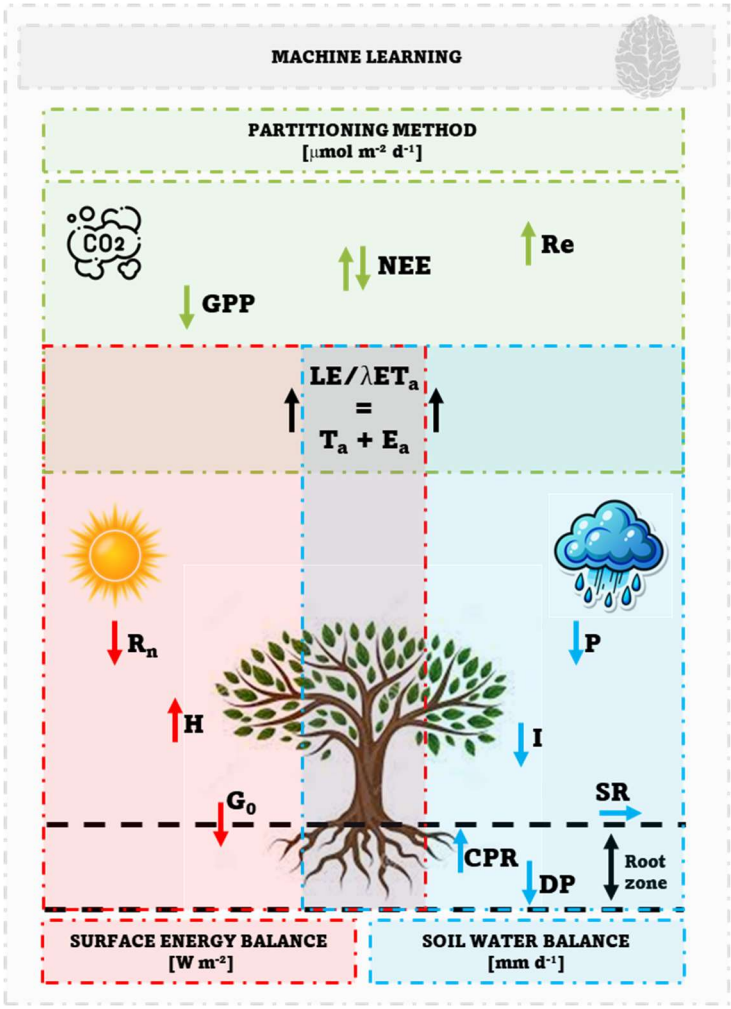

Figure 3.2 Machine learning, carbon, energy and water approaches

3.1 Surface energy balance model

The most important variable of energy balance system is the R_n. It is the net amount of radiation energy available for heating soil and air, or for evaporating soil water. R_n is the driving force of all the processes occurring in any SPA continuum. The sensible heat flux (H) arising from surface represents the rate of heat loss in the air by convection and conduction due to differences in temperatures, and it is involved in heating and cooling the system. G_0 is the rate of soil heat storage due to conduction. The last component of the energy balance is the LE or λET_a, which represents the evaporative energy able to change the state of water and to transfer energy in the form of latent heat. In SPA continuum, it is the most important variable related to CWR, and it represents the rate of latent heat loss from the surface due to ET processes. Usually, the energy terms such as heat stored or released in the plant and the energy used in the metabolic activity of the plants, are usually neglected in the surface energy balance equation. Gates (1980) and Larcher (1983) showed that the energy used for metabolic activity accounts for a tiny portion of the total energy and could be considered negligible in comparison to other energy terms. Similarly, the rate of heat storage, is considered negligible even if it can reach a percentage of about 5% of the global radiation on a sunny summer day (Brutsaert, 2005). Based on these assumptions, the surface energy balance equation considers only four components of energy fluxes:

$$R_n - G_0 - H - LE \text{ or } \lambda ET_a = 0 \quad \textbf{(3.1)}$$

The surface energy balance considers the diurnal R_n during clear sky hours as a positive component directed downward to a specific surface, to which supplies energy, while the remaining components, removing energy from that surface, are negative when directed away from the surface. Water evaporation process requires supplying sensible energy or radiant energy to transform water molecules into vapor. Therefore, the process of ET is controlled by the amount of energy available and the energy transfer at vegetation and soil surface.

Because the energy exchange in the SPA continuum controls the ET process, for a fixed time interval, incoming energy on a surface must be equal to the outgoing energy. The latent component of the energy balance can be estimated by applying the concepts of energy conservation by subtracting G_0 and H from the surface net radiation flux (*i.e.*, *LE* or ET_a is calculated as residual of the surface energy balance).

The models based on the resolution of the SEB, in general use two different schematizations: the first is the "one source" or "big leaf" (Monteith, 1965) (Bastiaanssen et al., 1998); this consider the vegetation as an homogeneous, semi-transparent surface in which the phenomena of soil *E* and plant *T* are considered jointly. On the other hand, the second approach known as "two-layer" or "two-source" considers the two previous phenomena separated through a partition between energy fluxes in the soil and energy fluxes in the canopy alone (Shuttleworth and Wallace, 1985; Norman et al., 1995).

3.1.1 One-source

The energy fluxes modelling based on the "big leaf" approach starts from the theoretical background developed by Penman (1948) for surfaces characterised by wet surface-atmosphere interface (water bodies). The relationship retrieved for saturated surfaces was extended by Penman (1956) to the case of single leaf by introducing a resistance, in series with the aerodynamic one, which takes into account the resistance of the stomata to the flux of vapour, named stomatal resistance. Finally, the scaling up of the model from leaf to canopy scale was realised by Monteith (1965) introducing the "big leaf" concept.

3.1.2 Two-source

In the "two source" model, the land surface is treated differently, where the radiative exchanges, the thermal heat conduction and convection between the surface and low atmosphere are parameterized and partitioned between vegetation and soil. The key element of the "two source" SEB model is the partitioning of fluxes between soil and canopy. Partitioning of R_n represents the first step in

estimating the various components of temperature. The knowledge of soil and canopy temperatures allows distributing available energy (R_n - G_0) to the remaining components of SEB. The key boundary condition is the radiometric land surface temperature (Kustas and Anderson, 2009). The contributions of canopy and soil to land surface radiometric temperatures are different. If emissivity represents both soil and vegetation components, the Land Surface Temperature (*LST*) can be partitioned into soil and vegetation contributions on the basis of the *FVC*:

$$LST = [FVC \cdot T_c^4 - (1 - FVC) \cdot T_s^4]^{1/4} \quad \textbf{(3.2)}$$

where T_s is the soil surface temperature [°K], T_c is the canopy temperature [°K], and *FVC* is the fractional vegetation cover.

From RS point of view, the input dataset required for the application of the SEB model consists of: meteorological data (*e.g.*, global solar radiation, relative air humidity, air temperature, and wind speed); biophysical and radiometric vegetation parameters (*e.g.*, albedo, crop height, and Leaf Area Index); surface energy quantities (*e.g.*, emissivity and land surface temperature). In the original conceptual framework, the authors of the Surface Energy Balance Algorithm for Land (SEBAL), which is a "one source" or "big leaf, and the Two Source Energy Balance (TSEB), which is a "two source" model, proposed a series of algorithms for calculating the terms that appear in the energy balance equation, which are readily applicable using remote sensing data in the VIS/NIR and TIR bands, along with a limited number of *in situ* observations. Thus, scientific literature offers several examples of SEBAL/TSEB model applications over large territorial extents, utilizing images acquired from various types of aerial and/or satellite sensors, which enables its spatially distributed application (Awada et al., 2019; Corbari et al., 2023; Cammalleri et al., 2024).

3.2 Soil Water Balance Model

The resolution of the SWB between the incoming flux (*i.e.*, *P*, *I* and *CPR*) and exiting (*T* and *E* or thus, ET_a, *SR* and *DP*), allows to estimate, the *SWC* dynamic, in the SPA system:

$$\int_{t-1}^{t} SWC = \int_{t-1}^{t} P + I + CPR - (T + E) \text{ or } ET_a - DP - SR \quad \textbf{(3.3)}$$

The SWB models can be divided into two categories: the first considers the SPA continuum as a single reservoir in which the terms of the SWB are described through simple schematizations often based on empirical equations.

The other category is based instead on a more complex schematization that uses physics-based laws for the study of water fluxes in unsaturated systems coupled with equations or models describing roots drawn down in the soil.

The first category of models includes the FAO-56 model presented in FAO-56 paper (Allen et al., 1998), while in the second one are included HYDRUS-2D/3D (Šimůnek et al., 1998), SWAP (Kroes et al., 1999) and ACRU (Schulze, 1989) models, in which the equations that describes physical phenomena are solved to compute the balance terms.

3.2.1 FAO-56

The modelling of water exchanges within the SPA Continuum system is greatly simplified compared to physical models and is fundamentally based on a soil drying law. The well-known FAO-56 model (Allen et al., 1998) has been largely applied. This model schematizes the soil as a reservoir characterized by a fixed capacity depending on the depth of the root system (Z_r) and the soil retentivity parameters (*i.e.*, field capacity, wilting point). The FAO-56 model can be applied based on a single or a dual crop coefficient approach. Root water uptake processes are generally neglected, and simplified formulations are used to estimate T and the E (double approach). These terms are combined into the ET_a since these two phenomena occur simultaneously and are influenced by the same variables (single approach).

All inflows and outflows from the soil reservoir are expressed in millimeters, and the simulation time step is generally daily. The variation of the soil water storage, and consequently its depletion ($D_{r,i}$ [mm]), is described by the following equation:

$$D_{r,i} = D_{r,i-1} - P_i + SR_i - I_i - CPR_i + (E_i + T_i) \text{ or } ET_{a,i} + DP_i \quad \textbf{(3.4)}$$

where $D_{r,i}$ represents the soil water depletion at day i, $D_{r,i-1}$ the depletion at the previous time step, P_i the effective rainfall, SR_i the surface runoff, I_i the effective irrigation, CPR_i the capillary rise, E_i the actual soil evaporation and T_i the actual transpiration or thus ET_a actual evapotranspiration, and DP_i the deep percolation flux.

In this formulation, a positive variation of $D_{r,i}$ indicates an increase in soil water deficit (*i.e.*, depletion), while a negative variation corresponds to a soil water recharge.

The transition from D_r to SWC is based on the concept that depletion represents the amount of water missing with respect to field capacity, within the range of the Total Available Water (TAW), that is, the amount of water stored in the root zone between field capacity (SWC_{fc}) and the wilting point (SWC_{wp}).

$$TAW = \left(SWC_{fc} - SWC_{wp}\right) \cdot Z_r \quad \textbf{(3.5)}$$

SWC_{fc} represents the amount of water retained in the soil after excessing gravitational water has drained and the rate of percolation has significantly decreased, corresponding to the upper limit of water availability for plants.

SWC_{wp} is the SWC at which plants can no longer extract sufficient water to maintain their physiological functions, marking the lower limit of available water.

Both parameters can be determined by characterizing the soil through its soil water retention curve, which describes the relationship between SWC and ψ (**Figure 3.3**).

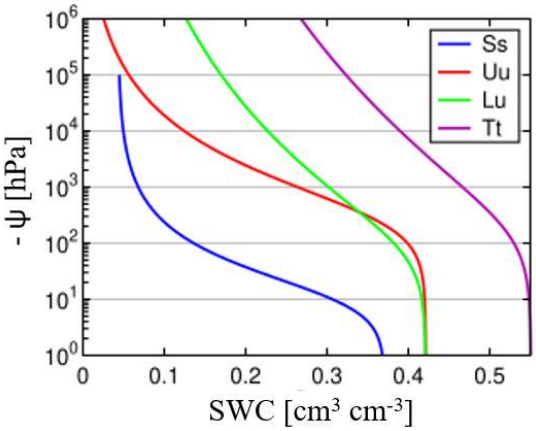

Figure 3.3 Examples of several retention curves; blue line is sand (Ss), red line is either silt or clay-loam (Uu), green line is either loam-silt or clay (Lu), and violet line is either clay or peat (Tt) (from: *https://en.wikipedia.org/wiki/Water_retention_curve*)

On a soil water retention curve, SWC_{fc} is determined by reading the water content at a matric potential of about −330 hPa (or −100 hPa for sandy soils), while the SWC_{wp} is identified by the water content at −15,000 hPa.

Moreover, Readily Available Water (*RAW*) represents the fraction of the *TAW* that can be extracted by the crop without inducing water stress. It defines the range of soil water content conditions over which transpiration occurs at its potential rate. When D_r exceeds the *RAW* threshold, plant transpiration begins to decrease due to increasing soil water stress. *RAW* is expressed as the product between *TAW* and the depletion factor (p_{FAO}). This latter depends on both the crop type and *ETo*. Crops with deeper or more efficient root systems generally tolerate higher depletion levels, while under conditions of high evaporative demand (high *ETo*), the value of p decreases, indicating that plants experience stress at smaller soil water deficits.

Thus, the soil water content can be expressed as

$$SWC = SWC_{FC} - \frac{D_r}{Z_r} \quad \textbf{(3.6)}$$

which relates the decrease in stored water within the root zone to the corresponding reduction in the *SWC*.

3.2.1.1 Single Approach

In the single coefficient approach, ET_a is calculated using a single crop coefficient (K_c) that combines both E and T components and a water stress coefficient (K_s).

$$\Delta SWC = (P + I - K_c K_s ET_0 - SR - DP + CPR)\frac{\Delta t}{Z_r} \quad \textbf{(3.7)}$$

K_c reflects the morphological and ecophysiological characteristics of the crop, as well as cultivation techniques, phenological phases, and soil coverage. Its value is strongly influenced by the environmental conditions of the plant's growth area. As K_c depends on the growth stage of the crop, it is essential to use distinct values for different phenological phases (Allen et al., 1998). Traditionally, K_c is defined through trapezoidal time series specific for each crops, suggested by Allen et al. (1998) and recently reviewed by Rallo et al. (2021) (**Figure 3.4**).

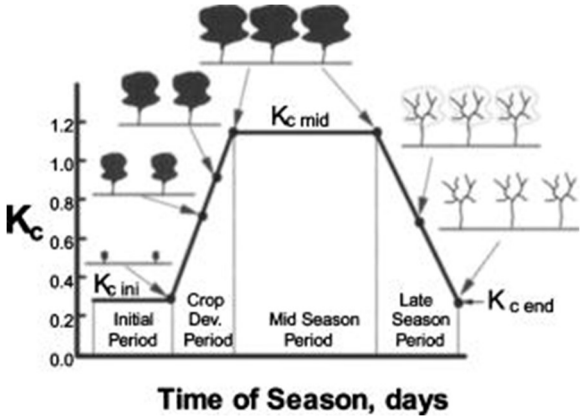

Figure 3.4 Temporal dynamic of the crop coefficient for a generic crop (from*: Allen et al., 1998*)

Once a certain SWC threshold is exceeded (SWC^*), the crop starts to be stressed, and the stress coefficient begins to decrease. This threshold value is a function of p_{FAO}, which represents the fraction of total available water that can be depleted from the root zone before water stress occurs.

Thus, K_s, expression of the actual crop water stress conditions, is typically calculated either as a linear function **(3.8)** (Allen et al., 1998)

or an exponential function **(3.9)** (Steduto et al., 2009) of *TAW* and *RAW*, thus soil water content within the root zone (**Figure 3.5**).

$$K_s = \frac{TAW - D_r}{(1 - p_{FAO}) \cdot TAW} \quad \textbf{(3.8)}$$

$$K_s = 1 - \frac{e^{\left(\frac{D_r - RAW}{TAW - RAW}\right) \cdot f_{shape}} - 1}{e^{f_{shape}} - 1} \quad \textbf{(3.9)}$$

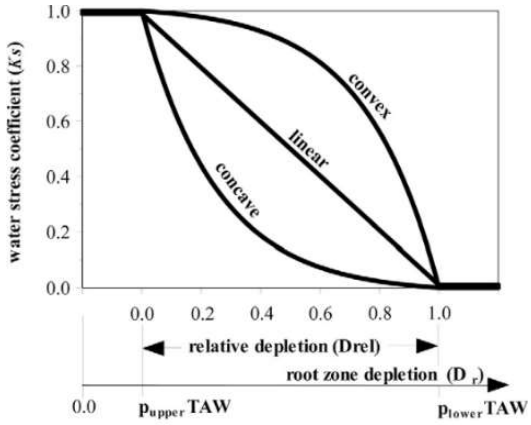

Figure 3.5 Water stress coefficient *vs* depletion (from: *Steduto et al., 2009*)

When no crop water stress is present, the value *Ks* is equal to 1. *ETo* reflects the atmospheric evaporative demand. *ETo* represents the evapotranspiration from a reference hypothetical crop, actively growing, adequately watered, completely shading the ground and with an assumed crop height of 0.12 m, a fixed surface resistance of 70 $s\ m^{-1}$ and an albedo of 0.23, which is, therefore, associated with the meteorological evaporative demand. Thus, *ETo* reflects the atmospheric evaporative demand. The most widely used method to estimate *ETo* is represented by the FAO-56 Penman–Monteith (PM) equation, where this quantity is function only of the climate variables (Allen et al., 1998):

$$\boldsymbol{ET_o} = \frac{\mathbf{0.408 \cdot \Delta \cdot (R_n - G) + \gamma \cdot \left(\frac{900}{T_a} + 273\right) \cdot [U_2 \cdot (e_s - e_a)]}}{\boldsymbol{\Delta + \gamma \cdot (1 + 0.34 \cdot U_2)}} \quad \textbf{(3.10)}$$

where Δ [kPa °C^{-1}] is the slope of saturation vapor pressure curve, R_n [MJ m^{-2} d^{-1}] is the net radiation at the crop surface, G_0 [MJ m^{-2} d^{-1}] is the soil heat flux density, (e_s−e_a) [kPa] is the actual vapor pressure deficit, γ [kPa °C^{-1}] is the psychrometric constant and U_2 [m s^{-1}] is the wind speed measured at 2m height.

3.2.1.2 Double approach

In the dual approach, ET_a is separated into two distinct components: T and E, each with its own coefficient, K_{cb} and K_e, respectively.

$$\Delta SWC = \{P + I - [(K_{cb}K_s + K_e) \cdot ET_0] - SR - DP + CPR\}\frac{\Delta t}{Z_r} \quad \textbf{(3.11)}$$

In this approach, K_c is divided into two separate components the basal crop coefficient (K_{cb}) and the soil evaporation coefficient (K_e).

K_{cb} represents the T from the crop under non-stressed conditions, depending mainly on the morphological characteristics of the crop, canopy development, and growth stage. It reflects the potential water use of vegetation when *SWC* is not limited.

Conversely, K_e accounts for direct soil E, which varies with soil wetness, irrigation frequency, and canopy cover. After irrigation or rainfall events, K_e increases temporarily and then decreases as the surface soil dries or becomes shaded by the crop.

Recently, Pôças et al. (2020) and Rocha et al. (2012) have proposed a summary of functional relationships between K_c and/or K_{cb} and RS VIs, which represent an innovative and rapidly expanding area of research for the monitoring of vegetation.

3.3 Carbon Cycle Model

The carbon cycle is based on the exchange of carbon dioxide (CO_2) between the atmosphere, vegetation, and soil. In terrestrial ecosystems, this cycle can be described through three main components: Net Ecosystem Exchange (*NEE*), Gross Primary Production (*GPP*), and Ecosystem Respiration (R_e) (Goulden et al., 1996; Aubinet et al., 1999; Loescher et al., 2006).

The carbon flux corresponds to the *NEE*, which represents the net amount of CO_2 exchanged between the ecosystem and the atmosphere, accounting for both respiratory and photosynthetic processes.

GPP represents the total amount of CO_2 fixed by plants through photosynthesis. It quantifies the potential carbon uptake of the ecosystem and depends primarily on solar radiation, *LAI*, and the photosynthetic efficiency of vegetation.

R_e corresponds to the total CO_2 released back to the atmosphere through both autotrophic respiration (from plant metabolic processes such as growth and maintenance) and heterotrophic respiration (from microbial decomposition of organic matter in the soil) (Lloyd and Taylor, 1994; Reichstein et al., 2005; Davidson and Janssens, 2006).

Within the SPAC continuum, carbon fluxes are closely linked to the energy and water balances. Photosynthesis (and therefore *GPP*) is driven by the availability of solar radiation and limited by stomatal conductance, which in turn depends on *SWC* and atmospheric Vapor Pressure Deficit (*VPD*). Likewise, respiration rates are strongly influenced by temperature and *SWC*, as both plant and microbial metabolic activities respond to these environmental drivers.

3.4 New Smart Solution: Machine Learning to support smart agriculture

In recent years, Machine Learning (ML) has emerged as one of the most powerful tools driving the transformation of smart agriculture (Waqas et al., 2025). By enabling data-driven decision-making, ML techniques can analyze vast and heterogeneous datasets collected from sensors, satellites, drones, and Internet of Things (IoT) devices, providing valuable insights for optimizing crop management, resource use, and environmental sustainability.

Machine Learning algorithms can automatically detect patterns (Janka et al., 2019), predict outcomes, gap filling time series (Granata, 2019; Pagano et al., 2023; De Caro et al., 2023; Pagano et al., 2025) and support management decisions that were traditionally based on empirical knowledge or manual monitoring. In agriculture, this translates into more efficient irrigation scheduling, early detection of

plant stress or disease, yield forecasting, soil water content estimation, and improved resource allocation. Despite their diversity in structure, application domain, and mathematical formulation, all ML algorithms share three fundamental components (Patil et al., 2024; Du et al., 2025): representation, evaluation, and optimization.

Representation; this defines how knowledge or patterns are expressed within the algorithm. It determines the hypothesis space, the set of all possible models that the algorithm can explore to describe the underlying data. Examples of representations include decision trees, linear models, neural networks, support vectors machine, and probabilistic graphical models. The choice of representation directly influences the expressiveness and complexity of the model, as well as its interpretability.

Evaluation; once a model representation is chosen, an evaluation mechanism is required to measure how well a particular hypothesis fits the observed data. The evaluation component defines the objective function or loss function, which quantifies model performance. Common evaluation criteria include measures such as accuracy, precision, recall, mean squared error, log-likelihood, or cross-entropy, depending on the nature of the task (*e.g.*, classification, regression, clustering).

Optimization; optimization provides the strategy to search through the hypothesis space and find the model parameters that minimize (or maximize) the chosen evaluation function. Optimization methods can be analytical (*e.g.*, solving for closed-form solutions) or iterative, such as gradient descent, evolutionary algorithms, or stochastic optimization techniques. The effectiveness and efficiency of an optimization method determine how well and how quickly the algorithm can learn from data.

Together, these three components form the conceptual backbone of any machine learning algorithm. Representation defines what can be learned, evaluation determines how learning success is measured, and optimization guides the learning process itself.

PART II

Materials and Methods

Chapter 4. Materials

4.1 Irrigation District 1A

The study area is represented by the irrigation District 1A of the Garcia-Arancio district managed by the "Consorzio di Bonifica Sicilia Occidentale" (ex Consorzio di Bonifica Agrigento 3) which includes the territories of cities of Sambuca di Sicilia, Sciacca, Menfi, Santa Margherita Belice, Partanna and Castelvetrano.

The area is predominantly cultivated with olive (cv. "Nocellara del Belice") orchards (70%), vineyards (24%) with sporadic presence of citrus (2.6%) orchards being other horticultural (3.4%) crops sporadic.

The soil characterization was carried out by Bono (1998) (**Figure 4.1**).

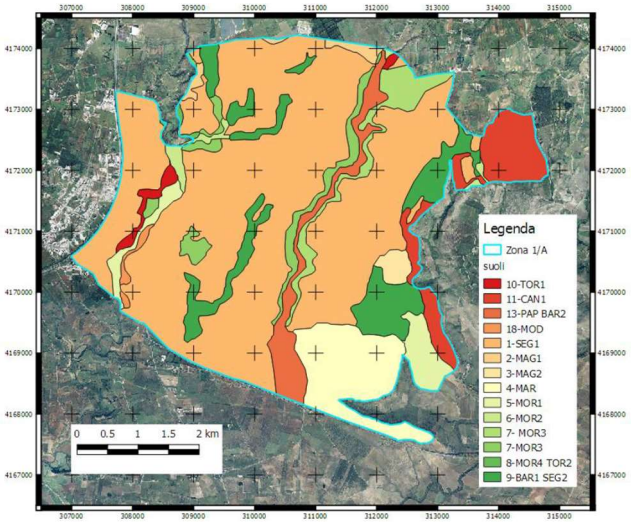

Figure 4.1 Pedologic map of the study area (from: *Bono et al., 1998*)

Eleven soil types were identified within the district. Characterization was performed by determining the percentages of clay, silt, and sand for each identified soil type. Nomenclature was then assigned based on these percentages, following the United States Department of Agriculture (USDA) soil texture triangle. The depth was also evaluated for each soil type. **Table 4.1** shows the

granulometric composition of the soil and the depth of the different soils type.

Table 4.1 Size distribution of the soil within the irrigation district (from: *Bono et al., 1998*)

SOIL	TEXTURE	PARTICULAR SIZE			DEPTH
		Clay [%]	Loam [%]	Sand [%]	[cm]
Torre (TOR1)	frank-sandy	5.41	35.37	59.22	30
Canotta (CAN1)	clay	41.07	41.44	17.49	120
Papa (PAP)	frank-sandy-clay	27.44	27.22	45.35	125
Barone (BAR2)	frank-sandy	18.50	13.50	68.00	75
Modione (MOD)	frank-clay	21.37	39.00	39.63	110
Seggio (SEG1)	frank-sandy-clay	10.28	24.20	65.52	85
Marzuchi (MAR)	frank-sandy-clay	35.43	17.65	46.93	90
Morici (MOR1)	frank-silty	10.44	51.41	38.15	100
Morici (MOR2)	frank	15.80	38.24	45.96	30
Morici (MOR4)	frank	19.54	33.24	47.22	80
Torre superficiali (TOR2)	frank	19.54	33.24	47.22	80

According to **Figure 4.1**, The prevalent type of soil is “Seggio (SEG1)” that covers ~1800 ha, about the 60 % of the total area.

Based on the soil granulometric composition and by means the pedo-transfer function implemented in the software “ROSETTA” (Schaap et al., 2001), the parameters of the soil water retention curve, expressed according to the model proposed by Van Genuchten (1980), were obtained (**Table 5.2)**.

Table 4.2 Soil water retention curve coefficients estimate by means “ROSETTA” software (from: *Schaap et al., 2001*)

SOIL	SWC_s [$cm^3\ cm^{-3}$]	SWC_r [$cm^3\ cm^{-3}$]	Ω [cm^{-1}]	X [cm^{-1}]	SWC_{fc} [$cm^3\ cm^{-3}$]	SWC_{wp} [$cm^3\ cm^{-3}$]
Torre (TOR1)	0.39	0.04	0.0347	1.7466	0.10	0.05
Canotta (CAN1)	0.46	0.09	0.0150	1.2529	0.33	0.19
Papa (PAP)	0.39	0.11	0.0334	1.2067	0.28	0.11
Barone (BAR2)	0.39	0.04	0.0347	1.7466	0.10	0.02
Modione (MOD)	0.44	0.07	0.0158	1.4145	0.26	0.12
Seggio (SEG1)	0.39	0.11	0.0334	1.2067	0.28	0.19
Marzuchi (MAR)	0.39	0.11	0.0334	1.2067	0.28	0.19
Morici (MOR1)	0.44	0.06	0.0051	1.6626	0.29	0.09
Morici (MOR2)	0.30	0.06	0.0111	1.4737	0.24	0.09
Morici (MOR4)	0.40	0.06	0.0111	1.4737	0.24	0.09
Torre superficiali (TOR2)	0.39	0.04	0.0347	1.7466	0.10	0.05

The saturated soil water content (SWC_s), the residual soil water content (SWC_r), as well as the parameters Ω and Ξ that define the shape of the soil water retention curve were determined. Based on the soil water retention curves, the soil hydrological constants were then calculated, specifically the soil water contents corresponding to field capacity and the wilting point.

The waters used for irrigation purposes are those stored in the artificial reservoirs Garcia and Arancio, which are characterized by a reservoir capacity of ~60 and ~25 Mm^3, respectively. The two tanks are interconnected by an abduction pipeline with an overall length of ~50 km, which allows the transfer of volumes from Lake Garcia to the Arancio reservoir by gravity. From the Garcia-Arancio tank split up two distribution pipes called "Diramazione Est" and "Diramazione Ovest", with a diameter of 1600 mm and 2000 mm, respectively, these supply the header tanks by gravity or pumping, which supply the irrigated areas divided according to altimetry zone.

The District 1A falls on the northern side of the irrigated area and covers a surface of about ~3000 ha. To deliver water from reservoir to hydrants a dense pipe-network extending ~215 km was implemented. The network is divided into main, secondary, and tertiary pipelines with different materials steel, glass fiber reinforced plastic, asbestos cement and polyvinyl chloride. Irrigation network is fed, by gravity, by two loading reservoirs, the first of which named 1/A1 has a volume of ~25000 m^3 located at ~250 m a.s.l., the second, named 1A/2, placed at ~200 m a.s.l. characterized by a volume of ~27000 m^3. Water derived from the main adductor of the Garcia lake is pumped into two reservoirs by a set of pumps working with variable speed drive installed at the "Zangara" pumping station.

The distribution network serves 139 sectors for more than 2000 water users. In each irrigation sector, water distribution is performed by turns, that means that the whole flow is diverted to the hydrants follow a fixed turn. Hydrant discharge equals to 15 l s^{-1}, with a minimum pressure of 2.5 bar. Volumetric water consumption in each sector is controlled and registered by a central control unit. The most common farm distribution systems are sprinkler and drip irrigation.

The volumes delivered in each hydrant located within the sector are registered on a paper format user card (**Figure 4.2**).

Figure 4.2 Example of the paper sheet referred to one user

For each user, the employees of the consortium, registers in a paper the information to draw up an effective irrigation plan. Each form are reports information regarding the location of the farms in the district, the number of the sector, the crop type, the farm extension, the date, and the volume of the water delivered.

For this study, the user cards were available for seven fields (A-G) within the consortium area, covering the irrigation seasons of 2018, 2019, and 2020.

4.1.1 Experimental Field I – Olive Orchard

The experimental field has an extension of ~13 ha (**Figure 4.3**).

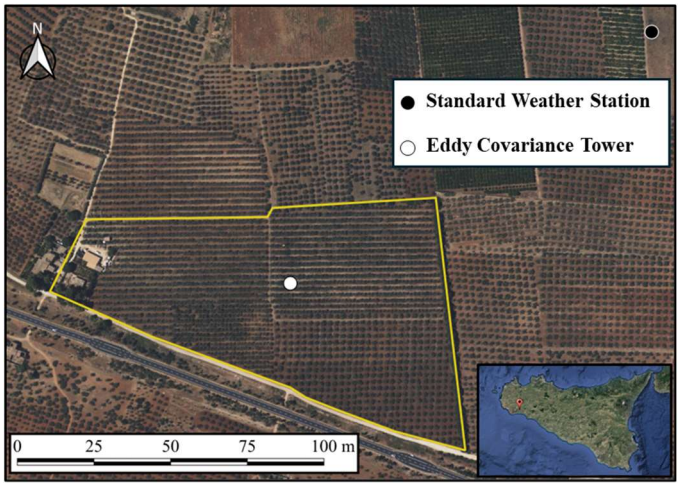

Figure 4.3 Map of the experimental field (yellow perimeter) with the position of the EC tower (white dot) and the SIAS standard weather station (black dot). The insert figure also shows the location of the experimental site within Sicily Island (Italy)

The plants, having a height of about 3.5 m, are spaced according to a regular 5×8 m grid (~ 250 plants ha^{-1}). The trees are characterized by an average height of ~5.6 m and a root zone 0.8 m

Irrigation water is supplied by a drip irrigation system (four emitters/plant providing 8 l h^{-1}).

The soil textural class is USDA classified as loam-sandy-clay (Seggio (SEG1)) with average clay, silt, and sand contents of 24, 16, and 60%, respectively.

A standard weather station of the Servizio Informativo Agrometeorologico Siciliano (SIAS) is installed near the experimental field. This weather station provides hourly data of the following meteorological data: air temperature, global solar radiation, relative air humidity, wind speed and direction at 2 m height, and rainfall. The quality assurance procedures applied to the data are reported in Fiebrich et al. (2010).

Also, an EC tower, operating in the experimental field, is installed. The system allows to obtain high frequency measurements of the three wind components and the H_2O and CO_2 concentrations by means of a three-dimensional sonic anemometer (CSAT3-3D, Campbell Scientific Inc.) and an infrared open-path gas analyzer (LI7500, Li-cor Biosciences Inc.), respectively. These instruments were installed 7 m a.g.l. and operate at a sample frequency of 20 Hz (for the raw data). The auxiliary experimental set-up is represented by a low frequency (30 min), 4-components net radiometer (CNR-1 Kipp & Zonen) located at 8.5 m a.g.l. and two self-calibrated flux plates (HFP01SC, Hukseflux) placed, respectively, in the exposed and shadowed bare soil, at a depth of about 0.1 m b.g.l.. All the data (high- and low- frequencies) were stored in a CR5000 data logger (Campbell Scientific Inc.) equipped with a PCMCIA memory card.

The SIAS weather station provides continuous meteorological records available since 2002, whereas the Eddy Covariance tower offers high-frequency flux measurements for the period 2009–2011.

4.2 Experimental Field II – Citrus Orchard

The second experimental field is a Mediterranean citrus orchard (Citrus reticulata Blanco, cv. “Mandarino Tardivo di Ciaculli”) of

about 1 ha, located near Palermo, Italy (38◦ 4' 53.4'' N, 13◦ 25' 8.2'' E) (**Figure 4.4**).

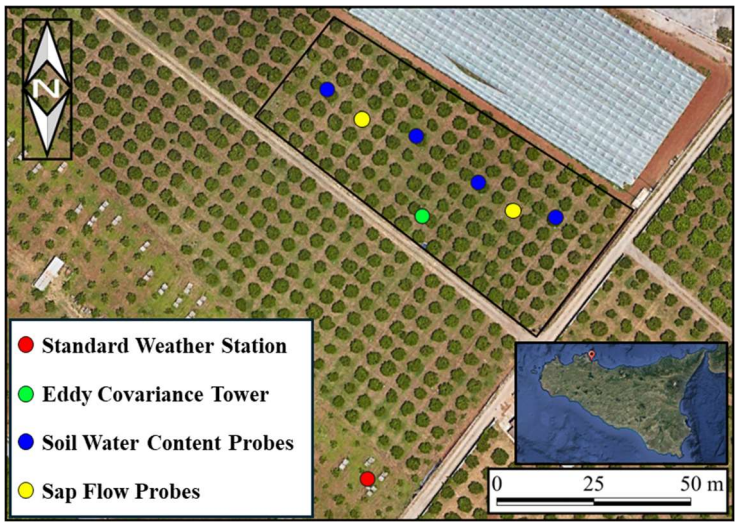

Figure 4.4 Experimental site (black perimeter) map with the location of the measurement instruments: red dot indicates the standard weather station, green dot the EC tower, blue dots the soil water content probes, and yellow dots the sap flow probes. The insert figure also shows the location of the experimental site within Sicily Island (Italy)

The field is characterized by planting spacing of 5.0×5.0 m (density of 400 trees ha^{-1}), with plant rows roughly oriented from North-East to South-West. The trees are characterized by an average height of about 2.5 m and a root zone 0.5 m depth characterized by the highest root density at 0.3 m b.g.l. approximately. Moreover, in **Figure 4.4**, a greenhouse adjacent to the field can also be observed. This structure is installed only during certain periods of the year to cover the neighboring vineyard.

Irrigation season in the area ordinarily starts in the middle of May and finishes around the end of September, during periods with scarce or absent precipitations. Since 2018, the field is irrigated with a subsurface drip system with two pipes per plant row, one on each side of the tree, at 1.1 m from the trunks. The lateral pipes contain co-extruded emitters discharging 2.3 l h-1 at a pressure of 100 kPa; the spacing between emitters is 1.0 m (i.e., 10 emitters/tree). However, the old micro-sprinklers irrigation system is still occasionally

activated mainly before weeding and/or for aid irrigation supplies. The citrus, between the flowering phase and the fruit set stage in spring, require large amount of water (Johnson et al., 2013), which is ensured via the high average rainfall in this season. In case of drought events in spring, the farmer provides aid irrigation volumes via micro-sprinklers. Under these conditions, weeds often grow in spring and are usually removed in mid-July. Thus, weeds partially cover the field until July in almost all the irrigation seasons, except for 2021 when, due to a lack of maintenance, weeds heavily grown and were not removed by the farmer. Irrigation management includes, depending on the environmental conditions (*e.g.*, no drought and/or heatwave conditions), the Regulated Deficit Irrigation (RDI) strategy. The adopted RDI, accounting for the actual climate conditions, is designed to define moderate crop water stress only during phase II of vegetative growth (initial fruit enlargement phase), generally occurring between July 1 and August 15, during which the lower threshold of Midday Stem Water Potential (MSWP) ranged between − 1.4 and − 2.0 MPa. During the other phases of crop growth, the values of MSWP ranged between − 0.4 and − 1.4 MPa.

The dominant textural class of the topsoil is sandy-clay-loam (USDA classification) with average clay, silt and sand content of 22.2%, 18.0% and 59.8%, respectively.

Meteorological data are collected by a WatchDog 2000 series weather station (Spectrum Technologies, Inc., Aurora, IL, USA) installed nearby the experimental field. The station is equipped by sensors measuring the main meteorological data with a time-step of 30 min. The quality assurance procedures applied to the data are reported in Fiebrich et al. (2010).

The temporal dynamic of soil water content is monitored, at a point scale, with four 0.6 m long "drill & drop" probes (Sentek Pty Ltd, Stepney, Australia). Each probe is installed at a distance of 0.8 m from the tree trunks and 30 cm far from an emitter.

Two standard Granier type (Granier, 1987) thermal dissipation probes (SFS2 type, UP GmbH Firmesitz, Germany) were installed on two citrus trees in the north and south cardinal directions. The probes

were inserted in the trunk, as directed by the manufacturer, to sample only the conductive area, and then insulated with reflecting materials after installation. The temperature difference between the upper heated and lower unheated needles, together with the temperature difference at night, allowed for the estimation of the sap velocity, which was then multiplied by the sapwood area to calculate the hourly sap fluxes.

An Eddy Covariance flux tower (EC) is also installed in the field. The tower is equipped with: a 4-component net radiometer (CNR4, Campbell Scientific Inch., Logan, Utah) installed at 3.0 m a.g.l. to measure low-frequency (30 min) net radiation; a three-dimensional sonic anemometer (CSAT3-D, Campbell Scientific Inch., Logan, Utah) providing high-frequency (20 Hz) wind speed measures (3D components); an infrared open patch gas analyzer (Li-7500, Li-cor bioscience inch., Lincoln, Nebraska) to measure H20 and CO2 concentrations (at 20 Hz); and, finally, one self-calibrated flux plate (HFP01SC, Hukseflux) placed at 0.15 m b.g.l.. All the high- and low-frequencies data are collected and pre-processed by means of a CR3000 datalogger (Campbell Scientific Inch., Logan, Utah) equipped with a 2 GB memory card.

Irrigation volumes supplied to the plants are available for the period 2018–2025, including the exact dates of each irrigation event. Meteorological data from the *in situ* standard weather station are also available for the same period (2018–2025). SWC measurements are available from 2018 to 2021, whereas sap flow data were collected only during the 2018 and 2019 irrigation seasons. Finally, Eddy Covariance flux data are available for the period 2019–2025.

4.3 Reanalysis and forecasting data

4.3.1 ERA5-Land

An alternative source of the *in situ* data is represented by the reanalysis database. ERA5-L, provided by the ECMWF in 2019, is the last generation of the global reanalysis climate database and is freely downloadable from the Copernicus portal. The product has a

spatial resolution of 0.1° latitude and 0.1° longitude with a temporal cover from 1950 to present (**Figure 4.5**).

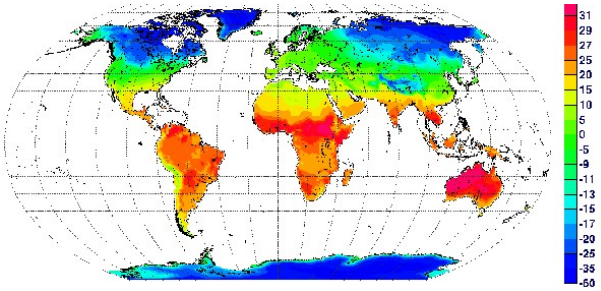

Figure 4.5 Overall vision of the ERA5-Land hourly database (from: *https://cds.climate.copernicus.eu/cdsapp#!/dataset/reanalysis-era5-land?tab=overview*)

The quality of ERA5-Land data was evaluated by direct comparison to many *in situ* observations collected mainly for the period 2001–2018, as well as by comparison to additional model or satellite-based global reference datasets (Muñoz-Sabater et al., 2021).

4.3.2 SIcilia Limited Area Model (SILAM) GFSE model

The SIcilia Limited Area Model (SILAM) is a hydrostatic mesoscale numerical weather prediction model developed and implemented by SIAS. It simulates the temporal evolution of meteorological conditions through mathematical equations that describe atmospheric physics, starting from an initial state (analysis fields at 00:00 UTC) and boundary conditions (three-hour forecasts) provided daily by the Global Forecast System (GFS) model, developed and managed by the National Center for Environmental Prediction (NCEP) of the NOAA (National Oceanic and Atmospheric Administration).

SILAM, recently implemented by SIAS over a spatial domain centered on Europe, produces daily forecast maps of air temperature at 2 m, precipitation, wind speed and direction at 2 m, sea-level atmospheric pressure, and geopotential height at 500 and 850 hPa, starting from 00:00 UTC of the current day and extending up to 144 hours ahead.

The model operates with a horizontal spatial resolution of approximately 20 km, 40 vertical levels, and a three-hour temporal resolution (+24h – "today for tomorrow", +48h, +72h).

4.4 Remote sensing data

4.4.1 Moderate Resolution Imaging Spectroradiometer (MODIS)

Within the framework of the Earth Observing System (EOS) program, developed by the National Aeronautics and Space Administration (NASA), the Moderate Resolution Imaging Spectroradiometer (MODIS) represents one of the key instruments designed to provide long-term global observations of the atmosphere of the Earth, land surface, and oceans. Two identical MODIS sensors operate onboard the Terra and Aqua satellites, launched on 18 December 1999 and 4 May 2002, respectively.

The Terra satellite crosses the equator in a descending orbit, while Aqua follows an ascending orbit, allowing near-daily global coverage when combined. Both satellites operate in a sun-synchronous polar orbit at a mean altitude of 705 km above the surface.

Each MODIS instrument is a passive multispectral radiometer capable of acquiring data in 36 spectral bands distributed between the visible (VIS), near-infrared (NIR), shortwave infrared (SWIR), mid-infrared (MIR), and thermal infrared (TIR) regions of the electromagnetic spectrum, covering wavelengths from 0.4 μm to 14.4 μm. The sensor has a radiometric resolution of 12 bits and a swath width of 2330 km, enabling complete global coverage every 1–2 days.

The spatial resolution of MODIS data depends on the specific spectral band:

- Bands 1–2: 250 m (red and NIR, used for vegetation monitoring);
- Bands 3–7: 500 m (VIS–SWIR, for land and ocean colour);
- Bands 8–36: 1,000 m (VIS–TIR, for atmospheric and surface temperature studies).

MODIS data are distributed at several processing levels. The Level 2 products provide geophysical parameters such as surface reflectance, land surface temperature, and aerosol optical depth,

atmospherically corrected and geolocated. Higher-level products, such as MOD13 (Vegetation Indices) (Spruce et al., 2011), MOD11 (Land Surface Temperature and Emissivity) (Hashimoto et al., 2008), and MOD16 (Evapotranspiration) (Autovino et al., 2016), are derived from temporal composites and are extensively used in environmental and climatic applications.

All MODIS data are freely available through the NASA LP DAAC and NASA Earthdata portals, in a sinusoidal projection referenced to WGS84.

Thanks to its high temporal frequency, broad spectral coverage, and global swath, MODIS plays a fundamental role in global change monitoring, enabling the analysis of vegetation dynamics, surface temperature variations, fire detection, and water resource monitoring at continental to global scales (Khosravi et al., 2024; Bhuyan and Udmale, 2025; Hojabri and Nguyen-Huy, 2026).

4.4.2 Sentinel-2

In the frame of the Copernicus mission, managed by the European Commission, the objective of the Sentinel-2 mission is providing global acquisition of MultiSpectral Images (MSI) with high spatial and temporal resolution, to allow land monitoring and detection of environmental changes. The triplet satellites Sentinel-2A, Sentinel-2B and Sentinel-2C launched by European Space Agency (ESA) in June 2015, in March 2017 and September 2024, respectively, operate simultaneously, phased at 180° to each other, in a sun-synchronous orbit at a mean altitude of 786 km from the earth's surface. The temporal resolution referred to each single satellite is 10 days. The three satellites are equipped with a passive multispectral sensor that allows a swath width equal to 290 km, with a radiometric resolution of 12-bit, able to acquire light intensity (radiance) values ranging between 0 to 4095. The data are acquired on 13 bands distributed between VIS and SWIR. The spatial resolution depends on the specific spectral band (**Figure 4.6**).

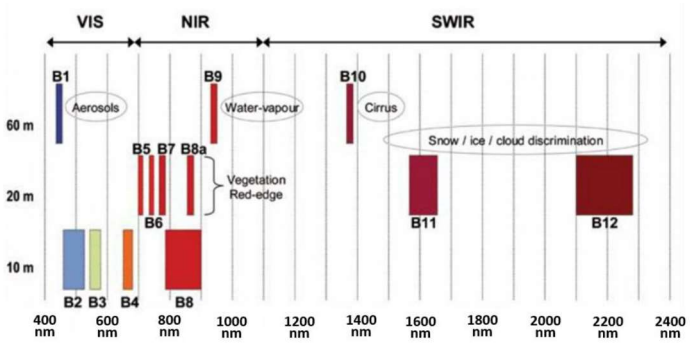

Figure 4.6 Spectral resolution referred to spatial resolution 10 m, 20 m and 60 m of the data acquired by the multispectral sensor (from: De Marinis et al., 2019) readapted

Specifically, there are four bands with spatial resolution equal to 10 m, centred on wavelengths equal to 490 nm (B2), 560 nm (B3), 665 nm (B4) and 842 nm (B8). Six bands with spatial resolution equal to 20 m, centred on wavelengths equal to 705 nm (B5), 740 nm (B6), 783 nm (B7), 865 nm (B8a), 1610 nm (B11) and 2190 nm (B12) and three bands at 60 m, centred on wavelengths equal to 443 nm (B1), 945 nm (B9) and 1 375 nm (B10).

The last product MSI level 2A released by ESA and free downloaded through the open access hub portal (https://scihub.copernicus.eu/dhus/#/home), provides bottom of atmosphere (BOA) reflectance atmospheric corrected (Main-Knorn et al., 2017), orthorectified and georeferenced with cartographic geometry (UTM/WGS84 EPSG:32633).

Thanks to the high spatial resolution joint with the good revisiting time, this product is able to monitor, at large scale, eventual quick changes in the plant chemical-physical system, as well as, to monitor and estimate plant water status and crop water requirement (Rozenstein et al., 2018; El Hachimi et al., 2022).

4.4.3 Landsat-8/-9

Within the framework of the Landsat mission, jointly managed by the NASA and the U.S. Geological Survey (USGS), aimed at ensuring a continuous and long-term global monitoring of the surface of the Earth through medium-resolution multispectral observations, operate

the Landsat-8 and Landsat-9 satellites. These two satellites are part of the Landsat series, which began in 1972, and represent the continuation of the longest-running space mission dedicated to systematic Earth observation.

The satellites Landsat-8, launched on February 2013, and Landsat-9, launched on September 2021, operate in nearly identical, sun-synchronous orbits at a mean altitude of approximately 705 km above the surface, with an inclination of 98.2°, and a revisit time of 16 days for each individual satellite.

Figure 4.7 shows the coverage of Landsat satellite imagery over the state of Nebraska, USA (Foolad, 2018).

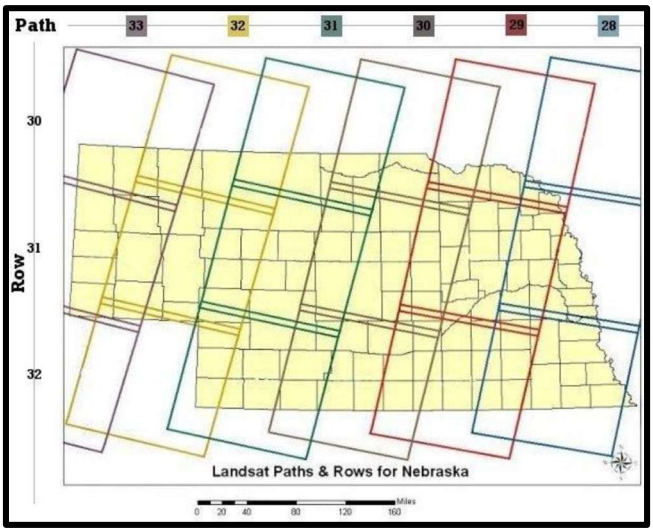

Figure 4.7 Coverage of Landsat-8 satellite imagery over the state of Nebraska, USA (from: Foolad, 2018)

The map displays the Worldwide Reference System (WRS) grid, which is used to catalogue and reference Landsat scenes. The colored rectangular outlines represent, as a specific Path/Row combination, the individual scenes or image footprints captured by the satellite. The horizontal axis indicates the Path numbers (from 33 to 28), which correspond to the satellite's ground track as it moves from north to south. The vertical axis indicates the Row numbers (from 30 to 32), which correspond to the center of the scene along the Path. The overlapping footprints illustrate how multiple scenes are required to

cover the entire state, and how adjacent paths and rows provide spatial redundancy.

Both satellites are equipped with two main instruments:

- the Operational Land Imager (OLI), a passive multispectral sensor designed to acquire reflected solar radiation;
- the Thermal Infrared Sensor (TIRS), which measures emitted thermal radiation from the surface.

The OLI sensor acquires data in 9 spectral bands distributed between the visible (VIS), near-infrared (NIR) and shortwave infrared (SWIR) regions, with a radiometric resolution of 12 bits (digital values ranging from 0 to 4095). Specifically, bands 1–7 and 9 have a spatial resolution of 30 m, while Band 8 (panchromatic) provides a 15 m spatial resolution. The TIRS instrument acquires data in two thermal infrared bands (Band 10 and Band 11) with a spatial resolution of 100 m, later resampled to 30 m in the standard products (**Figure 4.8**).

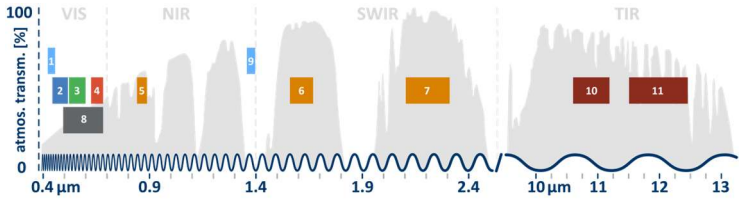

Figure 4.8 Landsat-8/-9 bands (from: *https://blogs.fu-berlin.de/reseda/landsat-8/*)

The OLI sensor covers a swath width of 185 km, comparable to that of previous Landsat missions. The data products, Level-2 Surface Reflectance (SR), distributed free of charge through the USGS EarthExplorer or NASA LP DAAC portals, provide Bottom of Atmosphere (BOA) reflectance, corrected for atmospheric effects, orthorectified, and georeferenced according to UTM/WGS84 cartographic geometry.

Thanks to the combination of good spatial detail, radiometric quality, and long temporal continuity, Landsat-8 and Landsat-9 products are particularly suitable for land cover and land use monitoring, vegetation and crop health assessment, water resources

management, and environmental change detection at regional to global scales (Roy et al., 2014; Masek et al., 2020).

4.4.4 PlanetScope

Within the framework of commercial Earth observation, the PlanetScope constellation, operated by Planet Labs PBC, is designed to provide high-frequency, high-resolution multispectral imagery for monitoring land cover, agriculture, and environmental changes at a global scale (Wildhaber at al., 2023).

PlanetScope consists of a large fleet of small satellites (CubeSats/Dove satellites), with more than 150 operational satellites as of 2025, forming one of the densest imaging constellations currently in orbit. PlanetScope satellites operate in a sun-synchronous orbit at an altitude of approximately 475–505 km, with near-polar orbital inclinations (~97.5°). The constellation is phased so that it provides daily global coverage, allowing frequent revisits for near-real-time monitoring of dynamic phenomena such as vegetation growth, crop stress, and urban development (Bueno et al., 2023; Sarkar et al., 2023).

Each PlanetScope satellite is equipped with a pushbroom multispectral imager that captures data in 4 spectral bands:

- Blue (B1): ~455–515 nm
- Green (B2): ~500–590 nm
- Red (B3): ~590–670 nm
- Near-Infrared (NIR, B4): ~780–860 nm

The spatial resolution of PlanetScope imagery is 3–5 m, depending on the satellite generation and imaging mode, with a radiometric resolution of 8 bits (digital values from 0–255). Each satellite acquires data with a swath width of ~24 km, allowing for rapid mosaicking across larger areas when combining multiple satellites in the constellation.

PlanetScope data products are orthorectified, georeferenced to WGS84/UTM, and delivered in Level-3 Surface Reflectance in some cases, corrected for atmospheric effects. The frequent revisit rate and high spatial resolution make PlanetScope particularly suitable for

agricultural monitoring, crop phenology assessment, disaster response, and environmental change detection (Tu et al., 2022).

Chapter 5. Methods

5.1 Data processing and analysis

5.1.1 Meteorological Data

The meteorological data was already provided in a usable format: by SIAS for the olive orchard and by the standard meteorological station for the citrus orchard. These datasets were aggregated to a daily scale and subsequently used to compute the *ETo* using the PM equation **(3.10)**.

5.1.2 Eddy covariance Data

For both orchards, the raw EC data were post-processed by means of the procedure implemented by Manca (2003), virtually analogous to the FLUXNET standard protocol (Mauder et al., 2008; Pastorello et al., 2014, 2020). Data de-trending was performed using a running mean, a coordinate rotation was applied to the sonic anemometer data to obtain a zero mean vertical and transversal wind speeds, and correction for spectral loss was performed. In addition, adjustments for high wind speeds on sonic temperature and Webb–Pearman–Leuning corrections for water vapor were applied (Moncrieff et al., 1997) before the final computation of half-hourly fluxes. Moreover, the protocol assesses units and sign conventions, timestamp alignments, trends, step changes, outliers based on site-specific historical ranges, multivariate comparisons, diurnal/seasonal patterns, friction velocity filtering, and variable availability. Quality checks are done over single variables, multiple/combined variables, or more specialized tests.

H [W m^{-2}], *LE* [W m^{-2}] as well as *NEE* [μmol m^{-2}] were evaluated, at sub-hourly scale (30 min), as:

$$H = \rho \cdot cp \cdot \sigma_{WT} \quad \textbf{(5.1)}$$

$$LE = \lambda \cdot \sigma_{WQ} \quad \textbf{(5.2)}$$

$$NEE = \sigma_{WC} \quad \textbf{(5.3)}$$

where ρ [g m^{-3}] is the air density, cp [J g^{-1} K^{-1}] is the air-specific heat capacity at constant pressure, σ_{WT} [m K s^{-1}] is the covariance between vertical wind speed and air temperature, λ [J g^{-1}] is the latent heat of vaporization and σ_{WQ} [g m^{-2} s^{-1}] is the covariance between vertical wind speed and water vapor density and, σ_{wC} [µmol m^{-2}] is the covariance between vertical wind and CO_2 concentration.

The method suggested by Prueger et al. (2005), based on the Closure Ratio (*CR*), was used to assess the surface energy balance closure. When the energy storage in the soil is neglected, *CR* represents the slope of the regression line between the available energy given by the difference of the net radiation (R_n) and the soil heat flux (G_0), and the sum of the turbulent heat fluxes ($LE + H$) only evaluated from the subset of half hourly data corresponding to $R_n \geq$ 100 W m^{-2}:

$$CR = \frac{LE+H}{R_n-G_0} \quad \textbf{(5.4)}$$

To guarantee the consistency of the daily data, only the days with 48 half-hourly measurements were considered.

The footprints of the flux towers, which identifies the area on the ground encompassing at least 70% of the flux source, are shown in **Figure 5.1**.

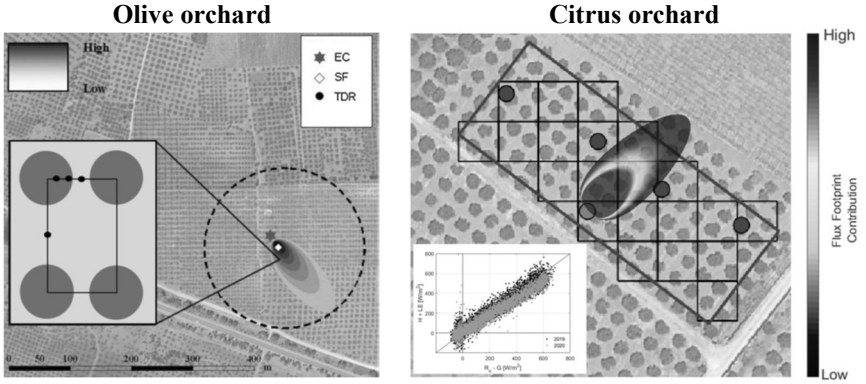

from: *Cammalleri et al., 2013* from: *Ippolito et al., 2023*

Figure 5.1 EC tower footprint in the experimental fields

For the EC tower in the olive orchard, it was retrieved by Cammalleri et al. (2013); instead, for the one in the citrus orchard from Ippolito et al. (2023).

Moreover, all the records acquired in days when the rainfall height was higher than 2.5 mm were excluded. Eddy covariance measurements are typically excluded on those days because precipitation can disrupt the accuracy of the vertical turbulent fluxes readings, introducing noise and skewing evapotranspiration estimates due to water accumulation on the sensors and temporary surface evaporation rather than natural atmospheric fluxes (Baldocchi, 2003; Aubinet et al., 2012).

All the fluxes at the half hourly time steps were then aggregated at the daily time step.

5.1.3 ERA5-Land

Daily reanalysis data of air temperature, global solar radiation, dew-point temperature, and the two components, eastward and northward, of wind speed measured at 10 m above the ground were downloaded using the ERA5-Land Daily Aggregated - ECMWF Climate Reanalysis dataset, available in the Google Earth Engine (GEE) platform (https://developers.google.com/earth-engine/datasets/catalog/ECMWF_ERA5_LAND_DAILY_AGGR?hl=it). GEE is a cloud-based platform designed for geospatial visualization and analysis of large-scale datasets at a planetary level. It is freely accessible to academic, non-profit, business, and government users (Gorelick et al., 2017). By leveraging cloud computing technologies, GEE effectively addresses the challenges of managing and processing big data, offering an innovative approach to handle remote sensing information.

The relative air humidity, not directly downloadable from the reanalysis database, was calculated as the ratio between actual ($e_a(T_{dew})$ [kPa]) and saturated ($e_s(T_a)$ [kPa]) vapour pressure calculated in function of T_{dew}, and T_a, respectively. Following the formulas suggested by Allen et al. (1998):

$$RH = 100 \cdot \frac{e_a(T_{dew})}{e_s(T_a)} \quad \textbf{(5.5)}$$

Wind speed at 10 m above the ground level (U_{10} [m s^{-1}]) was calculated using the two components according to the methodology proposed by Allen et al. (1998).

Moreover, the wind speed at 2 m above the ground (U_2 [m s^{-1}]) was calculated based on the wind speed at 10 m (U_{10} [m s^{-1}]) retrieved by the ERA5-L database, assuming valid the logarithmic wind speed profile (Allen et al. 1998):

$$U_2 = U_{10} \cdot \frac{4.87}{ln(67.8 \cdot 10 - 5.42)} \quad \textbf{(5.6)}$$

The application of this relationship results in a multiplication by a constant equal to 0.75. To assess the reliability of this coefficient, additional values were also tested within a range from 0.05 to 1.

A comparison between *in situ* and reanalysis data was conducted in both the experimental sites. This analysis, where both databases were available, allowed to evaluate the suitability of reanalysis meteorological variables when ground data are not available.

Moreover, three categorical indices were applied to analyse the precipitation against *in situ* data: Probability Of Detection (*POD*), False Alarm Ratio (*FAR*), and Critical Success Index (*CSI*). *POD* measures the fraction of observed events that were correctly predicted, *FAR* quantifies the fraction of predicted events that did not occur, and *CSI* accounts for both missed and falsely predicted events, providing a balanced assessment of categorical skill.

$$POD = \frac{Hits}{Hits+Misses} \quad \textbf{(5.7)}$$

$$FAR = \frac{False\ Alarms}{Hits+False\ Alarms} \quad \textbf{(5.8)}$$

$$CSI = \frac{Hits}{Hits+Misses+False\ Alarms} \quad \textbf{(5.9)}$$

where Hits are observed and predicted events, Misses are observed but not predicted events and False Alarms are predicted but not observed events.

5.1.4 SILAM Data

The SILAM data were downloaded for the reclamation consortium area and were provided in a usable format. The database id composed by global solar radiation, wind speed at 2 m height, precipitation depth, air temperature, maximum, mean and minimum, and relative air humidity, maximum, mean and minimum. These data, at daily scale, correspond to "today-for-tomorrow" forecasts, which were then compared with the *in situ* measurements from the SIAS station located near the olive orchard.

5.1.5 Remote sensing data

5.1.5.1 Olive orchard

MODIS. Since the EC tower acquisition period in the olive orchard is prior to 2017, it was possible to use only the MODIS data. MCD43A3 Version 6 product (MCD43A v006) (Schaaf and Wang, 2015) was considered to obtain continuous time-series of nadir reflectance at the different wavelengths. The continuous time series of MODIS nadir reflectance were downloaded using the Google Earth Engine (GEE) platform. The near-infrared, red and shortwave reflectance were detected respectively in band B2 ranging from 841 to 876 nm, in band B1 ranging from 620 to 670 nm and in band B6, from 1628 to 1652 nm of the MODIS electromagnetic spectrum.

PlanetScope. PlanetScope data with a 3.125 m spatial resolution from Planet Labs PBC were downloaded. The data were accessed from https://www.planet.com/ through a research and education license. The PlanetScope Ortho Tile Product (Level 3A) were used. Level 3A provides surface reflectance for 4 different bands (blue, green, red, and near-infrared (NIR)). This product provides orthorectified and preprocessed, including geometric, radiometric, and atmospheric corrections, scenes. The wavelengths, used to retrieve *NDVI*, are centered at 630 nm for the red band (B03) and at 820 nm for NIR (B04).

Sentinel-2. A database of high-resolution MSI acquired by the Sentinel-2 triplet satellites allowed a systematic monitoring of the soil-vegetation system of the irrigation district via time series of the *NDVI* and *NDWI*. Level 2A product was employed. A spatio-temporal matching filter developed under GEE platform allowed the selection of cloud-free scenes over the study area during the period in which the user cards were available (2017-2020). The R package toolbox "sen2r" (Ranghetti et al., 2020) allowed the downloading and pre-processing of all the scenes. The pre-processing included cropping the images to the study area and creating a multi-band stack of all available spectral bands.

Atmospherically corrected 665 nm (RED) and 842 nm (Near InfraRed - NIR) bands (labeled as "B4" and "B8", respectively) were used to derive the NDVI time-series.

Moreover, Atmospherically corrected 1610 nm (SWIR) band (labelled as "B11") was downscaled at 10 m resolution using a sharpening technique called DisTrad developed by Anderson et al. (2004). The approach was assessed inside the irrigation district by selecting two orchards for each fraction vegetation cover (*FVC*) type: Bare Soil (BS), Sparsely Vegetated (SV), Moderately Vegetated (MV), and Highly Vegetated (HV) (**Figure 5.2**).

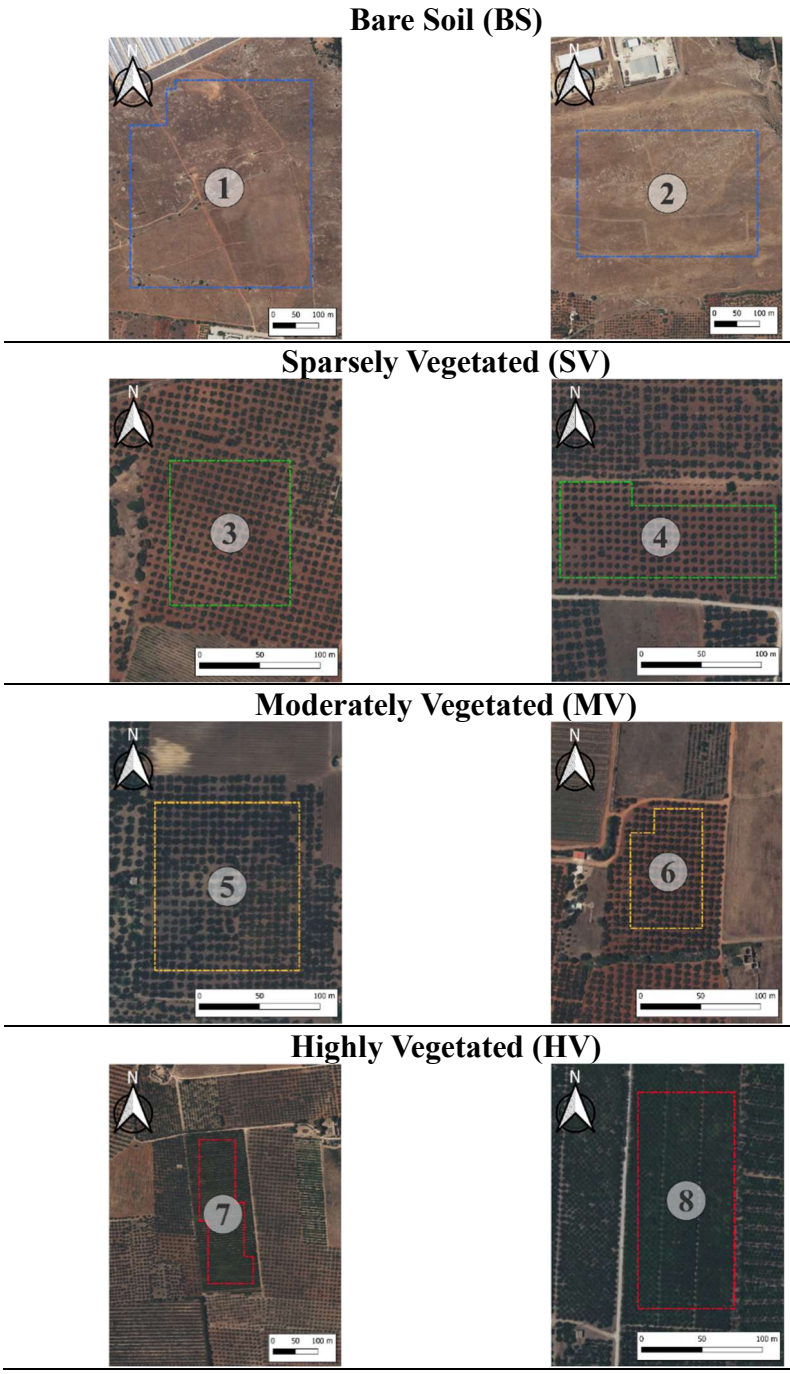

Figure 5.2 Study areas within the irrigation district showing the selected fields used for the DisTrad technique application. Two fields were selected for each FVC type: bare soil, sparsely vegetated, moderately vegetated, and highly vegetated

Thus, the downscaled SWIR band and NIR band (labeled as 'B11' and B8, respectively) were used to derive the *NDWI* time-series. Maps of *NDVI* and *NDWI* with a spatial resolution of 10 m, were generated.

A continuous time series of daily VIs were obtained based on linear interpolations carried out between consecutive pairs of Sentinel-2 images acquired at two different dates (Pan et al., 2017).

Proximity Sensing. The acquisition system encompassed an MCA-II multispectral camera (TETRACAM Inc.: Chatsworth, CA, USA). The multispectral camera is an 8-bit 6 bands CCD sensor with customized optical filters set up at 450, 650, 720, and 800 nm. The field of view was 43°x35°. A remote laptop, which was connected to an onboard mini personal computer, controlled the camera. The acquisition instrument was installed on an 8 m3 helium balloon flying at 120 m above ground level (a.g.l.). The balloon was secured to the ground through three Kevlar® ropes. Afterward, the balloon was slowly let go. An ASD Field Spec Hand-Held spectroradiometer (Analytical Spectral Device, Inc., Boulder, CO, USA) enabled the acquisition of ground reflectance between 325 and 1075 nm, which were used for in-reflectance calibration at the ground level, and the NDVI assessment. The image was acquired on August 1st 2009 with at spatial resolutions of 0.12 m.

5.1.5.2 Citrus orchard

Sentinel-2. The same Sentinel-2–based processing workflow was applied, including the selection of cloud-free Level-2A scenes, preprocessing with the sen2r toolbox, derivation of *NDVI* and *NDWI* at 10 m resolution, downscaling procedures, and the generation of continuous daily vegetation index time series through linear interpolation between consecutive acquisition dates.

Moreover, *LAI* was estimated from Sentinel-2 optical data by using the Neural Network approach and configuration from the SENTINEL 2 Toolbox level2 biophysical variables algorithm ATBD document (Weiss et al., 2020) and adapted on Google Earth Engine (GEE) for automated extraction.

Landsat-8/-9. The Landsat-8/-9 images, from Collection 2 Level 2, were downloaded from the US Geological Survey website

(http://glovis.usgs.gov/). Product is composed by atmospherically corrected surface reflectance and Land Surface Temperature (*LST*) both at 30 m spatial resolution.

Note that LST data are originally acquired at a 100 m resolution and subsequently resampled (cubic convolution) by USGS to align with the 30 m reflectance grid. The joint use of both satellites provided acquisitions over the experimental field every 8 days (16 days before Landsat-9 launch in 2021) before cloud filtering.

As done for Sentinel-2 images, the matching filtering procedure, with the cloud mask product of the Level 2, allowed selecting cloud-free scenes.

The *NDVI* was computed using 655 nm (RED) and 865 nm (NIR) bands (labeled as "SR_B4" and "SR_B5", respectively). *NDVI* was used to estimate the emissivity (ε) with the formula suggested by Valor (1996). Whereas the albedo (α) time series was retrieved according to the V03 methodology suggested by (Andres-Anaya et al., 2023). The LST time series was derived directly from the "ST_B10" band, which was derived from the thermal infrared (TIR, 11000 nm) band of Level 1 after correction for atmospheric and emissivity effects in Level 2. To approximate the original 100 m thermal resolution and avoid artifacts introduced by the cubic convolution resampling, the *LST* (product offered at 30 m) were upscaled to 90 m by computing the mean and the standard deviation of the nine pixels around the EC tower.

5.2 Soil Plant Atmosphere and Remote Sensing Evapotranspiration (SPARSE) model

The Soil Plant Atmosphere and Remote Sensing Evapotranspiration (SPARSE) is a Surface Energy Balance (SEB) model, which can be implemented in two versions (parallel and series soil-plant resistance network schemes). The SPARSE implementation requires *in situ* meteorological data (as global solar radiation, air temperature, relative air humidity and wind speed), NDVI, LST and albedo (α) and derived LAI intermediate products. The SPARSE model allows the estimation of the instantaneous soil (subscripted

with ‘s’) and vegetation (subscripted with ‘v’) energy fluxes (net radiation, R_{ns} and R_{nv}; sensible heat flux, H_s and H_v; latent heat flux, LE_s and LE_v; ground heat flux, G_0 at the time of satellite overpass. More details regarding SPARSE are reported in Boulet et al. (2015) and Lagouarde and Boulet (2016).

To upscale the latent heat fluxes at the satellite overpass time to daily scale, the approach proposed in Cammalleri et al. (2014), based on to the ratio between latent heat fluxes and global solar radiation, R_s, was used. Finally, daily LE_s and LE_v were converted into E and T, respectively, using the conversion factors table reported in Allen et al. (1998).

The rationale for using a SEB model driven by LST data lies in its independence from ancillary inputs such as irrigation volumes, which are often unavailable or highly uncertain. By relying on remotely sensed thermal data and basic meteorological inputs, this approach enables the estimation of surface energy fluxes, including evaporation and transpiration, without requiring explicit knowledge of supplied irrigation volumes or relying on potentially uncertain simulated irrigation.

Three combinations were employed: 1) using *in situ* meteorological data, *LST*, and albedo and Sentinel-2 derived *NDVI* and *LAI*; 2) replacing *NDVI*, *LST* and albedo with Landsat-8/9 data; 3) replacing *in situ* data with ERA5-Land reanalysis while maintaining Landsat-8/9 inputs and Sentinel-2 derived *LAI*. The SPARSE model was applied to the citrus orchard for irrigation seasons from 2019 to 2025.

5.3 SAtellite Montoring for IRrigation (SAMIR)

The SAtellite Montoring for Irrigation (SAMIR) is a spatially distributed FAO-2Kc-based (Allen et al., 1998) Soil Water Balance (SWB) model. The SAMIR implementation requires crop reference evapotranspiration and precipitation depth data, as well as soil texture and crop type characteristics (*i.e.*, root zone depth and hydraulic properties) and *NDVI* time series. This latter used to derive the basal crop coefficient, K_{cb}, and the fractional vegetation cover. SAMIR can be either forced with measured irrigation, or it can simulate irrigation

based on rules related to the modelled soil water content (*SWC*). SAMIR allowed estimating daily SWC, transpiration (*T*), evaporation (*E*), and actual evapotranspiration (ET_a, sum of *T* and *E*). More details regarding SAMIR are reported in Simonneaux et al. (2009), Saadi et al. (2015) and Laluet et al. (2023).

Two irrigation modes were tested: a) by considering the known farmer irrigations and b) by employing simulated irrigation triggered by SAMIR based on rules related to the modelled *SWC*. The mode-a was in turn tested considering two different combinations: 1a) using *in situ* and 2a) using ERA5-Land reanalysis meteorological variables to estimate crop reference evapotranspiration and precipitation depth. Both modes used Sentinel-2 *NDVI*-derived maps.

Testing two different modes and assessing differences between provided and simulated irrigation volumes allowed evaluating biases between these two irrigation strategies. Irrigation volumes data are generally unavailable or difficult to obtain for large areas. For this reason, it is essential to evaluate SAMIR ability to simulate irrigation volumes.

The SAMIR model was applied to the citrus orchard for irrigation seasons from 2018 to 2025.

5.4 NDVI-Cws method

The NDVI-Cws method involves the estimation of ET_a by separating the contribution of *E* from *T*, through the use of the concept of *FVC* (Maselli et al., 2014, 2019):

$$ET_a = ET_0 \cdot K_c \cdot [FVC \cdot Cws + (1 - FVC) \cdot AW] \quad \textbf{(5.10)}$$

where *FVC* is linearly derived from *NDVI* images (see section *5.4.1 FVC vs NDVI*); while *Cws*, which is also defined for woody and non-woody plants following Maselli et al. (2014, 2019), is a short-term water stress factor, and *AW*, which is the available water, is the ratio between *P+I* and $ETo \cdot K_c$, both cumulated over two months (TM=60) for trees and one month (TM=30) for grasses are two scalar coefficients that account for water stress:

$$AW = \sum_{day=1}^{TM} \frac{P + I}{ET_o \cdot K_c} \quad \textbf{(5.11)}$$

$$CSW = 0.5 + 0.5 \cdot Aw \quad \textbf{(5.12)}$$

Since *AW* is set to 1 when precipitation exceeds *ETo*, *Cws* can vary between 0.5 (when there is maximum water shortage) and 1 (when there is no water shortage).

The model was applied in the citrus orchard experimental field in the 2019-2025 irrigation seasons.

5.4.1 FVC *vs* NDVI

As anticipated in section *2.2.2 Plant-Atmosphere layer* on *plant optical properties*, *NDVI* can be considered a proxy for *FVC*. Through the application of advanced image processing techniques and spectral analysis, this approach sought to accurately quantify the proportion of the land surface covered by green vegetation by identifying a linear functional relationship between *FVC* and *NDVI*. The analysis was carried out within irrigation district 1A, where a set of irrigated plots was selected. These plots were characterized by different planting densities and different plant ages. Specifically, the study was conducted on 25 plots, each containing approximately 100 plants (**Table 5.1**).

Table 5.1 Plot characteristics

ID	Fields area [m^2]	Planting spacing [m]	n° of trees [-]
1	4384.76	8.0 x 8.0	81
2	3713.45	6.0 x 6.0	100
3	3862.62	6.0 x 6.0	98
4	4819.97	7.0 x 7.0	100
5	4950.07	7.0 x 7.0	100
6	3383.90	5.0 x 7.0	94
7	7892.35	9.0 x 9.0	100
8	4252.52	7.0 x 7.0	98
9	6865.30	8.0 x 8.0	108
10	7196.07	9.0 x 9.0	96
11	2107.3	6.0 x 4.0	88
12	4735.73	7.0 x 7.0	99
13	7663.64	8.0 x 9.0	100
14	3643.42	6.0 x 6.0	100
15	2717.15	5.0 x 5.0	100
16	5191.98	7.0 x 7.0	100
17	7839.79	9.0 x 9.0	100
18	3891.89	Random	104
19	4550.4	6.0 x 6.0	96
20	4256.07	6.0 x 6.0	97
21	5675.31	8.0 x 8.0	100
22	5172.50	7.0 x 7.0	98
23	4962.17	7.0 x 7.0	98
24	5755.28	8.0 x 8.0	100
25	4857.41	7.0 x 7.0	100

During the irrigation season, farmers regularly apply tillage practices to maintain the fields free of sporadic weeds, thereby minimizing soil background interference.

FVC was estimated using aerial imagery available from the Google Earth Pro® platform (version 7.3.4.8642), referring to July 04th 2019. At first, for each identified field, the tree canopy area was vectorized (**Figure 5.3**).

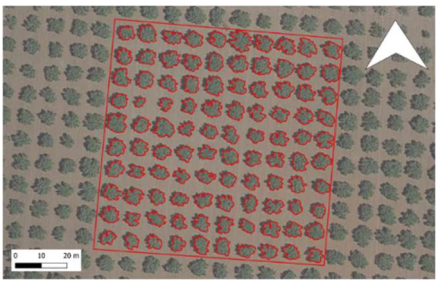

Figure 5.3 Example of tree canopy are digitization, showing the delineation of individual tree crowns within one field

Furthermore, data from different remote sensing platforms were used to assess the effect of spatial resolution on the linear relationship (*i.e.*, Sentinel-2 [July 02nd 2019], Landsat-8 [July 05th 2019] and PlanetScope [July 03th 2019]).

Thus, *FVC* was calculated as the ratio between the total area occupied by vegetation and the area of the examined portion (*e.g.*, field and/or pixel). Thus, the analysis was performed using two different approaches: a field scale approach and a pixel wise approach.

Field scale approach. Only the pixels entirely inside the plot perimeter were considered for each plot (**Figure 5.4**).

$$FVC = \frac{\sum(Canopy\ area)}{(n°\ pixel) \cdot (pixel\ area)} \quad \textbf{(5.13)}$$

The *NDVI* was obtained as the average value of all the pixel. In this approach, a pair of values (*FVC* and *NDVI*) was obtained for each field, resulting in a total of 25 pairs.

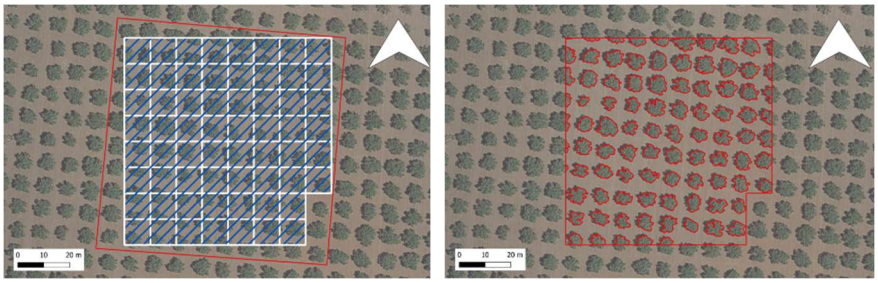

Figure 5.4 Example of a Sentinel-2 grid fully contained within the field perimeter (left) and the intersection of the grid with the field perimeter (right)

Pixel wise approach. FVC was evaluated pixel by pixel, always only for the pixel entirely inside the plot perimeter.

$$FVC = \frac{(Canpy\ Area)}{(Pixel\ area)} \quad \textbf{(5.14)}$$

The *NDVI* is related to the analyzed pixel. In this approach, for each field there were as many value pairs (*FVC* and *NDVI*) as the number of pixels contained within the field. For example for the field in **Figure 5.4**, 62 pairs were available.

Finally, considering only the Sentinel-2 data, the field scale approach was conducted using two tree canopy area vectorization approaches: the previously described (precise method) and a more rapid/simplified method (swift method).

Precise method. All trees within the examined portion were vectorized and the total canopy area was computed.

Swift method, only 25% of the trees were vectorized; the average canopy area, derived from this subset, was then multiplied by the total number of trees within the examined portion (**Figure 5.5**).

Precise method **Swift method**

Figure 5.5 Example of canopy digitization using the precise method (left) and the swift method (right)

The Field scale approach with the Precise method, using a Sentinel-2 [July 22th 2019] image, was subsequently applied to the citrus orchard. To further strengthen the analysis and enlarge the dataset, 15 additional neighboring fields with similar agronomic and structural characteristics were also included in the analysis (**Table 5.2**).

Table 5.2 Plot characteristics

ID	Fields area [m^2]	Planting spacing [m]	n° of trees [-]
1	1906.43	5.0 x 5.0	81
2	2043.30	5.0 x 5.0	80
3	1900.22	5.0 x 5.0	75
4	1973.64	5.0 x 5.0	81
5	1840.62	5.0 x 5.0	80
6	1978.64	7.0 x 7.0	82
7	2017.94	7.0 x 7.0	130
8	2005.29	6.0 x 6.0	80
9	2006.76	6.0 x 6.0	80
10	883.96	8.0 x 8.0	80
11	1906.07	7.0 x 7.0	80
12	953.13	8.0 x 8.0	84
13	1124.93	Random	114
14	2178.81	6.0 x 6.0	79
15	1975.01	7.0 x 7.0	68

FVC was estimated using aerial imagery available from the Google Earth Pro® platform (version 7.3.4.8642), referring to July 24th 2019.

5.5 Eddy Covariance-based partitioning method

The EC-based partitioning method is an approach to retrieve transpiration (*T*) and evaporation (*E*) from EC measurements via the estimation of soil and canopy conductances. The latter are assumed to be proportional to: i) the Gross Primary Production (*GPP*); ii) the ecosystem conductance, retrieved by inverting the *ETo* Penman-Monteith equation (Allen et al., 1998), G_s; iii) the leaflevel vapor pressure deficit, VPD_l (Lin et al., 2018) at the ecosystem scale; and iv) the *SWC* at the top soil layer.

Although a general description of the EC-based partitioning method is reported in Li et al. (2019), and while most of the inputs are directly derived from observations, the description of how *GPP* is estimated from EC observation is not sufficiently discussed. The *GPP*

was evaluated as the difference between the turbulent CO_2 flux, recorded by the EC tower, also called Net Ecosystem Exchange (*NEE*), and an estimation of the soil Respiration (*Re*). *NEE* was directly derived from the EC measurements as the covariance between the CO_2 concentration and the vertical wind speed and, a CO_2 storage term. The latter, accounts for CO_2 accumulation within the canopy air space and it is often neglected during daytime when the strong atmospheric mixing cause its considerably decreasing (Goulden et al., 1996; Aubinet et al., 1999; Loescher et al., 2006). According to Loescher et al. (2006), micrometeorological convention was used to discriminate positive and negative *NEE* values. *NEE* is negative when photosynthesis prevails over respiratory processes; thus, it stands for ecosystem carbon uptake.

According to Lloyd and Taylor (1994), Reichstein et al. (2005) and, Davidson and Janssens (2006) the diurnal respiration (Re_{day}) can be evaluated as:

$$Re_{day} = Re_{night} \cdot e^{\beta \cdot (T_{day} - T_{night})} \quad \textbf{(5.15)}$$

where Re_{night} is the nocturnal respiration, which is equal to the nocturnal *NEE* as there is no photosynthesis by night; T_{day} is the mean diurnal air temperature; and, T_{night} the nocturnal one. β is a parameter assumed equal to 0.1 (Lloyd and Taylor, 1994; Reichstein et al., 2005; Davidson and Janssens, 2006).

The EC-based partitioning method was applied to the citrus orchard only for two irrigation seasons (2018-2019).

5.6 Gaussian Process Regression (GPR) algorithm

To estimate the missing data in the ET_a time series and predict outcomes in both the experimental fields, the Gaussian Process Regression (GPR) model was exploited for its power, among other machine learning algorithms, to make predictions relying on a few parameters.

The model establishes a relation between the independent input variables, x_i, (*e.g.*, meteorological variables, soil water status, and VIs), and the dependent variable, *y*, represented by the actual crop

evapotranspiration. Specifically, the regression model built by the GPR is:

$$y = f(x) + \varepsilon \sim N\big(m(x), k(x,x')\big) + \varepsilon \quad \textbf{(5.16)}$$

where x and y denote the input and output in the training dataset and $f(x)$ is known as latent variable in the GPR model, and ε is the noisy observations of the true function expressed as a normal distribution characterized by a mean equal to zero and variance σ_n^2 estimated from the data. The Gaussian process $f(x)$ can be defined by its mean $m(x)$ and covariance kernel $k(x,x')$ functions, represented respectively by a vector and a matrix in the form:

$$m(x) = E[f(x)] \quad \textbf{(5.17)}$$

$$k(x,x') = E\big[\big(f(x) - m(x)\big) \cdot \big(f(x') - m(x')\big)\big] \quad \textbf{(5.18)}$$

The mean (basis) function of the GPR model can be assumed constant, with a value set to zero, equal to the mean of the training dataset, or by using a linear function. The kernel (covariance) function represents a geometrical distance measure assuming that the more closely located inputs would be more correlated in terms of their function values. The covariance kernel function can be assumed as rational quadratic, squared exponential, exponential, or using a Matern kernel. More details on the GPR model can be found in Rasmussen (2006).

To identify the best $m(x)$ and $k(x,x')$ functions, the machine learning model based on the GPR was implemented by using a Matlab® script, which was used to test fifteen possible combinations of the mean and covariance kernel functions: three mean functions (Zero, Constant, and Linear) and five covariance kernel functions (Squared Exponential, Matern 5/2, Matern 3/2, Rational Quadratic, and Exponential).

The Squared Exponential kernel, also called Gaussian kernel or RBF kernel, is defined as (Rasmussen, 2006):

$$k(x,x') = \sigma_S^2 exp\left(-\frac{1}{2}\frac{(x-x')^T(x-x')}{\lambda_S^2}\right) + \sigma_\varepsilon^2 X \quad \textbf{(5.19)}$$

where $(x - x')^T(x - x')$ can be regarded as the squared Euclidean distance between two eigenvectors and σ_S, λ_S and $\sigma\varepsilon$ are three hyperparameters. σ_S^2 controls the marginal variance of *f(x)* and is referred to as variance parameter, which is used to characterize the deviation of the fitting function from the signal mean value. When σ_S^2 is small, the fitting function deviates from the signal mean value slightly. When σ_S^2 is large, the fluctuation of the fitting function will become larger (Pan et al., 2021). λ_S is the relative characteristic length scale, which is used to describe the smoothness of the function. When λ_S is small, the dynamic response performance of the fitting function is better than when it is high, but it is accompanied by the risk of overshooting; when λ_S is large, the resultant function tends to be smooth. σ_ε^2 represent the measurement error. X is the indicator function.

The Matern function kernel is named by Stein (1999) after the work of Matérn (1986). It can be written as:

$$k(x,x') = \sigma_M^2 exp\left(-\frac{\sqrt{2\upsilon(x-x')^T(x-x')}}{\lambda_M}\right) \times \frac{\Gamma(p+1)}{\Gamma(2p+1)} \sum_{l=0}^{p} \frac{(p+l)!}{l!\,(p-l)!} \left(\frac{\sqrt{8\upsilon(x-x')^T(x-x')}}{\lambda_M}\right)^{p-l} \sigma_\varepsilon^2 X \qquad \textbf{(5.20)}$$

where υ is a chosen parameter equals to (p + ½), the definitions of σ_M and λ_M are like those of σ_S and λ_S, where the subscripts indicate the reference to the kernel function name. Γ is the Gamma function. The Matern kernel is characterized by the parameter υ. According to Rasmussen (2006), we set υ equal to 3/2 and 5/2.

The Rational Quadratic kernel can be treated as a scale mixture of Squared Exponential kernels with the different characteristic length-scales (Rasmussen, 2006):

$$k(x,x') = \sigma_R^2 \left(1 + \frac{(x-x')^T(x-x')}{2\alpha_R \lambda_R^2}\right)^{-\alpha_R} + \sigma_\varepsilon^2 X \qquad \textbf{(5.21)}$$

The hyperparameters σ_R, λ_R and σ_ε are like those in the definition of Squared Exponential and Matern, where the subscripts indicate the reference to the kernel function name. Rational Quadratic has a positive-valued scale-mixture parameter α_R that can determine the relative weighting of large-scale and small-scale variances. Rational

Quadratic kernel is equivalent to a scale mixture of Squared Exponential kernels with different relative characteristic length scales (Roberts et al., 2013). The rational quadratic kernel has a wide scope, which could help the prediction performance also when small input database is used and to improve the generalization ability and the dynamic response performance (Shi et al., 2022; Yang et al., 2022).

Finally, the mathematical formula of the Exponential kernel is as follow (Rasmussen, 2006):

$$k(x,x') = \sigma_f^2 exp\left(-\frac{\sqrt{(x-x')^T(x-x')}}{\lambda_f}\right) + \sigma_\varepsilon^2 X \quad \textbf{(5.22)}$$

The hyperparameters σ_f, λ_f and σ_ε are defined previously, where the subscripts indicate the reference to the kernel function name.

Thus, to find the best functions, the analysis was carried out by considering the complete dataset of the input variables acquired in the citrus orchard, from 2018 to 2025, including: the standard weather variables, accounting for the characteristics of ETo and two vegetation indices (VIs), such as *NDVI* and *NDWI*, accounting for the characteristics of the vegetation and the water content, with impact on K_c and K_s (Lei and Yang, 2014; Pôças et al., 2020). Once identified the best *m(x)* and *k(x,x')* functions, using the complete database, two more different possible combinations of the input variables were considered to reduce the computational burden and extend the time series.

The second combination considers only the meteorological variables, whereas the last combination (three) included only variables acquired from remote platforms and available online, such as the meteorological variables and the VIs.

To assess the model suitability using the best *m(x)* and *k(x,x')* functions previously retrieved, for the olive orchard, the three combinations were also assessed in 2009-2010-2011.

5.6.1 Feature analysis

The potential input features, as well as the target feature (ET_a), were analyzed by: i) calculating a set of descriptive statistics for each variable, including mean, the average value, representing the central

tendency of the data; standard deviation, a measure of the dispersion of the values around the mean; standard error, an estimate of the variability of the sample mean relative to the true population mean; Median, the middle value of the data when sorted, providing a robust measure of central tendency; variance, the square of the standard deviation, indicating the spread of the data; maximum, the largest observed value; minimum, the smallest observed value; range, the difference between the maximum and minimum values, showing the full span of the data; kurtosis, a measure of the "tailedness" of the distribution, indicating the presence of outliers; skewness, a measure of the asymmetry of the distribution around the mean; ii) a scatter matrix which shows at a glance the relationship between each two features: the scatter plot at row n and column m shows the n-th feature as a function of the m-th feature. This is helpful to spot correlations in the dataset, since the sparser are points in a plot, the more uncorrelated are the two corresponding features. Finally, the plots in the diagonal represent the kernel density estimation of each feature, which is an estimate of their probability density function; iii) the Pearson correlation coefficient, which measures the linear correlation of each couple of features. It ranges between 1 and -1; the sign of the coefficient reflects the slope of the linear relation); iv) the Feature Importance Scores (*FIS*), computed using the Gradient Boosting Regressor (Kadiyala and Kumar, 2018), of each variable in the dataset for the prediction of ET_a. The higher the *FIS*, the more important the feature. The importance of a feature is computed as the (normalized) total reduction of the criterion brought by that feature and is also known as the Gini importance (Ravindran et al., 2021).

5.6.2 K-fold cross-validation for machine learning model

The best combination of *m(x)* and *k(x,x')* functions of the GPR model, as well as the performances associated with the other variables combinations, were evaluated using the K-fold cross-validation (Mosteller et al., 1968). Cross-validation is a statistical method in which the database is randomly divided into K different groups, each one containing the records corresponding to the natural number closest to K_t/K, in which K_t is the total number of records. Model

validation follows an iterative procedure in which a group is used as test set, while the other K-1 groups are used for training. The procedure is stopped after K iterations and therefore after using each group as test set. This iterative statistical analysis reduces the possibility of overfitting problems (Nguyen et al., 2021) occurring when the model fits well the training data but fails in the prediction phase due to the noise or random fluctuations in the training data (Namasudra et al., 2023). In this study, the value of K was set up as equal to five and therefore 80% of the entire database was used for training, while the remaining 20% was used for testing purposes.

For each iteration, all the statistical indicators, shown in the next *5.8 Definition of the adopted statistical indices* section, were evaluated. Finally, the model performances were analyzed as the mean of all the K performed iterations.

5.7 IRRILEARNING model

On the olive orchard and at the larger scale of the irrigation district, once the ML model was trained and validated, it was integrated with the FAO-56 model. The combination of these two approaches led to the development of the IRRILEARNING model. This hybrid model combines the strengths of data-driven techniques with established agronomic methodologies to provide a comprehensive decision-support tool for irrigation management.

IRRILEARNING uses meteorological data, measured or forecasted, together with vegetation indices and either the irrigation calendar or specific irrigation intervention thresholds, to generate time series of ET_a and SWC. These outputs allow for the assessment of crop water stress and offer a robust basis for managing, analysing, and verifying irrigation practices. By integrating diverse sources of information within a single framework, IRRILEARNING supports informed decision-making aimed at optimizing water use, improving crop performance, and enhancing the sustainability of irrigation strategies.

Three different IRRILEARNING configurations are available (**Figure 5.6**):

i) *Support and check.* With this configuration, the model aids in assessing ongoing irrigation management by providing real-time or near-real-time feedback to check if the irrigation supplies are aligned with crop water needs;
ii) *Forecasting*. IRRILEARNING allows for the creation of optimized irrigation schedules based on forecast data, enabling farmers and water managers to forecast water requirements and organize resources accordingly;
iii) *Scenario Management*. The model supports scenario analysis, allowing users to simulate different irrigation strategies under varying climatic conditions (*i.e.* rain temporal distribution). This configuration is particularly valuable to consider changing weather patterns or resource constraints; thus, allowing driving the irrigation scheduling for an enhanced and resilience farming practice.

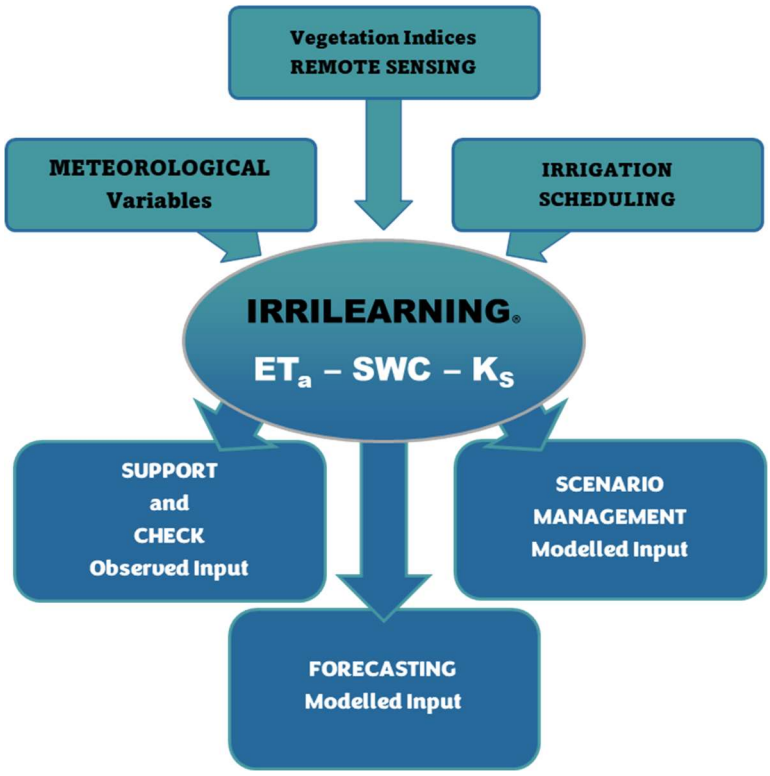

Figure 5.6 IRRILEARNING framework

5.8 Definition of the adopted statistical indices

To enable an objective assessment of the datasets considered in this work, (*i.e.*, *in situ* measurements, model outputs, and externally sourced data products) a set of widely used statistical indices was employed. These metrics provide a consistent framework for quantifying agreement, accuracy, and discrepancies among the different data sources, regardless of their origin or underlying generation process. The selected indices offer complementary information, capturing both systematic deviations and the overall dispersion relative to the reference values.

- The Root Mean Square Error (*RMSE*) whose target value is zero if there are no differences between simulated and observed values:

$$RMSE = \sqrt{\frac{\sum_{i=1}^{n}(x_i - y_i)^2}{n}} \quad \textbf{(5.23)}$$

- The Mean Bias Error (*MBE*), whose target value is zero; positive values represent an overestimation of the modelled values compared to the observations, and vice versa for negative values (Kennedy and Neville 1986):

$$MBE = \frac{\sum_{i=1}^{n}(x_i - y_i)}{n} \quad \textbf{(5.24)}$$

- The Mean Absolute Error (*MAE*) representing the distance between the predicted and observed values, with a target of zero:

$$MAE = \frac{\sum_{i=1}^{n}|x_i - y_i|}{n} \quad \textbf{(5.25)}$$

- The coefficient of determination (R^2) whose unitary target indicates that the variance of the observed values is totally explained by the model (Eisenhauer, 2003):

$$R^2 = 1 - \frac{\sum_{i=1}^{n}(x_i - y_i)^2}{\sum_{i=1}^{n}(x_i - \bar{x})^2} \quad \textbf{(5.26)}$$

- The regression coefficient (*b*), whose target is one, representing the angular coefficient of the regression line between simulated and observed values forced to the origin:

$$b = \frac{\sum_{i=1}^{n}(x_i \cdot y_i)}{\sum_{i=1}^{n}(x_i^2)} \quad \textbf{(5.27)}$$

- The coefficient of determination ($R^2[b]$) of the regression line between simulated and observed values forced to the origin:

$$R^2[b] = \left(\frac{\sum_{i=1}^{n}(x_i \cdot y_i)}{\sqrt{\sum_{i=1}^{n}(x_i^2)} \cdot \sqrt{\sum_{i=2}^{n}(y_i^2)}} \right)^2 \quad \textbf{(5.28)}$$

- The Nash-Sutcliffe efficiency coefficient (*NSE*), whose target values is one; a value of this indicator between 0.0 and 1.0 indicates an acceptable model performance, whereas a negative value indicates that the mean of observed values is a better predictor than the simulated ones and therefore the performance is unacceptable (Nash and Sutcliffe, 1970):

$$NSE = 1 - \frac{\sum_{i=1}^{n}(x_i \cdot y_i)^2}{\sum_{i=1}^{n}(x_i - \bar{x})^2} \quad \textbf{(5.29)}$$

where x_i are the reference data, y_i are the data that need to be analyzed, $\bar{x}$ is the mean of the reference data and n is the number of the data.

PART III

Applications, Results and Discussion

Chapter 6. Results and discussion

6.1 Meteorological conditions at experimental sites

6.1.1 Olive Orchard

According to the carried-out analyses, the experimental olive orchard was monitored from 2008 to 2011 and from 2017 to 2020.

During the period 2008–2011, the experimental site exhibited meteorological conditions characterized by an average $T_{a\text{-}mean}$ of 17.64 °C, with seasonal extremes ranging from 3.85 °C to 31.85 °C. The RH_{mean} showed an average value of 67.09%. R_s displayed marked seasonality, with maximum values in August and minimum values in December, reaching an average daily value of 17.29 MJ m^{-2} day^{-1}. Total annual precipitation amounted to 434.20 mm in 2008, 915.40 mm in 2009, 747.20 mm in 2010, and 538.20 mm in 2011, concentrated mainly between October and March, whereas the months from April to September were generally drier. In the second interval, 2017–2020, the average T_{mean} was 17.22 °C, while the mean relative humidity reached 69.12%. R_s confirmed the same seasonality observed in the first period. Total annual P reached 588.60 mm in 2017, 889.40 mm in 2018, 650.80 mm in 2019 and 557.40 mm, with the same seasonal distribution as in the first period (**Figure 6.1**).

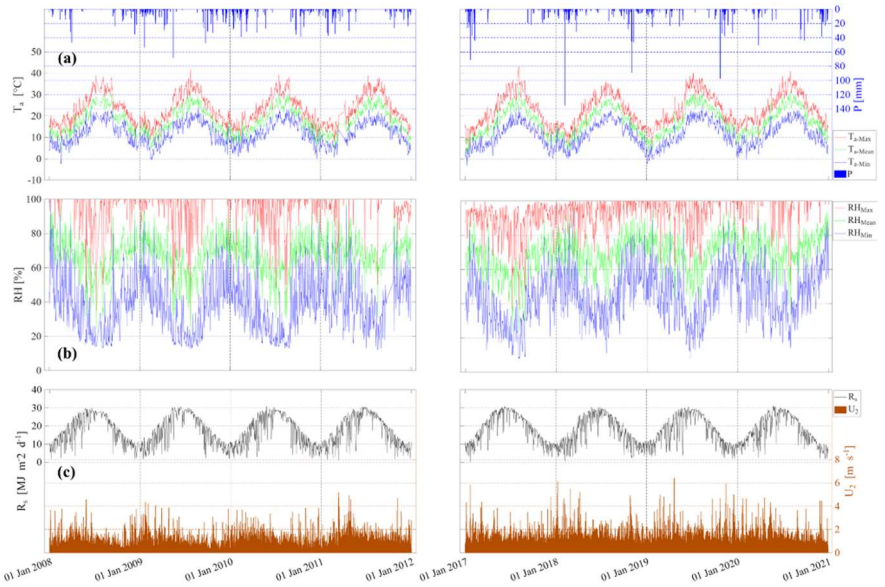

Figure 6.1 Daily temporal dynamic of: (a) precipitation depth (P) (blue bars), maximum ($T_{a\text{-}Max}$) (red line), mean ($T_{a\text{-}Mean}$) (green line) and minimum ($T_{a\text{-}Min}$) (blue line) air temperature; (b) maximum (RH_{Max}) (red line), mean (RH_{Mean}) (green line) and minimum (RH_{Min}) (blue line) relative air humidity; (c) global solar radiation (R_s) (black line) and wind speed measured at 2 m from the ground (U_2) (orange bars) in the periods 2008-2011 and 2017-2020

Thus, the orchard is characterized by a *Hot summer Mediterranean climate (Csa)* (Kottek et al., 2006), according to the last version of the Köppen climatic classification, with rainfall concentrated in fall and winter and quite hot and dry summer.

By comparing the cumulative annual rainfall with the volumes of irrigation applied, it is possible to observe that water is supplied to the crop primarily during the dry months. The irrigation events provided by the farmer consisted of three in 2009 with a total volume of 80 mm, one in 2010 with a total volume of 33 m, and five in 2011 with a total volume of 150 mm (**Figure 6.2**).

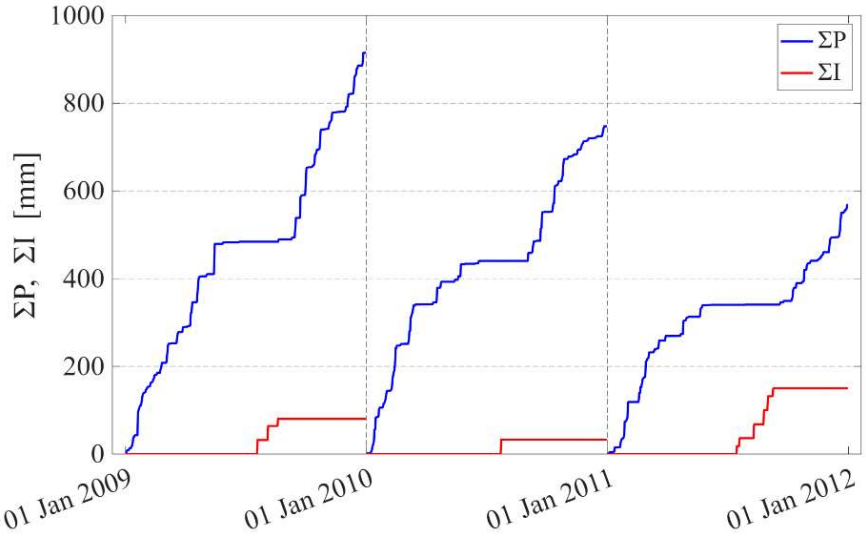

Figure 6.2 Cumulative precipitation depth (ΣP) (blue lines) and Irrigation volumes (ΣI) (red lines) in the period 2009-2011

The limited number of irrigations in the first two years can be attributed to higher rainfall in the previous months. Considering that the farm where the plots are located primarily produces olive oil, the crop was intentionally subjected to mild water stress, as stressed olive trees tend to produce higher-quality yields. Conversely, in 2011, due to a lower number of rainy events, the farmer had to supply a larger total volume of water, distributed over five irrigation events.

Figure 6.3 shows the temporal dynamics of ET_a, ET_0, and P. ET_0 reflects the atmospheric evaporative demand driven by meteorological conditions, whereas ET_a represents the actual water losses from the olive trees and soil, integrating *SWC* availability and vegetation physiological responses. Daily rainfall bars indicate the timing and magnitude of precipitation events. Both ET_a and ET_0 exhibit a pronounced seasonal pattern, with maximum values occurring in summer and minimum values in winter, closely following the annual course of R_s. Gaps in the ET_a time series are present. These missing data points are due both to instrumental malfunctions, as the sensors used are highly sensitive, and to the deliberate exclusion of days when daily rainfall exceeded 2.5 mm d^{-1}. On these rainy days, *ET* measurements were discarded to avoid

distortions associated with canopy and soil wetting and the consequent alteration of sensor signals.

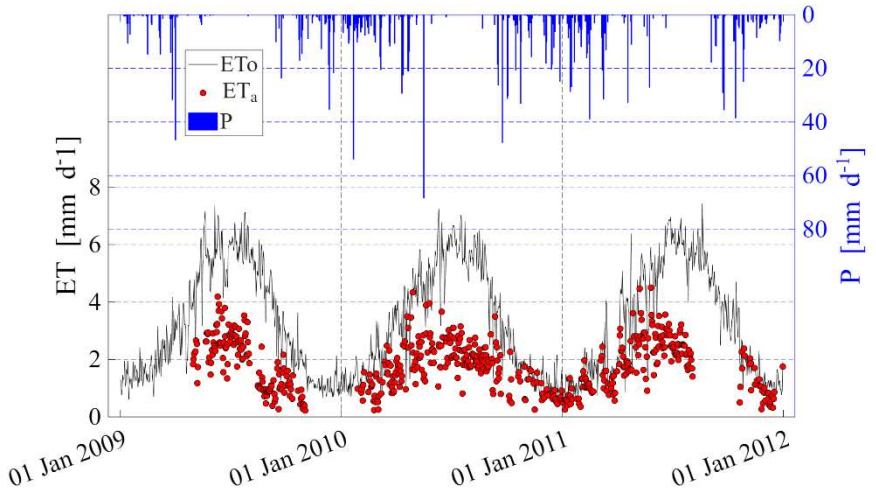

Figure 6.3 Daily temporal dynamic of precipitaion depth (P) (blue bars), crop reference evapotranspiration (ETo) (black line) and actual evapotranspiration (ET_a) (red dots) (2009-2011)

The ET_a accuracy was verified based on the CR **(5.4)** (**Figure 6.4**).

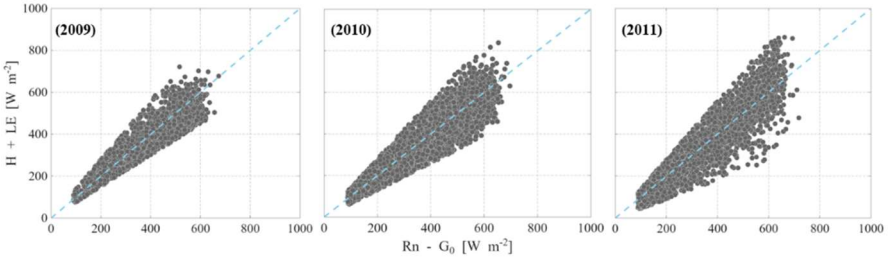

Figure 6.4 Closure ratio computed only when $R_n \geq 100$ W m^{-2}. Relationships between available energy (R_n-G_0) and turbulent heat fluxes (H + LE) measured by the EC tower in the period 2009-2011; the dashed light blue lines are the 1:1 lines (perfect match)

The average values of *CR* resulted equal to 0.98 in 2009, 0.99 in 2010 and 0.99 in 2011.

For tree crops, Kustas et al. (1999) considered acceptable values of *CR* ranging between 0.80 and 0.90. Values of the *CR*, equal to 1.08 and 1.03, were obtained by Er-Raki et al. (2009) in two citrus orchards in south Morocco characterized by a semi-arid Mediterranean climate.

6.1.2 Citrus Orchard

Also the experimental citrus orchard is located in a zone characterized by a hot-summer Mediterranean climate (Csa) (Kottek et al., 2006), according to the latest version of the Köppen climate classification, with rainfall concentrated in autumn and winter and hot, dry summers. Thus, during the period 2018–2025, the site exhibited climatic conditions characterized by an average $T_{a\text{-}Mean}$ of 18.92 °C, with seasonal extremes ranging from -4.44 to 45.94 °C. The relative humidity showed an average value of 71.04 %. Global solar radiation displayed marked seasonality, with maximum values in July and minimum values in December, reaching an average daily value of 16.50 MJ m^{-2} day^{-1}. Total annual precipitation amounted to 923.65 mm in 2018, 550.90 mm in 2019, 541.70 mm in 2020, 917.55 mm in 2021, 518.39 mm in 2022, 455.17 mm in 2023, 530.57 mm in 2024, and 746.02 mm in 2025, concentrated mainly between October and March, whereas the months from April to September were generally drier (**Figure 6.5**).

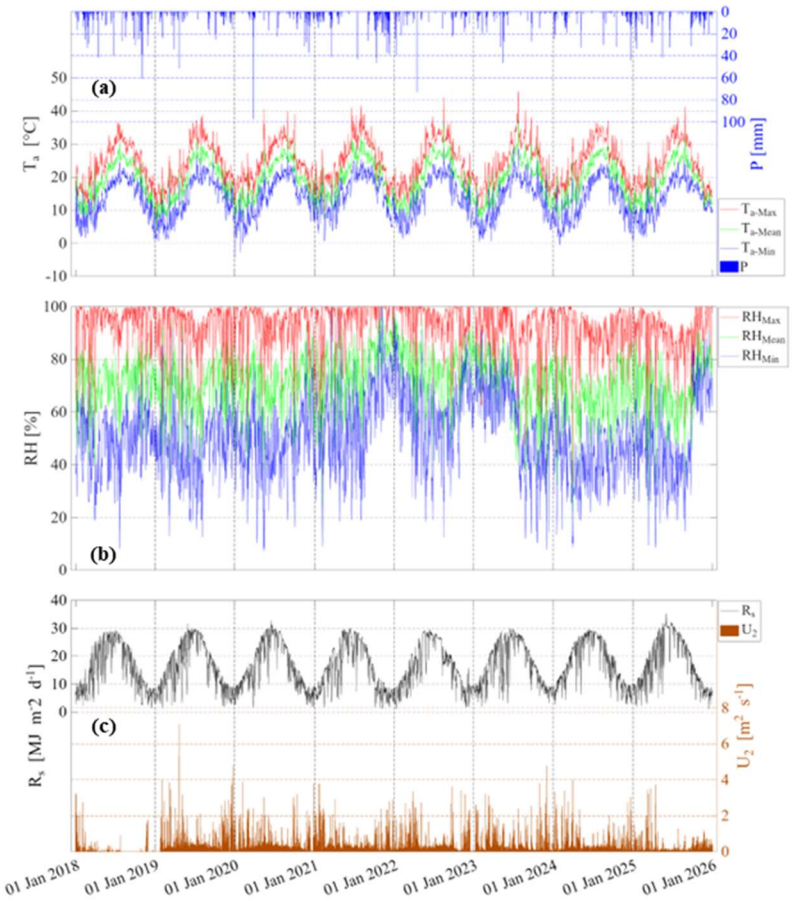

Figure 6.5 Daily temporal dynamic of: (a) precipitation depth (P) (blue bars), maximum ($T_{a\text{-}Max}$) (red line), mean ($T_{a\text{-}Mean}$) (green line) and minimum ($T_{a\text{-}Min}$) (blue line) air temperature; (b) maximum (RH_{Max}) (red line), mean (RH_{Mean}) (green line) and minimum (RH_{Min}) (blue line) relative air humidity; (c) global solar radiation (R_s) (black line) and wind speed measured at 2 m from the ground (U_2) (orange bars) in the period 2018-2025

As in the olive orchard, irrigation volumes are supplied during the dry season (May–September). However, in this case, since the crop is citrus and the farmer's objective is to obtain fruits of high quality and quantity, the irrigation volumes applied are higher. The RDI strategy introduced in *4.2, Experimental Field II – Citrus Orchard*, was applied in the years 2018, 2019, 2020, and 2022. In 2021 and 2023, due to the heatwave conditions during the summer, the farmer chose not to apply for the RDI. Throughout these six irrigation seasons, irrigations were nevertheless carried out predominantly using the

subsurface drip irrigation system, while sporadic aid irrigations were supplied using the old micro-sprinklers system.

Conversely, in 2024 and 2025, extremely heatwaves conditions were accompanied by severe drought conditions, which forced the farmer to return to the traditional irrigation strategy, based on bi-weekly applications, with water supplied through the micro-sprinkler system (**Figure 6.6**).

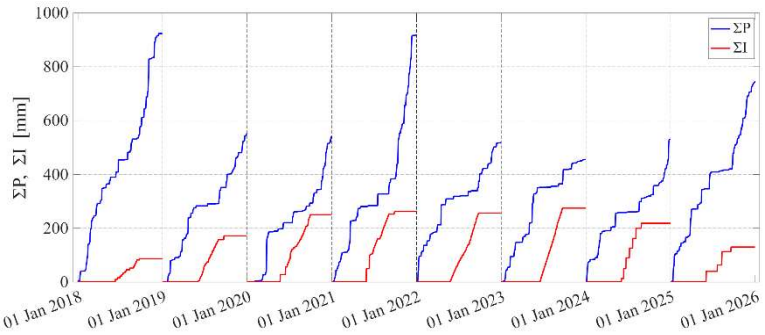

Figure 6.6 Cumulative precipitation depth (ΣP) (blue lines) and Irrigation volumes (ΣI) (red lines) in the period 2018-2025

SWC dynamics were monitored using Drill & Drop probes. Measurements were carried out down to a depth of 60 cm, with readings taken every 10 cm. The dynamics shown in **Figure 6.7** refer exclusively to the irrigation season (15 May – 30 September). The black dots represent the soil water content averaged between 10 and 50 cm, where citrus roots are most active. These averaged series are characterized by low standard deviation values, indicating a relatively uniform *SWC* distribution within the active root zone. The coloured band at the bottom of the figure instead shows the *SWC* at each 10 cm layer. It can be observed that smaller irrigation events supplied by the subsurface drip irrigation system cause an increase in *SWC* only between 30 and 40 cm depth, where the drip line is located. Larger irrigation volumes, on the other hand, are supplied using the old micro-sprinkler system, as evidenced by an increase in *SWC* in the upper soil layer, which then propagates to deeper layers over the following days. The same behavior is observed after rainfall events.

The time series are characterized by a few gap-filled intervals due to temporary malfunctioning of the probes.

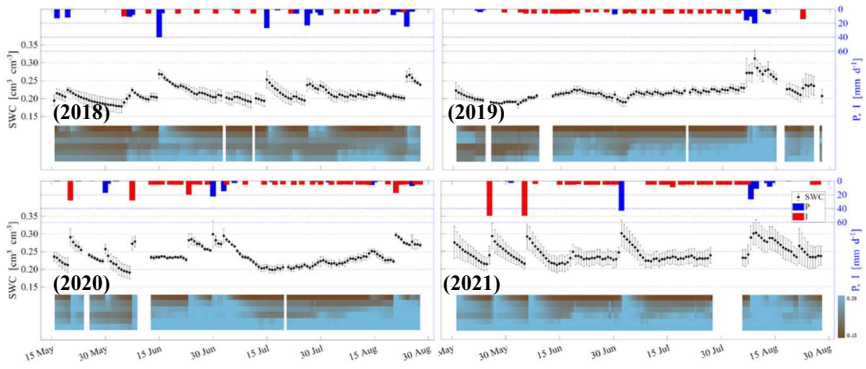

Figure 6.7 Daily temporal dynamics of precipitation depth (P) (blue bars), irrigation supllies (I) (red bands), mean SWC in layers from 10 cm to 50 cm and standard deviation (black dots and vertical lines) in the irrigation seasons 2018-2021; for each irrigation season the detail of SWC measured each 10 cm depth in the layer 10 cm – 60 cm is also shown

The citrus orchard was monitored with sap-flow sensors only during the irrigation seasons of 2018 and 2019, whereas ET_a has been monitored since 2019 (**Figure 6.8**) by the eddy covariance tower. As in the olive orchard, the seasonality of both ET_a and ETo is clearly evident, with maximum values in summer and minimum values in winter. These dynamics closely follow those of R_s. The farmer generally allows to keep the soil weed-free, performing recurrent weed control in order to avoid water competition. However, this management activity was somewhat neglected in 2021, when a marked increase in ET_a values can be observed, most likely probably due to transpiration from weeds. In the years when irrigation volumes were supplied through the subsurface drip irrigation system, the increase and decrease of ET_a were gradual and followed the seasonal cycle, since water was applied approximately every 2–3 days. Conversely, in 2024 and 2025, when irrigation volumes were supplied exclusively via the old micro-sprinkler system, there was a sharp increase in ET_a immediately after each irrigation event and a pronounced decrease until the following irrigation can be observed. This behavior demonstrates that water supplied through subsurface

drip irrigation tends to maintain plant water stress under control, even when the RDI strategy is applied. In contrast, severe stress conditions are reached under the traditional bi-weekly irrigation strategy.

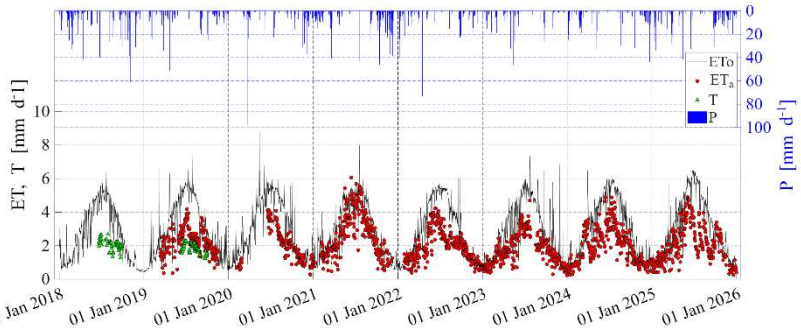

Figure 6.8 Daily temporal dynamic of precipitaion depth (P) (blue bars), crop reference evapotranspiration (ETo) (black line), actual evapotranspiration (ET_a) (red dots) and transpiration (T) in the period 2018-2025

ET_a time series contains several gaps, which are mainly due to the sensitivity of the instruments composing the EC tower and the need for careful maintenance. A prolonged period of gaps is also present in 2020, caused by the COVID-19 lockdown.

ET_a accuracy was verified based on the *CR* **(5.4)** (**Figure 6.9**). The average *CR* values were 0.98 in 2019, 0.88 in 2020, 1.03 in 2021, 0.90 in 2022, 1.09 in 2023, 0.92 in 2024, and 0.98 in 2025. These values are consistent with those reported in the literature by Kustas et al. (1999) and Er-Raki et al. (2009).

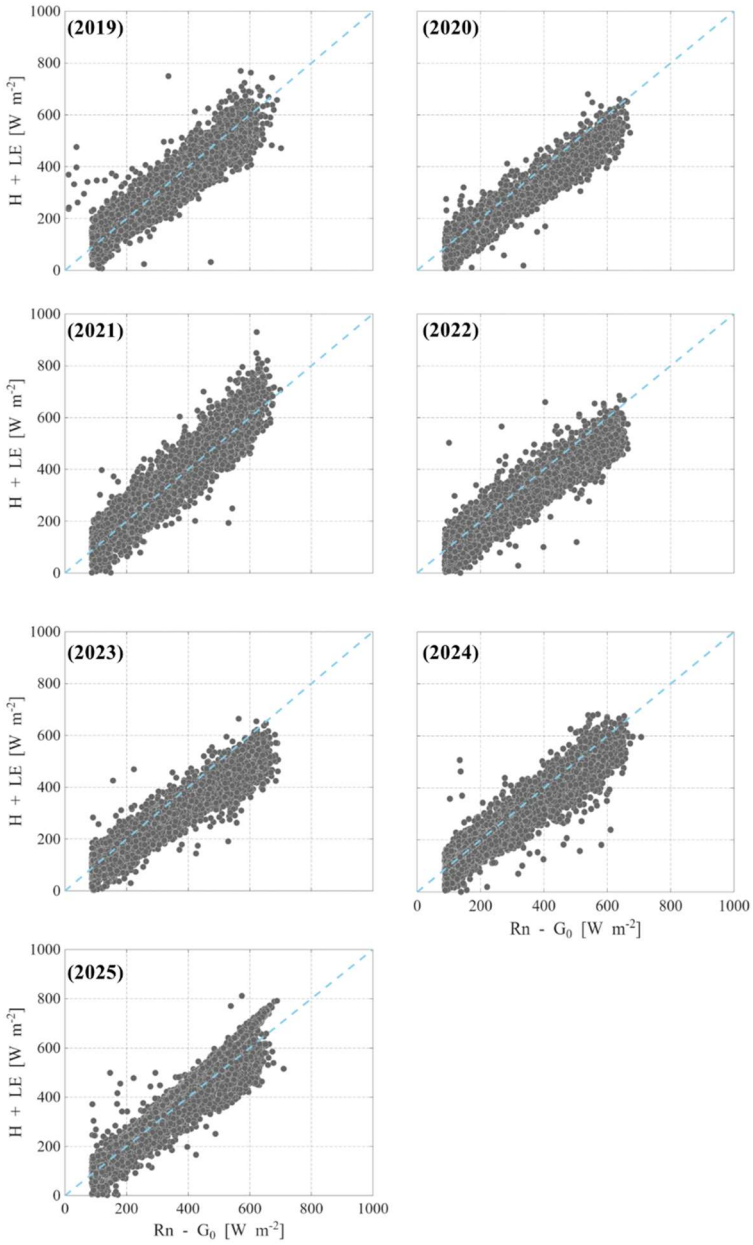

Figure 6.9 Closure ratio computed only when $R_n \geq 100$ W m^{-2}. Relationships between available energy (R_n - G_0) and turbulent heat fluxes (H + LE) measured by the EC tower in the period 2019-2025; the dashed light blue lines are the 1:1 lines (perfect match)

6.2 Reanalysis data accuracy

A comparison between *in situ* and reanalysis data was conducted. This analysis, applied in both experimental orchards, where both databases were available, allowed to evaluate the suitability of using reanalysis climate variables when ground data are not available. The analysis was conducted during 2009-2011 for the olive orchard and from 2018 to 2025 for the citrus orchard.

6.2.1 Olive Orchard

Analyzing the scatterplots shown in **Figure 6.10**, it can be observed that, during the three years, the $T_{a\text{-}Min}$ is slightly overestimated, while the $T_{a\text{-}Max}$ is underestimated. Consequently, the $T_{a\text{-}Mean}$ is well distributed around the 1:1 perfect match line. *RHmin* exhibits the highest *RMSE* when compared to the RH_{max} and RH_{mena} values (**Table 6.1**). The RH_{max} aligns well with the perfect match line, with only a slight underestimation. These two conditions result in a reasonably accurate estimation of the RH_{mean}. Finally, R_s is the best predicted variable, characterized by a low *RMSE* and a high *NSE* value (**Table 6.1**), even though no bias correction was applied.

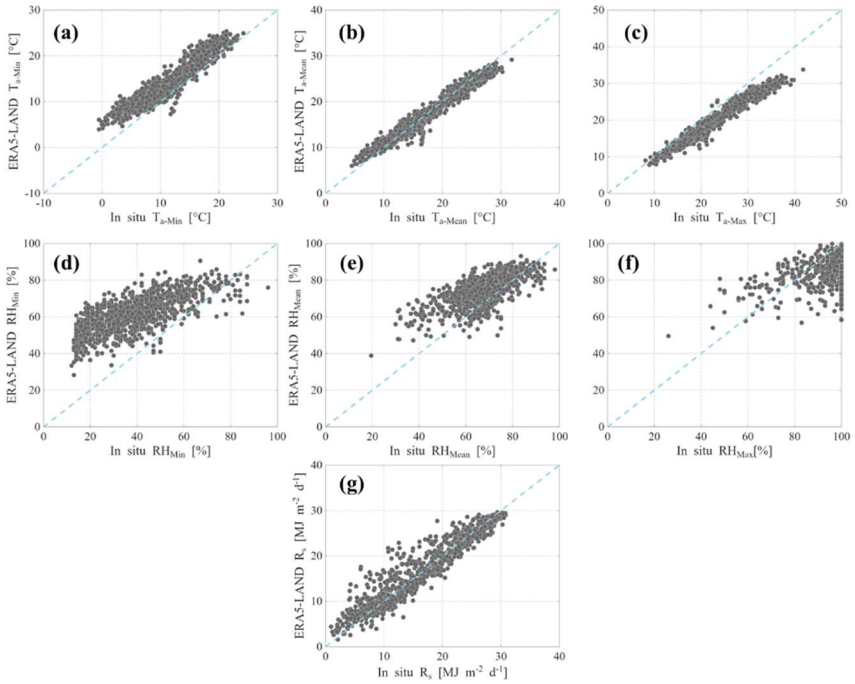

Figure 6.10 Comparison between daily: (a) minimum air temperature ($T_{a\text{-}Min}$), (b) mean air temperature ($T_{a\text{-}Mean}$), (c) maximum air temperature ($T_{a\text{-}Max}$), (d) minimum relatve air humidity (RH_{Min}), (e) mean relatve air humidity (RH_{Mean}), (f) maximum relatve air humidity (RH_{Max}), and (g) global solar radiation (R_s) measured by the *in situ* SIAS weather station installed near the olive orchard and retrieved by the ERA5-LAND reanalysis data in the period 2009-2011; the dashed light blue lines are the 1:1 lines (perfect match)

Table 6.1 Statistical indices for maximum air temperature ($T_{a\text{-}Max}$), mean air temperature ($T_{a\text{-}Mean}$), minimum air temperature ($T_{a\text{-}Min}$), maximum relatve air humidity (RH_{Max}), mean relatve air humidity (RH_{Mean}), minimum relatve air humidity (RH_{Min}) and global solar radiation (R_s)

	RMSE	***MBE***	***MAE***	***R^2***	***b***	***R^2[b]***	***NSE***
		[°C]				[-]	
$T_{a\text{-}Min}$	3.29	2.80	2.89	0.89	1.18	0.98	0.61
$T_{a\text{-}Mean}$	3.45	-3.01	3.03	0.96	0.87	0.99	0.74
$T_{a\text{-}Max}$	1.29	-0.11	1.01	0.96	0.98	0.99	0.95
		[%]				[-]	
RH_{Min}	25.29	22.54	23.02	0.50	1.41	0.91	-1.46
RH_{Mean}	12.01	-8.36	10.08	0.24	0.91	0.99	-0.69
RH_{Max}	10.58	7.09	8.58	0.46	1.09	0.99	0.01
		[MJ m^{-2} d^{-1}]				[-]	
R_s	2.39	0.35	1.71	0.92	1.00	0.98	0.91

Similar results were obtained in Sicily by Negm et al. (2017), using the POWER-NASA database; by Vanella et al. (2022), using ERA5 and ERA5-Land; and by Pelosi and Chirico (2021) and Ippolito et al. (2024), using only ERA5-Land. The results obtained here are also consistent with studies carried out outside Sicily (Bai et al., 2010; Pelosi et al., 2020; Gourgouletis et al., 2023). Moreover, other authors have tested alternative satellite-based solar radiation datasets, such as CM-SAF (Pelosi and Chirico, 2021) and LSA-SAF (Paredes et al., 2021), replacing the corresponding ERA5-Land variable to estimate ET_0. These studies indicate that solar radiation data from ERA5-Land provide satisfactory performance for *ETo* estimation, which is essential for various applications in hydrology and irrigation management. Finally, Vanella et al. (2022) and Gourgouletis et al. (2023) obtained reliable and encouraging *ETo* estimations without implementing bias correction procedure. Moreover, although Paredes et al. (2021) applied the bias correction procedure, they verified that after the application of bias correction to the R_s, the performance of *ETo* estimation does not significantly improve.

To scale wind speed from 10 m to 2 m, the logarithmic wind profile approach proposed by Allen et al. (1998) was adopted. By applying **(5.6)**, the wind speed at 10 m is simply multiplied by a coefficient of 0.75. To assess the accuracy of this procedure, wind speeds at 10 m were multiplied by a range of coefficients from 0.05 to 1.00, with a step of 0.05. Each resulting estimate was then compared with the *in situ* measurements at 2 m, and the coefficient yielding the minimum *RMSE* was identified (**Figure 6.11**).

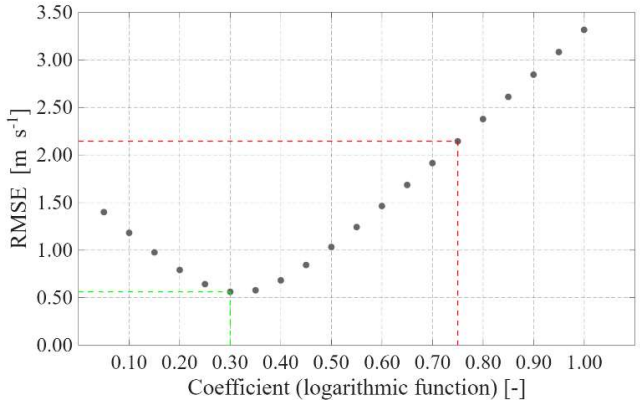

Figure 6.11 RMSE variability as a function of the coefficient representative of the logarithmic wind speed profile. Red lines indicates the RMSE value related to the classical coefficient (0.75) suggested by Allen et al., 1998; *viceversa*, green line indicates the best coefficient, the one with the lowest RMSE

The red lines indicate the *RMSE* values obtained by applying the coefficient (0.75) suggested by Allen et al. (1998), while the green lines correspond to the *RMSE* values obtained using the coefficient (0.30), which yields the lowest *RMSE*.

Figure 6.12 shows the scatterplot comparing U_2 values, considering the coefficient that produces the best performance (*RMSE* = 0.56 m s^{-1}; *MBE* = -0.13 m s^{-1}; *MAE* = 0.44 m s^{-1}; R^2 = 0.45; *b* = 0.83; $R^2[b]$ = 0.88; *NSE* = 0.41).

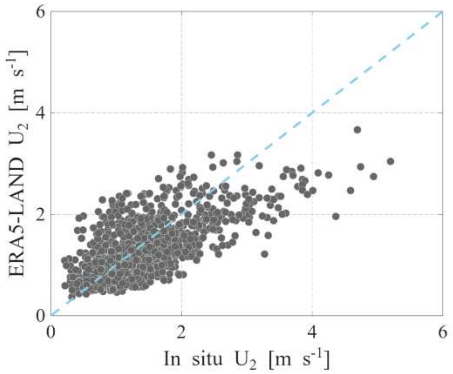

Figure 6.12 Comparison between daily wind speed measure at 2 m from the ground (U_2) measured by the *in situ* SIAS weather station installed near the olive orchard and retrieved by the ERA5-LAND reanalysis data ,scaled with a coefficient equal to 0.30, in the period 2009-2011; the dashed light blue lines are the 1:1 lines (perfect match)

Thus, using the Penman-Monteith equation **(3.10)**, *ETo* was calculated by using as input the reanalysis data, and the resulting values were compared with those obtained using *in situ* measurements as input (**Figure 6.13**).

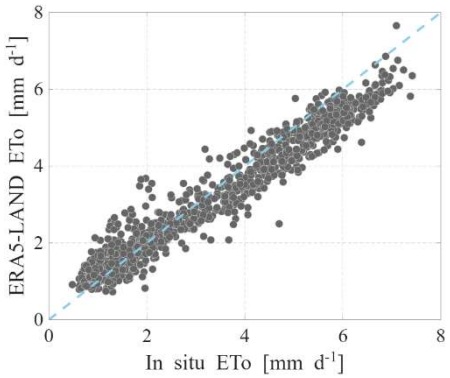

Figure 6.13 Comparison between daily crop reference evapotranspiration (ETo) retrieved using the Penman-Monteith equation using measured *in situ* SIAS weather station installed near the olive orchard and retrieved by the ERA-5 LAND reanalysis data in the period 2009-2011; the dashed light blue lines are the 1:1 lines (perfect match)

The results are very encouraging. Values < 2 mm d^{-1} are slightly overestimated, whereas values above this threshold are slightly underestimated (*RMSE* = 0.53 mm d^{-1}; *MBE* = -0.16 mm d^{-1}; *MAE* = 0.42 mm d^{-1}; R^2 = 0.94; *b* = 0.92; $R^2[b]$ = 0.98; *NSE* = 0.92).

The values of *RMSE* associated to *ETo* found by Negm et al. (2017), using POWER-NASA database, were also similar to those found in this analysis. Instead, similar results, using the *ERA5-L* database, were obtained by Pelosi et al. (2020), who considered 18 standard weather stations over the Campania region. In terms of R^2, the average value found in this analysis shows good performance considering all the 8 years. This result agrees with the study by Pelosi and Chirico (2021), who considered to replace the R_s values from ERA5-Land with the ones retrieved by the CM-SAF database, only during irrigation seasons. The good performance in terms of *RMSE* and R^2 obtained in this analysis highlights the capacity of the ERA5-Land meteorological variables to estimate ETo when ground data are not available.

Regarding precipitation height, the scatterplot (**Figure 6.14**) shows that the correlation is very low, indicating a poor agreement between reanalysis data and *in situ* measurements (RMSE = 4.55 mm; MBE = -0.1 mm; MAE = 1.58 mm; R^2 = 0.45; b = 0.56; R^2[b] = 0.51; NSE = 0.44).

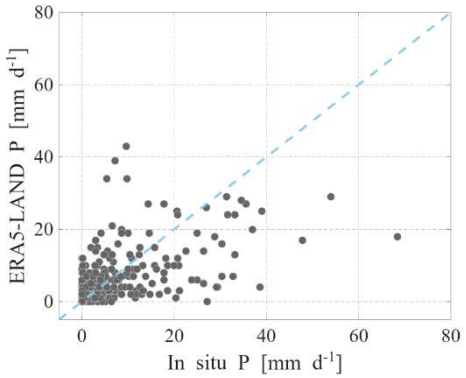

Figure 6.14 Comparison between daily precipitation depth (P) measured by the *in situ* SIAS weather station installed near the olive orchard and reteived by the ERA-5 LAND reanalysis data in the period 2009-2011; the dashed light blue lines are the 1:1 lines (perfect match)

Since the scatterplot revealed a very low correlation for precipitation depth, it was necessary to further evaluate whether the reanalysis dataset was unable to reproduce the observed rainfall dynamics. For this reason, cumulative precipitation over the three study years was also analyzed, as cumulative values are less affected by single-event timing errors (**Figure 6.15**).

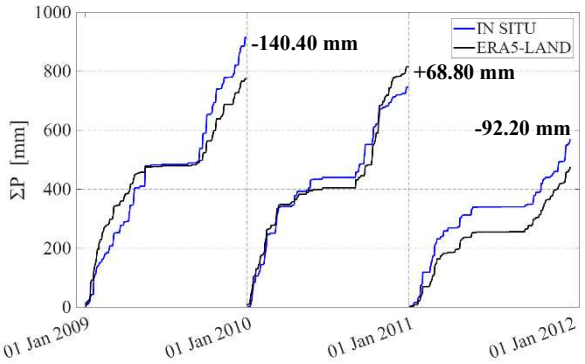

Figure 6.15 Cumulative precipitation depth (ΣP) retrieved by measured *in situ* SIAS weather station installed near the olive orchard and by the ERA-5 LAND reanalysis data in the period 2009-2011

The comparison between cumulative precipitation showed that, although the correlation at event scale was low, the reanalysis dataset was in reasonable agreement with the general trend of observed rainfall. ERA5-Land data resulted in −140.40 mm in 2009, +68.80 mm in 2010 and −92.20 mm in 2011 with respect to the measured cumulative precipitation. The trend of cumulative curves is generally similar in all years, and the discrepancies can mainly be attributed to the magnitude of single rainfall events rather than to systematic bias. In 2009, the dry season was almost perfectly reproduced. Rainfall events occurring before the dry period were generally overestimated, whereas those after the dry period were underestimated. In 2010, the two cumulative curves were nearly identical before the onset of the dry season; a single intense event generated a marked divergence between the datasets. After the dry period, the first events were underestimated and subsequently overestimated by ERA5-Land. Conversely, in 2011, after an initial phase of close agreement, the reanalysis product systematically underestimated all the following rainfall events.

Finally, event-based comparisons (**Figure 6.16**) further illustrated mismatches in rainfall detection, including missed and false rainfall events. Precipitation events were defined as any day with precipitation greater than 0 mm.

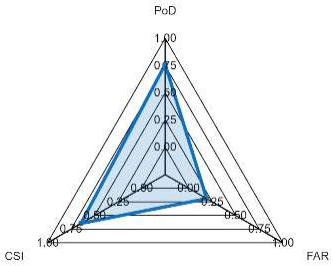

Figure 6.16 Event-based verification of daily precipitation occurrence from *in situ* observations against ERA5-LAND data

PoD, equal to 0.76, indicates that the model correctly detected 76% of the observed events, thus showing a good ability to identify real occurrences, while still missing a non-negligible fraction of events that were not predicted. *FAR*, equal to 0.19, reveals that 19%

of detected events did not actually occur, meaning that most predicted events were correctly observed, with a relatively low rate of false alarms. *CSI*, equal to 0.65, which integrates both missed and false events, indicates a good overall skill in detecting precipitation events, meaning that 65% of all events (including hits, misses, and false alarms) were correctly predicted, reflecting a reasonably high level of agreement between reanalysis and observations.

Similar results were obtained by Longo-Minnolo et al. (2022) in Sicily and by Tarek et al. (2020) in North America.

6.2.2 Citrus Ochard

A similar analysis was also conducted for the citrus orchard, covering the period from 2018 to 2025.

Analyzing the scatterplots of the meteorological variables (**Figure 6.17**), similar results to those observed at the previous experimental site can be identified. In the citrus orchard, the $T_{a\text{-}Min}$ is frequently overestimated, whereas the $T_{a\text{-}Max}$ is slightly underestimated. These two conditions result in the $T_{a\text{-}Mean}$ being well distributed around the 1:1 perfect agreement line. RH_{Min} and RH_{Mean} are still overestimated, while RH_{Max} is often underestimated. R_s remains the best-predicted variable (**Table 6.2**).

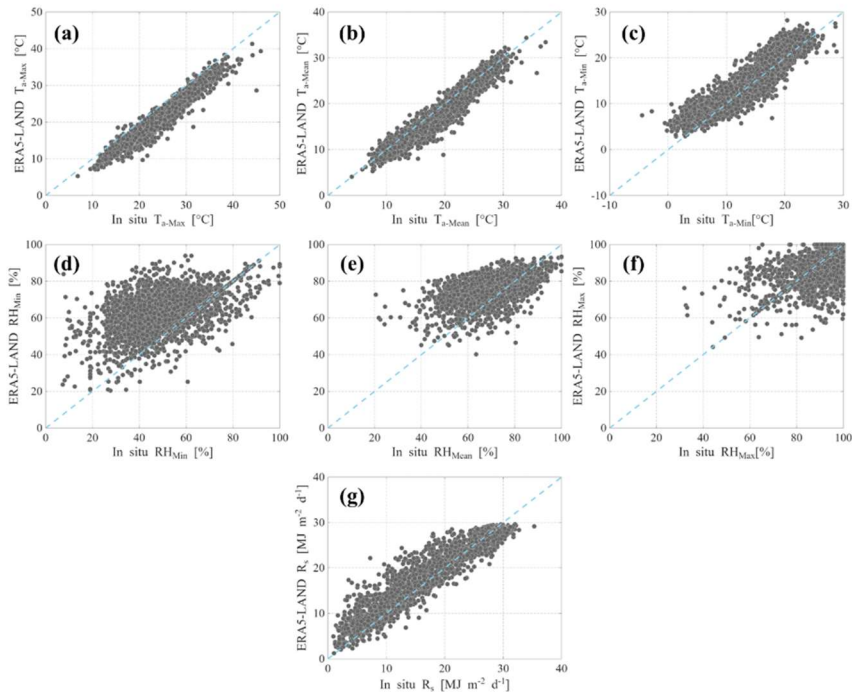

Figure 6.17 Comparison between daily: (a) minimum air temperature (T_{a-Min}), (b) mean air temperature (T_{a-Mean}), (c) maximum air temperature (T_{a-Max}), (d) minimum relatve air humidity (RH_{Min}), (e) mean relatve air humidity (RH_{Mean}), (f) maximum relatve air humidity (RH_{Max}), and (g) global solar radiation (R_s) measured by the *in situ* weather station installed near the citrus orchard and retrieved by the ERA5-LAND reanalysis data in the period 2018-2025; the dashed light blue lines are the 1:1 lines (perfect match)

Table 6.2 Statistical indices for maximum air temperature (T_{a-Max}), mean air temperature (T_{a-Mean}), minimum air temperature (T_{a-Min}), maximum relatve air humidity (RH_{Max}), mean relatve air humidity (RH_{Mean}), minimum relatve air humidity (RH_{Min}) and global solar radiation (R_s)

	RMSE	***MBE***	***MAE***	***R^2***	***b***	***R^2[b]***	***NSE***
		[°C]				[-]	
T_{a-Min}	2.63	1.05	2.10	0.84	1.05	0.97	0.80
T_{a-Mean}	3.54	-3.24	3.26	0.95	0.87	0.99	0.69
T_{a-Max}	1.90	-1.10	1.48	0.93	0.95	0.99	0.90
		[%]				[-]	
RH_{Min}	18.32	12.31	14.22	0.25	1.17	0.94	-0.44
RH_{Mean}	9.10	-2.78	6.24	0.31	0.96	0.99	0.10
RH_{Max}	10.20	5.27	7.93	0.34	1.06	0.99	0.08
		[MJ m^{-2} d^{-1}]				[-]	
R_s	2.65	0.94	1.80	0.91	1.02	0.98	0.90

The analysis of the coefficient derived from the adoption of the logarithmic profile was also carried out (**Figure 6.18**).

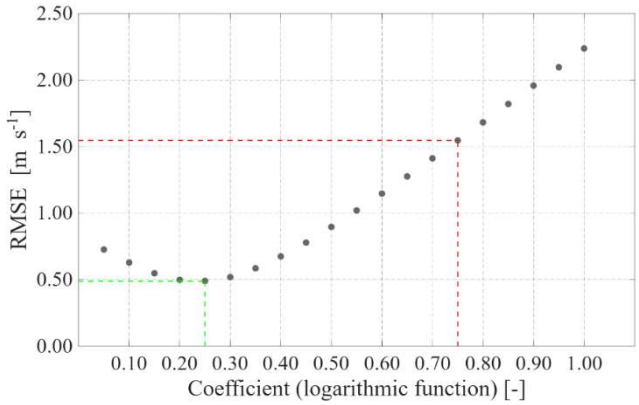

Figure 6.18 RMSE variability as a function of the coefficient representative of the logarithmic wind speed profile. Red lines indicates the RMSE value related to the classical coefficient (0.75) suggested by Allen et al., 1998; *viceversa*, green line indicates the best coefficient, the one with the lowest RMSE

At this site, the coefficient that minimized *RMSE* was found to be 0.25. **Figure 6.19** shows the scatterplot comparing U_2 values, considering the coefficient that produces the best performance (*RMSE* = 0.49 m s^{-1}; *MBE* = 0.10 m s^{-1}; *MAE* = 0.33 m s^{-1}; R^2 = 0.49; *b* = 0.69; $R^2[b]$ = 0.66; *NSE* = 0.45).

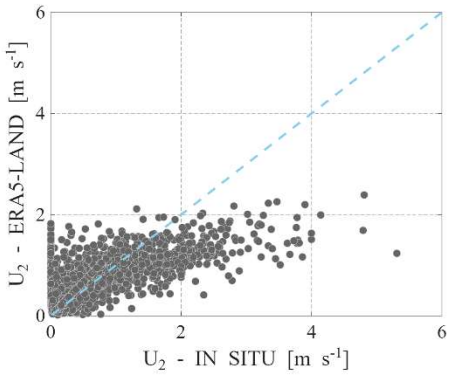

Figure 6.19 Comparison between daily wind speed measure at 2 m from the ground (U2) measured by the *in situ* SIAS weather station installed near the olive orchard and retrieved by the ERA5-LAND reanalysis data ,scaled with a coefficient equal to 0.25, in the period 2018-2025; the dashed light blue lines are the 1:1 lines (perfect match)

Thus, using the Penman-Monteith equation **(3.10)**, *ETo* was calculated by using as input the reanalysis data, and the resulting values were compared with those obtained using *in situ* measurements as input (**Figure 6.20**).

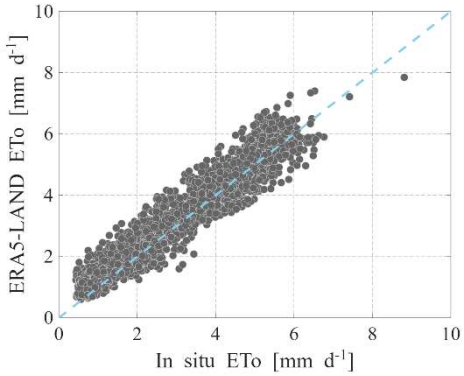

Figure 6.20 Comparison between daily crop reference evapotranspiration (ETo) retrieved using the Penman-Monteith equation using measured *in situ* SIAS weather station installed near the olive orchard and retrieved by the ERA-5 LAND reanalysis data in the period 2018-2025; the dashed light blue lines are the 1:1 lines (perfect match)

Also in this analysis the results are very encouraging. The entire series is subject to a slight overestimation (*RMSE* = 0.57 mm d^{-1}; *MBE* = 0.25 mm d^{-1}; *MAE* = 0.42 mm d^{-1}; R^2 = 0.91; *b* = 1.05; $R^2[b]$ = 0.98; *NSE* = 0.89).

Regarding precipitation height, the scatterplot (**Figure 6.21**) shows again that the correlation is very low, indicating a poor agreement between reanalysis data and *in situ* measurements (*RMSE* = 4.56 mm; *MBE* = -0.01 mm; *MAE* = 1.60 mm; R^2 = 0.40; *b* = 0.55; $R^2[b]$ = 0.66; *NSE* = 0.37).

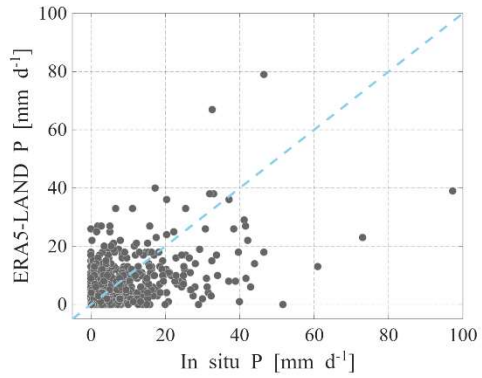

Figure 6.21 Comparison between daily precipitation depth (P) measured by the *in situ* SIAS weather station installed near the olive orchard and retrived by the ERA-5 LAND reanalysis data in the period 2018-2025; the dashed light blue lines are the 1:1 lines (perfect match)

Cumulative values were also analyzed in the citrus orchard (**Figure 6.22**).

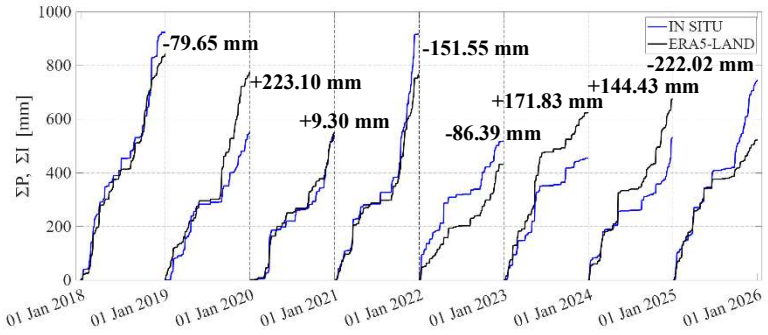

Figure 6.22 Cumulative precipitation depth (ΣP) retrieved by measured *in situ* SIAS weather station installed near the citrus orchard and by the ERA-5 LAND reanalysis data in the period 2018-2025

Also in the citrus orchard, the cumulative precipitation derived from the ERA5-Land product showed variable agreement across the analyzed years. In some years, the differences were relatively small, on the order of ±100 mm (−79.65 mm in 2018, +9.30 mm in 2020, and −86.39 mm in 2022). In other years, the discrepancies were more pronounced, with differences equal to or greater than ±100 mm (+223.10 mm in 2019, −151.55 mm in 2021, +171.83 mm in 2023, +144.43 mm in 2024, and −222.02 mm in 2025).

The event-based comparison, with the same previous threshold equal to 0 mm, was realized (**Figure 6.23**).

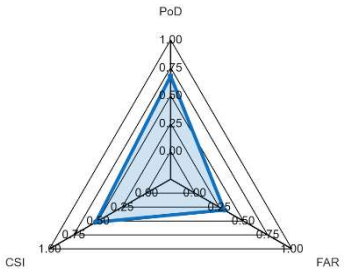

Figure 6.23 Event-based verification of daily precipitation occurrence from *in situ* observations against ERA5-LAND data

The *PoD* of 0.68 indicates that 68% of the observed precipitation events were correctly detected, while a *FAR* of 0.30 shows that 30% of the predicted events did not occur. The resulting *CSI* of 0.52 reflects a moderate overall skill in precipitation event detection, accounting for both missed and false events.

6.3 Forecasting data accuracy

For the configuration of the IRRILEARNING model, it was necessary to evaluate the SILAM forecast data provided by SIAS, which were used as input variables. The data used corresponds to short-term forecasts, specifically "today-for-tomorrow" predictions. These forecasts allow anticipation of the boundary conditions of models, thereby reducing systematic errors and ensuring consistency with the temporal scale of the physical and decision-making processes of the SPA continuum system. Moreover, the uncertainty associated with meteo forecasts tends to increase much faster than the useful decision horizon of irrigation models. Consequently, the adoption of short-term forecasts results in more contained errors and limits error accumulation within the model, improving the overall reliability of irrigation scheduling.

The comparison was carried out for the period 2017–2020 within the irrigation district, using the *in situ* measurements collected by the standard weather station located near the experimental olive orchard as a benchmark (**Figure 6.24** and **Table 6.3**).

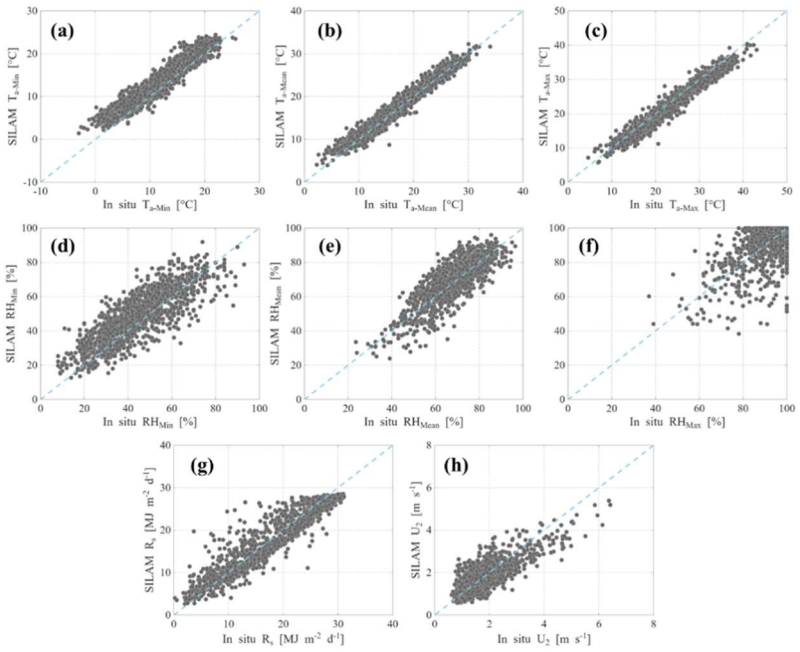

Figure 6.24 Comparison between daily: (a) minimum air temperature (T_{a-Min}), (b) mean air temperature (T_{a-Mean}), (c) maximum air temperature (T_{a-Max}), (d) minimum relatve air humidity (RH_{Min}), (e) mean relatve air humidity (RH_{Mean}), (f) maximum relatve air humidity (RH_{Max}), (g) global solar radiation (R_s) and, (h) wind speed measure at 2 m from the ground (U_2) measured by the *in situ* SIAS weather station installed near the olive orchard and retrieved by the SILAM forecast data in the period 2008-2011; the dashed light blue lines are the 1:1 lines (perfect match)

Table 6.3 Statistical indices for maximum air temperature (T_{a-Max}), mean air temperature (T_{a-Mean}), minimum air temperature (T_{a-Min}), maximum relatve air humidity (RH_{Max}), mean relatve air humidity (RH_{Mean}), minimum relatve air humidity (RH_{Min}), global solar radiation (R_s) and, wind speed measure at 2 m from the ground (U_2)

	RMSE	***MBE***	***MAE***	***R^2***	***b***	***R^2[b]***	***NSE***
		[°C]				[-]	
T_{a-Min}	2.42	1.76	2.01	0.92	1.10	0.98	0.83
T_{a-Mean}	1.86	-1.00	1.49	0.95	0.96	0.99	0.94
T_{a-Max}	1.31	0.38	1.03	0.96	1.01	0.99	0.96
		[%]				[-]	
RH_{Min}	9.84	4.04	7.90	0.68	1.06	0.97	0.60
RH_{Mean}	8.87	-1.01	5.71	0.39	0.99	0.99	0.02
RH_{Max}	7.28	1.26	5.74	0.66	1.02	0.99	0.55
		[MJ m^{-2} d^{-1}]				[-]	
R_s	2.73	-0.32	2.08	0.88	0.96	0.98	0.88
		[m s^{-1}]					
U_2	0.48	0.01	0.36	0.64	0.95	0.94	0.64

In the case of air temperature and relative air humidity, short-term forecasts benefit from the high atmospheric persistence and the continuity of the diurnal cycle, providing estimates that are more consistent with SPA continuum exchange processes (Rajan and Prasad, 2023) compared to reanalysis data, which tend to smooth extremes and represent post hoc average conditions. Specifically, "today-for-tomorrow" meteorological forecasts are particularly effective for air temperature and relative air humidity, as they exploit the strong temporal persistence and preserve the diurnal dynamics, key elements for estimating evapotranspiration demand, whereas reanalysis products provide a smoothed reconstruction. This is confirmed by the good performance retrieved for all six variables. For global solar radiation, whereas a plateau is observed at approximately 28.5 MJ m^{-2} day^{-1}. This plateau in the forecasted global solar radiation does not indicate a measurement error, but rather reflects an intrinsic characteristic of GFS models: they smooth radiation maxima due to physical parameterizations and numerical stability constraints (Aguiar et al., 2016; Pereira et al., 2022). Reanalysis products, on the other hand, thanks to the assimilation of observations, can more accurately reproduce daily peaks. Finally, wind speed is provided directly at 2 m height, and the forecasts show good agreement with the *in situ* measurements.

By examining the scatterplot comparing ETo derived from *in situ* measurements and forecast data (**Figure 6.25**), a clear underestimation is evident. This is likely due to the plateau observed in global solar radiation, which drives the evapotranspiration processes.

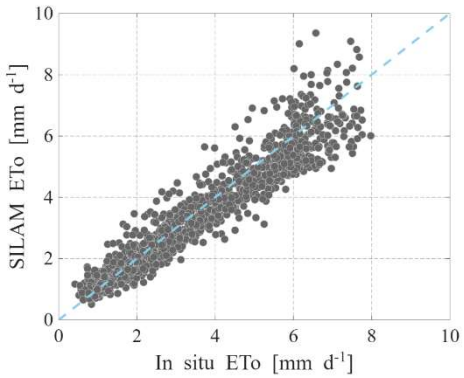

Figure 6.25 Comparison between daily crop reference evapotranspiration (ETo) retrieved using the Penman-Monteith equation using measured *in situ* SIAS weather station installed near the olive orchard and retrieved by the SILAM forecasting data in the period 2008-2011; the dashed light blue lines are the 1:1 lines (perfect match)

The underestimation is further confirmed by the statistics presented in **Table 6.4**.

Table 6.4 Statistical indices for crop reference evapotranspiration (ETo)

	RMSE	***MBE***	***MAE***	***R^2***	***b***	***$R^2[b]$***	***NSE***
	[mm d^{-1}]			[-]			
ETo	0.60	-0.14	0.44	0.91	0.94	0.98	0.91

Finally, the same comparison procedure applied to reanalysis precipitation was also conducted for forecast precipitation. Similarly, not all events are correctly predicted, nor is the magnitude accurately estimated (**Figure 6.26**) (*RMSE* = 6.20 mm; *MBE* = 0.34 mm; *MAE* = 1.79 mm; R^2 = 0.36; *b* = 0.56; $R^2[b]$ = 0.40; *NSE* = 0.29).

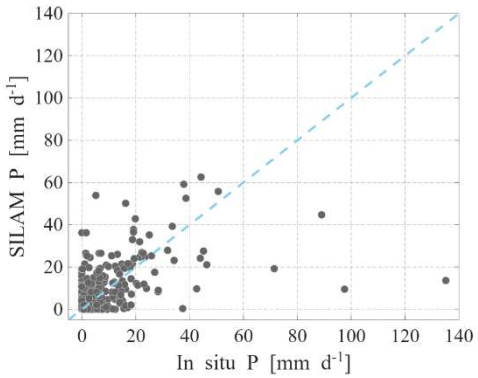

Figure 6.26 Comparison between daily precipitation depth (P) measured by the *in situ* SIAS weather station installed near the olive orchard and retrived by the SILAM forecasting data in the period 2018-2025; the dashed light blue lines are the 1:1 lines (perfect match)

In all years, the annual cumulative precipitation from forecasts exceeds the measured values (**Figure 6.27**), in particular: +73 mm in 2017, +86 mm in 2018, +159.20 mm in 2019, and +171.60 mm in 2020.

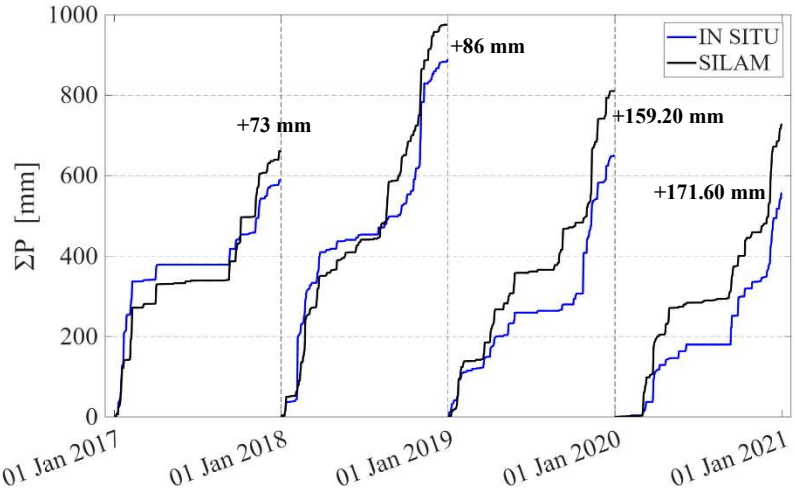

Figure 6.27 Cumulative precipitation depth (ΣP) retrieved by measured *in situ* SIAS weather station installed near the olive orchard and by the SILAM forecasting data in the period 2008-2011

The event-based comparison was also conducted using the same definition of rainfall events, where any day with precipitation greater than 0 mm was considered an event (**Figure 6.28**).

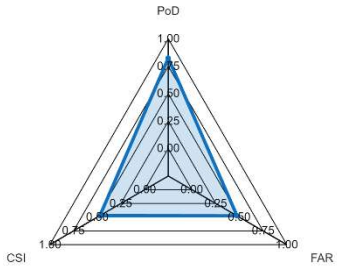

Figure 6.28 Event-based verification of daily precipitation occurrence from *in situ* observations against SILAM data

The results yielded a *PoD* of 0.83, indicating that 83 % of the observed rainfall events were correctly predicted by the forecast. *FAR* was 0.48, meaning that 48 % of the events predicted by the model did not actually occur. Finally, the *CSI* was 0.47, which accounts for both missed and false events and indicates that 47 % of all events (including hits, misses, and false alarms) were correctly forecast.

It is widely recognized that forecast rainfall data often require correction, as raw measurements (Feidas et al., 2007; Dong et al., 2023) or model-based estimates can contain biases, inaccuracies in event magnitude, or timing errors. However, for precision irrigation applications, which focus on irrigation scheduling and monitoring, such corrections are often unnecessary, particularly because attention is primarily directed toward dry periods when water management decisions are most critical.

6.4 Remote Sensing applications

6.4.1 DisTrad sharpening technique evaluation

In order to downscale Sentinel-2 Band 11 (SWIR) from 20 m to 10 m spatial resolution, the DisTrad sharpening technique was tested and evaluated. The method was assessed using eight fields within the irrigation district, characterized by different Fractional Vegetation Cover (*FVC*) types. To initialize the analysis, all Sentinel-2 images acquired during 2018 were used.

Initially, the correlation between the SWIR band and each of the four 10 m bands was evaluated (**Figure 6.29**). Considering the different spatial resolutions of the four 10 m bands (B02-BLUE, B03-GREEN, B04-RED, B08-NIR) and the SWIR band (20 m), the four

bands were aggregated to the coarser B11 resolution through linear averaging.

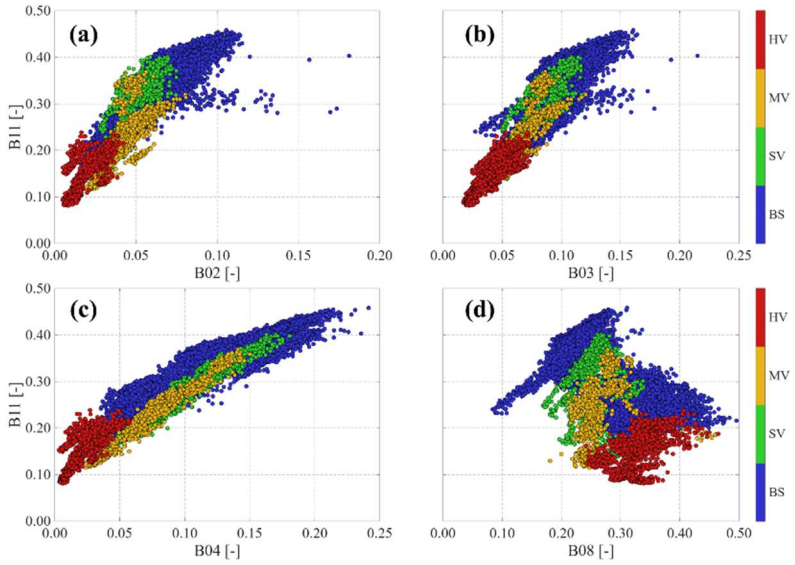

Figure 6.29 Comparison between: (a) BLUE band (B02) and SWIR band (B11); (b) GREEN band (B03) and SWIR band (B11); (c) RED band (B04) and SWIR band (B11); (d) NIR band and SWIR band (B11). All the bands are retrieved from Sentinel-2 twin satellites in 2018. The colorbar indicates the FVC types

As shown in **Figure 6.29**, the highest correlation was found between B04 and B11 through a linear interpolation, with an R^2 value of 0.90:

$$B11(B04_{20\,m}) = 1.60 \cdot B04_{20\,m} + 0.13 \quad \textbf{(6.1)}$$

The choice to analyze a full year of satellite images makes it possible to capture the entire range of reflectance values. This is further supported by the selection of orchards characterized by different *FVC* types, namely Bare Soil (BS), Sparsely Vegetated (SV), Moderately Vegetated (MV), and Highly Vegetated (HV). This behaviour is also confirmed in **Figure 6.30**, where data points are coloured according to their *NDVI* values.

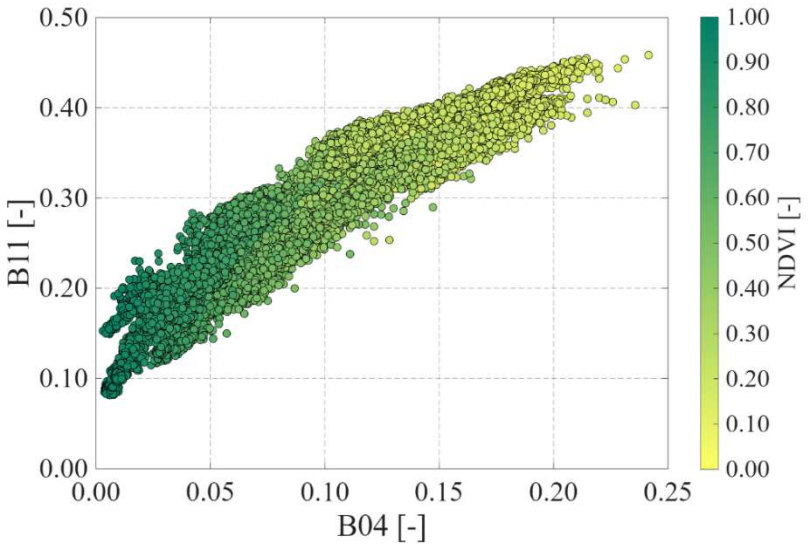

Figure 6.30 Comparison between RED band (B04) and SWIR band (B11). All the bands are retrieved from Sentinel-2 twin satellites in 2018. The colorbar indicates the NDVI

Finally, the remaining steps of the DisTrad sharpening technique formulation were completed:

$$B11_{10\,m} = B11(B04_{10\,m}) - \Delta B11_{20m} \quad \textbf{(6.2)}$$

where

$$B11(B04_{10\,m}) = 1.60 \cdot B04_{10\,m} + 0.13 \quad \textbf{(6.3)}$$

$$\Delta B11_{20m} = B11 - B11(B04_{20m}) \quad \textbf{(6.4)}$$

6.4.2 MODIS *vs* Sentinel-2

To train the ML model for the olive orchard (as shown in *6.6 Actual evapotranspiration machine learing modelled*), the ET_a time series from 2009 to 2011 was used. The trained model is then employed within the IRRILEARNING framework (introduced in *5.7 IRRILEARNING model* and described in detail in *6.8 IRRILEARNING applications*) to generate synthetic ET_a time series.

Since the training process requires VIs derived from satellite images, considering that the Copernicus Sentinel missions became

operational only in spring 2017, VIs used for model training were derived from MODIS images.

Then, the trained model was subsequently applied to generate synthetic actual evapotranspiration (ET_a) series for the period 2017–2020 within the IRRILEARNING application. But, within the framework of the model, to obtain ET_a time series at a finer spatial scale, the series are generated using VIs derived from Sentinel-2 images.

To justify this approach and ensure consistency between the training and application phases, a comparison between MODIS and Sentinel-2 reflectances (**Figure 6.31**) and VIs (**Figure 6.32**) was carried out for periods when data from both sensors were simultaneously available (2017-2020), inside the experimental olive orchard.

The Sentinel-2 reflectance values were obtained as the average of all pixels fully contained within a single MODIS pixel. Moreover, as previously described, a continuous time series from Sentinel-2 images was generated by applying linear interpolation between consecutive available acquisitions (blue line). Thus, the spectral bands used to compute the *NDVI* and *NDWI* were analyzed by comparing Sentinel-2 and MODIS data: Sentinel-2 B04 *vs* MODIS B1, Sentinel-2 B08 *vs* MODIS B2, and Sentinel-2 Band11 *vs* MODIS Band 6. In all cases, the resulting time series exhibit the same trend and seasonal behaviour.

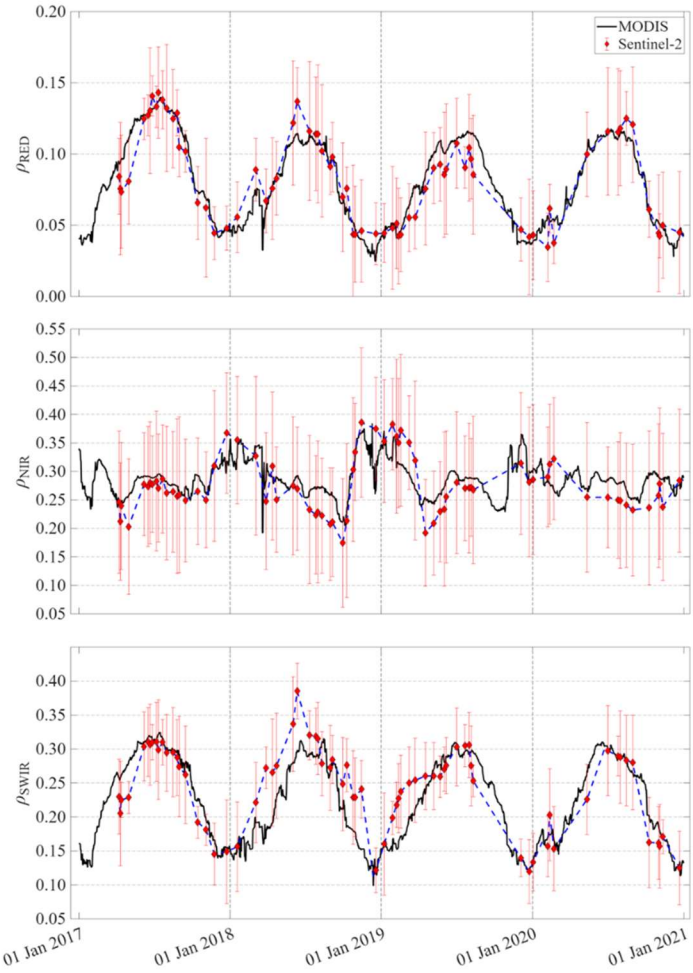

Figure 6.31 Temporal dynamic of RED, NIR and SWIR bands retrieved from Sentinel-2 (red dots and red line are the mean and the standard deviation obtained considering all the Sentinel-2 pixel which are entire contained in one MODIS pixel, respectively; the blue line is the linear interpolation between two available acquisitions) and MODIS (black line) in the period 2017-2020

After comparing the reflectance values, the *NDVI* and *NDWI* time series were finally analyzed and compared.

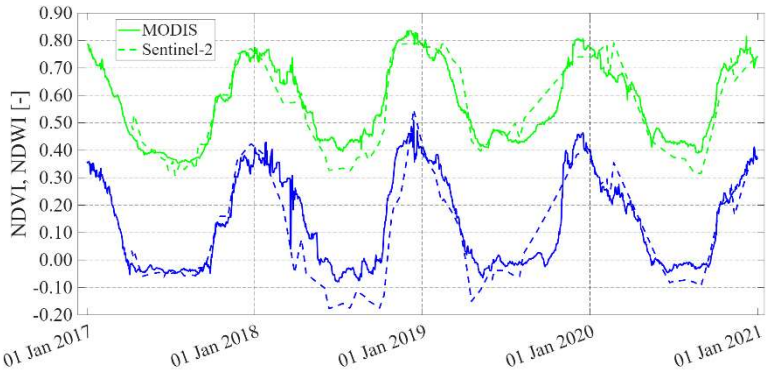

Figure 6.32 Temporal dynamic of NDVI and NDWI retrieved from Sentinel-2 (dashed line) and MODIS (solid line) in the period 2017-2020

The major differences between the two VIs are probably due to the presence of ground weeds that grow after rain events (Ippolito et al., 2023), which can be detected with the Sentinel-2 images and not with the MODIS ones. The generally good agreements between the *NDVI* and *NDWI* obtained from the two different platforms strongly depend on the homogeneity of soil and land characterizing the MODIS pixel (Autovino et al., 2016). Thus, the good agreement between the two curves allows us to conclude that *NDVI* and *NDWI* derived from MODIS can be reliably used to train the model for the period 2009–2011, while vegetation indices derived from Sentinel-2 can be used to generate synthetic time series using the trained model.

6.4.3 FVC retrieved from NDVI

Through the approaches and methods described in *6.4.1 FVC vs NDVI*, several linear functional relationships were derived to estimate *FVC* values from *NDVI* values obtained from different satellite platforms. **Table 6.5** reports the pixel numbers used for the analysis for each plot. The product differences are associated with spatial resolution.

Table 6.5 Number of pixel for each plot for each satellite: (a) olive orchards and, (b) citrus orchards

(a)	n° pixel [-]		
ID	**Sentinel-2**	**Landsat-8**	**PlanetScope**
1	28	1	395
2	25	1	340
3	25	1	353
4	32	1	439
5	35	1	457
6	19	-	295
7	62	4	748
8	29	1	384
9	48	3	639
10	51	2	666
11	11	-	178
12	26	-	416
13	50	-	695
14	18	-	305
15	16	-	238
16	34	1	471
17	58	3	735
18	26	1	351
19	33	1	418
20	27	2	389
21	37	2	516
22	32	-	459
23	27	-	432
24	40	2	523
25	33	-	442

(b) ID	n° pixel [-] Sentinel-2
1	7
2	9
3	8
4	7
5	4
6	10
7	9
8	8
9	10
10	2
11	9
12	2
13	3
14	9
15	11

6.4.3.1 Field scale approach and "precise" method

The combination of the field scale approach and the precise method was tested within the irrigation district using three satellite products: Sentinel-2, Landsat-8, and PlanetScope (**Figure 6.33**). Conversely, in the citrus orchard and in a few additional fields located in the same area, the analysis was conducted using only the Sentinel-2 product **(Figure 6.34**).

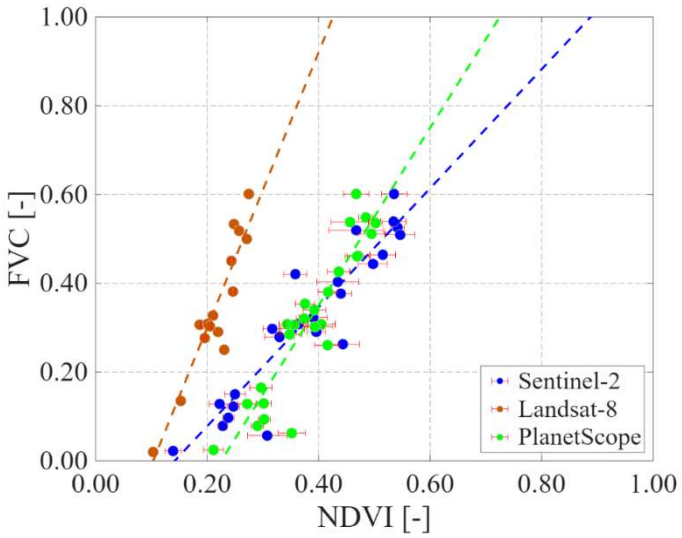

Figure 6.33 Comparison between mean NDVI (red lines indicates the standard deviation) and FVC, obtained with the precise method, in the olive orchards. The dashed lines indicate the interpolating lines

By analyzing the correlations obtained within the irrigation district, it can be stated that all the considered satellite products are able to reproduce *FVC* values accurately (**Table 6.5**).

Table 6.6 Slope, intercept and correlation coefficient values of the linear functional relationship between NDVI and FVC in the olive orchards

	Slope	**Intercept**	**R^2**
Sentinel-2	1.34	-0.19	0.86
Landsat-8	3.10	-0.32	0.86
PlanetScope	2.00	-0.45	0.85

Also in the citrus orchards, the correlation proved to be very strong (**Figure 6.34**), with a slope coefficient equal to 1.71 and an intercept equal to −0.25 and R^2 equal to 0.76.

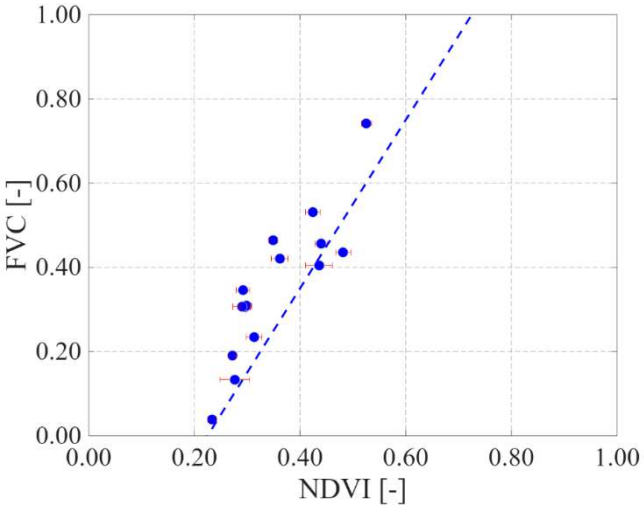

Figure 6.34 Comparison between mean NDVI (red lines indicates the standard deviation) and FVC in the citrus orchards. The dashed line indicates the interpolating line

6.4.3.2 Pixel wise approach and precise method

This combination shows that, even when adopting a pixel-wise approach, the Sentinel-2 and Landsat-8 sensors continue to produce good correlations (**Figure 6.35**), with slope (1.26 for Sentinel-2 and 3.17 for Landsat-8) and intercept (-0.15 for Sentinel-2 and -0.31 for Landsat-8) values consistent with those obtained using the previous combination. Conversely, the PlanetScope product does not preserve the same level of correlation. **Figure 6.35** illustrates the relationship between *NDVI* and *FVC* for a representative field; a similar pattern was observed for all the other fields.

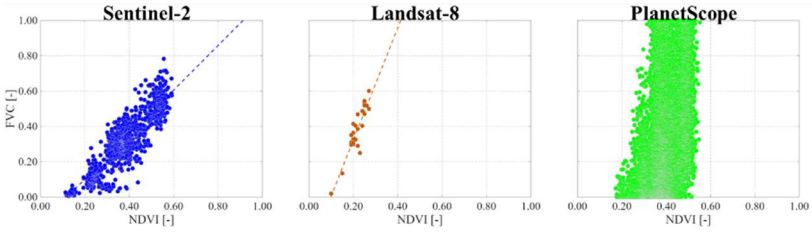

Figure 6.35 Comparison between pixel wised NDVI and FVC, obtained with the precise method, in the olive orchards. The dashed lines indicate the interpolating lines

Figure 6.35 shows that in the PlanetScope pixel-by-pixel analysis there is no relationship between the *NDVI* and the corresponding *FVC* values. This result, probably, is obtained because a cubic convolution kernel was applied to resample the images in the georeferencing process.

To support the results obtained for the Planet pixel-by-pixel analysis, the same experiment was conducted using the image acquired by the multispectral camera. The original spatial resolution of the image was 0.12 cm. Through a pixel aggregation, the new resolution (3 m) became similar to the PlanetScope one. The results were completely different (**Figure 6.36**).

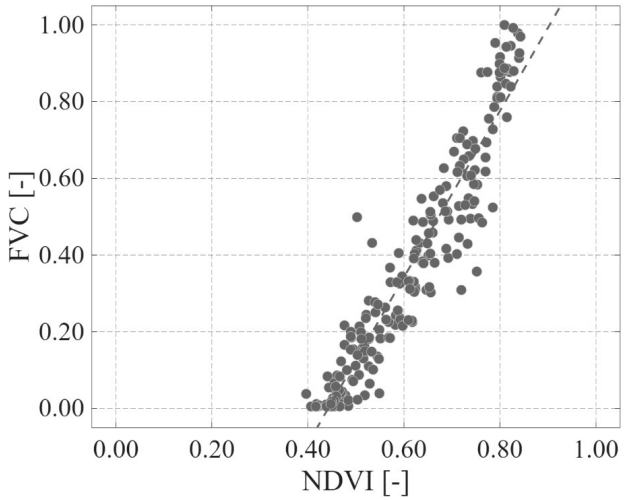

Figure 6.36 Comparison between pixel wised NDVI and FVC, obtained with the precise method, using aggregated multispectral camera image. The dashed line indicates the interpolating line

There is a good agreement between the *NDVI* and *FVC* values (slope equal to 2.17 and intercept equal to -0.96). R^2 equal to 0.90 confirms that the two variables are highly correlated.

The analysis conducted in the citrus orchards resulted in a correlation characterized by an R^2 value of 0.64, a slope of 1.42, and an intercept of −0.16 (**Figure 6.37**). These latter coefficients are slightly different from those obtained with the previous combination.

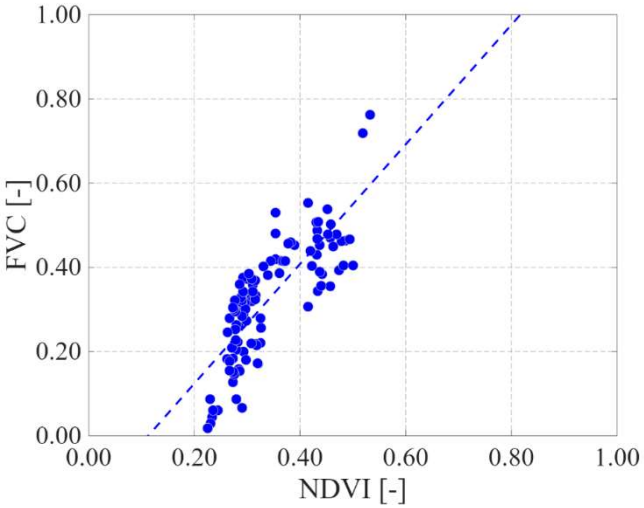

Figure 6.37 Comparison between pixel wised NDVI and FVC in the citrus orchards. The dashed line indicates the interpolating line

These differences could be ascribed to the presence of weeds along the rows in the citrus fields. Such discrepancies are not observed in the olive orchards, where weed control is a common management practice.

6.4.3.3 Field scale approach and swift method

Finally, the last combination, applied in the olive orchards, in which only 25% of the trees were vectorized, produced results similar to the two previous combinations, with a slope of 1.34, an intercept of −0.20, and an R^2 of 0.86 (**Figure 6.38**).

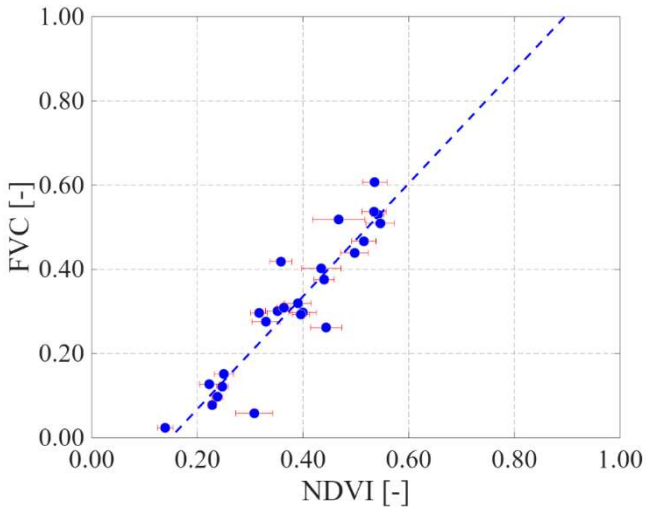

Figure 6.38 Comparison between mean NDVI (red lines indicates the standard deviation) and FVC, obtained with the swifth method, in the citrus orchards. The dashed line indicates the interpolating line

This result confirms that it is not necessary to vectorize all the trees within the areas of interest, and that this simplification does not lead to a loss of performance in the linear functional relationship.

6.5 Actual evapotranspiration modelling at the citrus orchard

This section presents the results of ET_a modelling carried out in the citrus orchard. Both soil water balance and surface energy balance models are applied, making use of remote sensing data as input to enable a distributed approach over the study area. The performance of these models is evaluated and discussed. Additionally, results from models based on the analysis of CO_2 fluxes are also presented and compared. Approaches outputs were validated against *in situ* observations to quantify their accuracy.

6.5.1 Remote Sensing data input

As discussed in *4 Actual Evapotranspiration Modelling* and *Chapter 6 Methods*, RS data used as inputs in the ET_a estimation models allow the transition from the classical point scale to a distributed scale. For the application of the models in the experimental citrus orchard, VIs (*NDVI* from Sentinel-2 and Landsat-8/9 and *NDWI*

from Sentinel-2), α (from Landsat-8/9), and *LST* (from Landsat-8/9) were retrieved.

The temporal dynamic of the examined VIs for the citrus orchard, is shown in **Figure 6.39** . For both the VIs, the annual trends resulted quite similar, with values in winter generally higher than in summer.

In summer, the *NDVI* and *NDWI* values were around 0.55 and 0.10, respectively, which resulted lower than in winter when the values fluctuated around 0.90 and 0.45. On the other hand, the trend tended to decrease in spring (March-May) and to increase in fall. The Sentinel-2 intra-field variability for both VIs resulted quite limited, with values of standard deviation ranging between 0 and a maximum of 0.13 for *NDVI* and from 0 and 0.11 for *NDWI*.

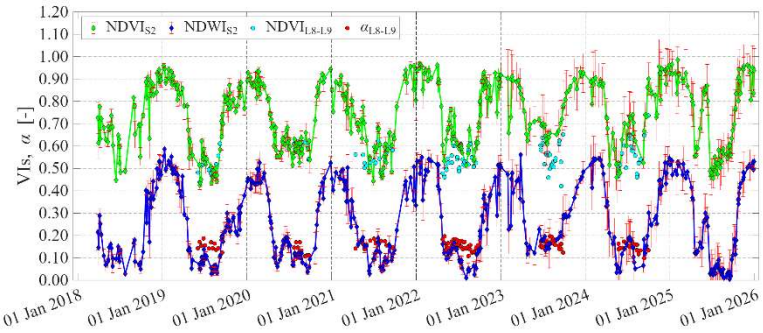

Figure 6.39 Temporal dynamic, in the period 2018-2025, of: Sentinel-2 NDVI ($NDVI_{S2}$) (green dots are acquisitions and green line is the linear interpolation); Sentinel-2 NDWI ($NDWI_{S2}$) (blue dots are acquisitions and blue line is the linear interpolation); Landsat-8/-9 NDVI ($NDVI_{L8-L9}$) (cyan dots); Landsat-8/-9 albedo (α_{L8-L9});

By inverting the Stefan-Boltzmann equation, it was possible to compare the *LST* measured by the net radiometer inside the field of view with the *LST* derived from Landsat-8/9 for all available acquisition dates (**Figure 6.40**).

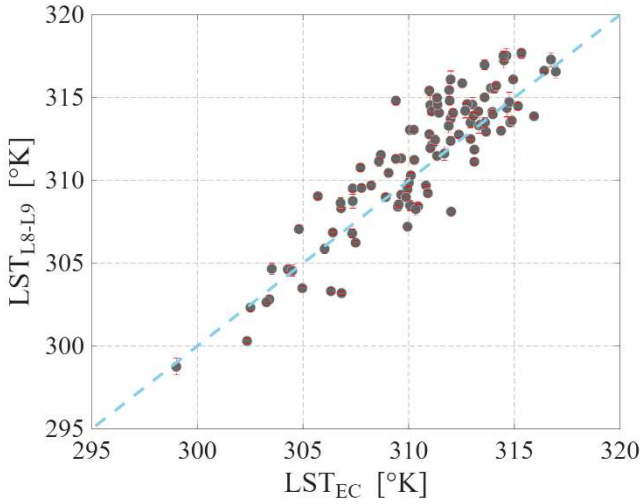

Figure 6.40 Comparison between LST measured by the EC tower, in the net radiometer field of view, and the LST from Landsat-8/-9 (values are the mean of nine pixel, otherwise the red line are the standard deviations) ; the dashed light blue line is the 1:1 lines (perfect match)

The *LST* derived from the average of the nine Landsat pixels shows good agreement with the measurements from the net radiometer within the field of view (*RMSE* = 1.99 °K, *MBE* = 0.73 °K, *MAE* = 1.57 °K, R^2 = 0.80, *b* = 1.00, $R^2[b]$ = 0.99, *NSE* = 0.71). Its variability is also very limited, with a maximum standard deviation of 0.60 °K.

6.5.2 Soil Plant Atmosphere and Remote Sensing Evapotranspiration (SPARSE) output

Both in-series and in-parallel resistance networks schemes were implemented; outcomes highlighted that best performances were achieved using the latter scheme; thus, outcomes of the in-parallel scheme are hereinafter shown exclusively.

SPARSE performance was evaluated considering all the irrigation seasons. SPARSE best performance for *LE* (sum of LE_s and LE_v) was obtained using 1-combination with *RMSE* equal to 53 W m^{-2} when considering all *in situ* data (**Figure 6.41** and

Table 6.7).

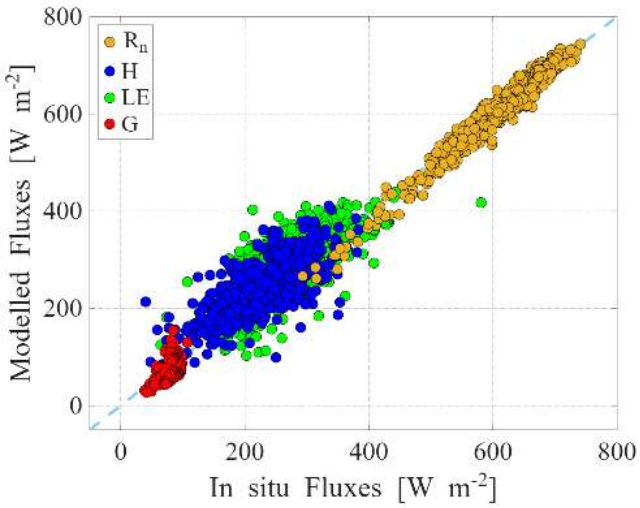

Figure 6.41 Scatterplots of instantaneous *in situ* versus 1-combination SPARSE modelled energy fluxes for 2019-2025 irrigation seasons; the dashed light blue line is the 1:1 lines (perfect match)

Table 6.7 Statistical indices associated to instantaneous *in situ* versus 1-combination SPARSE modelled energy fluxes for 2019-2025 irrigation seasons

1	***RMSE***	***MBE***	***MAE***	***R^2***	***b***	***R^2/b***	***NSE***
	[W m^{-2}]			[-]			
R_n	18	-2	14	0.96	0.99	0.99	0.94
H	45	16	36	0.53	1.05	0.97	0.40
LE	53	20	43	0.47	1.06	0.97	0.21
G_0	15	-6	13	0.29	0.92	0.97	-1.42

This value remains unchanged when only data acquired contextually to satellite observations are considered in the performance evaluation (**Figure 6.42** and **Table 6.8**).

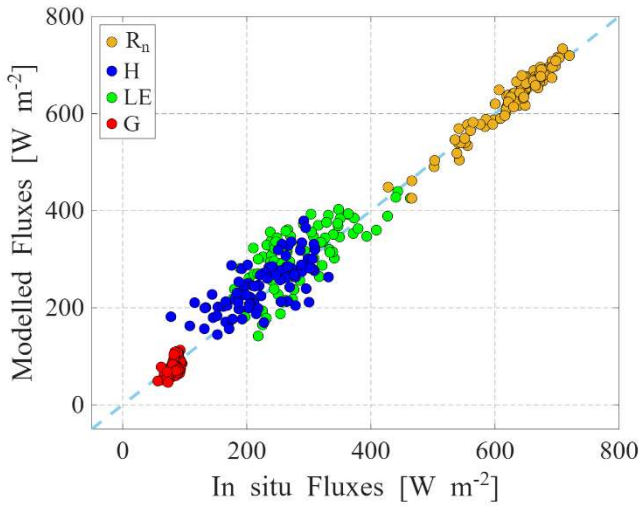

Figure 6.42 Scatterplots of instantaneous *in situ* versus 1-combination SPARSE modelled energy fluxes for 2019-2025 irrigation seasons, only when data are acquired contextually to satellite observations; the dashed light blue line is the 1:1 lines (perfect match)

Table 6.8 Statistical indices associated to instantaneous *in situ* versus 1-combination SPARSE modelled energy fluxes for 2019-2025 irrigation seasons, only when data are acquired contextually to satellite observations

1	***RMSE***	***MBE***	***MAE***	***R²***	***b***	***R²/b|***	***NSE***
	[W m^{-2}]			[-]			
Rn	16	2	12	0.94	1.00	1.00	0.93
H	45	20	36	0.52	1.07	0.97	0.36
LE	53	21	44	0.50	1.06	0.97	0.28
G0	14	-6	12	0.21	0.92	0.97	-2.34

Considering combination-2, the worst *RMSE* was achieved for *LE* which is ~60 W m-² (~10% of the maximum *LE*). Whereas best *RMSE* values were achieved for R_n and G_0, with *RMSE* values of ~20 and ~15 W m^{-2}, respectively. Finally, *RMSE* for *H* is slightly less than that achieved for *LE* (~50 W m^{-2}). *MBE* values analysis further confirms that R_n is well simulated by the model, ~0 W m-². In contrast, *H* and *LE* tend to be overestimated, ~2 W m-² and ~40 W m-², respectively; while G_0) is underestimated, ~5 W m-² (**Table 6.9**).

Table 6.9 Statistical indices associated to instantaneous *in situ* versus 2-combination SPARSE modelled energy fluxes for 2019-2025 irrigation seasons, only when data are acquired contextually to satellite observations

2	***RMSE***	***MBE***	***MAE***	R^2	***b***	R^2/b	***NSE***
	[W m^{-2}]			[-]			
R_n	19	0	15	0.88	0.99	0.99	0.88
H	48	2	37	0.47	0.99	0.96	0.34
LE	66	39	54	0.41	1.11	0.97	0.03
G_0	15	-5	13	0.06	0.93	0.97	-3.42

These very encouraging metrics and the *in situ* vs modelled scatterplot demonstrate the agreement of modelled fluxes using SPARSE. It is to point out that data points are tightly clustered around the 1:1 (**Figure 6.43**).

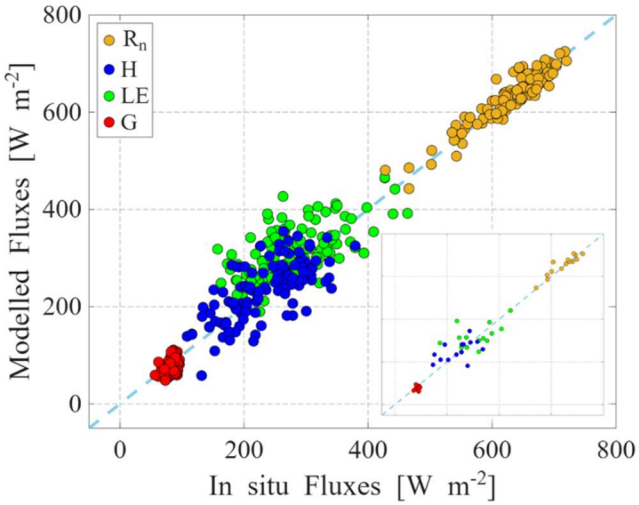

Figure 6.43 Scatterplots of instantaneous *in situ* versus 2-combination SPARSE modelled energy fluxes for 2019-2025 irrigation seasons; the insert scatterplot shows the instantaneous *in situ* versus 2-combination SPARSE modelled energy fluxes only for 2021 irrigation season; the dashed light blue lines are the 1:1 lines (perfect match)

The observed vs modelled scatterplot clearly evidence that SPARSE fluxes well agree with the *in situ* ones especially for which concerning R_n (R^2 ~0.88). Whereas, latent (R^2 ~0.41) and sensible (R^2

~0.47) heat fluxes are reasonably well modelled even if points are slightly scattered around the 1:1 line. This behaviour, agreeing with other studies (Mwangi et al., 2022), suggests a moderate degree of uncertainty in the simulating turbulent fluxes. Finally, although G_0 is modelled with less accuracy (R^2 ~0.06), due to its very limited range of variability and magnitude, it slightly contributes to the final *LE* assessment, at daily scale. Noticeably that, the overall scatterplot is characterized by very limited dispersion around the 1:1 line. This behaviour associated with the absence of significant bias, suggests that the model provides encouragingly accurate estimates of all four instantaneous components of the surface energy balance. Moreover, based on the scatterplot (**Figure 6.43**) and the accuracy metrics analysis, it can be concluded that the model can capture the contribution of weeds. This is further supported by the fact that the 2021 data, when weed presence was significant, did not behave differently from the other years (insert scatterplot) (**Figure 6.43**). Results of the SPARSE model demonstrate that the use of satellite data for the instantaneous estimation of energy balance components, inside a citrus orchard, is both feasible and reliable, providing spatially distributed *LE*. Also, this method is valuable for applications requiring large-scale assessments. The results are consistent with those obtained by Boulet et al. (2015), where SPARSE was evaluated over both irrigated and rainfed wheat (homogeneous crop), demonstrating that the model can also be effectively applied to estimate instantaneous energy fluxes in orchards (sparse crop). Moreover, achieved results agree with those reported by other authors who have implemented the TSEB model (Anderson et al., 2005; Yang et al., 2017; Burchard-Levine et al., 2022; Volk et al., 2024; Cammalleri et al., 2010, 2012a, 2024, 2025). Daily transpiration assessed from SPARSE vegetation *LE*, for combination-2, well agrees with that *in situ* measured through the sap flow probes in 2019 irrigation season (**Figure 6.44**).

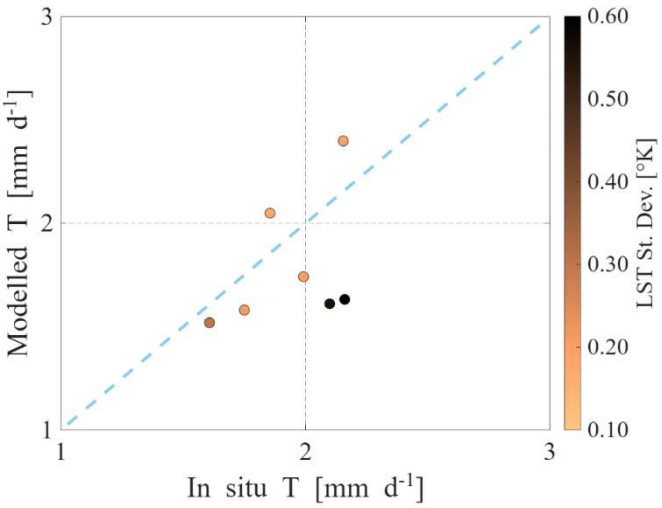

Figure 6.44 Scatterplots of daily *in situ* versus 2-combination SPARSE modelled T for 2019 irrigation season. Colorbar shows the nine LST pixels standard deviation retrieved from Landsat-8 satellite images; the dashed light blue line is the 1:1 lines (perfect match)

Noticeably, the dates with the largest differences are the ones characterized by the higher *LST* spatial standard deviation (*LST St. Dev.*, computed over nine pixels) inside the study area due to the greenhouse covering the neighbour crop (vineyard) contextually to two of the satellite acquisitions. A slight underestimation is found by considering the whole period (*MBE* equal to −0.16 mm d^{-1}), whereas, *MBE* equal to -0.01 mm d^{-1} is found if only dates with *LST St. Dev.* < 0.55 °K are considered. The *RMSE* value is equal to 0.32 and 0.20 mm d^{-1} for the whole period and for the selected days, respectively. These outcomes, especially those achieved for the selected days, are particularly encouraging also considering that the instantaneous to daily scaling technique is applied. Moreover, it can be concluded that the errors associated with transpiration are primarily due to the presence of the greenhouse, rather than to the weeds potential contribution. Finally, it needs to be highlighted that a good agreement with *in situ* measures was achieved in a small study area, if compared to the real spatial resolution of the Landsat thermal infrared acquisitions.

Before assessing combination 3, the hourly meteorological variables, required for model implementation, derived from the ERA5-Land product, were compared with those measured by the EC tower (R_s, $T_{a\text{-}Mean}$, and U_2) and by the standard weather station (WD) (RH_{Mean}) (**Figure 6.45** and **Table 6.10**)

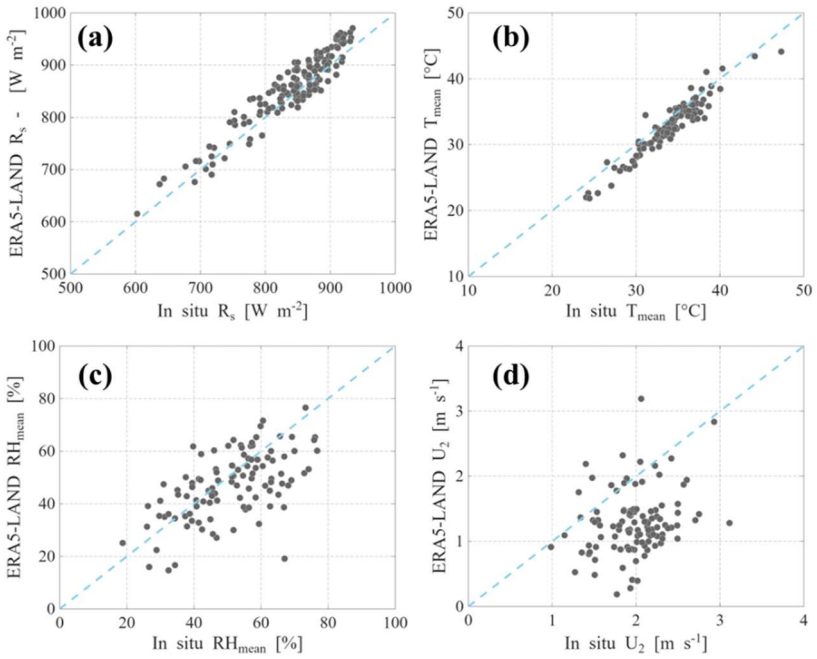

Figure 6.45 Comparison between hourly: (a) global solar radiation (R_s), (b) mean air temperature ($T_{a\text{-}Mean}$), (c) mean relatve air humidity (RH_{Mean}) and, wind speed measure at 2 m from the ground (U_2) measured by the *in situ* weather station installed near the citrus orchard or *in situ* EC tower inside the citrus orchard and retrieved by the ERA5-LAND reanalysis data, only when data are acquired contextually to satellite observations; the dashed light blue lines are the 1:1 lines (perfect match)

Table 6.10 Statistical indices for global solar radiation (Rs), mean air temperature (Ta-Mean), mean relatve air humidity (RHMean) and, wind speed measure at 2 m from the ground (U_2)

	RMSE	***MBE***	***MAE***	***R^2***	***b***	***R^2[b]***	***NSE***
R_s		[W m^{-2}]				[-]	
	26.22	11.41	21.67	0.88	1.01	0.99	0.84
$T_{a\text{-}Mean}$		[°C]				[-]	
	1.77	-1.24	1.50	0.91	0.96	0.99	0.77
RH_{Mean}		[%]				[-]	
	11.82	-3.39	9.19	0.37	0.91	0.95	0.16
U_2		[m s^{-}				[-]	
	0.87	-0.69	0.76	0.08	0.64	0.88	-4.42

The results are consistent with those presented in *6.2 Reanalysis data accuracy* at *6.2.2 Citrus orchard*, where the comparison was conducted at the daily scale.

Consequently, SPARSE was applied using the reanalysis data as meteorological input variables (**Figure 6.46** and **Table 6.11**).

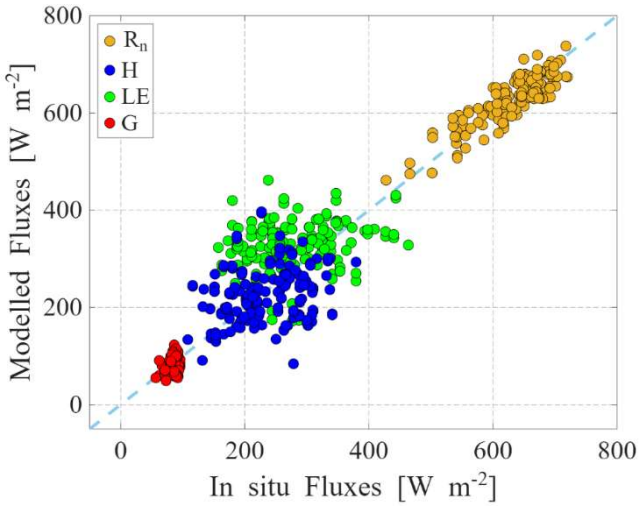

Figure 6.46 Scatterplots of instantaneous *in situ* versus 3-combination SPARSE modelled energy fluxes for 2019-2025 irrigation seasons; the dashed light blue line is the 1:1 lines (perfect match)

Table 6.11 Statistical indices associated to instantaneous *in situ* versus 3-combination SPARSE modelled energy fluxes for 2019-2025 irrigation seasons

1	*RMSE*	*MBE*	*MAE*	R^2	*b*	$R^2[b]$	*NSE*
	[W m^{-2}]			[-]			
R_n	27	-3	22	0.75	0.99	0.99	0.75
H	69	-8	53	0.09	0.93	0.92	-0.38
LE	87	46	72	0.06	1.11	0.94	-0.69
G_0	16	-6	14	0.03	0.93	0.97	-4.09

Unlike the previous combinations, the statistical metrics show a degradation in performance. This deterioration can be attributed to a poorer estimation of R_n, which represents the driving energy for evapotranspiration processes.

6.5.3 SAtellite Montoring for IRrigation (SAMIR) output

6.5.3.1 Results of Mode-a in combination 1 and 2

Soil Water Content. The SWC was well modeled by both combinations (Combination-1a (**Table 6.12**) and Combination-2a (**Table 6.13**)) with some discrepancies observed between the two combinations due to the different distribution of rainfall throughout the irrigation seasons (**Figure 6.47**).

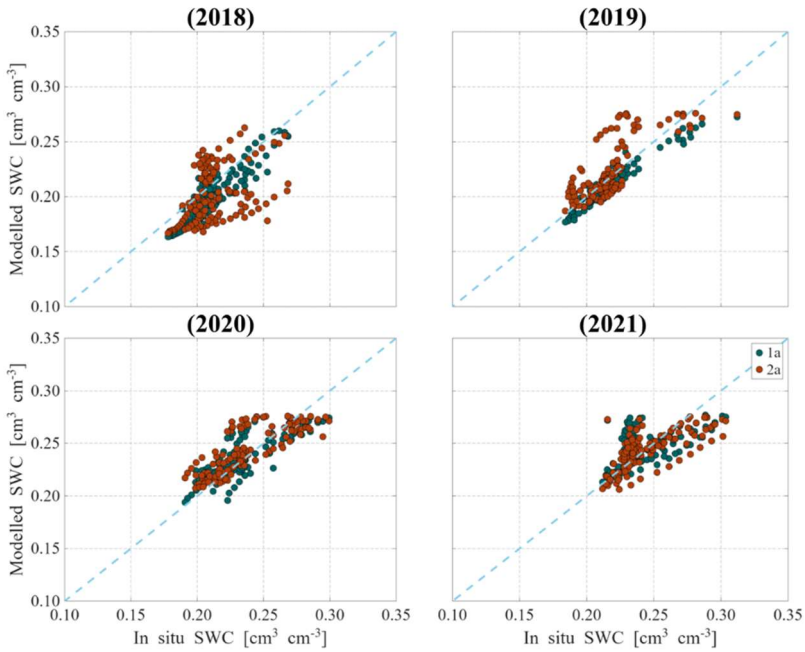

Figure 6.47 Comparison between daily *in situ* soil water content and obtained from SAMIR with two combinations (1a dark green dots; 2a orange dots); the dashed light blue lines are the 1:1 lines (perfect match)

Table 6.12 Statistical indices associated to daily *in situ* versus 1a SAMIR modelled SWC for 2019-2025 irrigation seasons

SWC	***RMSE***	***MBE***	***MAE***	***R^2***	***b***	***R^2[b]***	***NSE***
1a	[cm^3 cm^{-3}]			[-]			
2018	0.01	-0.01	0.01	0.82	0.95	0.99	0.44
2019	0.01	-0.01	0.01	0.89	0.97	0.99	0.80
2020	0.01	0.01	0.01	0.70	1.00	0.99	0.70
2021	0.02	0.01	0.02	0.33	1.01	0.99	0.28

Table 6.13 Statistical indices associated to daily *in situ* versus 2a SAMIR modelled SWC for 2019-2025 irrigation seasons

SWC	***RMSE***	***MBE***	***MAE***	***R^2***	***b***	***R^2[b]***	***NSE***
2a	[cm^3 cm^{-3}]			[-]			
2018	0.03	-0.01	0.02	0.16	0.95	0.99	-0.85
2019	0.02	0.01	0.01	0.58	1.02	0.99	0.40
2020	0.02	0.01	0.01	0.67	1.02	0.99	0.63
2021	0.02	0.01	0.01	0.48	0.99	0.99	0.48

Actual Evapotranspiration. The comparison in terms of ET_a shows that SAMIR accurately estimated ET_a except for the 2021 irrigation season due to the presence of weeds resulting from a lack of field maintenance by the farmer (**Figure 6.48, Table 6.14, Table 6.15**).

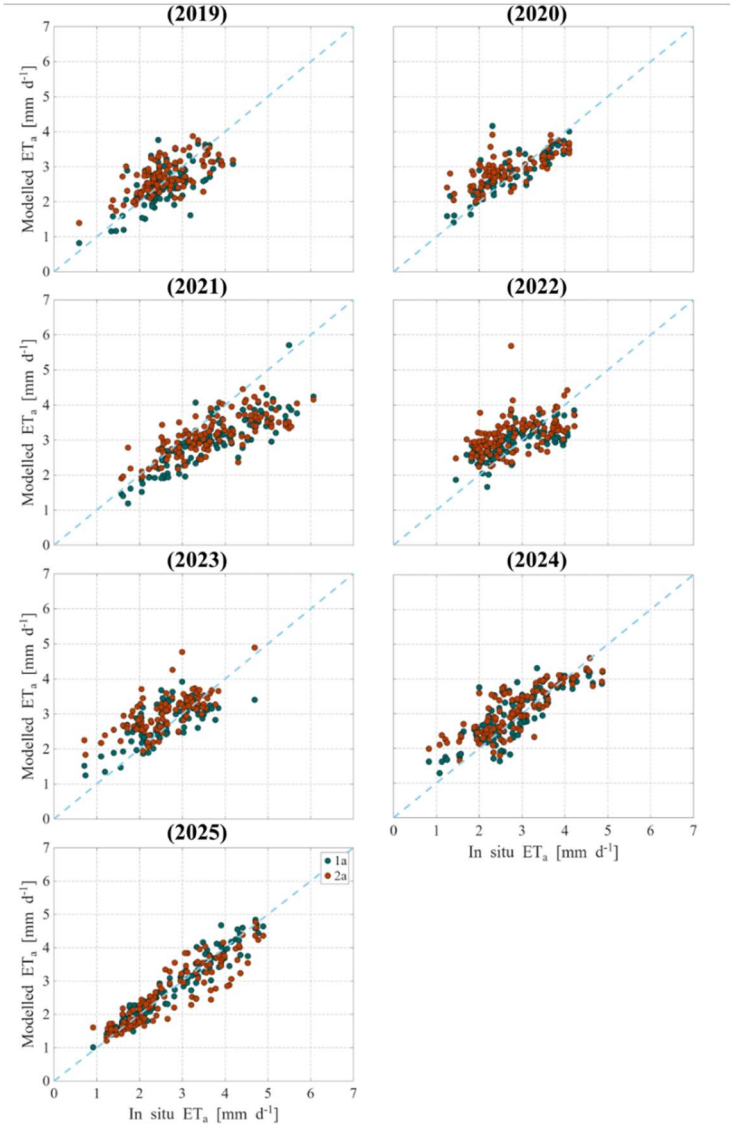

Figure 6.48 Comparison between daily *in situ* actual evapotranspiration and obtained from SAMIR with two combinations (1a dark green dots; 2a orange dots); the dashed light blue lines are the 1:1 lines (perfect match)

Table 6.14 Statistical indices associated to daily *in situ* versus 1a SAMIR modelled ET_a for 2019-2025 irrigation seasons

ET_a	***RMSE***	***MBE***	***MAE***	***R^2***	***b***	***R^2[b]***	***NSE***
1a	[cm^3 cm^{-3}]			[-]			
2019	0.47	-0.08	0.35	0.46	0.95	0.97	0.39
2020	0.43	0.12	0.33	0.67	1.02	0.98	0.64
2021	0.87	-0.68	0.71	0.71	0.80	0.98	0.21
2022	0.51	0.10	0.43	0.51	1.00	0.97	0.47
2023	0.54	0.19	0.44	0.51	1.04	0.97	0.43
2024	0.51	0.13	0.42	0.66	1.02	0.97	0.62
2025	0.27	0.04	0.21	0.94	1.00	0.99	0.93

Table 6.15 Statistical indices associated to daily *in situ* versus 2a SAMIR modelled ET_a for 2019-2025 irrigation seasons

ET_a	***RMSE***	***MBE***	***MAE***	***R^2***	***b***	***R^2[b]***	***NSE***
2a	[cm^3 cm^{-3}]			[-]			
2019	0.47	0.10	0.37	0.42	1.01	0.97	0.38
2020	0.56	0.24	0.45	0.53	1.05	0.97	0.40
2021	0.85	-0.54	0.65	0.57	0.83	0.97	0.24
2022	0.70	0.34	0.58	0.25	1.08	0.96	-
2023	0.66	0.42	0.51	0.50	1.12	0.97	0.14
2024	0.54	0.24	0.41	0.66	1.05	0.97	0.58
2025	0.44	-0.09	0.33	0.83	0.95	0.98	0.82

Transpiration. The comparison in terms of *T*, highlights that SAMIR provided accurate estimations using both combinations. It was conducted exclusively for the 2018-2019 irrigation seasons (due to data availability) (**Figure 6.49, Table 6.16, Table 6.17**).

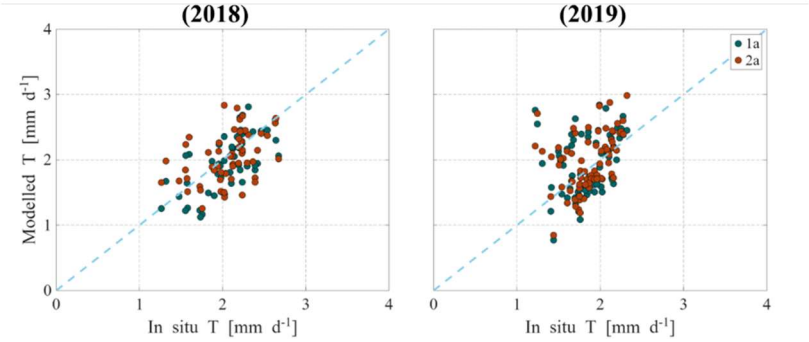

Figure 6.49 Comparison between daily *in situ* transpiration and obtained from SAMIR with two combinations (1a dark green dots; 2a orange dots); the dashed light blue lines are the 1:1 lines (perfect match)

Table 6.16 Statistical indices associated to daily *in situ* versus 1a SAMIR modelled T for 2019-2025 irrigation seasons

T	***RMSE***	***MBE***	***MAE***	***R^2***	***b***	***R^2/b/***	***NSE***
1a	[cm^3 cm^{-3}]			[-]			
2018	0.33	-0.10	0.27	0.43	0.95	0.98	-0.10
2019	0.45	0.05	0.36	0.08	1.02	0.95	-2.11

Table 6.17 Statistical indices associated to daily *in situ* versus 2a SAMIR modelled T for 2019-2025 irrigation seasons

T	***RMSE***	***MBE***	***MAE***	***R^2***	***b***	***R^2/b/***	***NSE***
2a	[cm^3 cm^{-3}]			[-]			
2018	0.37	-0.03	0.29	0.19	0.97	0.97	-0.38
2019	0.42	0.09	0.32	0.15	1.04	0.96	-1.65

SAMIR outcomes must be discussed in the framework of the recent literature, concerning the same test site. In Ippolito et al. (2023), ET_a was estimated only for three irrigation seasons (2018-2020) using an approach based on the citrus crop coefficient (K_c) derived from a combination of two vegetation indices (*NDVI* and *NDWI*). The results were very promising and comparable to those obtained in this study. However, the relationship used in their approach was site specific (calibrated exclusively for this specific crop); thus, limiting its applicability to other agricultural systems.

Differently, SAMIR, even if applied employing the default parameterizations to retrieve K_{cb} and *FVC* from *NDVI* (Saadi et al., 2015), achieved high performances, making it highly flexible and suitable for a wide range of crop types. Moreover, in Ippolito et al. (2023) *SWC* was estimated using the single crop coefficient FAO-56 approach (Allen et al., 1998), achieving very good results comparable to those obtained in the present work. As previously highlighted, SAMIR overcomes the problem of the site-specific model calibration; moreover, SAMIR allows separating *T* and *E* dynamics.

More recently, De Caro et al. (2023) developed a machine learning model for ET_a estimations. As in this case, results were comparable to those obtained in the present study. However, again, this model is site specific (*i.e.*, trained using *in situ* data); thus, its applicability to other fields or different environmental conditions is not guaranteed.

6.5.3.2 Mode-a *vs* Mode-b both in combination 1

In terms of cumulative irrigation volumes (ΣI) (**Figure 6.50a**) and actual evapotranspiration (ΣET_a) (**Figure 6.50b**) the comparison between the two combinations allows analysing the irrigation management strategy of the farmer. Indeed, in terms of cumulative irrigation, higher irrigation volumes were simulated in 2018, 2019 and 2025 by the model using a ruled irrigation scheme (Mode-b). This suggests that the farmer seems to limit the irrigation volumes applied during those years. On the contrary, the farmer provided more irrigation volumes than SAMIR rules in the period 2020-2024; meaning that, simply based on the ruled irrigation which only accounts for the *SWC* values, the farmer over-irrigated the field. Consequently, 2018, 2019 and 2025 irrigation seasons show that ET_a from Mode-a (farmer irrigation) are lower than those resulting from Mode-b (ruled irrigation). Noticeably, that the access to the water resource from the irrigation consortium is scheduled. Also, the farmer often supplies irrigation volumes based on his experience/convictions about his own crop. For instance, the 2018 irrigation season was very humid and rainy; consequently, the farmer was expecting that less irrigation volumes were enough to restore the crop needs incorrectly. It is likewise noteworthy that another example of discrepancy is the

2021 irrigation season in which the field was covered by weeds. In particular, the farmer increased the irrigation volumes to compensate for the increased water demanding caused by weeds and to protect the fruits during a very hot irrigation season. In this case, discrepancies in terms of both I and ET_a are due to the model setup which did not account for the presence of the citrus plus weeds vegetation cover.

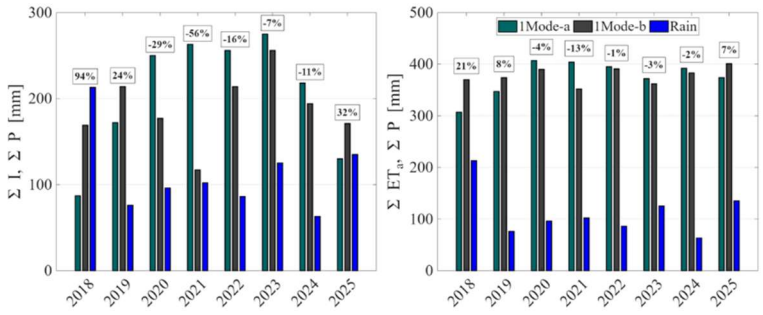

Figure 6.50 (a) Irrigation seasons cumulative I, for both modes, and P; (b) Irrigation seasons cumulative ETa, for both modes, and P. Dark green bars are referred to Mode-a, black bars to Mode-b, while blue bares are referred to precipitation depth.

6.5.4 NDVI-Cws method output

For the implementation of the NDVI–Cws method, *FVC* values were obtained by applying the linear relationship developed in *5.4 FVC vs NDVI*, while K_c values were derived using the functional relationship proposed by Ippolito et al. (2023):

$$K_c = 0.304 \cdot e^{0.939 \cdot (NDVI + NDWI)} \quad \textbf{(6.5)}$$

As indicated by Maselli et al. (2019, 2014), the time window was set to 60 days (TW=60).

The results obtained, considering the simplicity of the model, indicate that it produces good performance (**Figure 6.51**). Unlike more complex models, it requires knowledge of far fewer parameters. However, it should be noted that information on *FVC*, K_c, meteorological variables, precipitation depth, and a good understanding of the irrigation schedule is still necessary.

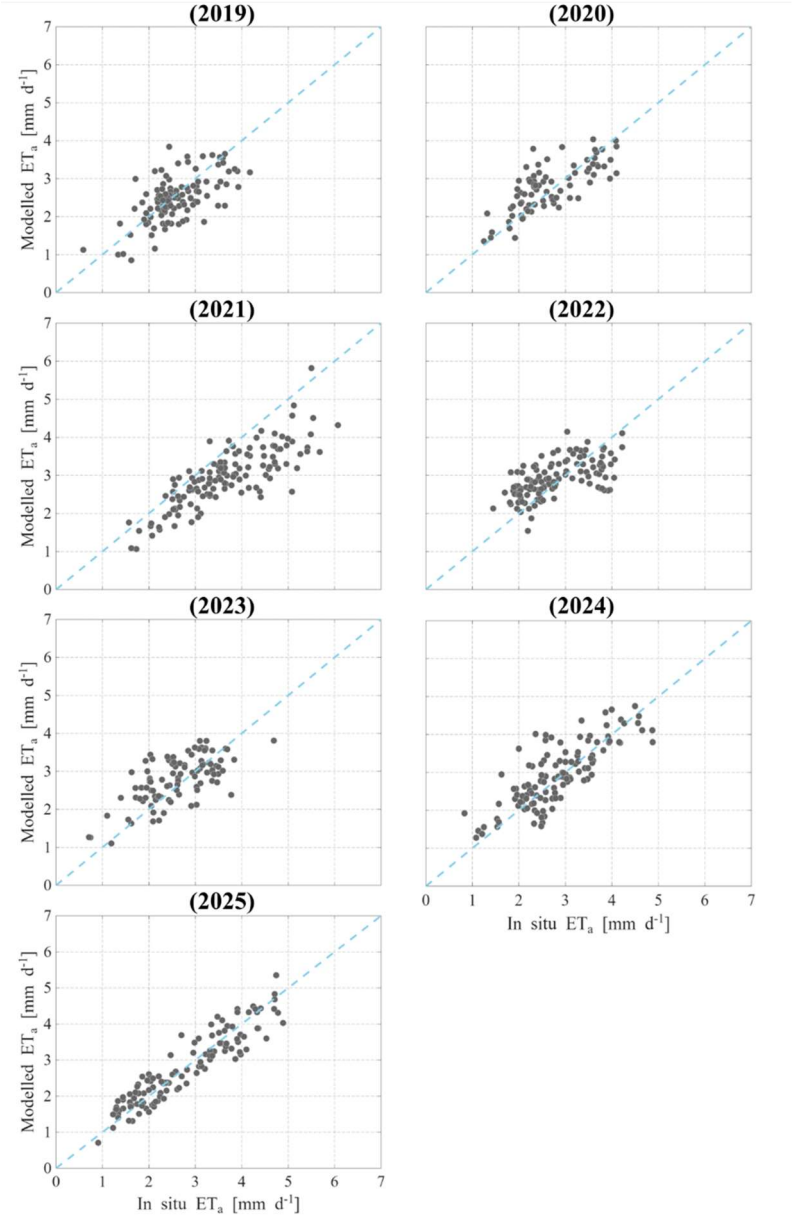

Figure 6.51 Comparison between daily *in situ* actual evapotranspiration and obtained from NDVI-Cws; the dashed light blue lines are the 1:1 lines (perfect match)

In this model, water stress is estimated based on precipitation, irrigation volume, and ET_p, without considering *SWC*, soil retention curve parameters, or the threshold value beyond which a plant starts

being stressed. Likely, some of the observed errors can be attributed to this last condition, because the actual onset of stress in plants depends on the dynamic interaction between *SWC*, root distribution, and plant water demand, which can vary spatially and temporally within the field. As a result, using only irrigation and precipitation data to define stress may lead to over- or under- estimation in certain periods, particularly during intermittent dry spells or following uneven water distribution (**Table 6.18**).

Table 6.18 Statistical indices associated to daily *in situ* versus NDVI-Cws modelled ET_a for 2019-2025 irrigation seasons

ET_a	***RMSE***	***MBE***	***MAE***	***R^2***	***b***	***R^2[b]***	***NSE***
2a	[cm^3 cm^{-3}]			[-]			
2019	0.52	-0.10	0.40	0.39	0.94	0.96	0.24
2020	0.49	0.10	0.39	0.56	1.01	0.97	0.53
2021	0.91	-0.70	0.74	0.66	0.80	0.98	0.14
2022	0.58	0.11	0.47	0.35	1.00	0.96	0.31
2023	0.57	0.19	0.46	0.45	1.04	0.96	0.35
2024	0.55	0.10	0.42	0.62	1.02	0.97	0.57
2025	0.38	0.01	0.32	0.87	0.99	0.98	0.87

6.5.5 Eddy Covariance-based partitioning method output

During the 2019 irrigation season, it was also possible to compare the transpiration estimated through the EC-based partitioning method with the measurements obtained from sap flow sensors (**Figure 6.52**).

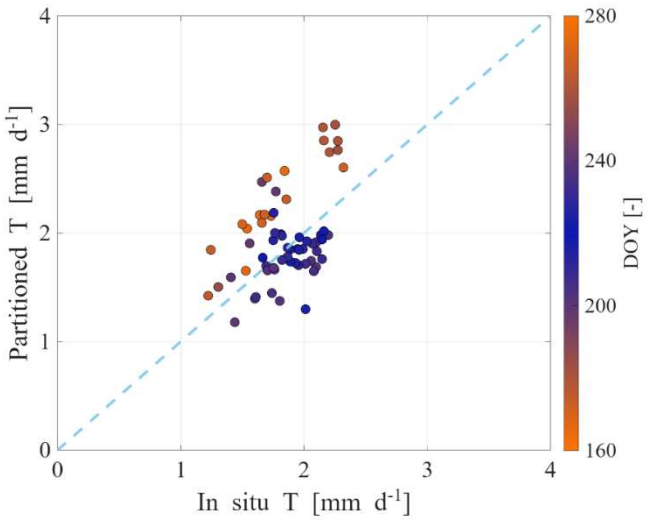

Figure 6.52 Scatterplots of daily *in situ* versus EC- based partitioned T for 2018-2019 irrigation seasons. Cluster-1, orange dots and Cluster-2, dark blue dots

Noticeably, two different clusters of data can be observed: the first corresponding to the period before mid-July (DOY 200) and after mid-September (DOY 240) (Cluster-1, orange dots) in which the EC-based partitioning method overestimate the *in situ* transpiration; and the second, in the period between mid-July and mid-September (Cluster-2, blue dots), where the model underestimates the *in situ* sap flow transpiration. This behaviour can be explained by the fact that while the sap flow measures the transpiration fluxes from the plants only, the EC-based partitioning method likely includes also the contribution of the weeds.

Encouraging performance of the method is observed in terms of *RMSE* which is of 0.39, 0.55 and 0.25 mm d^{-1} by considering the whole period, cluster-1 and cluster-2, respectively.

6.6 Actual evapotranspiration machine learning modelled

This section focuses on the estimation of ET_a using ML algorithm. Building upon the input features derived from remote sensing data, and meteorological variables, ML algorithm is trained to gap fill and generate synthetic ET_a time series. The methodology, including feature selection, model training, and validation, is presented, and the

results are discussed. The aim is to evaluate the potential of ML techniques in the citrus and olive orchards.

6.6.1 Feature analysis

Before implementing the model and identifying the most suitable *m(x)* and *k(x,x')* functions, an analysis of the input features was conducted, focusing on both their mutual correlations and their correlation with the target variable, ET_a.

The analysis of a set of descriptive statistics allowed for a comprehensive understanding of the statistical properties of both input features and the target variable, providing insights into their variability, distribution, and potential influence on model performance (**Table 6.19**).

Table 6.19 Mean, standard deviation, standard error, median, maximum (Max), minimum (Min), range, variance, Kurtosis, Skewness for all the possible features and the target feature in the olive and citrus orchard

Olive	$T_{a\text{-}Min}$	$T_{a\text{-}Max}$	$T_{a\text{-}Mean}$	RH_{Min}	RH_{Max}	RH_{Mean}	R_s	U_2	$NDVI$	$NDWI$	ET_a
		[°C]			[%]		[MJ m^{-2} d^{-1}]	[m s^{-1}]	[-]		[mm d^{-1}]
Mean	14.46	25.65	20.06	50.54	91.68	70.40	18.51	0.49	0.73	0.25	2.09
Standard Deviation	5.99	6.20	5.89	15.02	9.64	10.63	7.61	0.60	0.15	0.16	1.05
Standard Error	0.00	0.00	0.00	0.01	0.01	0.01	0.00	0.00	0.00	0.00	0.00
Median	15.39	25.69	20.40	50.15	94.60	71.45	18.35	0.30	0.73	0.20	1.96
Max	28.86	45.94	37.28	99.50	100.00	99.75	35.30	7.09	0.99	0.56	6.07
Min	0	9.58	6.43	8.50	32.65	21.75	3.39	0.00	0.43	0.01	0.24
Range	28.97	36.36	30.85	91.00	67.35	78.00	31.91	7.09	0.56	0.56	5.83
		[(°C)^2]			[(%)^2]		[(MJ m^{-2} d$^{-1)2}$]	[(m s^{-1})^2]	[-]		[(mm d^{-1})^2]
Variance	35.88	38.50	34.69	225.72	92.93	112.96	57.86	0.36	0.02	0.03	1.10
						[-]					
Kurtosis	2.12	2.15	1.96	2.59	7.86	3.71	1.70	19.91	1.71	1.71	2.98
Skewness	-0.32	0.04	-0.14	-0.01	-1.93	-0.64	-0.04	3.27	-0.13	0.36	0.64

Citrus	$T_{a\text{-}Min}$	$T_{a\text{-}Max}$	$T_{a\text{-}Mean}$	RH_{Min}	RH_{Max}	RH_{Mean}	R_s	U_2	NDVI	NDWI	ET_a
		[°C]			[%]		[MJ m^{-2} d^{-1}]	[m s^{-1}]	[-]		[mm d^{-1}]
Mean	13.65	25.37	19.51	33.36	94.25	63.81	20.82	1.45	0.54	0.10	1.83
Standard Deviation	4.88	6.42	5.49	14.41	10.77	10.50	7.34	0.67	0.14	0.16	0.87
Standard Error	0.01	0.01	0.01	0.03	0.02	0.02	0.01	0.00	0.00	0.00	0.00
Median	14.30	25.35	20.10	32.00	100.00	65.00	22.94	1.36	0.46	0.00	1.82
Max	24.20	41.80	31.85	78.00	100.00	89.00	30.81	4.94	0.85	0.43	4.50
Min	0	9.80	5.95	13.00	26.00	19.50	3.18	0.32	0.40	-0.05	0.22
Range	24.20	32.00	25.90	65.00	74.00	69.50	27.63	4.62	0.44	0.48	4.28
		[(°C)^2]			[(%)^2]		[(MJ m^{-2} d$^{-1)2}$]	[(m s^{-1})^2]	[-]		[(mm d^{-1})^2]
Variance	23.82	41.24	30.11	207.51	115.98	110.29	53.89	0.44	0.02	0.03	0.76
						[-]					
Kurtosis	2.27	2.03	2.04	2.74	9.34	3.85	1.99	6.31	2.05	2.11	2.43
Skewness	-0.29	0.02	-0.16	0.61	-2.41	-0.66	-0.53	1.40	0.82	0.88	0.23

Skewness measures the asymmetry of a probability distribution around its mean value. While theoretically it can take any real value from negative to positive infinity, most practical datasets fall within approximately −3 to +3. A skewness close to zero indicates a symmetric distribution, whereas positive skewness reflects a long tail on the right and negative skewness a long tail on the left. Kurtosis quantifies the "tailedness" or peakedness of a distribution. A normal distribution has a kurtosis of 3. Values greater than 3 indicate a leptokurtic distribution with heavier tails and a sharper peak, while values less than 3 indicate a platykurtic distribution with lighter tails and a flatter peak.

The matrices in **Figure 6.53** show at a glance the relationship between each two features: the scatter plot at row n and column m shows the n-th feature as a function of the m-th feature. This is helpful to spot correlations in the dataset, since the sparser are points in a plot, the more uncorrelated are the two corresponding features. In particular, it is clear and obvious that R_S have a higher correlation with

ET_a than other variables. A slight positive correlation is also observed with both $T_{a\text{-}Max}$ and $T_{a\text{-}Mean}$, while a slight negative correlation is found with the VIs. Finally, the plots in the diagonal represent the kernel density estimation of each feature, which is an estimate of their probability density function. The results are consistent across the two experimental sites.

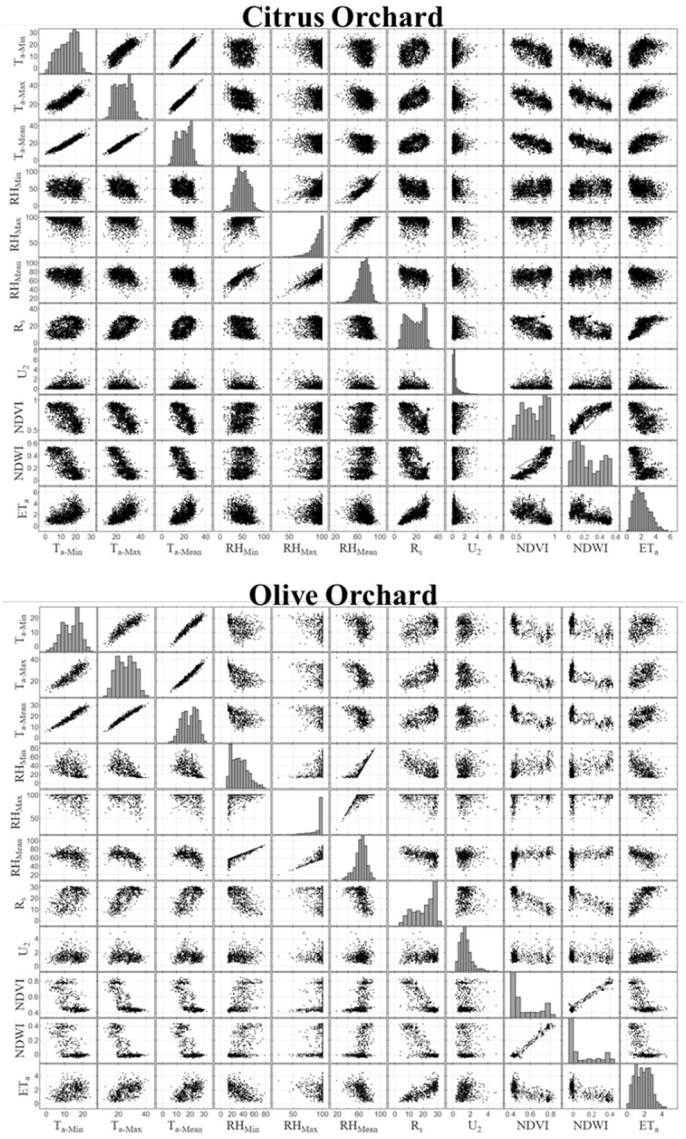

Figure 6.53 Scatter matrix used for overview and features analysis in citrus and olive orchards

Figure 6.54 shows the Pearson correlation coefficient. In both experimental sites, ET_a has a positive Pearson correlation coefficient with the following features: $T_{a\text{-}Min}$, $T_{a\text{-}Max}$, $T_{a\text{-}mean}$, R_s. R_s show a strong positive Pearson correlation coefficient (0.81 referred to the citrus orchard; 0.77 referred to the olive orchard) On the other hand, the features RH_{Min}, RH_{Max}, RH_{Mean}, $NDVI$ and $NDWI$, show a negative Pearson correlation coefficient with ET_a. The VIs show the strongest negative Pearson correlation coefficient.

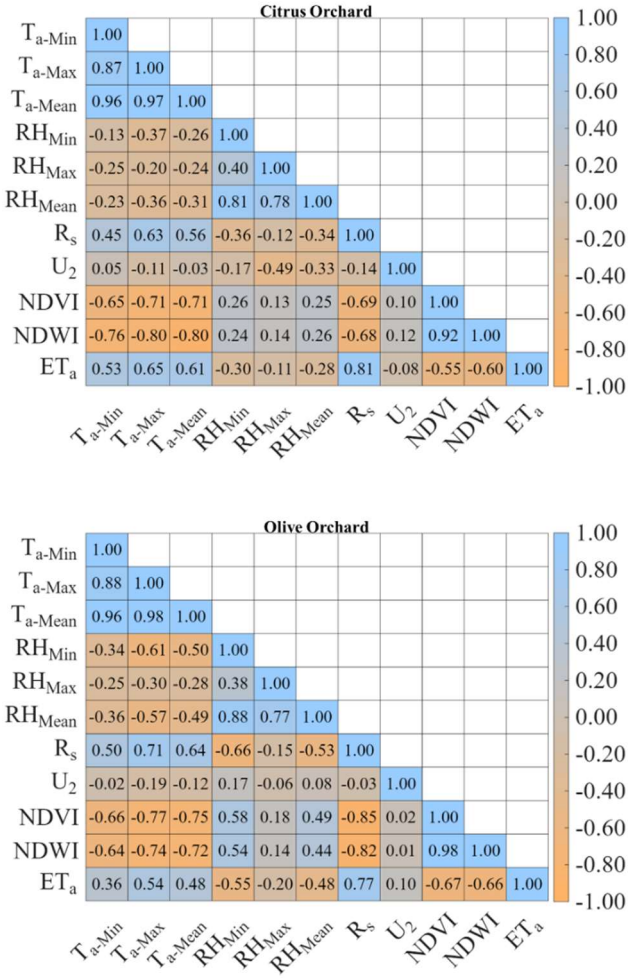

Figure 6.54 Pearson correlation coefficient between each pair of features in citrus and olive orchards

By analyzing the *FIS* for both experimental sites (**Figure 6.55**), it clearly emerges that R_s is, obviously, the most relevant feature for predicting ET_a. In both sites, *NDWI* consistently appears among the top three features, confirming its strong explanatory power in ET_a estimation.

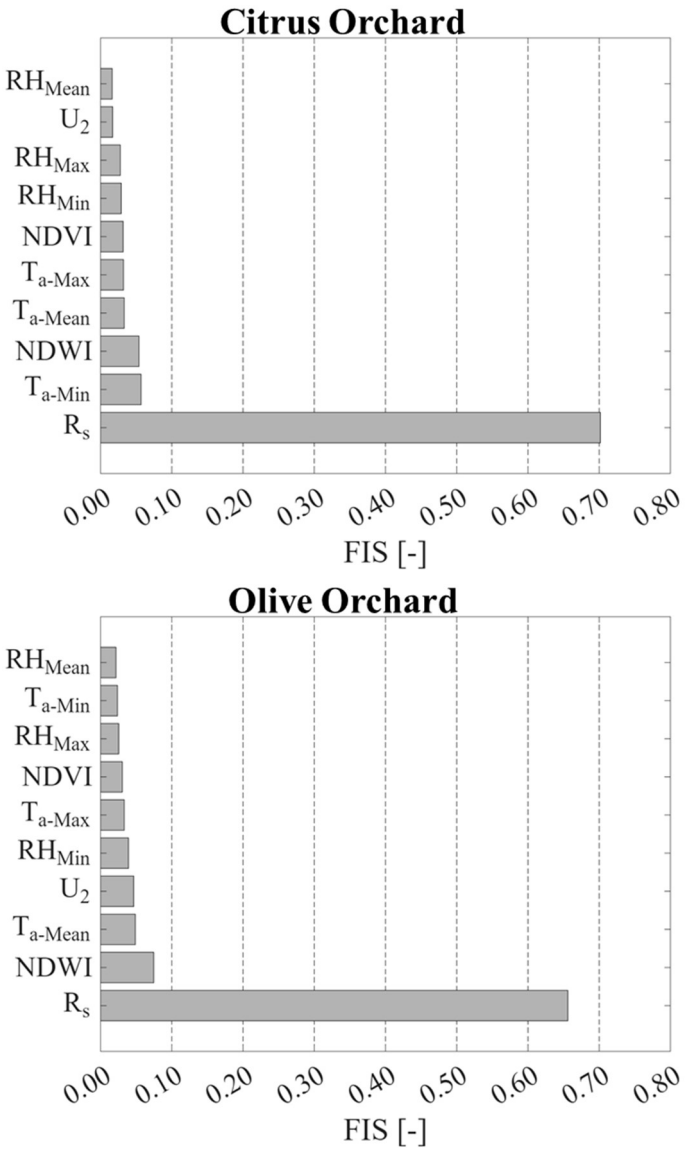

Figure 6.55 Feature importance score (FIS) of each feature of the dataset in the ET_a prediction in citrus and olive orchards

Therefore, following the feature analysis, different input combinations were constructed to assess the performance of the machine learning model for ET_a prediction (**Table 6.20**).

Table 6.20 Different combinations of input variables

Variables' combination	Input	Tool	Symbol	Unit
1	Global Solar Radiation	WatchDog 2000 or SIAS	R_s	[MJ m^{-2} d^{-1}]
	Maximum Air Temperature		$T_{a\text{-}Max}$	[°C]
	Minimum Air Temperature		$T_{a\text{-}Min}$	[°C]
	Maximum Relative Air Humidity		RH_{Max}	[%]
	Minimum Relative Air Humidity		RH_{Min}	[%]
	Wind Speed at 2 m		U_2	[m s^{-1}]
	Normalized Difference Vegetation Index	Sentinel-2 or MODIS	$NDVI$	[-]
	Normalized Difference Water Index		$NDWI$	[-]
2	Global Solar Radiation	WatchDog 2000 or SIAS	R_s	[MJ m^{-2} d^{-1}]
	Maximum Air Temperature		$T_{a\text{-}Max}$	[°C]
	Minimum Air Temperature		$T_{a\text{-}Min}$	[°C]
	Maximum Relative Air Humidity		RH_{Max}	[%]
	Minimum Relative Air Humidity		RH_{Min}	[%]
	Wind Speed at 2 m		U_2	[m s^{-1}]
3	Global Solar Radiation	ERA5-Land	R_s	[MJ m^{-2} d^{-1}]
	Maximum Air Temperature		$T_{a\text{-}Max}$	[°C]
	Minimum Air Temperature		$T_{a\text{-}Min}$	[°C]
	Maximum Relative Air Humidity		RH_{Max}	[%]
	Minimum Relative Air Humidity		RH_{Min}	[%]
	Wind Speed at 2 m		U_2	[m s^{-1}]
	Normalized Difference Vegetation Index	Sentinel-2 or MODIS	$NDVI$	[-]
	Normalized Difference Water Index		$NDWI$	[-]

$T_{a\text{-}Mean}$ and RH_{Mean} were excluded, since the daily variability is already represented by minimum and maximum values. The three combinations were applied to both experimental sites. In particular, for the citrus orchard, the first combination was used to derive the most suitable $m(x)$ and $k(x, x')$ functions. This criterion was adopted because a longer data series was available for this site (2019–2025).

6.6.2 Application at the Citrus Orchard

The best *m(x)* and *k(x,x')*, functions were assessed by the complete dataset (Combination 1) related to the citrus orchard, which includes all the examined variable. **Table 6.21** summarizes the statistical indicators associated with the fifteen combinations of the examined *m(x)* and *k(x,x')* functions.

Table 6.21 Statistical indices for mean, *m(x)*, and kernel covariance, *k(x,x')*, functions obtained by considering the entire database which includes all the examined variables (combination 1)

		Covariance kernel functions k(x,x')				
	Mean	Rational	Squared	Mater	Mater	Exponentia
RMSE [mm d^{-1}]	Zero	0.49	0.53	0.54	0.49	**0.46**
	Const.	0.52	0.54	0.56	0.53	0.48
	Linea.	0.55	0.53	0.53	0.49	0.50
MBE [mm d^{-1}]	Zero	0.01	0.00	-0.04	-0.03	**0.01**
	Const.	0.00	-0.03	0.02	-0.03	-0.03
	Linea.	0.03	0.02	0.01	-0.03	0.05
MAE [mm d^{-1}]	Zero	0.36	0.40	0.39	0.39	**0.34**
	Const.	0.40	0.37	0.40	0.40	0.37
	Linea.	0.36	0.38	0.37	0.40	0.39
R^2 [-]	Zero	0.77	0.80	0.79	0.80	**0.81**
	Const.	0.77	0.80	0.80	0.80	0.79
	Linea.	0.78	0.77	0.80	0.79	0.78
b [-]	Zero	0.94	0.95	0.95	0.95	**0.96**
	Const.	0.95	0.94	0.94	0.95	0.94
	Linea.	0.95	0.94	0.94	0.95	0.95
R^2[b] [-]	Zero	0.95	0.95	0.94	0.94	**0.96**
	Const.	0.95	0.94	0.95	0.95	0.95
	Linea.	0.94	0.94	0.95	0.95	0.95
NSE [-]	Zero	0.75	0.78	0.80	0.78	**0.81**
	Const.	0.77	0.76	0.80	0.75	0.77
	Linea.	0.76	0.75	0.77	0.76	0.76

Despite the fairly limited differences in terms of the examined statistical indicators, the best result was obtained when assuming a zero mean function and an exponential kernel covariance function (**Figure 6.56**).

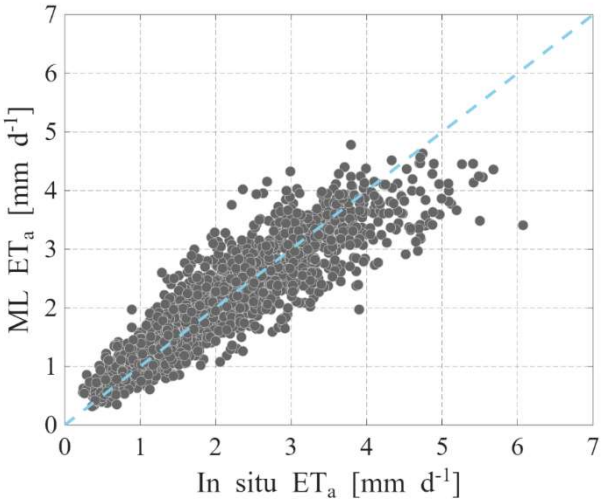

Figure 6.56 Comparison between daily *in situ* actual evapotranspiration and obtained from ML using combination 1; the dashed light blue lines are the 1:1 lines (perfect match)

Therefore, for the other variables' combinations and in olive orchard, the suitability of the ML model was tested using the best *m(x)* and *k(x,x')* functions.

For the other combinations of the input variables, in the citrus orchard **Figure 6.57** shows the scatterplots of *in situ* versus estimated daily ET_a by implementing in the GPR model the best *m(x)* and *k (x,x')* functions.

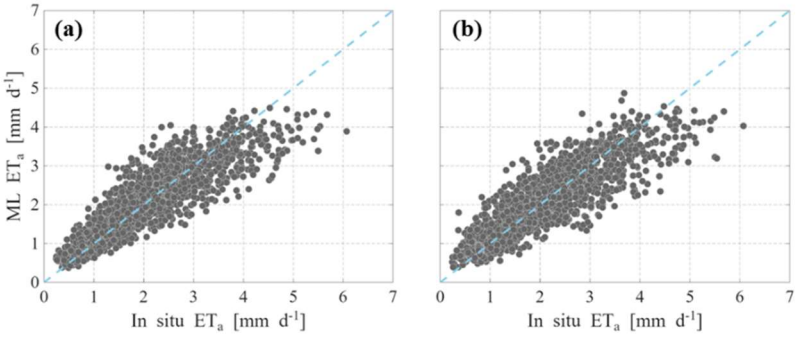

Figure 6.57 Comparison between daily *in situ* actual evapotranspiration and obtained from ML using combination 2 (a) and combination 3 (b); the dashed light blue lines are the 1:1 lines (perfect match)

The estimated values are in better agreement with the measured ones in fall and winter days ($ET_a < 2.5$ mm d^{-1}). In spring and summer days, the dispersion increases for values higher than about 2.5 mm d-1. For the citrus orchard, **Table 6.22** summarizes the statistical indicators associated with the GPR model implemented with the best *m(x)* and *k(x,x')* functions and the three input variables' combinations.

Table 6.22 Statistical indices associated with the GPR model implemented with the best *m(x)* and *k(x,x')* functions and the three combinations of the input variables, for the citrus orchard

	RMSE [mm d^{-1}]	***MBE*** [mm	***MAE*** [mm d^{-}	R^2 [-]	***b*** [-]	R^2/b [-]	***NSE*** [-]
1	0.46	-0.01	0.34	0.81	0.96	0.96	0.81
2	0.50	-0.01	0.37	0.77	0.95	0.95	0.77
3	0.52	-0.01	0.39	0.76	0.95	0.95	0.76

Noticeable that the introduction of the VIs improved the model performances, as shown by (Carter and Liang, 2019) and (Mosre and Suárez, 2021). The worst performances were associated with combination 3, in which all the input variables are detected from information freely available online. However, even if compared to the others, the statistical parameters evidenced that the joint use of reanalysis and remote sensing data can still be considered acceptable for practical applications related to irrigation management, considering that all the required input data can be downloaded from the web, avoiding costly and time-consuming field measurements in areas where ground data are not available. According to Faraminan et al. (2021) and Kang et al. (2019) the use of reanalysis and remoted sensed data could be a good alternative to retrieve ET_a with ML techniques.

6.6.3 Application at the olive orchard

Similar good results were obtained when considering the daily actual evapotranspiration data collected in the olive orchard.

Figure 6.58 shows the scatterplots between measured and estimated ET_a by assuming a zero mean function and an exponential

kernel covariance function and the three combinations of the input variables.

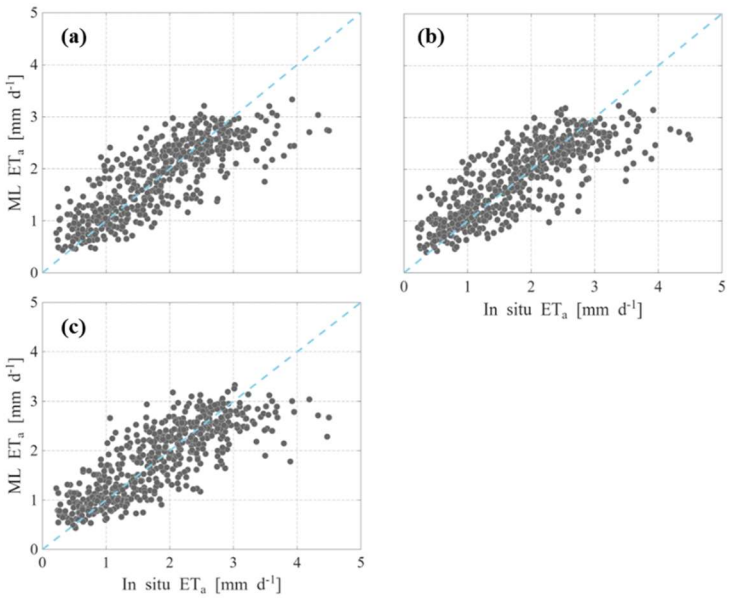

Figure 6.58 Comparison between daily *in situ* actual evapotranspiration and obtained from ML using combination 1 (a), combination 2 (b) and combination 3 (c); the dashed light blue lines are the 1:1 lines (perfect match)

The estimated values are in better agreement with the measured ones in fall and winter days ($ET_a < 1$ mm d^{-1}). The dispersion increases for values higher than about 3 mm d^{-1}. The statistical indicators associated with the three different variable combinations are summarized in **Table 6.23**.

Table 6.23 Statistical indices associated with the GPR model implemented with the best *m(x)* and *k(x,x')* functions and the three combinations of the input variables, for the citrus orchard

	RMSE [mm d^{-}	***MBE*** [mm d^{-}	***MAE*** [mm d^{-}	R^2 [-]	***b*** [-]	R^2/b [-]	***NSE*** [-]
1	0.49	-0.01	0.37	0.68	0.94	0.94	0.68
2	0.51	-0.01	0.38	0.66	0.94	0.94	0.66
3	0.50	-0.01	0.39	0.66	0.94	0.94	0.66

As can be observed, all the combinations are characterized by quite similar results. The results of combination 3 are a consequence of the good performance of the ERA5-L in depicting the meteorological data measured on the ground nearby the olive orchard.

6.7 IRRILEARNING model modules

Before presenting the results obtained from the different model configurations, it was necessary to develop and implement specific model modules required for their application.

6.7.1 Water Stress Coefficient Modelling

The main objective of this module was to identify the most suitable function for transforming *SWC* into a water stress coefficient (K_s). As described in section *4.2 Soil Water Balance Model,* SWC can be transformed into K_s either by means of exponential functions (concave or convex) or through a linear function. Thus, the best shape factor was identified.

The analysis was carried out in the experimental olive orchard by applying the FAO-56 model using: *in situ* data acquired from the standard meteorological station and the temporal dynamics of the crop coefficient (K_c) followed a reversed trapezoidal pattern, in accordance with Rallo et al. (2021), assuming a *traditional, medium-density* planting system. Values of Z_r and p_{FAO} were fixed according to information retrieved from the field farmer and from Allen et al., (1998), respectively. Z_r was fixer equal to 80 cm and p_{FAO} equal to 0.60. Values of SWC_{fc} and SWC_{wp} were fixed according to the soil characterization carried out by Bono (1998). The shape factor, was determined based on the comparison metrics between simulated and *in situ* measurements of ET_a, exploring a wide range of values from −1.00 to 2.50. The performance metrics considered in the identification included the *RMSE* and the *MAE*, which were the most significant. The overall investigated period covered the years 2008–2011, while the comparative analysis with EC tower measurements was performed for the 2009–2011 period. The FAO-56 model was applied by including an initialization phase, since the initial *SWC* was unknown. Four different initial soil water content (SWC_0) values were

considered, and the model results were analysed at the time when the different simulations converged to the same *SWC* value, ensuring that the comparison was not influenced by the choice of the initial condition. Thus, the length of the initialization window required to make the effects of the initial model condition (initial *SWC*) negligible was found to be 257 days.

From the analysis of the *RMSE* and *MAE* trends computed for the period 2009–2011 as a function of the shape factor (*fs*), it was possible to identify the minimum values of the interpolating functions of the considered metrics (**Figure 6.59**)

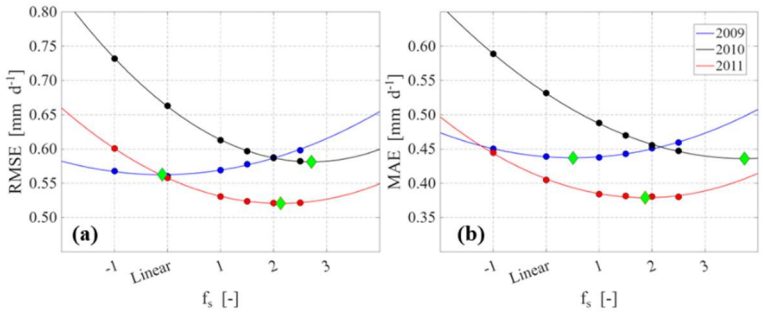

Figure 6.59 RMSE (a) and MAE (b) variability as a function of the shape coefficient in the 2009 (blue curve), 2010 (black curve) and, 2011 (red curve), the green diamond indicates the minus values of the two statistical indices and the relative values of the shape coefficient, for each year of simulation

The mean values of *fs* over the investigated period were *fs,RMSE* = 1.58 and *fs,MAE* = 2.04, which are close to the value suggested by Rallo and Provenzano (2013) (*fs*~1.41) for the same experimental field, retrieved through field measurement of Midday Steam Water Potential and *SWC*.

It is noteworthy that *fs* varies from year to year, suggesting that, from a purely modeling perspective, this parameter should ideally be estimated on a period-by-period basis. However, from an operational standpoint, it is necessary to adopt a single representative value. In this study, an *fs* value of 1.81 was selected as a compromise, defined as the average of the previously derived *fs* values (**Figure 6.60**).

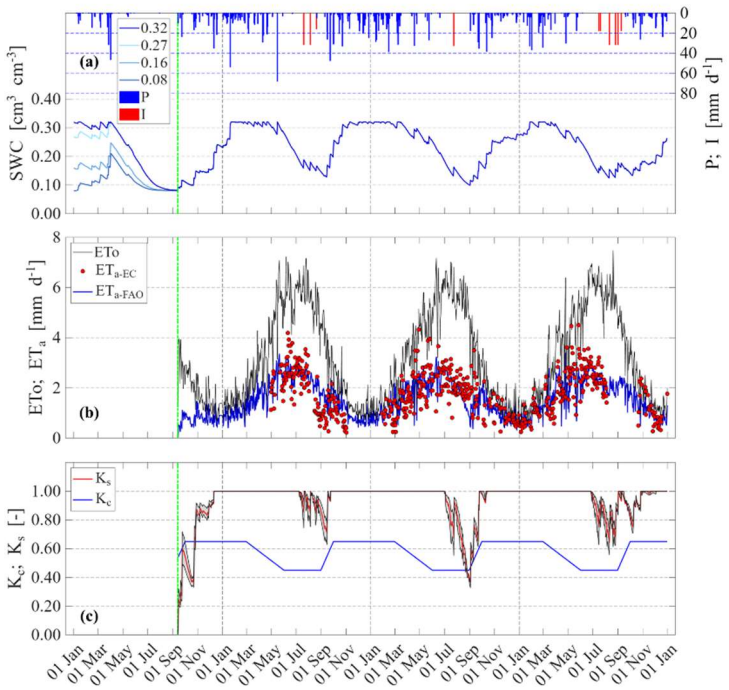

Figure 6.60 Temporal dynamic of: (a) prcipitation depth (P) (blue bars), irrigation volumes (I) (red bars), soil water content (SWC) imputed considering different values of SWC_o; crop reference evapotranspiration (ETo) (black curve), EC tower measured actual evapotranspiration ($ET_{a\text{-}EC}$) (red dots) and, FAO-56 modelled actual evapotranspiration ($ET_{a\text{-}FAO}$) (blue curve); stress coefficient (K_s) (red curve) considering a shape coefficient of 1.81 and confidence bands and, crop coefficient (K_c) according to Rallo et al. (2021)

The adoption of the mean value *fs* = 1.81 results in modeled evapotranspiration dynamics that are in good agreement with the *in situ* measurements and are consistent with the timing of precipitation and irrigation events. In particular, when focusing on the irrigation seasons (May - September), *RMSE* values range between 0.52 and 0.59 mm d^{-1}, *MAE* values between 0.38 and 0.45 mm d^{-1}, regression coefficient *b* values between 0.89 and 0.97, and $R^2[b]$ values between 0.95 and 0.97 (**Table 6.24**).

Table 6.24 Statistical indices associated to ET_a, computed during irrigation seasons in the period 2009-2011

	RMSE	*MBE*	*MAE*	R^2	*b*	$R^2[b]$	*NSE*
	[mm d^{-1}]			[-]			
2009	0.58	0.09	0.45	0.54	0.97	0.95	0.45
2010	0.59	-0.09	0.46	0.16	0.93	0.93	-0.18
2011	0.52	-0.20	0.38	0.38	0.89	0.97	0.27

Considering instead the overall performance across the three-year period, the aggregated statistics yield a *RMSE* of 0.58 mm d^{-1}, a *MBE* of 0.06 mm d-1, a *MAE* of 0.45 mm d^{-1}, R^2 of 0.57, b and $R^2[b]$ values of 0.95 and 0.92, respectively, finally, a Nash–Sutcliffe efficiency coefficient of 0.56.

6.7.2 Satellite NDVI and NDWI prediction

For the prediction of satellite data, two different approaches were tested in the olive experimental orchard: a more complex one and a simplified one. The complex approach relies on the calibration of a fourth-degree polynomial curve linking VIs values to the Day Of the Year (DOY), whereas the simplified approach exploits the short-term invariance of VIs over limited temporal windows.

Complex. Each *NDVI* and *NDWI* value was associated with the corresponding DOY (**Figure 6.61**).

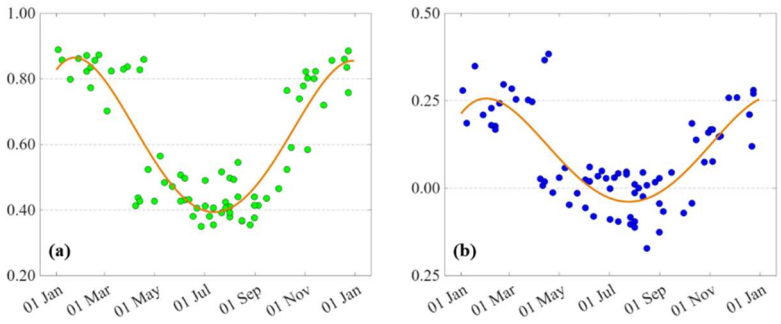

Figure 6.61 (a) NDVI (green dots) and (b) NDWI (blue dots), retrived from Sentinel-2 acquisition in the period 2017-2020, function of DOYs; the red curves indicate the interpolator fourth degree polynomial (complex approach)

Two different functional relationships were derived:

$$NDVI = -6 \cdot 10^{-10} \cdot DOY^4 + 4.34 \cdot 10^{-7} \cdot DOY^3 - 9.36 \cdot 10^{-5} \cdot DOY^2 + 4 \cdot 10^{-3} \cdot DOY + 8.2 \cdot 10^{-1} \quad \textbf{(6.6)}$$

$$NDWI = -3 \cdot 10^{-10} \cdot DOY^4 + 2.63 \cdot 10^{-7} \cdot DOY^3 - 6.2 \cdot 10^{-5} \cdot DOY^2 + 3 \cdot 10^{-3} \cdot DOY + 2.1 \cdot 10^{-1} \quad \textbf{(6.7)}$$

Simplified. This approach involves keeping the VIs values constant between two consecutive acquisitions. Specifically, the value of an index on the day following an acquisition is assumed to remain unchanged until the day of the next available acquisition.

The temporal evolution of the two vegetation indices, *NDVI* and *NDWI*, following the two approaches described above, is shown in (**Figure 6.62**).

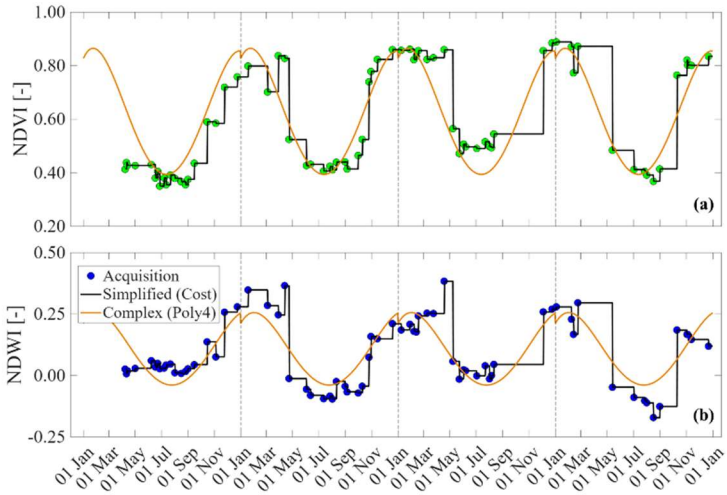

Figure 6.62 Temporal dynamic of: (a) NDVI (green dots represent the values retrived from Sentinel-2 acquisition in the period 2017-2020; the red curve the values obtained using the complex approach and the black lines using the simplified approach); (b) NDWI (blue dots represent the values retrived from Sentinel-2 acquisition in the period 2017-2020; the red curve the values obtained using the complex approach and the black lines using the simplified approach) (green dots) and (b) NDWI (blue dots), retrived from Sentinel-2 acquisition in the period 2017-2020, function of DOYs; the red curves indicate the interpolator fourth degree polynomial (complex approach)

The qualitative analysis of the scatterplots (**Figure 6.63**) shows that the simplified method is more prone to both underestimation and overestimation.

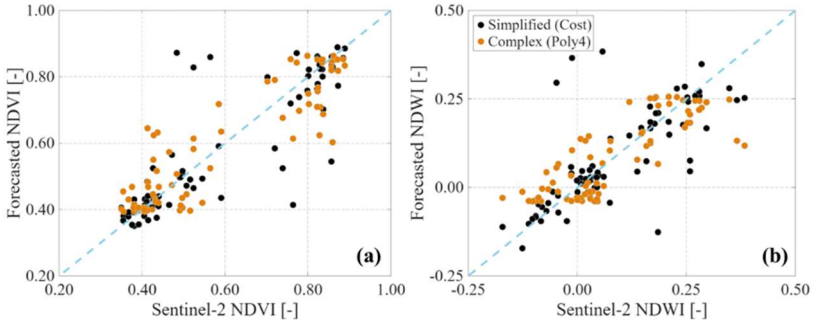

Figure 6.63 Qualitative analysis of: (a) NDVI and (b), obtained from the Sentinel-2 acquisitions in the period 2017-2020, and retrieved from the complex approach (red dots) and simplified approach (black dots)

6.7.3 Irrigation intervention thresholds

As described in Section 5.*7 IRRILEARNING Model*, the model is also configured to estimate the irrigation volumes to be applied to the olive trees. To achieve this, it is necessary to define both a lower and an upper *SWC* threshold. Specifically, a minimum *SWC* value must be established, below which the model provides an irrigation dose to restore *SWC* up to a predefined upper threshold. Since water stress in olive trees can enhance oil quality, while the absence of stress allows the production of high-quality table olives (Marra et al., 2016), a proper knowledge and definition of these thresholds is particularly important.

Some authors (Marino et al., 2018; Sánchez-Piñero et al., 2023) have suggested three levels of Midday Stem Water Potential (*MSWP*) in olive trees to guide irrigation management: up to −2 MPa (no stress), from −2 to −3.5 MPa (moderate stress), and below −3.5 MPa (high stress). Values over −2.5 MPa were less effective in increasing productivity, reduced oil quality and produced excessive crop set that strongly affected vegetative growth and fruit production the following season. Thus, in general, moderate stress is described by a MSWP between about −2 and −3.5 MPa and is characterized by stomatal regulation of gas exchange. Maintaining *SWC* within this range can improve Water Use Efficiency (WUE) and reduce water consumption. According to the study by Marra et al. (2016), this stress level benefits oil quality without compromising overall productivity and it is

optimal for moderate annual yields of good quality oil. Finally, below approximately −3.5 MPa, non-stomatal limitations to photosynthesis become predominant, thus it reduced current season productivity. This represents a threshold for high stress levels, which should be avoided because it poses risks to the plant and has a significant negative impact on both gas exchange and productivity.

This theoretical framework is consistent with Autovino et al. (2018), who investigated a functional relationship between *MSWP* and the water stress coefficient simulated by the HYDRUS-2D model:

$$K_S = \frac{|MSWP| - 5.40}{-4.51} \quad \textbf{(6.8)}$$

(6.8) shows that, for a given value of MSWP, it is possible to derive a corresponding value of the water stress coefficient. This coefficient can then be converted into an equivalent *SWC* value, allowing the definition of lower and upper *SWC* threshold values to be used for irrigation scheduling.

Their results demonstrated a clear correspondence between increasing soil water deficit, the modelled stress coefficient, and observed plant water status, supporting the use of soil-based indicators to define irrigation thresholds linked to physiological stress levels in olive trees.

6.7.4 Other parameters

IRRILEARNING model implementation also requires the definition of some other parameters.

For the selection of the Z_r, which determines the size of the soil water reservoir, the study carried out by Masmoudi-Charfi et al. (2011) was taken as a reference. It provides physically consistent and site-specific estimates derived from long-term observations and modelling at an experimental olive orchard. The adopted root depth reflects both the soil characteristics and the typical rooting behaviour of olive trees, ensuring a realistic representation of the soil water reservoir involved in water uptake. Therefore, depending on soil type and tree age, a representative value of Z_r is adopted, allowing the soil

water reservoir to be parameterized consistently with the physical characteristics of the site and the phenological development of the olive trees.

$p_{FAO,}$ which allows the identification of the threshold for the beginning of water stress, was retrieved from Allen et al. 1998, abd set equal to 0.60.

Values of SWC_{fc} and SWC_{wp} were fixed according to the soil characterization carried out by Bono (1998).

Finally, as explained in *6.7.1 Water Stress Coefficient Modelling*, IRRILEARNING also requires an initialization phase. The model is initialized using four different values of initial soil water content (*SWCo*), and the results are analysed once all four simulations converge to the same *SWC* value, ensuring that the model response is independent of the chosen initial condition.

6.7.5 Alternative Functions

The model is also designed to analyse climate change scenarios. In this framework, the precipitation pattern can be modified in terms of event magnitude by applying either a reduction or an increase, expressed as a percentage variation ($P_{VAR\%}$), to the intensity of the recorded rainfall events.

Finally, the analysis can be carried out either on a pixel wise basis or by adopting a field mean approach.

6.8 IRRILEARNING applications

Once the model modules were defined, the framework was ready to analyse the three model configurations across the seven fields for which irrigation volumes, provided by the farmers, were available for the period 2018–2020. The simulations were initialized in 2017, since the initial *SWC* was unknown, allowing an adequate warm up period to minimize the influence of the initial conditions. **Figure 6.64** shows the operational workflow of the model.

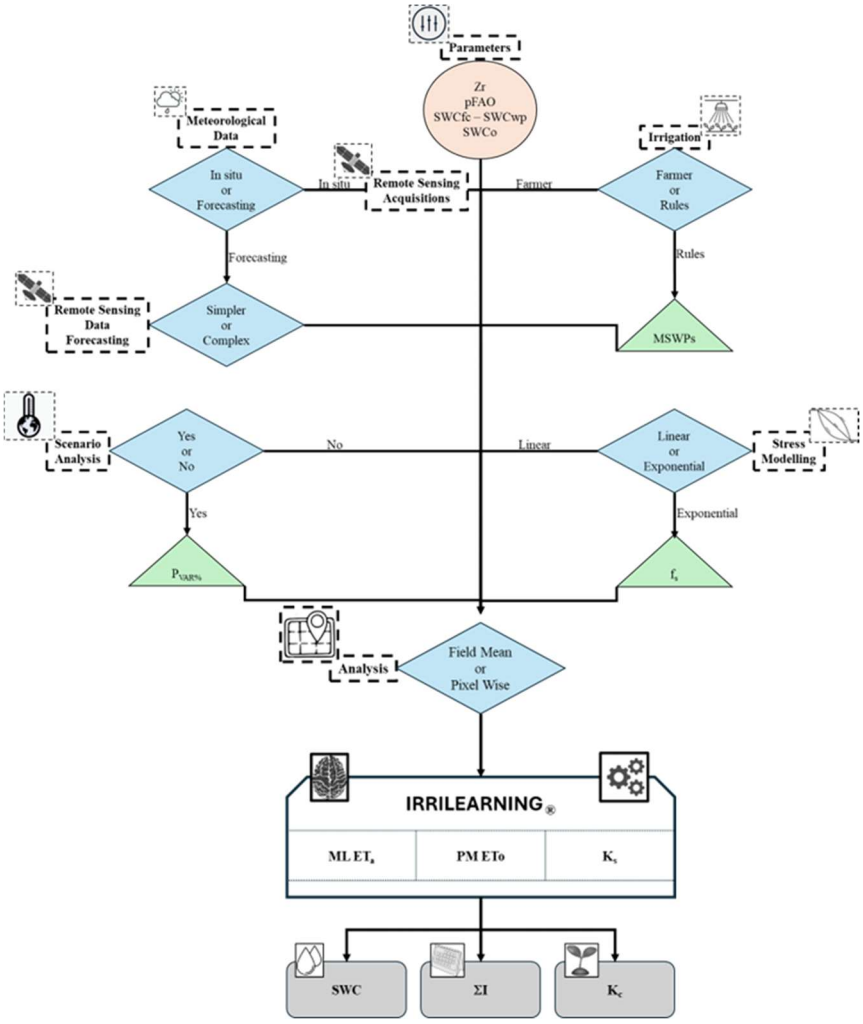

Figure 6.64 IRRELEARNING model operation scheme

The operational performance of IRRILEARNING was evaluated in the seven fields where user irrigation cards were available for the years 2018, 2019, and 2020, as previously described in Section *4.1 Irrigation District 1A*.

6.8.1 Support and check

The Support and Check (SaC) mode was initialized using meteorological inputs measured by the SIAS *in situ* station. VIs were derived from Sentinel-2 acquisitions and linearly interpolated between consecutive images. Irrigation scheduling was simulated

under two management objectives: oil production (lower *MSWP* threshold = −3.5 MPa; upper threshold = −2.5 MPa) and table olive production (lower *MSWP* threshold = −2.5 MPa; upper threshold = −2.0 MPa). No precipitation scenarios were considered. The functional relationship to convert *SWC* into the water stress coefficient (K_s) was performed using the exponential function **(3.9)** with a f_s equal to 1.81.

Figure 6.65 shows the actual irrigation volume supplied by the farmer and the volume provided by IRRILEARNING in SaC mode, for both oil and table olive production. It also exhibits the number of irrigation events through which these volumes are provided across the seven selected fields.

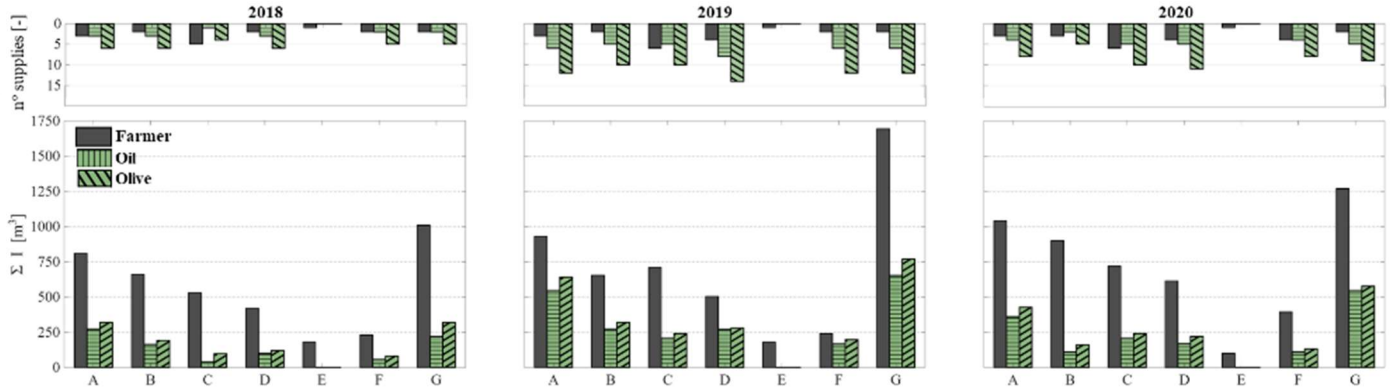

Figure 6.65 Irrigation volume provide by the farmers (dark grey bar) *vs*. irrigation volume provide by the model using the SaC mode for oil (green bar with horizontal lines) and olive table production (green bar with skewed lines) (bottom row); In the upper row, the bars represent the number of supplies used to provide the irrigation volumes (dark grey bars for farmers; green bars with horizontal liner for SaC mode for oil production; and, green bars with skewed liner for SaC mode for olive table production)

Conversely, **Table 6.25** reports the absolute errors (simulated − supplied) and the percentage errors (|simulated − supplied| / supplied × 100) associated with the irrigation volumes simulated by the model and those actually applied by the farmer.

Table 6.25 Absolute and percentage errors between the irrigation volumes provided by the farmer and those predicted by the model in SaC mode, for both productions, oil and olive table

Oil		A	B	C	D	E	F	G
					[m^3]			
ERROR	2018	-538	-497	-489	-318	-180	-174	-792
		-66%	-75%	-92%	-76%	-100%	-76%	-78%
	2019	-385	-383	-504	-234	-180	-73	-1041
		-41%	-58%	-71%	-46%	-100%	-30%	-61%
	2020	-677	-791	-514	-446	-100	-284	-725
		-65%	-88%	-71%	-73%	-100%	-72%	-57%

Olive		A	B	C	D	E	F	G
					[m^3]			
ERROR	2018	-490	-468	-433	-300	-180	-148	-690
		-60%	-71%	-82%	-71%	-100%	-64%	-68%
	2019	-289	-335	-468	-226	-180	-44	-926
		-31%	-51%	-66%	-45%	-100%	-18%	-55%
	2020	-613	-740	-478	-396	-100	-264	-693
		-59%	-82%	-66%	-64%	-100%	-67%	-55%

The model results indicate that substantial water savings can be achieved under both management strategies. When irrigation is scheduled to optimize oil production, water savings range from a minimum of 30% (Field F, 2019) to a maximum of 100% (Field E), the latter reflecting a season in which irrigation was applied by the farmer despite conditions that likely did not require it. Similarly, when irrigation is managed to support table olive production, potential water savings vary from 18% (Field F, 2019) up to 100% (Field E), again highlighting cases where irrigation was supplied during a season when it was probably unnecessary.

6.8.2 Forecasting

The Forecasting mode was designed to assess both the operational functionality of the model when driven by forecast meteorological

data and its capability to support scenario management. However, the SILAM forecast data consistently overestimated precipitation during the three investigated years (see *6.3 Forecasting data accuracy*). When these data are used without correction, none of the seven fields requires irrigation over the entire period. Moreover, for the model to simulate irrigation events, the magnitude of forecast precipitation must be reduced by ~40%, a condition that can be considered excessively extreme and therefore unrealistic for operational applications.

6.8.3 Scenario Management

To evaluate the Scenario Management mode, a percentage reduction of the precipitation pattern measured at the SIAS station was adopted. Only the magnitude of rainfall events was modified, while the temporal distribution was preserved. Four different scenarios were analysed, and the percentage reductions were defined according to the Representative Concentration Pathways (RCPs) developed by the Intergovernmental Panel on Climate Change. RCPs describe possible trajectories of atmospheric greenhouse gas concentrations and other climate forcings up to the year 2100.

Sicily lies within the Mediterranean region, which is widely recognized as a climate change hotspot, where warming rates are higher and precipitation regimes are expected to change more markedly than the global average. Regional climate projections and local studies indicate a decline in total annual rainfall and an increase in seasonal irregularity, with autumn and winter periods characterized by long dry spells alternating with short, high-intensity precipitation events. By the end of the century, mean precipitation in Sicily and surrounding areas is projected to decrease by approximately 10–20% or more, depending on the scenario and season. At the same time, an intensification of short, intense storms and increasing seasonal variability are expected, leading to longer dry periods and greater pluviometric irregularity (Van Vuuren et al., 2011a).

Based on these projections, the following precipitation reduction scenarios were considered for south-western Sicily:

- **RCP2.6**: strong mitigation scenario, with rapid emission reductions and early stabilization of global warming. Large decreases in annual rainfall are not expected, although variability and extreme events may increase; assumed precipitation reduction of 5% (Van Vuuren et al., 2011b);
- **RCP4.5**: intermediate scenario with moderate mitigation policies; assumed precipitation reduction of 15% (Thomson et al., 2011);
- **RCP6.0**: intermediate-high scenario with late stabilization of emissions and strengthening of the northward expansion of the subtropical high-pressure system, leading to a robust reduction in rainfall, particularly during the agriculturally critical season; assumed precipitation reduction of 17% (Fujino et al., 2006);
- **RCP8.5**: high-emission scenario with no significant climate policies; assumed precipitation reduction of 20% (Riahi et al., 2011).

Therefore, the four precipitation reduction scenarios were applied across all seven fields. **Figure 6.66** shows how cumulative precipitation is reduced under each scenario across three periods of the year: from January to April, from May to September (irrigation season), and from October to December.

For each scenario, the model was evaluated under both irrigation management strategies: one aimed at maximizing oil production and the other oriented toward table olive production. The evaluation of the model was evaluated by considering the number of irrigation events supplied and the total volume applied, compared against the measured data recorded in the user cards (**Figure 6.67**).

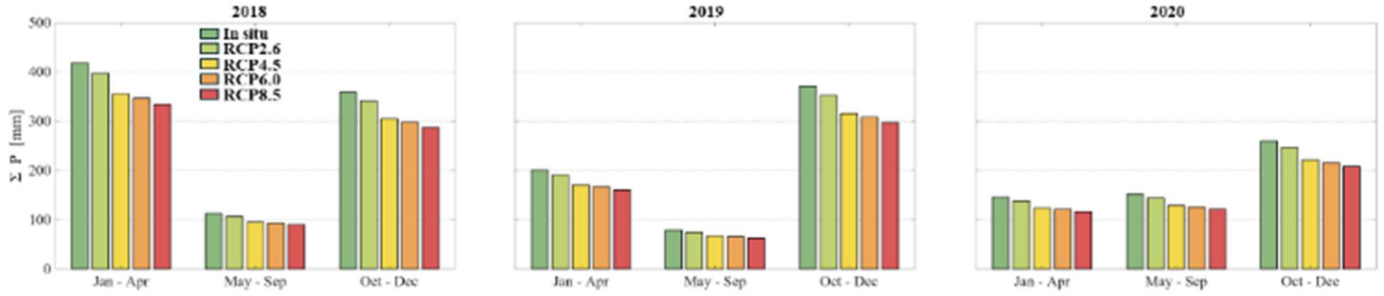

Figure 6.66 Variation in precipitation patterns over different periods (January-April, May-September, October-December) across the three years, in accordance with the RCP scenarios projections (green bar *in situ* measurement, light green RCP2.6, yellow RCP4.5, orange RCP6.0, red RCP8.5)

.

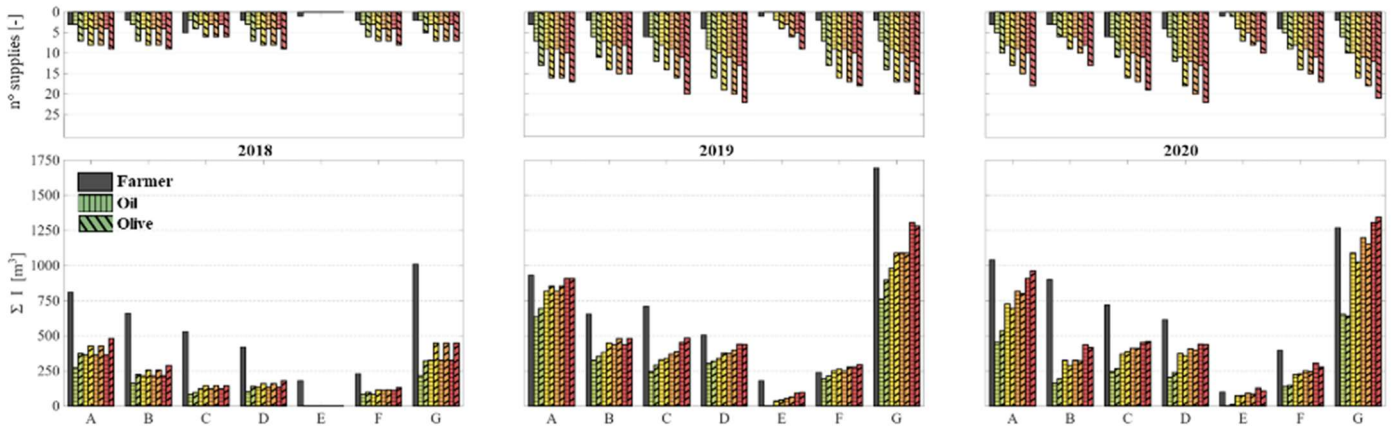

Figure 6.67 Irrigation volume provide by the farmers (dark grey bar) *vs.* irrigation volume provide by the model using the Scenario Management mode for oil (bar with horizontal lines) and olive table production (bar with skewed lines) (bottom row); green bar indicate *in situ* measurement, light green RCP2.6, yellow RCP4.5, orange RCP6.0, and red RCP8.5. In the upper row, the bars represent the number of supplies used to provide the irrigation volumes (dark grey bars for farmers; bars with horizontal liner for Scenario Management mode for oil production; and, bars with skewed liner for Scenario Management mode for olive table production); green bar indicate *in situ* measurement, light green RCP2.6, yellow RCP4.5, orange RCP6.0, and red RCP8.5

As expected, increasing the percentage reduction in precipitation leads to a corresponding rise in both the number of irrigation events and the total irrigation volume applied. In 2018, lower irrigation volumes were observed compared with the other years; this can be explained by the particularly wet conditions recorded during the January–April period, which increased *SWC* prior to the irrigation season (May–September). In most cases, the irrigation volume supplied for olive production is slightly higher than that provided for oil production, although the differences are not significant. This occurs because, under the oil production strategy, the model schedules fewer irrigation events with larger supplies depths, whereas for olive production it provides more frequent irrigations with smaller volumes. In the few cases where this pattern is reversed and the volume supplied for oil exceeds that for olive production, irrigation was provided on days when rainfall also occurred. This behaviour was observed under the olive production strategy: because irrigation coincided with precipitation, *SWC* increased above the upper threshold, further delaying the return toward the lower intervention threshold. This behaviour arises from the model decision logic, which determines irrigation on day i based on conditions observed on day $i-1$; consequently, it cannot anticipate precipitation events occurring on the same day.

With the exception of 2018, which was characterized by a particularly wet Jan–Apr period, and excluding Field E from the analysis, the number of irrigation events shows, for oil production, irrigation events in 2019 range from a minimum of 6 to a maximum of 13, while in 2020 they vary between 2 and 13; for table olive production, the number of interventions is generally higher, ranging from 10 to 22 in 2019 and from 5 to 22 in 2020.

Table 6.26 summarizes the irrigation volumes supplied by the farmer and under the different model configurations and years, together with their frequency. The latter is calculated as the inverse of the average number of days between two consecutive irrigation events.

Table 6.26 Irrigation volumes provided by the farmer and under different model configurations across the years, and their irrigation frequency, for both productions, oil and olive table

		2018							2019							2020						
	Volume	A	B	C	D	E	F	G	A	B	C	D	E	F	G	A	B	C	D	E	F	G
SCENARIO	Farmer	810	660	530	420	180	230	1010	930	655	710	505	180	240	1695	1040	900	720	615	100	395	1270
	SaC	272	163	41	102	0	56	218	545	272	206	271	0	167	654	363	109	206	169	0	111	545
	RCP2.6	272	163	82	102	0	84	218	635	327	247	305	0	195	763	454	163	247	203	0	139	654
	RCP4.5	363	218	123	136	0	84	327	817	381	329	339	37	251	980	726	327	370	373	73	223	1089
	RCP6.0	363	218	123	136	0	111	327	817	436	370	373	55	251	1089	817	327	412	407	91	251	1198
	RCP8.5	363	218	123	136	0	111	327	908	436	453	441	91	278	1307	908	436	453	441	128	306	1307

		2018							2019							2020						
	Volume	A	B	C	D	E	F	G	A	B	C	D	E	F	G	A	B	C	D	E	F	G
	Farmer	810	660	530	420	180	230	1010	930	655	710	505	180	240	1695	1040	900	720	615	100	395	1270
	SaC	320	192	97	120	0	82	320	641	320	242	279	0	196	769	427	160	242	219	0	131	577
	RCP2.6	374	224	97	140	0	98	320	694	352	290	319	0	213	897	534	192	266	239	11	147	641
	RCP4.5	427	256	145	159	0	115	448	854	448	339	379	43	262	1089	694	288	387	359	75	229	1025
	RCP6.0	427	256	145	159	0	115	448	854	480	387	399	65	278	1089	801	320	411	399	86	246	1153
	RCP8.5	480	288	145	179	0	131	448	907	480	484	438	97	295	1281	961	416	460	438	108	278	1345

	Frequency							
SCENARIO	Farmer	0.13	0.01	0.07	0.02	-	0.02	0.02
	SaC	0.13	0.13		0.13	-	0.14	0.14
	RCP2.6	0.07	0.07	0.11	0.07	-	0.13	0.14
	RCP4.5	0.09	0.08	0.13	0.09	-	0.07	0.14
	RCP6.0	0.09	0.09	0.13	0.09	-	0.08	0.14
	RCP8.5	0.08	0.09	0.13	0.07	-	0.08	0.09

	Farmer	0.02	0.03	0.08	0.05	-	0.02	0.03
	SaC	0.11	0.10	0.10	0.10	-	0.11	0.11
	RCP2.6	0.13	0.11	0.11	0.10	-	0.13	0.09
	RCP4.5	0.10	0.13	0.10	0.11	0.09	0.10	0.11
	RCP6.0	0.10	0.10	0.13	0.13	0.10	0.11	0.11
	RCP8.5	0.11	0.13	0.11	0.13	0.13	0.14	0.13

	Farmer	0.04	0.05	0.08	0.05	-	0.02	0.07
	SaC	0.14	0.17	0.14	0.14	-	0.14	0.14
	RCP2.6	0.14	0.14	0.14	0.17	-	0.14	0.17
	RCP4.5	0.17	0.17	0.17	0.17	0.20	0.17	0.17
	RCP6.0	0.17	0.17	0.17	0.17	0.20	0.17	0.17
	RCP8.5	0.17	0.17	0.17	0.17	0.20	0.17	0.17

	Farmer	0.13	0.01	0.07	0.02	-	0.02	0.02
	SaC	0.11	0.11	0.20	0.11	-	0.11	0.20
	RCP2.6	0.13	0.13	0.25	0.13	-	0.14	0.13
	RCP4.5	0.14	0.14	0.14	0.14	-	0.13	0.14
	RCP6.0	0.14	0.14	0.14	0.14	-	0.14	0.13
	RCP8.5	0.17	0.17	0.14	0.14	-	0.14	0.13

	Farmer	0.02	0.03	0.08	0.05	-	0.02	0.03
	SaC	0.14	0.20	0.20	0.17	-	0.17	0.17
	RCP2.6	0.20	0.20	0.17	0.20	-	0.20	0.17
	RCP4.5	0.20	0.17	0.17	0.20	0.09	0.20	0.20
	RCP6.0	0.20	0.17	0.20	0.20	0.10	0.20	0.20
	RCP8.5	0.20	0.20	0.20	0.25	0.13	0.20	0.20

	Farmer	0.02	0.03	0.08	0.05	-	0.02	0.03
	SaC	0.14	0.20	0.20	0.17	-	0.17	0.17
	RCP2.6	0.20	0.20	0.17	0.20	-	0.20	0.17
	RCP4.5	0.20	0.17	0.17	0.20	0.20	0.20	0.20
	RCP6.0	0.20	0.17	0.20	0.20	0.20	0.20	0.20
	RCP8.5	0.20	0.20	0.20	0.25	0.20	0.20	0.20

Overall, the irrigation volumes supplied by the model are lower than those actually applied by farmers, even under the precipitation reduction. The only exceptions occur in Field F (2019) and Fields E and G (2020), where the simulated volumes slightly exceed the recorded irrigation amounts in both production configurations (underlined values).

The frequency increases year by year; clearly, higher frequencies are observed for table olive production compared to oil production. The highest frequencies occur in 2020, probably because that year was overall drier than 2019, despite rainfall during the summer of 2020 being higher than in the summer of 2019.

Nevertheless, it is important to note that, despite the analysis being conducted under scenarios that assume reduced precipitation, the model generally recommends lower irrigation volumes than those applied.

6.8.4 Closing remarks – One field analysis

Considering the Field A, **Figure 6.68** illustrates the plot outputs produced by the model in SaC mode for both oil and olive production.

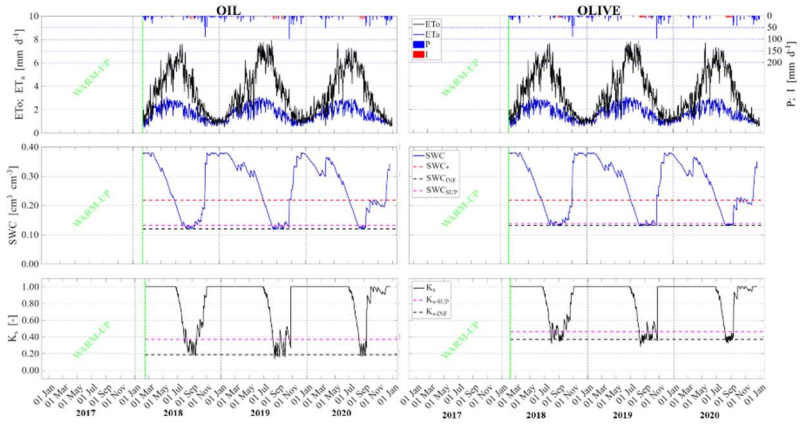

Figure 6.68 Output of IRRILEARNING in SaC mode for field A for both oil and olive table production. The upper row show the temporal dynamic of ETo (black function) from PM equation, ET_a for the ML model (blue function), precipitation depth (blue bar) and the irrigiation supplies and the provide relative volume (red bar); the midlle row show the SWC temporal dynamic (blue function), the red line indicate the stress threshold, the blue line indicate the SWC after that the irrigation start and the magenta line the irrigation stop; finally the bottom line show the K_s temporal dynamic, the black line indicate the K_s after that the irrigation start and the magenta line the irrigation stop

The first row shows the temporal evolution of crop reference evapotranspiration computed using the PM equation **(3.10)** , the actual evapotranspiration estimated through ML, the distribution and magnitude of precipitation, and the irrigation volumes supplied by the model according to the imposed irrigation rules. It can be observed that, under the oil production strategy, the model supplies fewer irrigation events with larger depths, whereas for table olive production it applies more frequent irrigations with smaller depths.

The second row illustrates the temporal dynamics of *SWC*, together with the threshold for the beginning of water stress and the irrigation intervention thresholds. The variability range is slightly wider for the oil production scenario and more constrained for table olive production.

The third row presents the evolution of the K_s and its variability range as determined by the selected irrigation thresholds.

Regarding the K_c, a comparison was performed between the residual K_c and the tabulated K_c values suggested by Rallo et al. (2021) and Allen et al. (1998). The residual K_c was computed as:

$$Residual\ K_c = \frac{ML\ ET_a}{ET_o \cdot\ K_s(SWC)} \tag{6.9}$$

Figure 6.69 shows the comparison with the tabulated K_c values in SaC mode for oil production, while **Figure 6.70** displays the comparison for table olive production, for all the years.

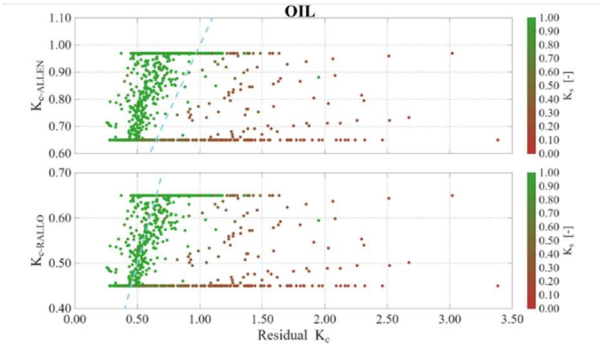

Figure 6.69 Comparison between Residual and tabled K_c for oil production; in the upper row, residuals are against the ones retrieved by Allen et al. (1998); in the bottom row, residualds are against the ones retrived by Rallo et al. (2021); the color bar indicates the corresponding values of K_s

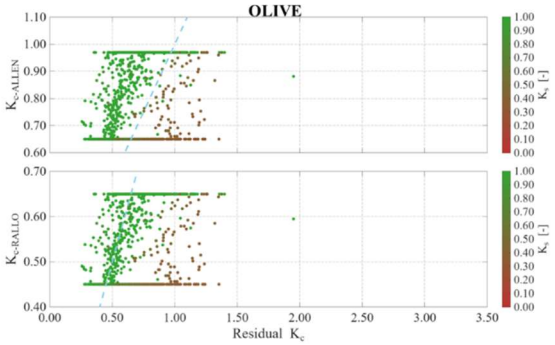

Figure 6.70 Comparison between Residual and tabled K_c for live table production; in the upper row, residuals are against the ones retrieved by Allen et al. (1998); in the bottom row, residualds are against the ones retrived by Rallo et al. (2021); the color bar indicates the corresponding values of K_s

As observed in the two figures, before the onset of severe stress ($K_s > 0.40$), the residual K_c values align well with the tabulated values from Rallo et al. (2021), with points distributed closely around the 1:1 line. In this review, the authors updated the tabulated K_c values for different crop stages. However, as stress becomes more severe ($K_s > 0.40$), the residual K_c values start to deviate from this behavior. The plots also display plateaus, reflecting the trapezoidal pattern of the tabulated K_c, which includes extended periods with constant values.

Figure 6.71 shows the irrigation volumes supplied by the farmer, those simulated by IRRILEARNING in SaC mode and those obtained under the Scenario Management mode, over the three years.

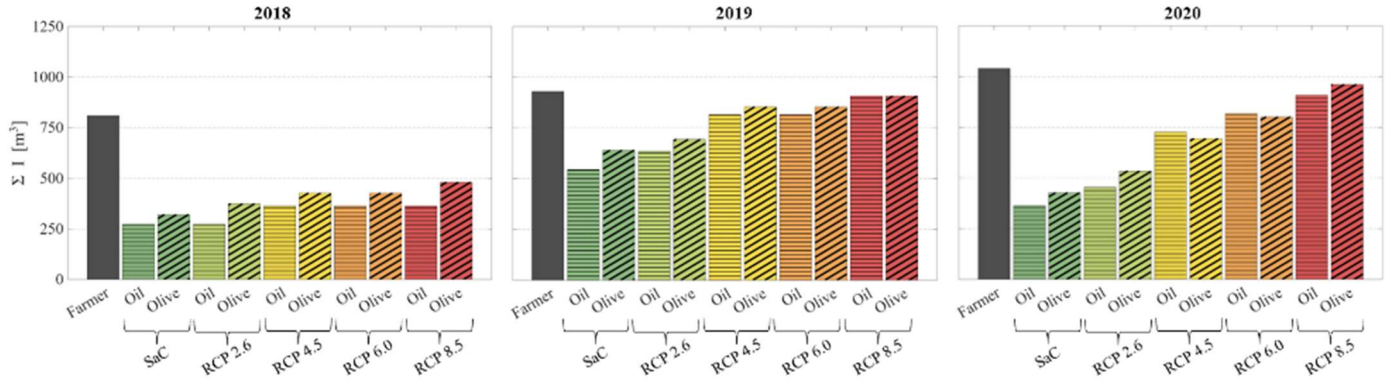

Figure 6.71 Exploded view of a field (A) showing the irrigation volume provided by farmers (dark grey bars) compared with the irrigation volume provided by IRRILEARNING using the SaC and Scenario Management modes (light green: RCP2.6; yellow: RCP4.5; orange: RCP6.0; red: RCP8.5) for oil production (green bars with horizontal lines) and table olive production (green bars with skewed lines) (bottom row)

As previously discussed, for a given scenario the differences between oil and table olive production are not significant. This is because, in the case of oil production, the model schedules fewer irrigation events with larger volumes, whereas for table olive production it recommends a higher number of irrigation events with smaller volumes.

To analyze the irrigation schedules, Gantt charts were used.

Figure 6.72 shows that, for oil production, the irrigation seasons in 2018 are consistently shifted compared with the actual ones, considering that the Jan–Apr period was particularly rainy.

As a result, irrigation events are concentrated toward the end of the irrigation window; in 2019, the irrigation schedules are again shifted, although in this case the events are more concentrated at the beginning of the irrigation season; finally, in 2020, irrigation events appear to be more evenly distributed throughout the irrigation windows.

For table olive production, **Figure 6.73** shows that most irrigation windows are longer, with earlier starting dates and later ending dates compared with the oil production. The temporal distribution of irrigation events remains generally similar; however, the number of interventions is noticeably higher.

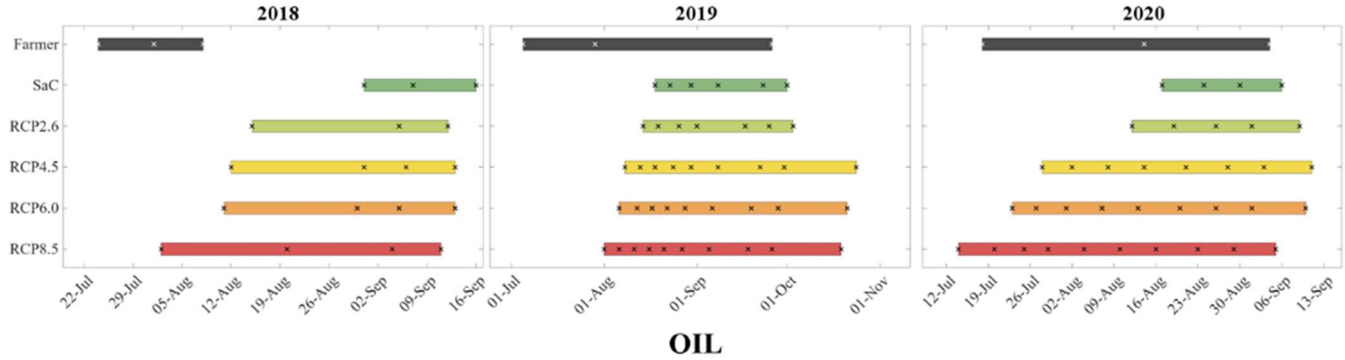

Figure 6.72 Gantt charts showing, for each year in field A, the duration of the irrigation season and the days on which either the farmer or the model performs irrigation for oil production

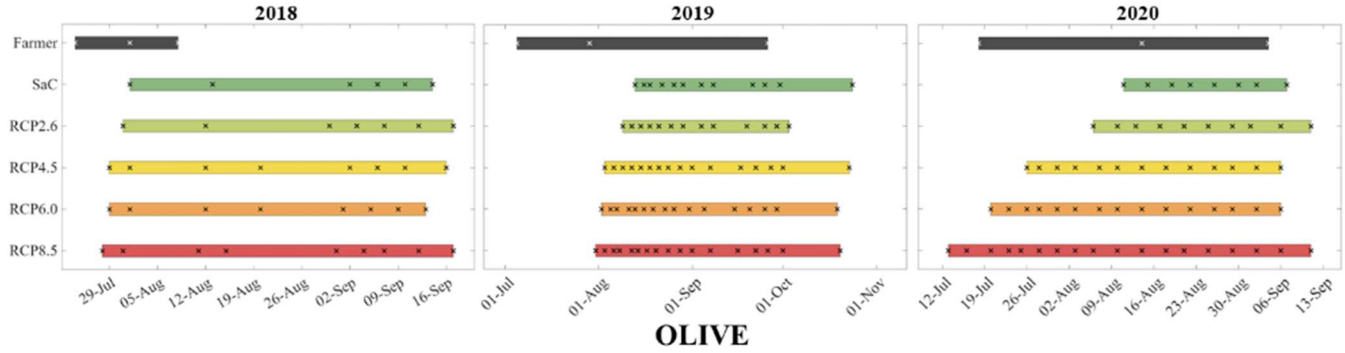

Figure 6.73 Gantt charts showing, for each year in field A, the duration of the irrigation season and the days on which either the farmer or the model performs irrigation for olive production

Conclusions and recommendations

In the framework of increasing pressure on water resources and the need to enhance the sustainability of irrigated agriculture, this thesis has investigated innovative approaches for the estimation and modelling of water footiprint, with particular attention to actual evapotranspiration and crop water requirement. By integrating *in situ* measurements, reanalysis and forecast datasets, remote sensing observations, and advanced modelling techniques, the study has provided a comprehensive assessment of the SPA continuum and its role in regulating water fluxes in Mediterranean agroecosystems, specifically in citrus and olive orchard.

The multidisciplinary approach adopted in this thesis, combining physically based models, data assimilation, and Earth Observation technologies, has enabled the identification of both opportunities and limitations associated with each methodology, as well as the potential benefits arising from their integration. Emphasis has been placed on the applicability of these approaches in operational contexts, especially in data-scarce regions and under climate variability scenarios, where reliable and scalable tools for irrigation management are increasingly required.

Within this context, the research has been guided by a set of key RQs aimed at evaluating the reliability of alternative data sources, the performance of ML techniques, the integration of modelling frameworks, and the comparative strengths of different approaches for water footprint estimation. The following section provides a synthesis of the main findings of the study, structured as direct answers to these RQs:

- *RQ1 Answer.* The results show that reanalysis data, particularly ERA5-Land database, can be considered reliable surrogates of *in situ* measurements for several key meteorological variables, especially mean air temperature

and global solar radiation, which exhibited high correlation coefficients ($R^2_{Ta\text{-}Mean}$ = 0.96 and R^2_{Rs} = 0.92 for olive orchard; $R^2_{Ta\text{-}Mean}$ = 0.95 and R^2_{Rs} = 0.91 for citrus orchard) and good agreement with *in situ* observations. This reliability translates into encouraging performances in the estimation of crop reference evapotranspiration (*ETo*), with high R^2 values (0.94 for olive orchard; 0.91 for citrus orchard) and relatively low errors (*RMSE* = 0.53 mm d^{-1} and *MBE* = -0.16 mm d^{-1} for olive orchard; *RMSE* = 0.57 mm d^{-1}; *MBE* = 0.25 mm d^{-1} for citrus orchard).

However, the analysis also highlights some important limitations. Precipitation showed low correlation with *in situ* data at daily scale (R^2 = 0.45 for olive orchard; R^2 = 0.40 for citrus orchard), indicating that reanalysis products may struggle to reproduce local rainfall dynamics. Despite this, cumulative precipitation trends were reasonably well captured (from -140.40 mm to +68.80 mm, for olive orchard; from -222.02 mm to +223.10 mm, for citrus orchard), suggesting suitability for long-term analyses rather than event-scale applications.

Overall, reanalysis data can effectively replace *in situ* measurements in data-scarce regions for estimating water footprint (*i.e.*, $LE_{SPARSE;3\text{-}combination}$ = 87 W m^{-2}; $SWC_{;SAMIR;2a}$ = 0.02 cm^3 cm^{-3} and $ET_{a;SAMIR;2a}$ = 0.60 mm d^{-1}; $ET_{a;ML;3\text{-}combination}$ = 0.52 mm d^{-1} for citrus orchard and $ET_{a;ML;3\text{-}combination}$ = 0.50 mm d^{-1} for olive orchard), although caution is needed for variables characterized by high spatial variability, such as precipitation.

- *RQ2 Answer.* The Machine Learning (ML) models, particularly the Gaussian Process Regression (GPR), demonstrated good performance in estimating actual evapotranspiration when trained using variables from the SPA continuum and satellite-derived inputs. The results show satisfactory agreement with *in situ* measurements (with R^2 values up to 0.81 and low *RMSE* values from 0.46

to 0.52 mm d^{-1} for citrus orchard; with R^2 values up to 0.68 and low *RMSE* values from 0.49 to 0.51 mm d^{-1} for olive orchard), confirming the robustness of the approach.

The inclusion of VIs derived from remote sensing significantly improved model performance, highlighting the importance of integrating satellite data for capturing crop dynamics. Even when using only freely available data (reanalysis and remote sensing), the models maintained acceptable accuracy (*RMSE* = 0.52 mm d^{-1} for citrus orchard; *RMSE* = 0.50 mm d^{-1} for olive orchard), demonstrating their applicability in operational contexts where field measurements are unavailable.

Nevertheless, model performance tends to decrease at higher evapotranspiration values (*e.g.*, ET_a > 2.5–3 mm d^{-1}), indicating some limitations in capturing extreme conditions. Overall, ML models proved to be flexible, scalable, and effective tools for spatially distributed ET_a estimation.

- *RQ3 Answer.* The integration of the ML model with a SWB model represents a key advancement of the research. ML models provide accurate and continuous estimates of ET_a, which can be used as dynamic inputs within SWB frameworks to simulate soil water content and crop water status (stress coefficient) over time.

  Thus, this integration enables the development of advanced decision-support tools, named IRRILEARNING, which combines ML predictions, soil water content dynamics, and vegetation stress to support irrigation scheduling. In particular, the system allows for the identification of optimal irrigation thresholds, improving both irrigation management and forecasting capabilities. The model has been specifically designed to support different production objectives, including both olive oil production and table olive cultivation, thus

ensuring its applicability across diverse management strategies.

Moreover, the use of forecast data as inputs allows extending this framework to predictive scenarios, making it suitable for climate change applications. In this regard, specific scenarios based on IPCC projections have been analyzed to evaluate the response of the system under future climatic conditions. In this way, irrigation strategies can be adapted proactively based on expected meteorological conditions, enhancing resilience and water use efficiency.

- *RQ4 Answer.* The comparative analysis, set up in the citrus orchard, highlights that each modelling approach presents specific strengths and limitations, which can be quantitatively assessed through dedicated performance metrics.

  SPARSE, which is a SEB model based on LST retrieved from satellite images, provides spatially distributed estimates and is particularly effective for large-scale applications, but it is sensitive to input uncertainties, especially in meteorological variables. Its performance assessment, based on comparisons with eddy covariance measurements, highlights a good capability in reproducing instantaneous fluxes ($RMSE_{Rn}$ from 17 to 27 W m^{-2}; $RMSE_H$ from 48 to 69 W m^{-2}; $RMSE_{LE}$ from 64 to 87 W m^{-2}; $RMSE_{G0}$ from 15 to 16 W m^{-2}).

  SAMIR, the SWB model, is simple, physically interpretable, and directly applicable to irrigation management, but it requires accurate parameterization and high-quality input data. Its performance was evaluated by comparing simulated and observed soil water content and actual evapotranspiration and transpiration values, showing generally good agreement, as confirmed by satisfactory statistical indicators ($RMSE_{SWC}$ from 0.01 to 0.02 cm^3 cm^{-3}; $RMSE_{ETa}$ from 0.51 to 0.60 mm d^{-1}; $RMSE_T$

from 0.39 mm d^{-1} to 0.40 mm d^{-1}), which demonstrate its reliability under well-calibrated conditions.

The Eddy Covariance-based partitioning method offers a highly accurate partitioning of monitored actual evapotranspiration into transpiration and evaporation, making it a reliable reference for model validation. The robustness of this method is supported by the consistency and high temporal resolution of flux measurements, typically reflected in low uncertainty levels and strong internal energy balance closure, although its application is limited to point-scale measurements and requires complex and costly instrumentation.

The main outcome of the research is that these approaches are not mutually exclusive but complementary. Their integration allows exploiting their respective strengths. This synergy leads to more robust, scalable, and operational tools for estimating water footprint and supporting efficient irrigation management in agricultural systems.

In conclusion, this research demonstrates that the integration of advanced technologies, such as remote sensing, ML, and multi-source data assimilation, represents an effective and innovative strategy for improving irrigation volumes savings in agriculture. These approaches contribute to reducing water consumption, increasing water use efficiency, and strengthening the resilience of agricultural systems to climate variability and change, in line with the principles of Agriculture 4.0. Furthermore, they are consistent with the strategic priorities of Horizon Europe, particularly the missions on Climate Change Adaptation and Soil Health and Food, as well as with the Sustainable Development Goals (SDGs), including Goal 2 (Zero Hunger), Goal 13 (Climate Action), and Goal 15 (Life on Land), thereby supporting the transition towards more sustainable and climate-resilient farming systems.

Future research line

Building on the results obtained in this thesis, several future developments can be identified to further enhance the robustness, scalability, and applicability of the proposed approaches. A first research direction concerns the extension of the implemented models to different climatic contexts and cropping systems. While the present study focused on Mediterranean environments and perennial crops such as citrus and olive orchards, testing the performance of Soil Water Balance models, Surface Energy Balance models, CO_2-base partitioning method and Machine Learning approaches under diverse climatic conditions (*e.g.*, arid, semi-arid, or temperate regions) and for different crop types (*e.g.*, annual crops or intensive horticultural systems) would allow for a more comprehensive assessment of their generalization capability and operational potential.

In addition, further research should explore the use of climate projection datasets, such as those provided by the CORDEX initiative, to assess the impacts of climate change on crop water requirements and irrigation management. Integrating these projections within the IRRILEARNING framework would enable the simulation of future scenarios, supporting the development of adaptive irrigation strategies under changing climatic conditions. This would represent a significant step towards the implementation of climate-resilient decision-support systems.

Another relevant line of research involves improving the reliability of precipitation data derived from reanalysis products. As highlighted in this work, precipitation remains one of the main sources of uncertainty, particularly at local scale. Future efforts could focus on the development of bias-correction techniques, data assimilation strategies, or hybrid approaches combining reanalysis data with ground observations and satellite-based rainfall estimates, to enhance the accuracy of precipitation inputs and, consequently, the performance of hydrological and evapotranspiration models.

Finally, future studies could focus on the continuous improvement of the integration among modelling approaches, remote sensing data, and Machine Learning techniques, with particular attention to real-

time applications and operational deployment. The development of user-friendly platforms and tools for stakeholders, including farmers and water managers, could further enhance the practical impact of the proposed methodologies, contributing to the advancement of precision agriculture and sustainable water resource management.

References

Aguiar, L.M., Pereira, B., Lauret, P., Díaz, F., David, M., 2016. Combining solar irradiance measurements, satellite-derived data and a numerical weather prediction model to improve intra-day solar forecasting. Renewable Energy 97, 599–610. https://doi.org/10.1016/j.renene.2016.06.018

Allen, R.G., Pereira, L.S., Raes, D., Smith, M. (Eds.), 1998. FAO irrigation and drainage paper No. 56., repr. ed, FAO irrigation and drainage paper. Food and Agriculture Organization of the United Nations, Rome.

Amato, F., Ippolito, M., De Caro, D., Croce, D., Pagano, A., 2026. Machine learning models for actual crop coefficient estimation on sensor-less fields. Smart Agricultural Technology 13, 101708. https://doi.org/10.1016/j.atech.2025.101708

Anderson, M.C., Norman, J.M., Kustas, W.P., Li, F., Prueger, J.H., Mecikalski, J.R., 2005. Effects of Vegetation Clumping on Two–Source Model Estimates of Surface Energy Fluxes from an Agricultural Landscape during SMACEX. Journal of Hydrometeorology 6, 892–909. https://doi.org/10.1175/JHM465.1

Anderson, M.C., Norman, J.M., Mecikalski, J.R., Torn, R.D., Kustas, W.P., Basara, J.B., 2004. A Multiscale Remote Sensing Model for Disaggregating Regional Fluxes to Micrometeorological Scales. J. Hydrometeor 5, 343–363. https://doi.org/10.1175/1525-7541(2004)005%3C0343:AMRSMF%3E2.0.CO;2

Anderton, S., Latron, J., Gallart, F., 2002. Sensitivity analysis and multi-response, multi-criteria evaluation of a physically based distributed model. Hydrological Processes 16, 333–353. https://doi.org/10.1002/hyp.336

Andres-Anaya, P., Sanchez-Aparicio, M., Del Pozo, S., Lagüela, S., Hernández-López, D., Gonzalez-Aguilera, D., 2023. A New Methodology for Estimating Surface Albedo in Heterogeneous Areas

from Satellite Imagery. Applied Sciences 14, 75. https://doi.org/10.3390/app14010075

Arneth, A., 2015. Uncertain future for vegetation cover. Nature 524, 44–45. https://doi.org/10.1038/524044a

Asrar, G., Fuchs, M., Kanemasu, E.T., Hatfield, J.L., 1984. Estimating Absorbed Photosynthetic Radiation and Leaf Area Index from Spectral Reflectance in Wheat[1]. Agronomy Journal 76, 300–306. https://doi.org/10.2134/agronj1984.00021962007600020029x

Aubinet, M., Grelle, A., Ibrom, A., Rannik, Ü., Moncrieff, J., Foken, T., Kowalski, A.S., Martin, P.H., Berbigier, P., Bernhofer, Ch., Clement, R., Elbers, J., Granier, A., Grünwald, T., Morgenstern, K., Pilegaard, K., Rebmann, C., Snijders, W., Valentini, R., Vesala, T., 1999. Estimates of the Annual Net Carbon and Water Exchange of Forests: The EUROFLUX Methodology, in: Advances in Ecological Research. Elsevier, pp. 113–175. https://doi.org/10.1016/S0065-2504(08)60018-5

Aubinet, M., Vesala, T., Papale, D. (Eds.), 2012. Eddy Covariance: A Practical Guide to Measurement and Data Analysis. Springer Netherlands, Dordrecht. https://doi.org/10.1007/978-94-007-2351-1

Autovino, D., Minacapilli, M., Provenzano, G., 2016. Modelling bulk surface resistance by MODIS data and assessment of MOD16A2 evapotranspiration product in an irrigation district of Southern Italy. Agricultural Water Management 167, 86–94. https://doi.org/10.1016/j.agwat.2016.01.006

Autovino, D., Rallo, G., Provenzano, G., 2018. Predicting soil and plant water status dynamic in olive orchards under different irrigation systems with Hydrus-2D: Model performance and scenario analysis. Agricultural Water Management 203, 225–235. https://doi.org/10.1016/j.agwat.2018.03.015

Awada, H., Ciraolo, G., Maltese, A., Provenzano, G., Moreno Hidalgo, M.A., Còrcoles, J.I., 2019. Assessing the performance of a large-scale irrigation system by estimations of actual evapotranspiration obtained by Landsat satellite images resampled with cubic convolution. International Journal of Applied Earth

Observation and Geoinformation 75, 96–105. https://doi.org/10.1016/j.jag.2018.10.016

Awe, G.O., Akomolafe, T.N., Umam, J., Ayuba, M.B., 2020. Efficiency of small pan evaporimeter in monitoring evapotranspiration under poly-covered house and open-field conditions in a hot, tropical region of Nigeria. Journal of Hydrology: Regional Studies 32, 100735. https://doi.org/10.1016/j.ejrh.2020.100735

Bai, J., Chen, X., Dobermann, A., Yang, H., Cassman, K.G., Zhang, F., 2010. Evaluation of NASA Satellite- and Model-Derived Weather Data for Simulation of Maize Yield Potential in China. Agronomy Journal 102, 9–16. https://doi.org/10.2134/agronj2009.0085

Bal, S.K., Wakchaure, G.C., Potekar, S., Choudhury, B.U., Choudhary, R.L., Sahoo, R.N., 2021. Spectral Signature-Based Water Stress Characterization and Prediction of Wheat Yield under Varied Irrigation and Plant Bio-regulator Management Practices. J Indian Soc Remote Sens 49, 1427–1438. https://doi.org/10.1007/s12524-021-01325-6

Baldauf, M., Seifert, A., Förstner, J., Majewski, D., Raschendorfer, M., Reinhardt, T., 2011. Operational Convective-Scale Numerical Weather Prediction with the COSMO Model: Description and Sensitivities. Monthly Weather Review 139, 3887–3905. https://doi.org/10.1175/MWR-D-10-05013.1

Baldocchi, D.D., 2003. Assessing the eddy covariance technique for evaluating carbon dioxide exchange rates of ecosystems: past, present and future. Global Change Biology 9, 479–492. https://doi.org/10.1046/j.1365-2486.2003.00629.x

Bales, R.C., 2003. HYDROLOGY | Overview, in: Encyclopedia of Atmospheric Sciences. Elsevier, pp. 968–973. https://doi.org/10.1016/B0-12-227090-8/00166-4

Baret, F., Clevers, J.G.P.W., Steven, M.D., 1995. The robustness of canopy gap fraction estimates from red and near-infrared reflectances: A comparison of approaches. Remote Sensing of

Environment 54, 141–151. https://doi.org/10.1016/0034-4257(95)00136-O

Barlage, M., Zeng, X., 2004. The Effects of Observed Fractional Vegetation Cover on the Land Surface Climatology of the Community Land Model. J. Hydrometeor 5, 823–830. https://doi.org/10.1175/1525-7541(2004)005%3C0823:TEOOFV%3E2.0.CO;2

Bastiaanssen, W.G.M., Menenti, M., Feddes, R.A., Holtslag, A.A.M., 1998. A remote sensing surface energy balance algorithm for land (SEBAL). 1. Formulation. Journal of Hydrology 212–213, 198–212. https://doi.org/10.1016/S0022-1694(98)00253-4

Bates, B.C., Charles, S.P., Hughes, J.P., 1998. Stochastic downscaling of numerical climate model simulations. Environmental Modelling & Software 13, 325–331. https://doi.org/10.1016/S1364-8152(98)00037-1

Bauer, P., Thorpe, A., Brunet, G., 2015. The quiet revolution of numerical weather prediction. Nature 525, 47–55. https://doi.org/10.1038/nature14956

Bellido-Jiménez, J.A., Gualda, J.E., García-Marín, A.P., 2021. Assessing Machine Learning Models for Gap Filling Daily Rainfall Series in a Semiarid Region of Spain. Atmosphere 12, 1158. https://doi.org/10.3390/atmos12091158

Benli, B., Kodal, S., Ilbeyi, A., Ustun, H., 2006. Determination of evapotranspiration and basal crop coefficient of alfalfa with a weighing lysimeter. Agricultural Water Management 81, 358–370. https://doi.org/10.1016/j.agwat.2005.05.003

Bhuyan, J.M., Udmale, P.D., 2025. Forest fire occurrence patterns and hotspot analysis in Maharashtra using MODIS fire points from FIRMS. Sustainable Geosciences: People, Planet and Prosperity 1, 100009. https://doi.org/10.1016/j.susgeo.2025.100009

BJERKNES, V., 1904: Das Problem der Wettervorhersage, betrachtet vonStandpunkt der Mechanik und Physik. – Meteorol. Z. 21,1–7.

Bono et al., 1998. Carta dei suoli dell‟area Castelvetrano est: Contrada Seggio e limitrofe. Regione Siciliana, Assessorato Agricoltura e Foreste.

Boulet, G., Mougenot, B., Lhomme, J.-P., Fanise, P., Lili-Chabaane, Z., Olioso, A., Bahir, M., Rivalland, V., Jarlan, L., Merlin, O., Coudert, B., Er-Raki, S., Lagouarde, J.-P., 2015. The SPARSE model for the prediction of water stress and evapotranspiration components from thermal infra-red data and its evaluation over irrigated and rainfed wheat. Hydrol. Earth Syst. Sci. 19, 4653–4672. https://doi.org/10.5194/hess-19-4653-2015

Bouttier, F., & Courtier, P. (2002). Data assimilation concepts and methods. Meteorological Training Course Lecture Series, ECMWF.

Boyer, M., Miller, J., Belanger, M., Hare, E., Wu, J., 1988. Senescence and spectral reflectance in leaves of northern pin oak (Quercus palustris Muenchh.). Remote Sensing of Environment 25, 71–87. https://doi.org/10.1016/0034-4257(88)90042-9

Brutsaert, W., 2005. Hydrology: An Introduction, 1st ed. Cambridge University Press. https://doi.org/10.1017/CBO9780511808470

Bueno, I.T., Antunes, J.F.G., Dos Reis, A.A., Werner, J.P.S., Toro, A.P.S.G.D.D., Figueiredo, G.K.D.A., Esquerdo, J.C.D.M., Lamparelli, R.A.C., Coutinho, A.C., Magalhães, P.S.G., 2023. Mapping integrated crop-livestock systems in Brazil with planetscope time series and deep learning. Remote Sensing of Environment 299, 113886. https://doi.org/10.1016/j.rse.2023.113886

Burchard-Levine, V., Nieto, H., Kustas, W.P., Gao, F., Alfieri, J.G., Prueger, J.H., Hipps, L.E., Bambach-Ortiz, N., McElrone, A.J., Castro, S.J., Alsina, M.M., McKee, L.G., Zahn, E., Bou-Zeid, E., Dokoozlian, N., 2022. Application of a remote-sensing three-source energy balance model to improve evapotranspiration partitioning in vineyards. Irrig Sci 40, 593–608. https://doi.org/10.1007/s00271-022-00787-x

Burt, C.M., Clemmens, A.J., Strelkoff, T.S., Solomon, K.H., Bliesner, R.D., Hardy, L.A., Howell, T.A., Eisenhauer, D.E., 1997. Irrigation Performance Measures: Efficiency and Uniformity. J. Irrig.

Drain Eng. 123, 423–442. https://doi.org/10.1061/(ASCE)0733-9437(1997)123:6(423)

Buyantuyev, A., Wu, J., Gries, C., 2007. Estimating vegetation cover in an urban environment based on Landsat ETM+ imagery: A case study in Phoenix, USA. International Journal of Remote Sensing 28, 269–291. https://doi.org/10.1080/01431160600658149

Cammalleri, C., Anderson, M.C., Bambach, N.E., McElrone, A.J., Knipper, K., Roby, M.C., Ciraolo, G., DeCaro, D., Ippolito, M., Corbari, C., Ceppi, A., Mancini, M., Kustas, W.P., 2024. A fully remote sensing-based implementation of the two-source energy balance model: an application over Mediterranean crops. Agricultural Water Management 306, 109207. https://doi.org/10.1016/j.agwat.2024.109207

Cammalleri, C., Anderson, M.C., Bambach, N.E., McElrone, A.J., Knipper, K., Roby, M.C., Kustas, W.P., 2025. Field scale partitioning of Landsat land surface temperature into soil and canopy components for evapotranspiration assessment using a two-source energy balance model. Irrig Sci 43, 715–729. https://doi.org/10.1007/s00271-024-00976-w

Cammalleri, C., Anderson, M.C., Ciraolo, G., D'Urso, G., Kustas, W.P., La Loggia, G., Minacapilli, M., 2012a. Applications of a remote sensing-based two-source energy balance algorithm for mapping surface fluxes without in situ air temperature observations. Remote Sensing of Environment 124, 502–515. https://doi.org/10.1016/j.rse.2012.06.009

Cammalleri, C., Anderson, M.C., Ciraolo, G., D'Urso, G., Kustas, W.P., La Loggia, G., Minacapilli, M., 2010. The impact of in-canopy wind profile formulations on heat flux estimation in an open orchard using the remote sensing-based two-source model. Hydrol. Earth Syst. Sci. 14, 2643–2659. https://doi.org/10.5194/hess-14-2643-2010

Cammalleri, C., Anderson, M.C., Kustas, W.P., 2014. Upscaling of evapotranspiration fluxes from instantaneous to daytime scales for thermal remote sensing applications. Hydrol. Earth Syst. Sci. 18, 1885–1894. https://doi.org/10.5194/hess-18-1885-2014

Cammalleri, C., Ciraolo, G., La Loggia, G., Maltese, A., 2012b. Daily evapotranspiration assessment by means of residual surface energy balance modeling: A critical analysis under a wide range of water availability. Journal of Hydrology 452–453, 119–129. https://doi.org/10.1016/j.jhydrol.2012.05.042

Cammalleri, C., Rallo, G., Agnese, C., Ciraolo, G., Minacapilli, M., Provenzano, G., 2013. Combined use of eddy covariance and sap flow techniques for partition of ET fluxes and water stress assessment in an irrigated olive orchard. Agricultural Water Management 120, 89–97. https://doi.org/10.1016/j.agwat.2012.10.003

Carlson, T.N., Ripley, D.A., 1997. On the relation between NDVI, fractional vegetation cover, and leaf area index. Remote Sensing of Environment 62, 241–252. https://doi.org/10.1016/S0034-4257(97)00104-1

Carter, C., Liang, S., 2019. Evaluation of ten machine learning methods for estimating terrestrial evapotranspiration from remote sensing. International Journal of Applied Earth Observation and Geoinformation 78, 86–92. https://doi.org/10.1016/j.jag.2019.01.020

Caturegli, L., Matteoli, S., Gaetani, M., Grossi, N., Magni, S., Minelli, A., Corsini, G., Remorini, D., Volterrani, M., 2020. Effects of water stress on spectral reflectance of bermudagrass. Sci Rep 10, 15055. https://doi.org/10.1038/s41598-020-72006-6

Ceccato, P., Flasse, S., Tarantola, S., Jacquemoud, S., Grégoire, J.-M., 2001. Detecting vegetation leaf water content using reflectance in the optical domain. Remote Sensing of Environment 77, 22–33. https://doi.org/10.1016/S0034-4257(01)00191-2

Charney, J.G., Fjörtoft, R., Von Neumann, J., 1950. Numerical Integration of the Barotropic Vorticity Equation. TellusA 2, 237–254. https://doi.org/10.3402/tellusa.v2i4.8607

Charney, J.G., Phillips, N.A., 1953. NUMERICAL INTEGRATION OF THE QUASI-GEOSTROPHIC EQUATIONS FOR BAROTROPIC AND SIMPLE BAROCLINIC FLOWS. J. Meteor. 10, 71–99. https://doi.org/10.1175/1520-0469(1953)010%3C0071:NIOTQG%3E2.0.CO;2

Chehbouni, A., 2000. Estimation of heat and momentum fluxes over complex terrain using a large aperture scintillometer. Agricultural and Forest Meteorology 105, 215–226. https://doi.org/10.1016/S0168-1923(00)00187-8

Chen, S., He, C., Huang, Z., Xu, X., Jiang, T., He, Z., Liu, J., Su, B., Feng, H., Yu, Q., He, J., 2022. Using support vector machine to deal with the missing of solar radiation data in daily reference evapotranspiration estimation in China. Agricultural and Forest Meteorology 316, 108864. https://doi.org/10.1016/j.agrformet.2022.108864

Clemmens, A.J., Burt, C.M., 1997. Accuracy of Irrigation Efficiency Estimates. J. Irrig. Drain Eng. 123, 443–453. https://doi.org/10.1061/(ASCE)0733-9437(1997)123:6(443)

Consoli, S., Stagno, F., Roccuzzo, G., Cirelli, G.L., Intrigliolo, F., 2014. Sustainable management of limited water resources in a young orange orchard. Agricultural Water Management 132, 60–68. https://doi.org/10.1016/j.agwat.2013.10.006

Corbari, C., Paciolla, N., Rossi, G., Mancini, M., 2023. A double two-sources energy-water balance model for improving evapotranspiration estimates and irrigation management in fruit trees fields. Agricultural Water Management 289, 108522. https://doi.org/10.1016/j.agwat.2023.108522

Corbari, C., Skokovic Jovanovic, D., Nardella, L., Sobrino, J., Mancini, M., 2020. Evapotranspiration Estimates at High Spatial and Temporal Resolutions from an Energy–Water Balance Model and Satellite Data in the Capitanata Irrigation Consortium. Remote Sensing 12, 4083. https://doi.org/10.3390/rs12244083

Dasberg, S., Hopmans, J.W., 1992. Time Domain Reflectometry Calibration for Uniformly and Nonuniformly Wetted Sandy and Clayey Loam Soils. Soil Science Soc of Amer J 56, 1341–1345. https://doi.org/10.2136/sssaj1992.03615995005600050002x

Davidson, E.A., Janssens, I.A., 2006. Temperature sensitivity of soil carbon decomposition and feedbacks to climate change. Nature 440, 165–173. https://doi.org/10.1038/nature04514

De Bruin, H.A.R., Meijninger, W.M.L., Smedman, A.-S., Magnusson, M., 2002. Displaced-Beam Small Aperture Scintillometer Test. Part I: The Wintex Data-Set. Boundary-Layer Meteorology 105, 129–148. https://doi.org/10.1023/A:1019639631711

De Caro, D., Ippolito, M., Cannarozzo, M., Provenzano, G., Ciraolo, G., 2023. Assessing the performance of the Gaussian Process Regression algorithm to fill gaps in the time-series of daily actual evapotranspiration of different crops in temperate and continental zones using ground and remotely sensed data. Agricultural Water Management 290, 108596. https://doi.org/10.1016/j.agwat.2023.108596

De Marinis, P., G. Manfron, G., Sali, C., Provolo, G., Facchi, A., Sali, G., 2019. Integrating remote sensing and census information for land securing in Nord Kivu, DRC. JUNCO | Journal of UNiversities and international development COoperation N. 1-2, Milano 1415 settembre 2017. https://doi.org/10.13135/2531-8772/3680

Delamater, P.L., Messina, J.P., Qi, J., Cochrane, M.A., 2012. A hybrid visual estimation method for the collection of ground truth fractional coverage data in a humid tropical environment. International Journal of Applied Earth Observation and Geoinformation 18, 504–514. https://doi.org/10.1016/j.jag.2011.10.005

DESA/POP, U., 2022. United Nations Department of Economic and Social Affairs, Population Division (2022). World Population Prospects 2022: Summary of Results. UN DESA/POP/2022/TR/NO. 3.. Montreal, Canada.

Dirksen, C., Dasberg, S., 1993. Improved Calibration of Time Domain Reflectometry Soil Water Content Measurements. Soil Science Soc of Amer J 57, 660–667. https://doi.org/10.2136/sssaj1993.03615995005700030005x

Do, F., Rocheteau, A., 2002. Influence of natural temperature gradients on measurements of xylem sap flow with thermal dissipation probes. 2. Advantages and calibration of a noncontinuous

heating system. Tree Physiology 22, 649–654. https://doi.org/10.1093/treephys/22.9.649

Dolman, A.J., Miralles, D.G., De Jeu, R.A.M., 2014. Fifty years since Monteith's 1965 seminal paper: the emergence of global ecohydrology. Ecohydrology 7, 897–902. https://doi.org/10.1002/eco.1505

Dong, J., Zeng, W., Wu, L., Huang, J., Gaiser, T., Srivastava, A.K., 2023. Enhancing short-term forecasting of daily precipitation using numerical weather prediction bias correcting with XGBoost in different regions of China. Engineering Applications of Artificial Intelligence 117, 105579. https://doi.org/10.1016/j.engappai.2022.105579

Du, K.-L., Zhang, R., Jiang, B., Zeng, J., Lu, J., 2025. Understanding Machine Learning Principles: Learning, Inference, Generalization, and Computational Learning Theory. Mathematics 13, 451. https://doi.org/10.3390/math13030451

Eames, I.W., Marr, N.J., Sabir, H., 1997. The evaporation coefficient of water: a review. International Journal of Heat and Mass Transfer 40, 2963–2973. https://doi.org/10.1016/S0017-9310(96)00339-0

Eisenhauer, J.G., 2003. Regression through the Origin. Teaching Statistics 25, 76–80. https://doi.org/10.1111/1467-9639.00136

El Hachimi, J., El Harti, A., Lhissou, R., Ouzemou, J.-E., Chakouri, M., Jellouli, A., 2022. Combination of Sentinel-2 Satellite Images and Meteorological Data for Crop Water Requirements Estimation in Intensive Agriculture. Agriculture 12, 1168. https://doi.org/10.3390/agriculture12081168

Er-Raki, S., Chehbouni, A., Guemouria, N., Ezzahar, J., Khabba, S., Boulet, G., Hanich, L., 2009. Citrus orchard evapotranspiration: Comparison between eddy covariance measurements and the FAO-56 approach estimates. Plant Biosystems - An International Journal Dealing with all Aspects of Plant Biology 143, 201–208. https://doi.org/10.1080/11263500802709897

Evett, S.R., Colaizzi, P.D., Marek, G.W., Copeland, K.S., Ruthardt, B.B., 2025. Analysis and quality control of weighing

lysimeter water storage data. Agricultural Water Management 317, 109674. https://doi.org/10.1016/j.agwat.2025.109674

Faraminan, A.M.G., Degano, M.F., Carmona, F., Rodriguez, P.O., 2021. Estimation of actual evapotranspiration using NASA-POWER data and Support Vector Machine, in: 2021 XIX Workshop on Information Processing and Control (RPIC). Presented at the 2021 XIX Workshop on Information Processing and Control (RPIC), IEEE, SAN JUAN, Argentina, pp. 1–5. https://doi.org/10.1109/RPIC53795.2021.9648425

Feidas, H., Kontos, T., Soulakellis, N., Lagouvardos, K., 2007. A GIS tool for the evaluation of the precipitation forecasts of a numerical weather prediction model using satellite data. Computers & Geosciences 33, 989–1007. https://doi.org/10.1016/j.cageo.2006.12.001

Feldhake, C.M., Boyer, D.G., 1988. Use of Bellani plate evaporimeters for estimation of pet. Agricultural and Forest Meteorology 42, 219–227. https://doi.org/10.1016/0168-1923(88)90079-2

Fiebrich, C.A., Morgan, C.R., McCombs, A.G., Hall, P.K., McPherson, R.A., 2010. Quality Assurance Procedures for Mesoscale Meteorological Data. Journal of Atmospheric and Oceanic Technology 27, 1565–1582. https://doi.org/10.1175/2010JTECHA1433.1

Fisher, J.B., Melton, F., Middleton, E., Hain, C., Anderson, M., Allen, R., McCabe, M.F., Hook, S., Baldocchi, D., Townsend, P.A., Kilic, A., Tu, K., Miralles, D.D., Perret, J., Lagouarde, J., Waliser, D., Purdy, A.J., French, A., Schimel, D., Famiglietti, J.S., Stephens, G., Wood, E.F., 2017. The future of evapotranspiration: Global requirements for ecosystem functioning, carbon and climate feedbacks, agricultural management, and water resources. Water Resources Research 53, 2618–2626. https://doi.org/10.1002/2016WR020175

Foolad, F. (2018). Integration of Remote Sensing and Proximal Sensing for Improvement of Field Scale Water Management (Doctoral dissertation). University of Nebraska–Lincoln

French, A.N., Hunsaker, D.J., Sanchez, C.A., Saber, M., Gonzalez, J.R., Anderson, R., 2020. Satellite-based NDVI crop coefficients and evapotranspiration with eddy covariance validation for multiple durum wheat fields in the US Southwest. Agricultural Water Management 239, 106266. https://doi.org/10.1016/j.agwat.2020.106266

Fujino J, Nair R, Kainuma M, Masui T, Matsuoka Y (2006) Multigas mitigation analysis on stabilization scenarios using aim global model. The Energy Journal Special issue #3:343–354

Gao, B., 1996. NDWI—A normalized difference water index for remote sensing of vegetation liquid water from space. Remote Sensing of Environment 58, 257–266. https://doi.org/10.1016/S0034-4257(96)00067-3

Gao, Z., Yang, D., Li, C., Zhang, J., Wang, Q., 2025. A review of lysimeters from the perspective of measurement performance and intelligent development in China. Irrigation and Drainage 74, 276–298. https://doi.org/10.1002/ird.2997

Gates, D.M., 1980. Biophysical ecology, Springer advanced texts in life sciences. Springer-Verlag, New York.

Ghazouani, H., De Caro, D., Ippolito, M., Capodici, F., Ciraolo, G., 2025. Assessment of AquaCrop Inputs from ERA5-Land and Sentinel-2 for Soil Water Content Estimation and Durum Wheat Yield Prediction: A Case Study in a Tunisian Field. Water 17, 3522. https://doi.org/10.3390/w17243522

Giardini, L., 2004. Agronomia generale, ambientale e aziendale, 5. ed., rist. corretta. ed. Pàtron, Bologna.

Gong, L., Xu, C., Chen, D., Halldin, S., Chen, Y.D., 2006. Sensitivity of the Penman–Monteith reference evapotranspiration to key climatic variables in the Changjiang (Yangtze River) basin. Journal of Hydrology 329, 620–629. https://doi.org/10.1016/j.jhydrol.2006.03.027

Gong, Z., Gao, F., Chang, X., Hu, T., Li, Y., 2024. A review of interactions between irrigation and evapotranspiration. Ecological Indicators 169, 112870. https://doi.org/10.1016/j.ecolind.2024.112870

GonzÁlez-Altozano, P., Castel, J.R., 2000. Regulated deficit irrigation in 'Clementina de Nules' citrus trees. II: Vegetative growth. The Journal of Horticultural Science and Biotechnology 75, 388–392. https://doi.org/10.1080/14620316.2000.11511256

Gorelick, N., Hancher, M., Dixon, M., Ilyushchenko, S., Thau, D., Moore, R., 2017. Google Earth Engine: Planetary-scale geospatial analysis for everyone. Remote Sensing of Environment 202, 18–27. https://doi.org/10.1016/j.rse.2017.06.031

Goulden, M.L., Munger, J.W., Fan, S., Daube, B.C., Wofsy, S.C., 1996. Measurements of carbon sequestration by long-term eddy covariance: methods and a critical evaluation of accuracy. Global Change Biology 2, 169–182. https://doi.org/10.1111/j.1365-2486.1996.tb00070.x

Gourgouletis, N., Gkavrou, M., Baltas, E., 2023. Comparison of Empirical ETo Relationships with ERA5-Land and In Situ Data in Greece. Geographies 3, 499–521. https://doi.org/10.3390/geographies3030026

Granata, F., 2019. Evapotranspiration evaluation models based on machine learning algorithms—A comparative study. Agricultural Water Management 217, 303–315. https://doi.org/10.1016/j.agwat.2019.03.015

Granier, A., 1987. Evaluation of transpiration in a Douglas-fir stand by means of sap flow measurements. Tree Physiology 3, 309–320. https://doi.org/10.1093/treephys/3.4.309

Guo, Z., Shrestha, R., Zhang, W., Bhandary, P., Yu, G., Di, L., 2015. Land cover classification and change detection analysis using LandSat series and geospatial datasets in Nepal from 1980 to 2010, in: 2015 Fourth International Conference on Agro-Geoinformatics (Agro-Geoinformatics). Presented at the 2015 Fourth International Conference on Agro-Geoinformatics, IEEE, Istanbul, Turkey, pp. 414–418. https://doi.org/10.1109/Agro-Geoinformatics.2015.7248159

Gutman, G., Ignatov, A., 1998. The derivation of the green vegetation fraction from NOAA/AVHRR data for use in numerical

weather prediction models. International Journal of Remote Sensing 19, 1533–1543. https://doi.org/10.1080/014311698215333

Haltiner, G.J., Williams, R.T., 1980. Numerical prediction and dynamic meteorology, 2d ed. ed. Wiley, New York.

Hartmann, D.L., 2016. The Hydrologic Cycle, in: Global Physical Climatology. Elsevier, pp. 131–157. https://doi.org/10.1016/B978-0-12-328531-7.00005-0

Hartogensis, O.K., De Bruin, H.A.R., Van De Wiel, B.J.H., 2002. Displaced-Beam Small Aperture Scintillometer Test. Part Ii: Cases-99 Stable Boundary-Layer Experiment. Boundary-Layer Meteorology 105, 149–176. https://doi.org/10.1023/A:1019620515781

Hashimoto, H., Dungan, J., White, M., Yang, F., Michaelis, A., Running, S., Nemani, R., 2008. Satellite-based estimation of surface vapor pressure deficits using MODIS land surface temperature data. Remote Sensing of Environment 112, 142–155. https://doi.org/10.1016/j.rse.2007.04.016

Hemakumara, H.M., Chandrapala, L., Moene, A.F., 2003. Evapotranspiration fluxes over mixed vegetation areas measured from large aperture scintillometer. Agricultural Water Management 58, 109–122. https://doi.org/10.1016/S0378-3774(02)00131-2

Herkelrath, W.N., Hamburg, S.P., Murphy, F., 1991. Automatic, real-time monitoring of soil moisture in a remote field area with time domain reflectometry. Water Resources Research 27, 857–864. https://doi.org/10.1029/91WR00311

Hojabri, J., Nguyen-Huy, T., 2026. Spatio-temporal dynamics of vegetation and water bodies in the Lake Urmia Basin (1984–2022): an analysis using MODIS and Landsat data with new perspective. Journal of Arid Environments 232, 105500. https://doi.org/10.1016/j.jaridenv.2025.105500

Hölttä, T., Linkosalo, T., Riikonen, A., Sevanto, S., Nikinmaa, E., 2015. An analysis of Granier sap flow method, its sensitivity to heat storage and a new approach to improve its time dynamics. Agricultural and Forest Meteorology 211–212, 2–12. https://doi.org/10.1016/j.agrformet.2015.05.005

Huete, A.R., HuiQing Liu, Van Leeuwen, W.J.D., 1997. The use of vegetation indices in forested regions: issues of linearity and saturation, in: IGARSS'97. 1997 IEEE International Geoscience and Remote Sensing Symposium Proceedings. Remote Sensing - A Scientific Vision for Sustainable Development. Presented at the IGARSS'97. 1997 IEEE International Geoscience and Remote Sensing Symposium Proceedings. Remote Sensing - A Scientific Vision for Sustainable Development, IEEE, Singapore, pp. 1966–1968. https://doi.org/10.1109/IGARSS.1997.609169

Inglezakis, V.J., Poulopoulos, S.G., Arkhangelsky, E., Zorpas, A.A., Menegaki, A.N., 2016. Aquatic Environment, in: Environment and Development. Elsevier, pp. 137–212. https://doi.org/10.1016/B978-0-444-62733-9.00003-4

Intergovernmental Panel On Climate Change (Ipcc), 2023. Climate Change 2022 – Impacts, Adaptation and Vulnerability: Working Group II Contribution to the Sixth Assessment Report of the Intergovernmental Panel on Climate Change, 1st ed. Cambridge University Press. https://doi.org/10.1017/9781009325844

Iordache, M.-D., Tits, L., Bioucas-Dias, J.M., Plaza, A., Somers, B., 2014. A Dynamic Unmixing Framework for Plant Production System Monitoring. IEEE J. Sel. Top. Appl. Earth Observations Remote Sensing 7, 2016–2034. https://doi.org/10.1109/JSTARS.2014.2314960

Ippolito, M., De Caro, D., Cannarozzo, M., Provenzano, G., Ciraolo, G., 2024. Evaluation of daily crop reference evapotranspiration and sensitivity analysis of FAO Penman-Monteith equation using ERA5-Land reanalysis database in Sicily, Italy. Agricultural Water Management 295, 108732. https://doi.org/10.1016/j.agwat.2024.108732

Ippolito, M., De Caro, D., Ciraolo, G., Minacapilli, M., Provenzano, G., 2023. Estimating crop coefficients and actual evapotranspiration in citrus orchards with sporadic cover weeds based on ground and remote sensing data. Irrig Sci 41, 5–22. https://doi.org/10.1007/s00271-022-00829-4

Irmak, S., 2008. Evapotranspiration, in: Encyclopedia of Ecology. Elsevier, pp. 1432–1438. https://doi.org/10.1016/B978-008045405-4.00270-6

ISTAT, 2014. 6° Censimento Generale dell'Agricoltura Utilizzo della risorsa idrica a fini irrigui in agricoltura.

Jacquemoud, Stéphane, Ustin, Susan L, Jacquemoud, S, Ustin, S L, 2003. Application of radiative transfer models to moisture content estimation and burned land mapping NASA TE View project Gulf Deepwater Horizon oil spill View project Application of radiative transfer models to moisture content estimation and burned land mapping.

Janka, D., Lenders, F., Wang, S., Cohen, A., Li, N., 2019. Detecting and locating patterns in time series using machine learning. Control Engineering Practice 93, 104169. https://doi.org/10.1016/j.conengprac.2019.104169

Jégo, G., Pattey, E., Liu, J., 2012. Using Leaf Area Index, retrieved from optical imagery, in the STICS crop model for predicting yield and biomass of field crops. Field Crops Research 131, 63–74. https://doi.org/10.1016/j.fcr.2012.02.012

Jiang, Z., Huete, A.R., Chen, J., Chen, Y., Li, J., Yan, G., Zhang, X., 2006. Analysis of NDVI and scaled difference vegetation index retrievals of vegetation fraction. Remote Sensing of Environment 101, 366–378. https://doi.org/10.1016/j.rse.2006.01.003

Jiapaer, G., Chen, X., Bao, A., 2011. A comparison of methods for estimating fractional vegetation cover in arid regions. Agricultural and Forest Meteorology 151, 1698–1710. https://doi.org/10.1016/j.agrformet.2011.07.004

Johnson, K., Sankaran, S., Ehsani, R., 2013. Identification of Water Stress in Citrus Leaves Using Sensing Technologies. Agronomy 3, 747–756. https://doi.org/10.3390/agronomy3040747

Jones, J.W., Hoogenboom, G., Porter, C.H., Boote, K.J., Batchelor, W.D., Hunt, L.A., Wilkens, P.W., Singh, U., Gijsman, A.J., Ritchie, J.T., 2003. The DSSAT cropping system model. European Journal of Agronomy 18, 235–265. https://doi.org/10.1016/S1161-0301(02)00107-7

Kadiyala, A., Kumar, A., 2018. Applications of python to evaluate the performance of decision tree-based boosting algorithms. Env Prog and Sustain Energy 37, 618–623. https://doi.org/10.1002/ep.12888

Kaimal, J.C., Finnigan, J.J., 1994. Atmospheric Boundary Layer Flows: Their Structure and Measurement. Oxford University Press. https://doi.org/10.1093/oso/9780195062397.001.0001

Kalnay, E., 2002. Atmospheric Modeling, Data Assimilation and Predictability, 1st ed. Cambridge University Press. https://doi.org/10.1017/CBO9780511802270

Kang, M., Ichii, K., Kim, J., Indrawati, Y.M., Park, J., Moon, M., Lim, J.-H., Chun, J.-H., 2019. New Gap-Filling Strategies for Long-Period Flux Data Gaps Using a Data-Driven Approach. Atmosphere 10, 568. https://doi.org/10.3390/atmos10100568

Katul, G., Novick, K., 2009. Evapotranspiration, in: Encyclopedia of Inland Waters. Elsevier, pp. 661–667. https://doi.org/10.1016/B978-012370626-3.00012-0

Kennedy, J. B., & Neville, A. M. (1986). Basic statistical methods for engineers and scientists (3rd ed.). Harper and Row, New York.

Khosravi, Y., Homayouni, S., Ouarda, T.B.M.J., 2024. Spatio-temporal evaluation of MODIS temperature vegetation dryness index in the Middle East. Ecological Informatics 84, 102894. https://doi.org/10.1016/j.ecoinf.2024.102894

Kim, N., Kim, K., Lee, S., Cho, J., Lee, Y., 2020. Retrieval of Daily Reference Evapotranspiration for Croplands in South Korea Using Machine Learning with Satellite Images and Numerical Weather Prediction Data. Remote Sensing 12, 3642. https://doi.org/10.3390/rs12213642

Kottek, M., Grieser, J., Beck, C., Rudolf, B., Rubel, F., 2006. World Map of the Köppen-Geiger climate classification updated. metz 15, 259–263. https://doi.org/10.1127/0941-2948/2006/0130

Koudahe, K., Djaman, K., Adewumi, J.K., 2018. Evaluation of the Penman–Monteith reference evapotranspiration under limited data and its sensitivity to key climatic variables under humid and semiarid conditions. Model. Earth Syst. Environ. 4, 1239–1257. https://doi.org/10.1007/s40808-018-0497-y

Kriegler, F., Malila, W., Nalepka, R., Richardson, W., 1969. Preprocessing transformations and their effect on multispectral recognition., in: Proceedings of the 6th International Symposium on Remote Sensing of Environment. . University of Michigan, Ann Arbor, MI, pp. 97–131.

Kroes, J. G., van Dam, J. C., Huygen, J., & Vervoort, R. W. (1999). User's guide of SWAP version 2.0: Simulation of water flow, solute transport and plant growth in the Soil-Water-Atmosphere-Plant environment (Report No. 81). Wageningen: Winand Staring Centre

Kustas, W., Anderson, M., 2009. Advances in thermal infrared remote sensing for land surface modeling. Agricultural and Forest Meteorology 149, 2071–2081. https://doi.org/10.1016/j.agrformet.2009.05.016

Kustas, W.P., Zhan, X., Jackson, T.J., 1999. Mapping surface energy flux partitioning at large scales with optical and microwave remote sensing data from Washita '92. Water Resources Research 35, 265–277. https://doi.org/10.1029/98WR02094

Lagouarde, J.-P., Boulet, G., 2016. Energy Balance of Continental Surfaces and the Use of Surface Temperature, in: Land Surface Remote Sensing in Continental Hydrology. Elsevier, pp. 323–361. https://doi.org/10.1016/B978-1-78548-104-8.50010-3

Laluet, P., Olivera-Guerra, L., Rivalland, V., Simonneaux, V., Inglada, J., Bellvert, J., Er-raki, S., Merlin, O., 2023. A sensitivity analysis of a FAO-56 dual crop coefficient-based model under various field conditions. Environmental Modelling & Software 160, 105608. https://doi.org/10.1016/j.envsoft.2022.105608

Lanza, L.G., Cauteruccio, A., Stagnaro, M., 2022. Rain gauge measurements, in: Rainfall. Elsevier, pp. 77–108. https://doi.org/10.1016/B978-0-12-822544-8.00002-0

Lap, B.Q., Phan, T.-T.-H., Nguyen, H.D., Quang, L.X., Hang, P.T., Phi, N.Q., Hoang, V.T., Linh, P.G., Hang, B.T.T., 2023. Predicting Water Quality Index (WQI) by feature selection and machine learning: A case study of An Kim Hai irrigation system. Ecological Informatics 74, 101991. https://doi.org/10.1016/j.ecoinf.2023.101991

Larcher, W., (1983). Physiological Plant Ecology, corrected printing of the 2nd Edition, translated by M.A. Biederman-Thorson, Springer Verlag, New York, p. 20.

Lechi, G., 2001. Dispense del corso di telerilevamento.

Lei, H., Yang, D., 2014. Combining the Crop Coefficient of Winter Wheat and Summer Maize with a Remotely Sensed Vegetation Index for Estimating Evapotranspiration in the North China Plain. J. Hydrol. Eng. 19, 243–251. https://doi.org/10.1061/(ASCE)HE.1943-5584.0000765

Li, X., Gentine, P., Lin, C., Zhou, S., Sun, Z., Zheng, Y., Liu, J., Zheng, C., 2019. A simple and objective method to partition evapotranspiration into transpiration and evaporation at eddy-covariance sites. Agricultural and Forest Meteorology 265, 171–182. https://doi.org/10.1016/j.agrformet.2018.11.017

Liang, L., Li, L., Zhang, L., Li, J., Li, B., 2008. Sensitivity of penman-monteith reference crop evapotranspiration in Tao'er River Basin of northeastern China. Chin. Geogr. Sci. 18, 340–347. https://doi.org/10.1007/s11769-008-0340-x

Lin, C., Gentine, P., Huang, Y., Guan, K., Kimm, H., Zhou, S., 2018. Diel ecosystem conductance response to vapor pressure deficit is suboptimal and independent of soil moisture. Agricultural and Forest Meteorology 250–251, 24–34. https://doi.org/10.1016/j.agrformet.2017.12.078

Liu, M., Lei, H., Wang, X., Paredes, P., 2025. High-resolution mapping of evapotranspiration over heterogeneous cropland affected by soil salinity. Agricultural Water Management 308, 109301. https://doi.org/10.1016/j.agwat.2025.109301

Lloyd, J., Taylor, J.A., 1994. On the Temperature Dependence of Soil Respiration. Functional Ecology 8, 315. https://doi.org/10.2307/2389824

Loescher, H.W., Law, B.E., Mahrt, L., Hollinger, D.Y., Campbell, J., Wofsy, S.C., 2006. Uncertainties in, and interpretation of, carbon flux estimates using the eddy covariance technique. J. Geophys. Res. 111, 2005JD006932. https://doi.org/10.1029/2005JD006932

Longo-Minnolo, G., Vanella, D., Consoli, S., Pappalardo, S., Ramírez-Cuesta, J.M., 2022. Assessing the use of ERA5-Land reanalysis and spatial interpolation methods for retrieving precipitation estimates at basin scale. Atmospheric Research 271, 106131. https://doi.org/10.1016/j.atmosres.2022.106131

Lorenz, E.N., 1963. Deterministic Nonperiodic Flow. J. Atmos. Sci. 20, 130–141. https://doi.org/10.1175/1520-0469(1963)020%3C0130:DNF%3E2.0.CO;2

Manca G (2003) Analisi dei flussi di carbonio di una cronosequenza di cerro (Quercus cerris L.) dell' Italia centrale attraverso la tecnica della correlazione turbolenta. PhD Dissertation Thesis. Universita` degli Studi della Tuscia, Viterbo, 225 pp (in Italian)

Main-Knorn, M., Pflug, B., Louis, J., Debaecker, V., Müller-Wilm, U., Gascon, F., 2017. Sen2Cor for Sentinel-2, in: Bruzzone, L., Bovolo, F., Benediktsson, J.A. (Eds.), Image and Signal Processing for Remote Sensing XXIII. Presented at the Image and Signal Processing for Remote Sensing, SPIE, Warsaw, Poland, p. 3. https://doi.org/10.1117/12.2278218

Mariani, S., Casaioli, M., Accadia, C., Llasat, M.C., Pasi, F., Davolio, S., Elementi, M., Ficca, G., Romero, R., 2005. A limited area model intercomparison on the "Montserrat-2000" flash-flood event using statistical and deterministic methods. Nat. Hazards Earth Syst. Sci. 5, 565–581. https://doi.org/10.5194/nhess-5-565-2005

Marino, G., Caruso, T., Ferguson, L., Marra, F., 2018. Gas Exchanges and Stem Water Potential Define Stress Thresholds for Efficient Irrigation Management in Olive (Olea europea L.). Water 10, 342. https://doi.org/10.3390/w10030342

Marletto, V., Ventura, F., Fontana, G., Tomei, F., 2007. Wheat growth simulation and yield prediction with seasonal forecasts and a numerical model. Agricultural and Forest Meteorology 147, 71–79. https://doi.org/10.1016/j.agrformet.2007.07.003

Marra, F.P., Marino, G., Marchese, A., Caruso, T., 2016. Effects of different irrigation regimes on a super-high-density olive grove cv.

"Arbequina": vegetative growth, productivity and polyphenol content of the oil. Irrig Sci 34, 313–325. https://doi.org/10.1007/s00271-016-0505-9

Masek, J.G., Wulder, M.A., Markham, B., McCorkel, J., Crawford, C.J., Storey, J., Jenstrom, D.T., 2020. Landsat 9: Empowering open science and applications through continuity. Remote Sensing of Environment 248, 111968. https://doi.org/10.1016/j.rse.2020.111968

Maselli, F., Chiesi, M., Pieri, M., 2019. A New Method to Enhance the Spatial Features of Multitemporal NDVI Image Series. IEEE Trans. Geosci. Remote Sensing 57, 4967–4979. https://doi.org/10.1109/TGRS.2019.2894850

Maselli, F., Papale, D., Chiesi, M., Matteucci, G., Angeli, L., Raschi, A., Seufert, G., 2014. Operational monitoring of daily evapotranspiration by the combination of MODIS NDVI and ground meteorological data: Application and evaluation in Central Italy. Remote Sensing of Environment 152, 279–290. https://doi.org/10.1016/j.rse.2014.06.021

Matérn, B., 1986. Spatial Variation, Lecture Notes in Statistics. Springer New York, New York, NY. https://doi.org/10.1007/978-1-4615-7892-5

Mauder, M., Foken, T., Clement, R., Elbers, J.A., Eugster, W., Grünwald, T., Heusinkveld, B., Kolle, O., 2008. Quality control of CarboEurope flux data – Part 2: Inter-comparison of eddy-covariance software. Biogeosciences 5, 451–462. https://doi.org/10.5194/bg-5-451-2008

Mechoso, C.R., Arakawa, A., 2015. NUMERICAL MODELS | General Circulation Models, in: Encyclopedia of Atmospheric Sciences. Elsevier, pp. 153–160. https://doi.org/10.1016/B978-0-12-382225-3.00157-2

Mendelsohn, R., Kurukulasuriya, P., Basist, A., Kogan, F., Williams, C., 2007. Climate analysis with satellite versus weather station data. Climatic Change 81, 71–83. https://doi.org/10.1007/s10584-006-9139-x

Miralles, D.G., Brutsaert, W., Dolman, A.J., Gash, J.H., 2020. On the Use of the Term "Evapotranspiration." Water Resources Research 56, e2020WR028055. https://doi.org/10.1029/2020WR028055

Mokhtarzadeh, H., Gorjian, S., Minaei, S., 2025. Design, development, and evaluation of a low-cost smart solar-powered weather station for use in agricultural environments. Results in Engineering 26, 104848. https://doi.org/10.1016/j.rineng.2025.104848

Moncrieff, J.B., Massheder, J.M., De Bruin, H., Elbers, J., Friborg, T., Heusinkveld, B., Kabat, P., Scott, S., Soegaard, H., Verhoef, A., 1997. A system to measure surface fluxes of momentum, sensible heat, water vapour and carbon dioxide. Journal of Hydrology 188–189, 589–611. https://doi.org/10.1016/S0022-1694(96)03194-0

Montandon, L., Small, E., 2008. The impact of soil reflectance on the quantification of the green vegetation fraction from NDVI. Remote Sensing of Environment 112, 1835–1845. https://doi.org/10.1016/j.rse.2007.09.007

Monteith, J. L. 1965. Evaporation and environment, in G. E. Fogg, (Ed.) The State and Movement of Water in Living Organisms, Proceedings of the XIX Symposium of the Society of Experimental Biology, University Press, Cambridge 19, 205{234.

Monteith, J.L., 1986. Howard Latimer Penman, 10 April 1909 - 13 October 1984. Biographical Memoirs of Fellows of the Royal Society 377–404. https://doi.org/10.1098/rsbm.1986.0012

Moriondo, M., Maselli, F., Bindi, M., 2007. A simple model of regional wheat yield based on NDVI data. European Journal of Agronomy 26, 266–274. https://doi.org/10.1016/j.eja.2006.10.007

Moroni, M., Porti, M., Piro, P., 2019. Design of a Remote-Controlled Platform for Green Roof Plants Monitoring via Hyperspectral Sensors. Water 11, 1368. https://doi.org/10.3390/w11071368

Mosre, J., Suárez, F., 2021. Actual Evapotranspiration Estimates in Arid Cold Regions Using Machine Learning Algorithms with In Situ and Remote Sensing Data. Water 13, 870. https://doi.org/10.3390/w13060870

Mosteller, F., Tukey, J.W., 1968. Data analysis, including statistics. In: Lindzey, G., Aronson, E. (Eds.), Handbook of Social Psychology, first edition 1954, Vol. 2. Addison–Wesley.

Muñoz-Sabater, J., Dutra, E., Agustí-Panareda, A., Albergel, C., Arduini, G., Balsamo, G., Boussetta, S., Choulga, M., Harrigan, S., Hersbach, H., Martens, B., Miralles, D.G., Piles, M., Rodríguez-Fernández, N.J., Zsoter, E., Buontempo, C., Thépaut, J.-N., 2021. ERA5-Land: a state-of-the-art global reanalysis dataset for land applications. Earth Syst. Sci. Data 13, 4349–4383. https://doi.org/10.5194/essd-13-4349-2021

Mwangi, S., Boulet, G., Olioso, A., 2022. Assessment of an extended SPARSE model for estimating evapotranspiration from directional thermal infrared data. Agricultural and Forest Meteorology 317, 108882. https://doi.org/10.1016/j.agrformet.2022.108882

Nadler, A., Dasberg, S., Lapid, I., 1991. Time Domain Reflectometry Measurements of Water Content and Electrical Conductivity of Layered Soil Columns. Soil Science Soc of Amer J 55, 938–943. https://doi.org/10.2136/sssaj1991.03615995005500040007x

Nagai, M., Tianen Chen, Shibasaki, R., Kumagai, H., Ahmed, A., 2009. UAV-Borne 3-D Mapping System by Multisensor Integration. IEEE Trans. Geosci. Remote Sensing 47, 701–708. https://doi.org/10.1109/TGRS.2008.2010314

Namasudra, S., Dhamodharavadhani, S., Rathipriya, R., 2023. Nonlinear Neural Network Based Forecasting Model for Predicting COVID-19 Cases. Neural Process Lett 55, 171–191. https://doi.org/10.1007/s11063-021-10495-w

Narasimhan, T.N., 2009. Hydrological Cycle and Water Budgets, in: Encyclopedia of Inland Waters. Elsevier, pp. 714–720. https://doi.org/10.1016/B978-012370626-3.00010-7

Nash, J.E., Sutcliffe, J.V., 1970. River flow forecasting through conceptual models part I — A discussion of principles. Journal of Hydrology 10, 282–290. https://doi.org/10.1016/0022-1694(70)90255-6

Negm, A., Jabro, J., Provenzano, G., 2017. Assessing the suitability of American National Aeronautics and Space Administration (NASA) agro-climatology archive to predict daily meteorological variables and reference evapotranspiration in Sicily, Italy. Agricultural and Forest Meteorology 244–245, 111–121. https://doi.org/10.1016/j.agrformet.2017.05.022

Newham, L.T.H., Norton, J.P., Prosser, I.P., Croke, B.F.W., Jakeman, A.J., 2003. Sensitivity analysis for assessing the behaviour of a landscape-based sediment source and transport model. Environmental Modelling & Software 18, 741–751. https://doi.org/10.1016/S1364-8152(03)00076-8

Nguyen, X.C., Nguyen, T.T.H., La, D.D., Kumar, G., Rene, E.R., Nguyen, D.D., Chang, S.W., Chung, W.J., Nguyen, X.H., Nguyen, V.K., 2021. Development of machine learning - based models to forecast solid waste generation in residential areas: A case study from Vietnam. Resources, Conservation and Recycling 167, 105381. https://doi.org/10.1016/j.resconrec.2020.105381

Norman, J.M., Kustas, W.P., Humes, K.S., 1995. Source approach for estimating soil and vegetation energy fluxes in observations of directional radiometric surface temperature. Agricultural and Forest Meteorology 77, 263–293. https://doi.org/10.1016/0168-1923(95)02265-Y

Pagano, A., Amato, F., Ippolito, M., De Caro, D., Croce, D., 2025. A machine learning framework to estimate crop coefficient dynamics of citrus orchards. Computers and Electronics in Agriculture 238, 110797. https://doi.org/10.1016/j.compag.2025.110797

Pagano, A., Amato, F., Ippolito, M., De Caro, D., Croce, D., Motisi, A., Provenzano, G., Tinnirello, I., 2023. Machine learning models to predict daily actual evapotranspiration of citrus orchards under regulated deficit irrigation. Ecological Informatics 76, 102133. https://doi.org/10.1016/j.ecoinf.2023.102133

Palmer, T., 2018. The ECMWF Ensemble Prediction System: Looking Back (more than) 25 Years and Projecting Forward 25 Years. https://doi.org/10.48550/ARXIV.1803.06940

Pan, Y., Zeng, X., Xu, H., Sun, Y., Wang, D., Wu, J., 2021. Evaluation of Gaussian process regression kernel functions for improving groundwater prediction. Journal of Hydrology 603, 126960. https://doi.org/10.1016/j.jhydrol.2021.126960

Pan, Z., Hu, Y., Cao, B., 2017. Construction of smooth daily remote sensing time series data: a higher spatiotemporal resolution perspective. Open geospatial data, softw. stand. 2, 25. https://doi.org/10.1186/s40965-017-0038-z

Papadavid, G., 2011. Mapping potato crop height and leaf area index through vegetation indices using remote sensing in Cyprus. J. Appl. Remote Sens 5, 053526. https://doi.org/10.1117/1.3596388

Paparoditis, N., Papelard, J.-P., Cannelle, B., Devaux, A., Soheilian, B., David, N., Houzay, E., 2014. Stereopolis II: A multi-purpose and multi-sensor 3D mobile mapping system for street visualisation and 3D metrology. RFPT 69–79. https://doi.org/10.52638/rfpt.2012.63

Paredes, P., Trigo, I., De Bruin, H., Simões, N., Pereira, L.S., 2021. Daily grass reference evapotranspiration with Meteosat Second Generation shortwave radiation and reference ET products. Agricultural Water Management 248, 106543. https://doi.org/10.1016/j.agwat.2020.106543

Parker, W.S., 2016. Reanalyses and Observations: What's the Difference? Bulletin of the American Meteorological Society 97, 1565–1572. https://doi.org/10.1175/BAMS-D-14-00226.1

Pastorello, G., Agarwal, D., Papale, D., Samak, T., Trotta, C., Ribeca, A., Poindexter, C., Faybishenko, B., Gunter, D., Hollowgrass, R., Canfora, E., 2014. Observational Data Patterns for Time Series Data Quality Assessment, in: 2014 IEEE 10th International Conference on E-Science. Presented at the 2014 IEEE 10th International Conference on e-Science (e-Science), IEEE, Sao Paulo, Brazil, pp. 271–278. https://doi.org/10.1109/eScience.2014.45

Pastorello, G., Trotta, C., Canfora, E., Chu, H., Christianson, D., Cheah, Y.-W., Poindexter, C., Chen, J., Elbashandy, A., Humphrey, M., Isaac, P., Polidori, D., Reichstein, M., Ribeca, A., Van Ingen, C., Vuichard, N., Zhang, L., Amiro, B., Ammann, C., Arain, M.A., Ardö,

J., Arkebauer, T., Arndt, S.K., Arriga, N., Aubinet, M., Aurela, M., Baldocchi, D., Barr, A., Beamesderfer, E., Marchesini, L.B., Bergeron, O., Beringer, J., Bernhofer, C., Berveiller, D., Billesbach, D., Black, T.A., Blanken, P.D., Bohrer, G., Boike, J., Bolstad, P.V., Bonal, D., Bonnefond, J.-M., Bowling, D.R., Bracho, R., Brodeur, J., Brümmer, C., Buchmann, N., Burban, B., Burns, S.P., Buysse, P., Cale, P., Cavagna, M., Cellier, P., Chen, S., Chini, I., Christensen, T.R., Cleverly, J., Collalti, A., Consalvo, C., Cook, B.D., Cook, D., Coursolle, C., Cremonese, E., Curtis, P.S., D'Andrea, E., Da Rocha, H., Dai, X., Davis, K.J., Cinti, B.D., Grandcourt, A.D., Ligne, A.D., De Oliveira, R.C., Delpierre, N., Desai, A.R., Di Bella, C.M., Tommasi, P.D., Dolman, H., Domingo, F., Dong, G., Dore, S., Duce, P., Dufrêne, E., Dunn, A., Dušek, J., Eamus, D., Eichelmann, U., ElKhidir, H.A.M., Eugster, W., Ewenz, C.M., Ewers, B., Famulari, D., Fares, S., Feigenwinter, I., Feitz, A., Fensholt, R., Filippa, G., Fischer, M., Frank, J., Galvagno, M., Gharun, M., Gianelle, D., Gielen, B., Gioli, B., Gitelson, A., Goded, I., Goeckede, M., Goldstein, A.H., Gough, C.M., Goulden, M.L., Graf, A., Griebel, A., Gruening, C., Grünwald, T., Hammerle, A., Han, S., Han, X., Hansen, B.U., Hanson, C., Hatakka, J., He, Y., Hehn, M., Heinesch, B., Hinko-Najera, N., Hörtnagl, L., Hutley, L., Ibrom, A., Ikawa, H., Jackowicz-Korczynski, M., Janouš, D., Jans, W., Jassal, R., Jiang, S., Kato, T., Khomik, M., Klatt, J., Knohl, A., Knox, S., Kobayashi, H., Koerber, G., Kolle, O., Kosugi, Y., Kotani, A., Kowalski, A., Kruijt, B., Kurbatova, J., Kutsch, W.L., Kwon, H., Launiainen, S., Laurila, T., Law, B., Leuning, R., Li, Yingnian, Liddell, M., Limousin, J.-M., Lion, M., Liska, A.J., Lohila, A., López-Ballesteros, A., López-Blanco, E., Loubet, B., Loustau, D., Lucas-Moffat, A., Lüers, J., Ma, S., Macfarlane, C., Magliulo, V., Maier, R., Mammarella, I., Manca, G., Marcolla, B., Margolis, H.A., Marras, S., Massman, W., Mastepanov, M., Matamala, R., Matthes, J.H., Mazzenga, F., McCaughey, H., McHugh, I., McMillan, A.M.S., Merbold, L., Meyer, W., Meyers, T., Miller, S.D., Minerbi, S., Moderow, U., Monson, R.K., Montagnani, L., Moore, C.E., Moors, E., Moreaux, V., Moureaux, C., Munger, J.W., Nakai, T., Neirynck, J., Nesic, Z.,

Nicolini, G., Noormets, A., Northwood, M., Nosetto, M., Nouvellon, Y., Novick, K., Oechel, W., Olesen, J.E., Ourcival, J.-M., Papuga, S.A., Parmentier, F.-J., Paul-Limoges, E., Pavelka, M., Peichl, M., Pendall, E., Phillips, R.P., Pilegaard, K., Pirk, N., Posse, G., Powell, T., Prasse, H., Prober, S.M., Rambal, S., Rannik, Ü., Raz-Yaseef, N., Rebmann, C., Reed, D., Dios, V.R.D., Restrepo-Coupe, N., Reverter, B.R., Roland, M., Sabbatini, S., Sachs, T., Saleska, S.R., Sánchez-Cañete, E.P., Sanchez-Mejia, Z.M., Schmid, H.P., Schmidt, M., Schneider, K., Schrader, F., Schroder, I., Scott, R.L., Sedlák, P., Serrano-Ortíz, P., Shao, C., Shi, P., Shironya, I., Siebicke, L., Šigut, L., Silberstein, R., Sirca, C., Spano, D., Steinbrecher, R., Stevens, R.M., Sturtevant, C., Suyker, A., Tagesson, T., Takanashi, S., Tang, Y., Tapper, N., Thom, J., Tomassucci, M., Tuovinen, J.-P., Urbanski, S., Valentini, R., Van Der Molen, M., Van Gorsel, E., Van Huissteden, K., Varlagin, A., Verfaillie, J., Vesala, T., Vincke, C., Vitale, D., Vygodskaya, N., Walker, J.P., Walter-Shea, E., Wang, H., Weber, R., Westermann, S., Wille, C., Wofsy, S., Wohlfahrt, G., Wolf, S., Woodgate, W., Li, Yuelin, Zampedri, R., Zhang, J., Zhou, G., Zona, D., Agarwal, D., Biraud, S., Torn, M., Papale, D., 2020. The FLUXNET2015 dataset and the ONEFlux processing pipeline for eddy covariance data. Sci Data 7, 225. https://doi.org/10.1038/s41597-020-0534-3

Patil, D., Rane, N.L., Desai, P., Rane, J., 2024. Machine learning and deep learning: Methods, techniques, applications, challenges, and future research opportunities, in: Trustworthy Artificial Intelligence in Industry and Society. Deep Science Publishing. https://doi.org/10.70593/978-81-981367-4-9_2

Pelosi, A., 2023. Performance of the Copernicus European Regional Reanalysis (CERRA) dataset as proxy of ground-based agrometeorological data. Agricultural Water Management 289, 108556. https://doi.org/10.1016/j.agwat.2023.108556

Pelosi, A., Chirico, G.B., 2021. Regional assessment of daily reference evapotranspiration: Can ground observations be replaced by blending ERA5-Land meteorological reanalysis and CM-SAF

satellite-based radiation data? Agricultural Water Management 258, 107169. https://doi.org/10.1016/j.agwat.2021.107169

Pelosi, A., Terribile, F., D'Urso, G., Chirico, G., 2020. Comparison of ERA5-Land and UERRA MESCAN-SURFEX Reanalysis Data with Spatially Interpolated Weather Observations for the Regional Assessment of Reference Evapotranspiration. Water 12, 1669. https://doi.org/10.3390/w12061669

Penman, H.L., 1948. Natural evaporation from open water, bare soil and grass. Proceedings of the Royal Society of London. Series A. Mathematical and Physical Sciences 193, 120–145. https://doi.org/10.1098/rspa.1948.0037

Penman, H. L. 1956. Estimating evaporation, Trans. Amer. Geoph. Union,37, 43{46.

Pereira, L.S., Paredes, P., Jovanovic, N., 2020. Soil water balance models for determining crop water and irrigation requirements and irrigation scheduling focusing on the FAO56 method and the dual Kc approach. Agricultural Water Management 241, 106357. https://doi.org/10.1016/j.agwat.2020.106357

Pereira, S., Abreu, E.F.M., Iakunin, M., Cavaco, A., Salgado, R., Canhoto, P., 2022. Method for solar resource assessment using numerical weather prediction and artificial neural network models based on typical meteorological data: Application to the south of Portugal. Solar Energy 236, 225–238. https://doi.org/10.1016/j.solener.2022.03.003

Philip, J.R., 1957. The physical principles of water movement during the irrigation cycle 8, 124–154.

Pôças, I., Calera, A., Campos, I., Cunha, M., 2020. Remote sensing for estimating and mapping single and basal crop coefficientes: A review on spectral vegetation indices approaches. Agricultural Water Management 233, 106081. https://doi.org/10.1016/j.agwat.2020.106081

Pokorný, J., Rejšková, A., 2008. Water Cycle Management, in: Encyclopedia of Ecology. Elsevier, pp. 3729–3737. https://doi.org/10.1016/B978-008045405-4.00081-1

Priestley, C.H.B., Taylor, R.J., 1972. On the Assessment of Surface Heat Flux and Evaporation Using Large-Scale Parameters. Mon. Wea. Rev. 100, 81–92. https://doi.org/10.1175/1520-0493(1972)100%3C0081:OTAOSH%3E2.3.CO;2

Prueger, J.H., Hatfield, J.L., Parkin, T.B., Kustas, W.P., Hipps, L.E., Neale, C.M.U., MacPherson, J.I., Eichinger, W.E., Cooper, D.I., 2005. Tower and Aircraft Eddy Covariance Measurements of Water Vapor, Energy, and Carbon Dioxide Fluxes during SMACEX. Journal of Hydrometeorology 6, 954–960. https://doi.org/10.1175/JHM457.1

Pugnaire, F.I., Valladares, F. (Eds.), 1999. Handbook of functional plant ecology, Books in soils, plants, and the environment. M. Dekker, New York.

Puig-Sirera, À., Provenzano, G., González-Altozano, P., Intrigliolo, D.S., Rallo, G., 2021. Irrigation water saving strategies in Citrus orchards: Analysis of the combined effects of timing and severity of soil water deficit. Agricultural Water Management 248, 106773. https://doi.org/10.1016/j.agwat.2021.106773

Rai, R.K., Singh, V.P., Upadhyay, A., 2017. Hydrologic Computations, in: Planning and Evaluation of Irrigation Projects. Elsevier, pp. 83–229. https://doi.org/10.1016/B978-0-12-811748-4.00004-2

Rajan, D., Prasad, V.S., 2023. Evaluation of NCMRWF numerical weather prediction models for SHAR region. Advances in Space Research 71, 3981–3994. https://doi.org/10.1016/j.asr.2022.06.030

Rallo, G., González-Altozano, P., Manzano-Juárez, J., Provenzano, G., 2017. Using field measurements and FAO-56 model to assess the eco-physiological response of citrus orchards under regulated deficit irrigation. Agricultural Water Management 180, 136–147. https://doi.org/10.1016/j.agwat.2016.11.011

Rallo, G., Minacapilli, M., Ciraolo, G., Provenzano, G., 2014. Detecting crop water status in mature olive groves using vegetation spectral measurements. Biosystems Engineering 128, 52–68. https://doi.org/10.1016/j.biosystemseng.2014.08.012

Rallo, G., Paço, T.A., Paredes, P., Puig-Sirera, À., Massai, R., Provenzano, G., Pereira, L.S., 2021. Updated single and dual crop

coefficients for tree and vine fruit crops. Agricultural Water Management 250, 106645. https://doi.org/10.1016/j.agwat.2020.106645

Rallo, G., Provenzano, G., 2013. Modelling eco-physiological response of table olive trees (Olea europaea L.) to soil water deficit conditions. Agricultural Water Management 120, 79–88. https://doi.org/10.1016/j.agwat.2012.10.005

Ranghetti, L., Boschetti, M., Nutini, F., Busetto, L., 2020. "sen2r": An R toolbox for automatically downloading and preprocessing Sentinel-2 satellite data. Computers & Geosciences 139, 104473. https://doi.org/10.1016/j.cageo.2020.104473

Rasmussen, C.E., 2006. Gaussian processes for machine learning, Adaptive computation and machine learning. MIT Press, Cambridge, Mass.

Ravindran, S.M., Bhaskaran, S.K.M., Ambat, S.K.N., 2021. A Deep Neural Network Architecture to Model Reference Evapotranspiration Using a Single Input Meteorological Parameter. Environ. Process. 8, 1567–1599. https://doi.org/10.1007/s40710-021-00543-x

Reda, I., Hickey, J.R., Stoffel, T., Myers, D., 2002. Pyrgeometer calibration at the National Renewable Energy Laboratory (NREL). Journal of Atmospheric and Solar-Terrestrial Physics 64, 1623–1629. https://doi.org/10.1016/S1364-6826(02)00133-5

Reichstein, M., Falge, E., Baldocchi, D., Papale, D., Aubinet, M., Berbigier, P., Bernhofer, C., Buchmann, N., Gilmanov, T., Granier, A., Grünwald, T., Havránková, K., Ilvesniemi, H., Janous, D., Knohl, A., Laurila, T., Lohila, A., Loustau, D., Matteucci, G., Meyers, T., Miglietta, F., Ourcival, J., Pumpanen, J., Rambal, S., Rotenberg, E., Sanz, M., Tenhunen, J., Seufert, G., Vaccari, F., Vesala, T., Yakir, D., Valentini, R., 2005. On the separation of net ecosystem exchange into assimilation and ecosystem respiration: review and improved algorithm. Global Change Biology 11, 1424–1439. https://doi.org/10.1111/j.1365-2486.2005.001002.x

Riahi, K., Rao, S., Krey, V., Cho, C., Chirkov, V., Fischer, G., Kindermann, G., Nakicenovic, N., Rafaj, P., 2011. RCP 8.5—A

scenario of comparatively high greenhouse gas emissions. Climatic Change 109, 33–57. https://doi.org/10.1007/s10584-011-0149-y

Richardson, L.F., Lynch, P., 2007. Weather Prediction by Numerical Process, 2nd ed. Cambridge University Press. https://doi.org/10.1017/CBO9780511618291

Roberts, S., Osborne, M., Ebden, M., Reece, S., Gibson, N., Aigrain, S., 2013. Gaussian processes for time-series modelling. Phil. Trans. R. Soc. A. 371, 20110550. https://doi.org/10.1098/rsta.2011.0550

Robinson, D.A., Campbell, C.S., Hopmans, J.W., Hornbuckle, B.K., Jones, S.B., Knight, R., Ogden, F., Selker, J., Wendroth, O., 2008. Soil Moisture Measurement for Ecological and Hydrological Watershed-Scale Observatories: A Review. Vadose Zone Journal 7, 358–389. https://doi.org/10.2136/vzj2007.0143

Rocha, J., Perdigo, A., Melo, R., Henriques, C., 2012. Remote Sensing Based Crop Coefficients for Water Management in Agriculture, in: Curkovic, S. (Ed.), Sustainable Development - Authoritative and Leading Edge Content for Environmental Management. InTech. https://doi.org/10.5772/48561

Rosenberg, N.J., Blad, B.L., Verma, S.B., 1983. Microclimate: the biological environment, 2nd ed. ed. Wiley, New York.

Roth, K., Schulin, R., Flühler, H., Attinger, W., 1990. Calibration of time domain reflectometry for water content measurement using a composite dielectric approach. Water Resources Research 26, 2267–2273. https://doi.org/10.1029/WR026i010p02267

Rouse, R.W.H., Haas, J.A.W., Deering, D.W., 1974. Monitoring vegetation systems in the great plains with erts

Roy, D.P., Wulder, M.A., Loveland, T.R., C.E., W., Allen, R.G., Anderson, M.C., Helder, D., Irons, J.R., Johnson, D.M., Kennedy, R., Scambos, T.A., Schaaf, C.B., Schott, J.R., Sheng, Y., Vermote, E.F., Belward, A.S., Bindschadler, R., Cohen, W.B., Gao, F., Hipple, J.D., Hostert, P., Huntington, J., Justice, C.O., Kilic, A., Kovalskyy, V., Lee, Z.P., Lymburner, L., Masek, J.G., McCorkel, J., Shuai, Y., Trezza, R., Vogelmann, J., Wynne, R.H., Zhu, Z., 2014. Landsat-8: Science and product vision for terrestrial global change research. Remote Sensing

of Environment 145, 154–172. https://doi.org/10.1016/j.rse.2014.02.001

Rozenstein, O., Haymann, N., Kaplan, G., Tanny, J., 2019. Validation of the cotton crop coefficient estimation model based on Sentinel-2 imagery and eddy covariance measurements. Agricultural Water Management 223, 105715. https://doi.org/10.1016/j.agwat.2019.105715

Rozenstein, O., Haymann, N., Kaplan, G., Tanny, J., 2018. Estimating cotton water consumption using a time series of Sentinel-2 imagery. Agricultural Water Management 207, 44–52. https://doi.org/10.1016/j.agwat.2018.05.017

Saadi, S., Simonneaux, V., Boulet, G., Raimbault, B., Mougenot, B., Fanise, P., Ayari, H., Lili-Chabaane, Z., 2015. Monitoring Irrigation Consumption Using High Resolution NDVI Image Time Series: Calibration and Validation in the Kairouan Plain (Tunisia). Remote Sensing 7, 13005–13028. https://doi.org/10.3390/rs71013005

Sabzevari, Y., Eslamian, S., 2023. Reference evapotranspiration in water requirement: Theory, concepts, and methods of estimation, in: Handbook of Hydroinformatics. Elsevier, pp. 269–289. https://doi.org/10.1016/B978-0-12-821961-4.00005-1

Saitta, D., Vanella, D., Ramírez-Cuesta, J.M., Longo-Minnolo, G., Ferlito, F., Consoli, S., 2020. Comparison of Orange Orchard Evapotranspiration by Eddy Covariance, Sap Flow, and FAO-56 Methods under Different Irrigation Strategies. J. Irrig. Drain Eng. 146, 05020002. https://doi.org/10.1061/(ASCE)IR.1943-4774.0001479

Sánchez-Piñero, M., Corell, M., Moriana, A., Castro-Valdecantos, P., Martin-Palomo, M.-J., 2023. Managing Water Stress in Olive (Olea europaea L.) Orchards Using Reference Equations for Midday Stem Water Potential. Horticulturae 9, 563. https://doi.org/10.3390/horticulturae9050563

Sarkar, S., Sagan, V., Bhadra, S., Rhodes, K., Pokharel, M., Fritschi, F.B., 2023. Soybean seed composition prediction from standing crops using PlanetScope satellite imagery and machine

learning. ISPRS Journal of Photogrammetry and Remote Sensing 204, 257–274. https://doi.org/10.1016/j.isprsjprs.2023.09.010

Scanlon, T.M., Albertson, J.D., Caylor, K.K., Williams, C.A., 2002. Determining land surface fractional cover from NDVI and rainfall time series for a savanna ecosystem. Remote Sensing of Environment 82, 376–388. https://doi.org/10.1016/S0034-4257(02)00054-8

Schaaf, C., Wang, Z., 2015. MCD43A4 MODIS/Terra+Aqua BRDF/Albedo Nadir BRDF Adjusted Ref Daily L3 Global - 500m V006. https://doi.org/10.5067/MODIS/MCD43A4.006

Schaap, M.G., Leij, F.J., Van Genuchten, M.Th., 2001. rosetta : a computer program for estimating soil hydraulic parameters with hierarchical pedotransfer functions. Journal of Hydrology 251, 163–176. https://doi.org/10.1016/S0022-1694(01)00466-8

Schrader, F., Durner, W., Fank, J., Gebler, S., Pütz, T., Hannes, M., Wollschläger, U., 2013. Estimating Precipitation and Actual Evapotranspiration from Precision Lysimeter Measurements. Procedia Environmental Sciences 19, 543–552. https://doi.org/10.1016/j.proenv.2013.06.061

Sellers, P.J., 1987. Canopy reflectance, photosynthesis, and transpiration, II. The role of biophysics in the linearity of their interdependence. Remote Sensing of Environment 21, 143–183. https://doi.org/10.1016/0034-4257(87)90051-4

Sheffield, J., Ziegler, A.D., Wood, E.F., Chen, Y., 2004. Correction of the High-Latitude Rain Day Anomaly in the NCEP–NCAR Reanalysis for Land Surface Hydrological Modeling. J. Climate 17, 3814–3828. https://doi.org/10.1175/1520-0442(2004)017%3C3814:COTHRD%3E2.0.CO;2

Shi, X., Jiang, D., Qian, W., Liang, Y., 2022. Application of the Gaussian Process Regression Method Based on a Combined Kernel Function in Engine Performance Prediction. ACS Omega 7, 41732–41743. https://doi.org/10.1021/acsomega.2c05952

Shiklamanov, I.A., 2009. Hydrological cycle / v. 1. Eolss Publishers, Oxford.

Shuttleworth, W.J., Wallace, J.S., 1985. Evaporation from sparse crops-an energy combination theory. Quart J Royal Meteoro Soc 111, 839–855. https://doi.org/10.1002/qj.49711146910

Simonneaux, V., Lepage, M., Helson, D., Metral, J., Thomas, S., Duchemin, B., Cherkaoui, M., Kharrou, H., Berjami, B., Chehbouni, A., 2009. Estimation spatialisée de l'évapotranspiration des cultures irriguées par télédétection : application à la gestion de l'irrigation dans la plaine du Haouz (Marrakech, Maroc). Sécheresse 20, 123–130. https://doi.org/10.1684/sec.2009.0177

Šimůnek, J., & van Genuchten, M. T. (1998). The HYDRUS-2D software package for simulating water flow and solute transport in two-dimensional variably saturated media: Version 2.0. Research report.

Sims, D.A., Gamon, J.A., 2003. Estimation of vegetation water content and photosynthetic tissue area from spectral reflectance: a comparison of indices based on liquid water and chlorophyll absorption features. Remote Sensing of Environment 84, 526–537. https://doi.org/10.1016/S0034-4257(02)00151-7

Skamarock, W., Klemp, J., Dudhia, J., Gill, D., Barker, D., Wang, W., Huang, X.-Y., Duda, M., 2008. A Description of the Advanced Research WRF Version 3. UCAR/NCAR. https://doi.org/10.5065/D68S4MVH

Soldevilla-Martinez, M., Quemada, M., López-Urrea, R., Muñoz-Carpena, R., Lizaso, J.I., 2014. Soil water balance: Comparing two simulation models of different levels of complexity with lysimeter observations. Agricultural Water Management 139, 53–63. https://doi.org/10.1016/j.agwat.2014.03.011

Spruce, J.P., Sader, S., Ryan, R.E., Smoot, J., Kuper, P., Ross, K., Prados, D., Russell, J., Gasser, G., McKellip, R., Hargrove, W., 2011. Assessment of MODIS NDVI time series data products for detecting forest defoliation by gypsy moth outbreaks. Remote Sensing of Environment 115, 427–437. https://doi.org/10.1016/j.rse.2010.09.013

Stagno, F., Intrigliolo, F., Consoli, S., Continella, A., Roccuzzo, G., 2015. Response of Orange Trees to Deficit Irrigation Strategies: Effects on Plant Nutrition, Yield, and Fruit Quality. J. Irrig. Drain Eng.

141, 04015014. https://doi.org/10.1061/(ASCE)IR.1943-4774.0000903

Stanhill, G., 2019. Evapotranspiration, in: Reference Module in Earth Systems and Environmental Sciences. Elsevier, p. B978012409548911797X. https://doi.org/10.1016/B978-0-12-409548-9.11797-X

Steduto, P., Hsiao, T.C., Raes, D., Fereres, E., 2009. AquaCrop—The FAO Crop Model to Simulate Yield Response to Water: I. Concepts and Underlying Principles. Agronomy Journal 101, 426–437. https://doi.org/10.2134/agronj2008.0139s

Stein, M.L., 1999. Interpolation of Spatial Data, Springer Series in Statistics. Springer New York, New York, NY. https://doi.org/10.1007/978-1-4612-1494-6

Stull, R.B., 1988. An introduction to boundary layer meteorology, Atmospheric sciences library. Kluwer Academic Publishers, Dordrecht ; Boston.

Tarek, M., Brissette, F.P., Arsenault, R., 2020. Evaluation of the ERA5 reanalysis as a potential reference dataset for hydrological modelling over North America. Hydrol. Earth Syst. Sci. 24, 2527–2544. https://doi.org/10.5194/hess-24-2527-2020

Thomson, A.M., Calvin, K.V., Smith, S.J., Kyle, G.P., Volke, A., Patel, P., Delgado-Arias, S., Bond-Lamberty, B., Wise, M.A., Clarke, L.E., Edmonds, J.A., 2011. RCP4.5: a pathway for stabilization of radiative forcing by 2100. Climatic Change 109, 77–94. https://doi.org/10.1007/s10584-011-0151-4

Thornthwaite, C.W., 1948. An Approach toward a Rational Classification of Climate. Geographical Review 38, 55. https://doi.org/10.2307/210739

Topp, G.C., Reynolds, W.D., 1998. Time domain reflectometry: a seminal technique for measuring mass and energy in soil. Soil and Tillage Research 47, 125–132. https://doi.org/10.1016/S0167-1987(98)00083-X

Toth, Z., Kalnay, E., 1993. Ensemble Forecasting at NMC: The Generation of Perturbations. Bull. Amer. Meteor. Soc. 74, 2317–2330.

https://doi.org/10.1175/1520-0477(1993)074%3C2317:EFANTG%3E2.0.CO;2

Tu, Y.-H., Johansen, K., Aragon, B., El Hajj, M.M., McCabe, M.F., 2022. The radiometric accuracy of the 8-band multi-spectral surface reflectance from the planet SuperDove constellation. International Journal of Applied Earth Observation and Geoinformation 114, 103035. https://doi.org/10.1016/j.jag.2022.103035

Valor, E., 1996. Mapping land surface emissivity from NDVI: Application to European, African, and South American areas. Remote Sensing of Environment 57, 167–184. https://doi.org/10.1016/0034-4257(96)00039-9

Van Genuchten, M.Th., 1980. A Closed-form Equation for Predicting the Hydraulic Conductivity of Unsaturated Soils. Soil Science Soc of Amer J 44, 892–898. https://doi.org/10.2136/sssaj1980.03615995004400050002x

Van Vuuren, D.P., Edmonds, J., Kainuma, M., Riahi, K., Thomson, A., Hibbard, K., Hurtt, G.C., Kram, T., Krey, V., Lamarque, J.-F., Masui, T., Meinshausen, M., Nakicenovic, N., Smith, S.J., Rose, S.K., 2011a. The representative concentration pathways: an overview. Climatic Change 109, 5–31. https://doi.org/10.1007/s10584-011-0148-z

Van Vuuren, D.P., Stehfest, E., Den Elzen, M.G.J., Kram, T., Van Vliet, J., Deetman, S., Isaac, M., Klein Goldewijk, K., Hof, A., Mendoza Beltran, A., Oostenrijk, R., Van Ruijven, B., 2011b. RCP2.6: exploring the possibility to keep global mean temperature increase below 2°C. Climatic Change 109, 95–116. https://doi.org/10.1007/s10584-011-0152-3

Vanella, D., Longo-Minnolo, G., Belfiore, O.R., Ramírez-Cuesta, J.M., Pappalardo, S., Consoli, S., D'Urso, G., Chirico, G.B., Coppola, A., Comegna, A., Toscano, A., Quarta, R., Provenzano, G., Ippolito, M., Castagna, A., Gandolfi, C., 2022. Comparing the use of ERA5 reanalysis dataset and ground-based agrometeorological data under different climates and topography in Italy. Journal of Hydrology:

Regional Studies 42, 101182. https://doi.org/10.1016/j.ejrh.2022.101182

Volk, J.M., Huntington, J.L., Melton, F.S., Allen, R., Anderson, M., Fisher, J.B., Kilic, A., Ruhoff, A., Senay, G.B., Minor, B., Morton, C., Ott, T., Johnson, L., Comini De Andrade, B., Carrara, W., Doherty, C.T., Dunkerly, C., Friedrichs, M., Guzman, A., Hain, C., Halverson, G., Kang, Y., Knipper, K., Laipelt, L., Ortega-Salazar, S., Pearson, C., Parrish, G.E.L., Purdy, A., ReVelle, P., Wang, T., Yang, Y., 2024. Assessing the accuracy of OpenET satellite-based evapotranspiration data to support water resource and land management applications. Nat Water 2, 193–205. https://doi.org/10.1038/s44221-023-00181-7

Waldner, F., Canto, G.S., Defourny, P., 2015. Automated annual cropland mapping using knowledge-based temporal features. ISPRS Journal of Photogrammetry and Remote Sensing 110, 1–13. https://doi.org/10.1016/j.isprsjprs.2015.09.013

Waqas, M., Naseem, A., Humphries, U.W., Hlaing, P.T., Dechpichai, P., Wangwongchai, A., 2025. Applications of machine learning and deep learning in agriculture: A comprehensive review. Green Technologies and Sustainability 3, 100199. https://doi.org/10.1016/j.grets.2025.100199

Waring, R.H., Running, S.W., 2007. Water Cycle, in: Forest Ecosystems. Elsevier, pp. 19–57. https://doi.org/10.1016/B978-012370605-8.50007-4

Warner, T.T., 2010. Numerical Weather and Climate Prediction, 1st ed. Cambridge University Press. https://doi.org/10.1017/CBO9780511763243

Weiss, M., Baret, F., Huc, M., Hagolle, O., Lelong, C., & Dedieu, G. (2020). S2ToolBox Level 2 products: LAI, FAPAR, FCOVER, version 2.0. Algorithm Theoretical Basis Document (ATBD). 24 August 2020.

Samuel Wildhaber, Lukas Valentin Graf, Helge Aasen - Assessing the Potential of High-Resolution Satellite Constellations for Agricultural Monitoring.

Wilks, D.S., 2011. Statistical methods in the atmospheric sciences, 3rd ed. ed, International geophysics series. Academic Press, Oxford Waltham, MA.

Williams, E.L., Walter, L.M., Ku, T.C.W., Kling, G.W., Zak, D.R., 2003. Effects of CO_2 and nutrient availability on mineral weathering in controlled tree growth experiments. Global Biogeochemical Cycles 17, 2002GB001925. https://doi.org/10.1029/2002GB001925

Wu, Y., Xue, W., 2024. Data-Driven Weather Forecasting and Climate Modeling from the Perspective of Development. Atmosphere 15, 689. https://doi.org/10.3390/atmos15060689

Xue, J., Su, B., 2017. Significant Remote Sensing Vegetation Indices: A Review of Developments and Applications. Journal of Sensors 2017, 1–17. https://doi.org/10.1155/2017/1353691

Yang, G., Pu, R., Zhang, J., Zhao, C., Feng, H., Wang, J., 2013. Remote sensing of seasonal variability of fractional vegetation cover and its object-based spatial pattern analysis over mountain areas. ISPRS Journal of Photogrammetry and Remote Sensing 77, 79–93. https://doi.org/10.1016/j.isprsjprs.2012.11.008

Yang, S., Li, H., Gou, X., Bian, C., Shao, Q., 2022. Optimized Bayesian adaptive resonance theory mapping model using a rational quadratic kernel and Bayesian quadratic regularization. Appl Intell 52, 7777–7792. https://doi.org/10.1007/s10489-021-02883-5

Yang, Y., 2023. Evapotranspiration, in: Encyclopedia of Soils in the Environment. Elsevier, pp. 501–508. https://doi.org/10.1016/B978-0-12-822974-3.00084-7

Yang, Y., Anderson, M.C., Gao, F., Hain, C.R., Semmens, K.A., Kustas, W.P., Noormets, A., Wynne, R.H., Thomas, V.A., Sun, G., 2017. Daily Landsat-scale evapotranspiration estimation over a forested landscape in North Carolina, USA, using multi-satellite data fusion. Hydrol. Earth Syst. Sci. 21, 1017–1037. https://doi.org/10.5194/hess-21-1017-2017

Zegelin, S.J., White, I., Jenkins, D.R., 1989. Improved field probes for soil water content and electrical conductivity measurement using time domain reflectometry. Water Resources Research 25, 2367–2376. https://doi.org/10.1029/WR025i011p02367

Zeng, X., Dickinson, R.E., Walker, A., Shaikh, M., DeFries, R.S., Qi, J., 2000. Derivation and Evaluation of Global 1-km Fractional Vegetation Cover Data for Land Modeling. J. Appl. Meteor. 39, 826–839. https://doi.org/10.1175/1520-0450(2000)039%3C0826:DAEOGK%3E2.0.CO;2

Zhang, M., Zhang, F., Huang, X.-Y., Zhang, X., 2011. Intercomparison of an Ensemble Kalman Filter with Three- and Four-Dimensional Variational Data Assimilation Methods in a Limited-Area Model over the Month of June 2003. Monthly Weather Review 139, 566–572. https://doi.org/10.1175/2010MWR3610.1

Zhang, W. (Ed.), 2012. Ecological modeling. Nova Science Publishers, Hauppauge, N.Y.

Zhang, X., Liao, C., Li, J., Sun, Q., 2013. Fractional vegetation cover estimation in arid and semi-arid environments using HJ-1 satellite hyperspectral data. International Journal of Applied Earth Observation and Geoinformation 21, 506–512. https://doi.org/10.1016/j.jag.2012.07.003

Zotarelli, L., Dukes, M.D., Scholberg, J.M.S., Femminella, K., Muñoz-Carpena, R., 2011. Irrigation Scheduling for Green Bell Peppers Using Capacitance Soil Moisture Sensors. J. Irrig. Drain Eng. 137, 73–81. https://doi.org/10.1061/(ASCE)IR.1943-4774.0000281

Annex

Chapter 2. Input data for actual evapotranspiration modelling

2.2 In situ measurements

2.2.2 Plant-Atmosphere layer

Plant optical properties. Solar radiation interacts with vegetation in a way that determines the spectral characteristics of plant canopies and the color perceived by the human eye (**Figure I**). The human eye, sensitive only to the visible part of the spectrum, perceives vegetation as green. Beyond the visible domain, however, plants display several patterns of reflectance in the other regions. Although these reflectances are invisible to human vision, they can be detected by optical sensors and are widely used in remote sensing to assess vegetation health and physiological condition.

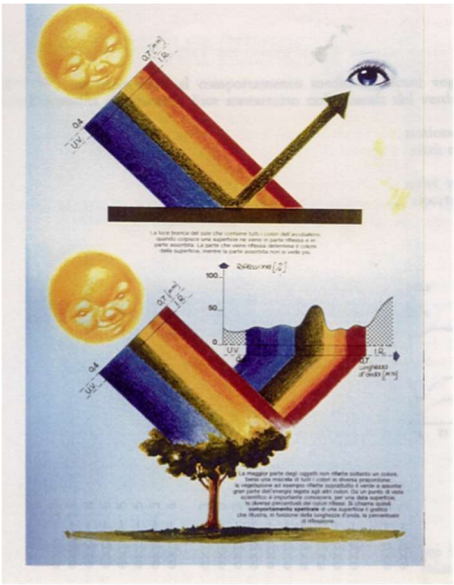

Figure I Interaction between solar radiation and plant; perception of the human eye *vs* several patterns of reflectance (from: *Lechi (2001)*)

The analysis of the vegetation spectral signature can provide information about the plant's health state and water status (Sims and Gamon, 2003; Rallo et al., 2014).

In the NIR region, high values of reflectance can indicate healthy vegetation (Moroni et al., 2019). With reference to the analysis of the plant water status, Bal et al. (2021) observed that in the VIS region (400 - 700 nm) the reflectance values, at milking stage of wheat were more accentuated in the vegetation with high degree of desiccation (line I7), rather than in the well-watered vegetation (line I1) (**Figure II**).

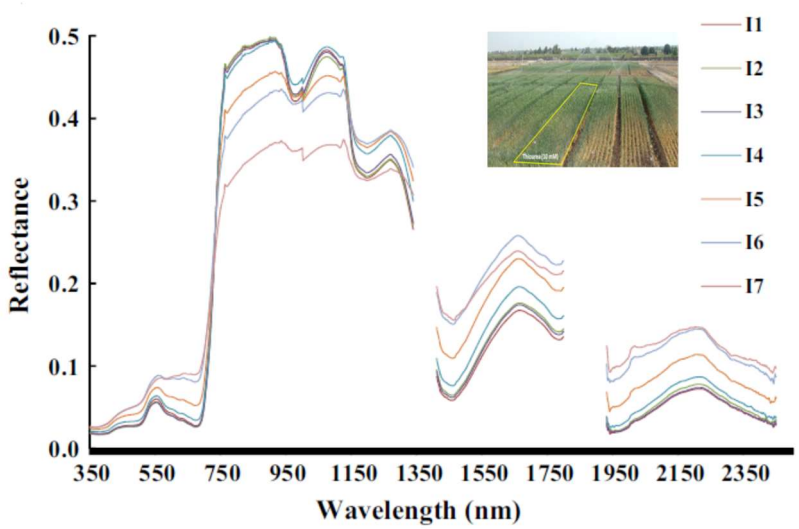

Figure II Changes in canopy reflectance spectra of wheat affected by irrigation at milking stage (from: *Bal et al., 2021*)

Moreover, Caturegli et al. (2020) illustrate the spectral reflectance profiles measured over bermudagrass subjected to three distinct levels of water stress: *i*. well-watered or saturated conditions (0 days without irrigation); *ii*. intermediate stress (7 days without irrigation); *iii*. severe water deficit (16 days without irrigation). The reflectance behavior clearly differentiates the three moisture conditions, revealing how the optical response of vegetation is strongly modulated by its water status (**Figure III**).

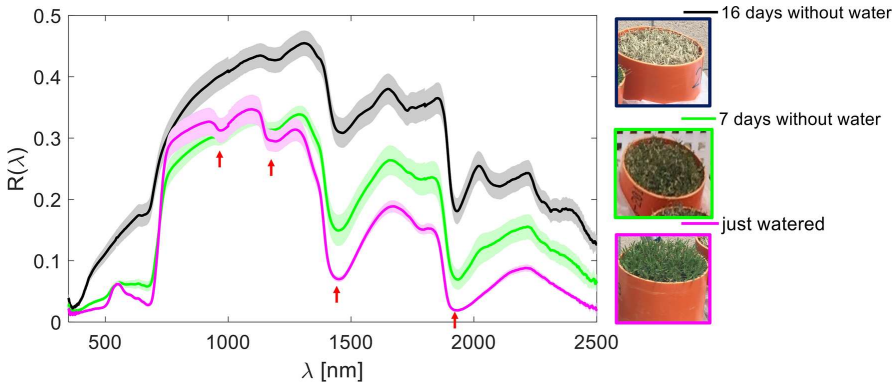

Figure III Spectral reflectance curves of bermudagrass under different levels of water deprivation: 16, 7, 0 days without watering. Each curve is the spectral reflectance averaged over the six replicates, whereas the shading shows the confidence bounds of one standard deviation around the mean. The arrows highlight the major water absorption troughs (from: *Caturegli et al., 2020*)

Across the entire spectral range, the bermudagrass under severe drought exhibits a marked increase in reflectance, consistent with the physiological desiccation of leaf tissues and a corresponding decrease in Leaf Relative Water Content (LRWC), which at 16 days without irrigation reached approximately 18%. The overall brightening of the spectrum under dry conditions reflects the loss of internal scattering efficiency and the reduction of water absorption within the leaf matrix. In the NIR and SWIR regions, four prominent absorption features can be identified. These are centered approximately at 970 nm and 1175 nm in the NIR, and at 1450 nm and 1950 nm in the SWIR, corresponding to well-known water absorption bands. Under well-watered conditions, these troughs appear deep and well-defined, reflecting the strong absorptive capacity of hydrated tissues. Conversely, in water-stressed bermudagrass, the attenuation of these features indicates reduced liquid water content and increased optical transparency of the leaf structure.

Such variations in spectral reflectance with plant water status demonstrate the sensitivity of the NIR and SWIR domains to vegetation water content, highlighting their diagnostic value for remote sensing applications. The shape and depth of water-related absorption features provide quantitative information on plant hydration and can be effectively used for the development of spectral

indices and retrieval models aimed at monitoring vegetation water stress and physiological performance.

2.4 Remote Sensing data

An example of passive proximity sensor, for plant water status detection is the spectroradiometer (**Figure IV**).

Figure IV Spectroradiometers a) from 325 to 1075 nm and b) up to 2500 nm

These instruments are able to record the values of reflectance referred to the wavelength interval ranging between 350-2500 nm. These instrument are most used for research purposes at plant or leaf scale, but over large areas, the spectroradiometric measurements are labour-intensive and time-consuming, due to the large number of observations necessary to characterize a single plot. Moreover, the high cost of the instruments and the necessity of proper calibration limit their usability.

A typical active remote sensor is the RADAR, that measures the amount of energy or backscattering coefficient ($\sigma 0$) reflected by the target hit by the EM wave generated by the sensor:

$$\sigma 0 = 10 \cdot \log (P_r \cdot P_s) \quad \textbf{(a)}$$

where P_r and P_s are the received and emitted power, respectively. In some cases, Pr can have a very low value, for this reason, $\sigma 0$ is expressed in decibel (dB) and the working wavelength range is in the microwave range (17.2-0.4 GHz).

LIght Detection And Ranging (LIDAR) system is also an active sensor that provides information about the concentration of chemical species in atmosphere, as well as the Synthetic Aperture Radar (SAR)

systems that provide accurate measurements of altitude useful for interferometric application.

Spectral resolution. The sensitivity of a single spectral band is defined by the relative spectral response function (**Figure V**).

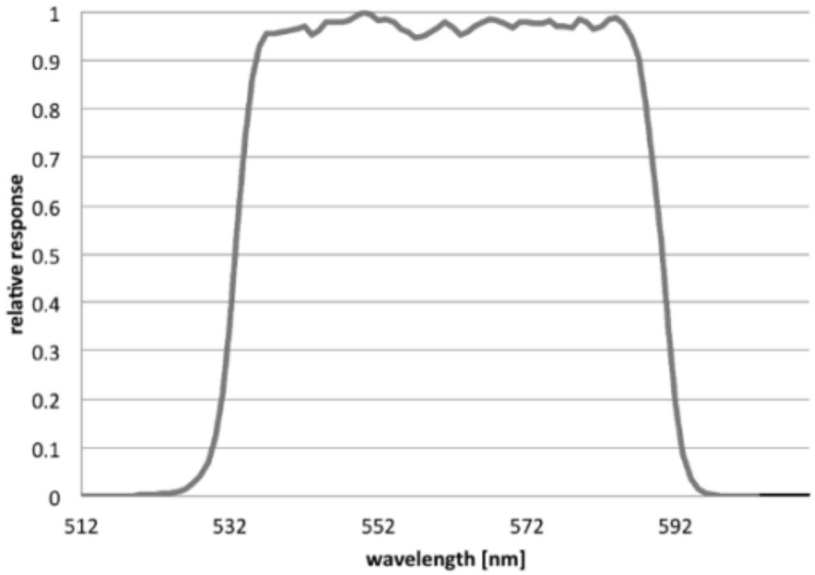

Figure V Example of relative spectral response of the band 1 (costal aerosol) characteristic of the operational land imager (OLI) sensor installed on the Landsat 8 and Landsat 9 mission (from: *https://landsat.gsfc.nasa.gov/article/preliminary-spectral-response-of-the-operational-land-imager-in-band-band-average-relative-spectral-response/*)

Based on the number of spectral bands present in the sensors, this can be identified as hyperspectral (*e.g.*, PRISMA) or multispectral (*e.g.*, Sentinel-2, Landsa-8, Landsat-9) sensor. The ability of the sensor to discriminate the energy differences between different surfaces depends by the radiometric resolution. The most sensitive sensors are those able to detect the small differences in reflected energy.

Radiometric resolution. **Figure VI** shows the comparison between images characterized by different radiometric resolution from 8- bit to 1- bit image.

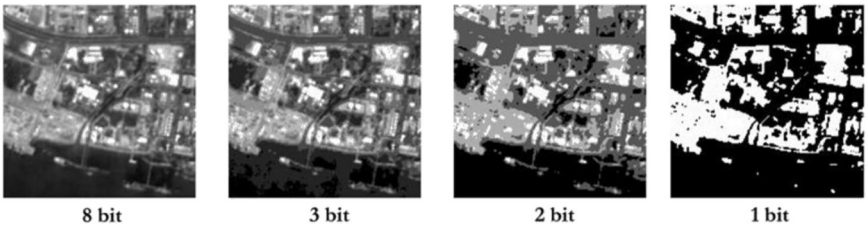

Figure VI Comparison between images characterized by different radiometric resolution from 1 to 8 bit (from: *Lechi (2001)*)

There is an evident difference in the level of detail discernible between 8-bit and 1-bit image which is dependent on their radiometric resolutions.

Spatial resolution. In RS applications, the spatial resolution is defined using angular characteristics: Field Of View (*FOV*) and Instant Field Of View (*IFOV*) (**Figure VII**).

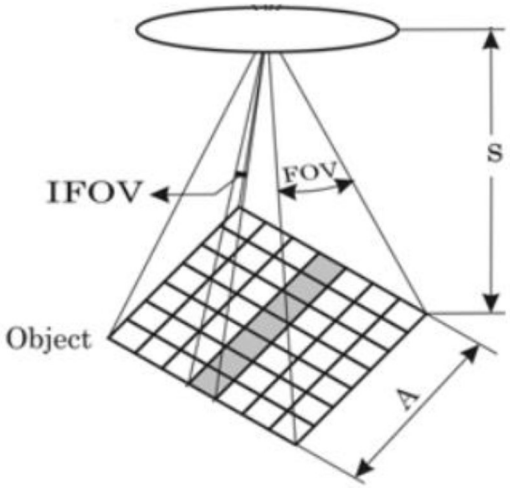

Figure VII Geometric representation of field of view (FOV) and instantaneous field of view (IFOV) for optical system (from: *Lechi (2001)*)

The *FOV* is defined as an angle of vision of the whole swath width (A):

$$A = FA \cdot FOV \qquad \textbf{(b)}$$

where *FA* is the flight altitude or earth-sensor distance, and IFOV is the angle of vision of one pixel expressed as Ground Simple Distance (*GSD*):

$$GSD = FA \cdot IFOV \quad \textbf{(c)}$$

The value of *IFOV* for a specific band defines the amount of reflected energy that the sensor can acquire. In the VIS region, the amount of available reflected energy is greater than in the SWIR region, thus the spatial resolution in this region will be worse than in the VIS region.

At 10 m resolution, individual features are clearly distinguishable, providing high spatial detail suitable for local-scale analyses. As the resolution decreases to 20 m and 40 m, fine details become progressively blurred, and small objects merge into larger, more homogeneous areas. At 60 m resolution, only the general land-cover patterns remain visible, while most small-scale features are lost. This comparison highlights how increasing pixel size reduces spatial detail but can still be valuable for large-scale or regional applications where fine resolution is not required (**Figure VIII**).

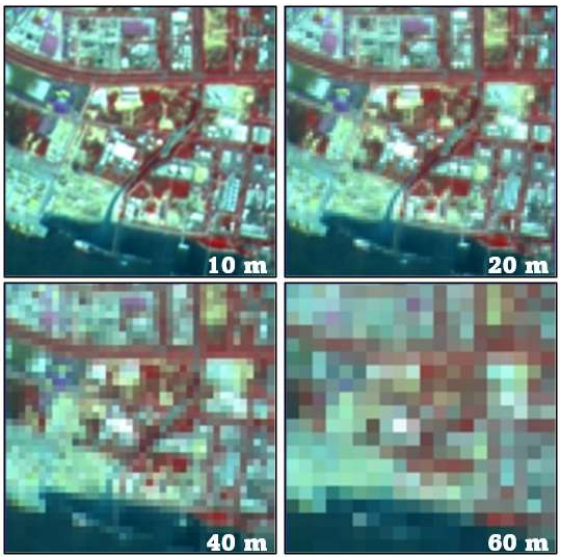

Figure VIII Comparison between images characterized by different radiometric spatial resolution (from: *Lechi (2001)*)

Temporal resolution. For earth observation purposes, there are two main types of orbits geostationary (**Figure IX -a**) and sun-synchronous (**Figure IX -b**).

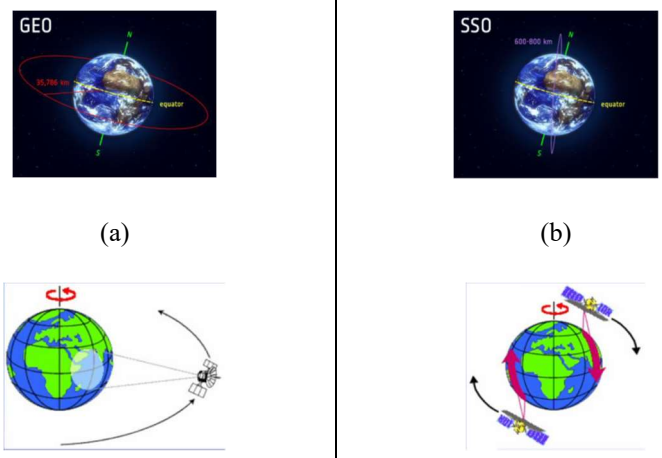

(a) (b)

Figure IX a) Geostationary orbit and b) sun-synchronous orbit (from: *https://www.esa.int/ESA_Multimedia/Images/2020/03/Geostationary_orbit*)

The satellites with a geostationary orbit are synchronous with the rotation of the earth. In particular, the satellites that need to stay constantly above a specific zone, such as telecommunication, weather or radar, use this kind of orbit.

Whereas the satellites with sun-synchronous orbit travel past earth from north to south, synchronous with the sun. Thus, the satellite always visits the same zone at the same local time.

The time interval between one acquisition and the next one is the temporal resolution. The possibility of monitoring the same place at different time instant is very important to detect the possible changes in the environment. For this reason, the satellites for earth observation and environmental applications are generally sun synchronous.

Remote sensing image. A remote sensing image can be conceptualized as a stack of multiple images, each corresponding to a specific spectral band captured by the sensor. The number of layers in this stack depends on the spectral configuration of the sensor, ranging from a few broad bands in multispectral systems to hundreds of narrow bands in hyperspectral sensors (**Figure X**).

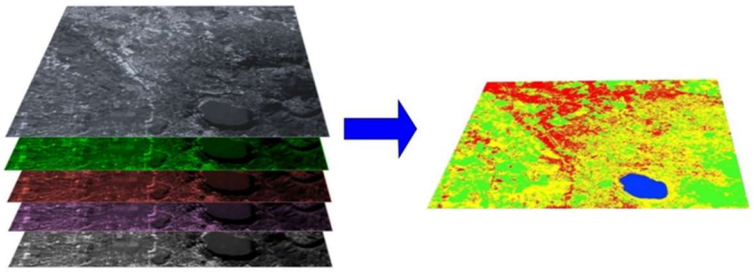

Figure X Example of a image stack and a composite image (from: *Lechi (2001)*)

Each individual band is composed of a matrix of pixels, where each pixel represents the average radiance or reflectance value measured from a specific area on the ground (**Figure XI**).

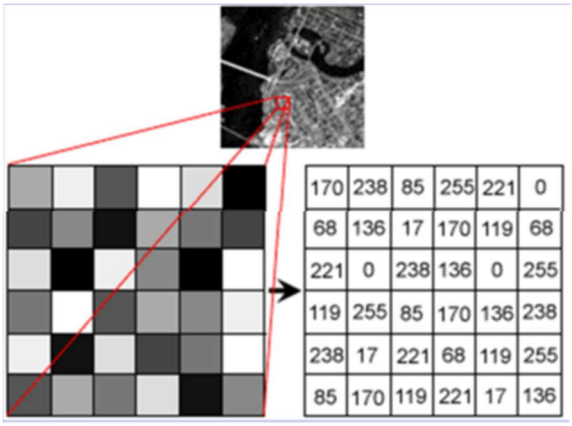

Figure XI Raster representation (from: *Lechi (2001)*)

When these single-band images are combined, they can be displayed in different color composites depending on which spectral channels are assigned to the Red, Green, and Blue (RGB) display components. By assigning the visible red, green, and blue bands to their corresponding channels, one obtains a true color image, which closely resembles what the human eye would perceive (**Figure XII**).

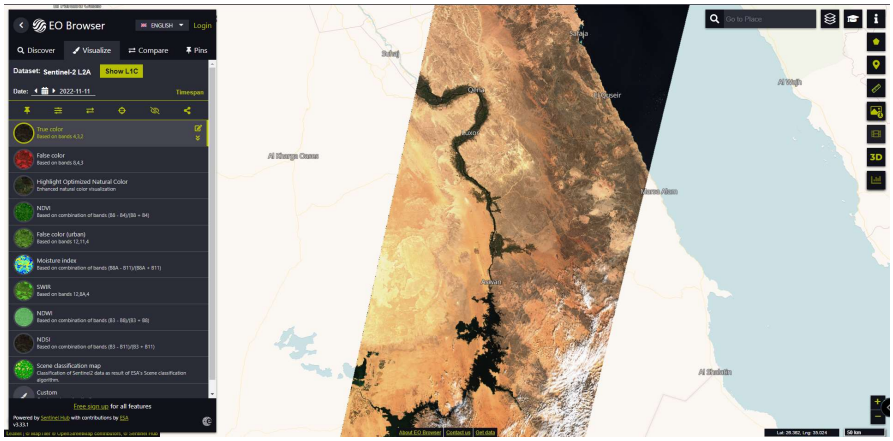

Figure XII RGB composition (from: *https://apps.sentinel-hub.com/eo-browser/*)

Alternatively, by assigning non-visible bands (*e.g.*, NIR, red, and green) to the RGB channels, a false color image can be produced. False color composites are particularly useful for highlighting specific surface features, such as vegetation vigor, soil moisture, or water bodies. that may not be easily distinguishable in natural color imagery (**Figure XIII**).

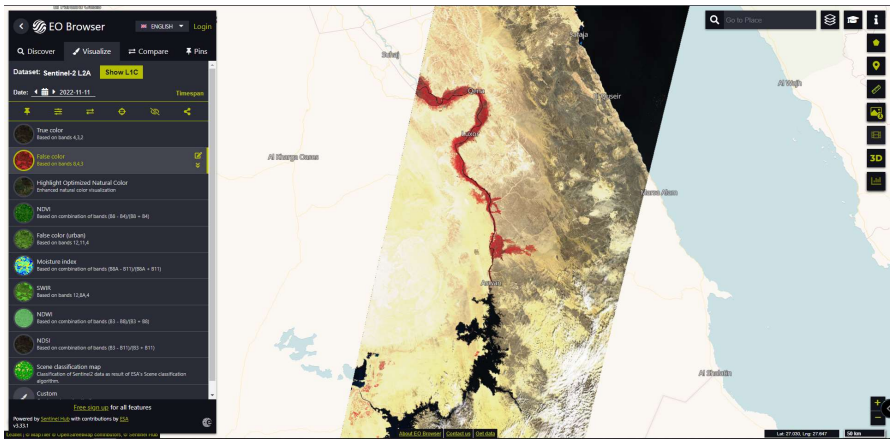

Figure XIII False color composition (from: *https://apps.sentinel-hub.com/eo-browser/*)

This layered structure, often referred to as an image cube or band stack, provides a rich source of spectral information that can be analyzed to derive biophysical parameters, classify land cover, and monitor environmental changes over time.

The ability to combine and interpret these spectral bands is fundamental to remote sensing analysis and underpins most modern applications in environmental monitoring, agriculture, and water resource management.

PR Sicilia FSE+ 2021-2027 - CCI 2021IT05SFPR014

Avviso 01/2022 per il finanziamento di borse regionali di dottorato di ricerca in Sicilia - A.A 2022/2023

CIP BORSE.SICILIA.REG.NAZ/3.10.5/2021.IT.05.SFPR.014/002/04.7/09.02.03/A01_22/0003 CUP G71I22001190006

UNIVERSITA' DEGLI STUDI DI PALERMO
DIPARTIMENTO DI INGEGNERIA

PALERMO
LUGLIO, 2026

Dario De Caro